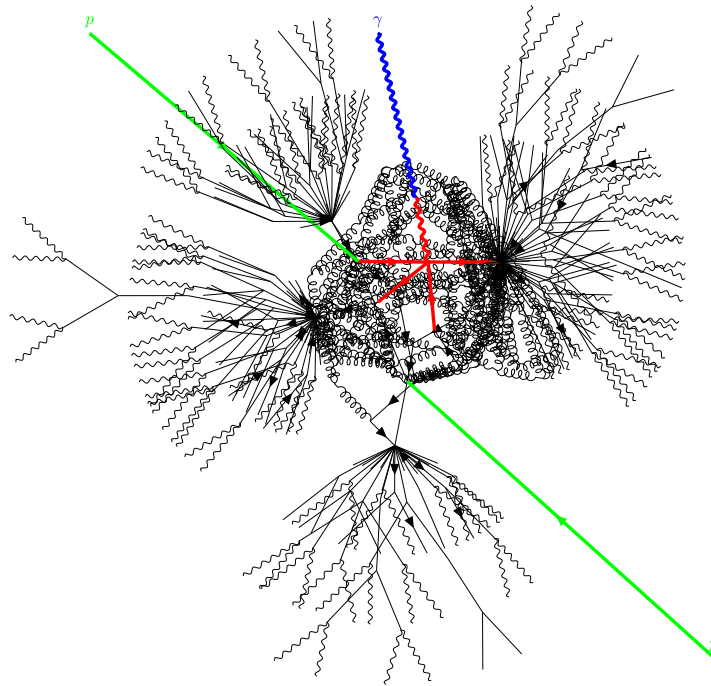


Alexander Puck Neuwirth

Precision computations for photons, jets and BSM-particles at the LHC

-2024-



Theoretische Physik

**Precision computations for photons, jets and
BSM-particles at the LHC**

Inaugural-Dissertation
zur Erlangung des Doktorgrades (Dr. rer. nat.)
der Naturwissenschaften im Fachbereich Physik
der Mathematisch-Naturwissenschaftlichen Fakultät
der Universität Münster

vorgelegt von
Alexander Puck Neuwirth
aus Waiblingen
-2024-

Dekan: Prof. Dr. Rudolf Bratschitsch

Erster Gutachter: Prof. Dr. Michael Klasen

Zweiter Gutachter: Prof. Dr. Christian Klein-Bösing

Tag der mündlichen Prüfung:

Tag der Promotion:

Kurzfassung

In dieser Arbeit werden verschiedene Methoden zur präzisen Berechnung von Prozessen am Large Hadron Collider erläutert, implementiert und durchgeführt.

Im Kontext der Quantenchromodynamik können Berechnungen fester Ordnung mit Partonschauern mithilfe der POWHEG-Methode kombiniert werden. Dadurch lässt sich die Produktion reeller und virtueller Photonen berechnen, die beide als Signale für das Quark-Gluon-Plasma dienen können. Da virtuelle Photonen, gemessen als Dileptonen, nicht einfach von semileptonischen Zerfällen schwerer Hadronen unterschieden werden können, müssen auch diese simuliert werden. Meine Berechnung eines neuen Prozesses für POWHEG BOX V2, um Monte-Carlo-Events von einem Photon mit zwei Jets in nächstführender Ordnung Quantenchromodynamik zu erzeugen, wird in dieser Arbeit beschrieben und mit Daten des ATLAS Experiments für isolierte Photonen mit zwei gemessenen Jets verglichen. Die Verwendung dieser mit sowohl Pythia- als auch Herwig-Partonschauer führen dazu, dass die Vorhersagen konsistent zu Ergebnissen der nächst-nächst-führender Ordnung sind.

Für die Untersuchungen elektroschwacher supersymmetrischer Teilchen am Large Hadron Collider bietet sich die Resummation niederenergetischer Gluonen an, da potenziell große Logarithmen berücksichtigt werden. Ich berechne die Erzeugung eines Squarks und eines Elektroweakino in nächstführender Ordnung Quantenchromodynamik kombiniert mit nächstführenden Logarithmen. Für Squarkmassen im Teraelektronenvoltbereich kommt es zu einer Vergrößerung des Wirkungsquerschnitts um einige Prozentpunkte und zu einer Verringerung der theoretischen Unsicherheiten. Dieser Prozess wird mit Elektroweakinopaar und Squarkpaar Produktion kombiniert, um ein stärkeres experimentelles Signal für Supersymmetrie zu erhalten. Darüber hinaus können die Massenausschlussgrenzen im minimalen supersymmetrischen Standardmodell durch die Kombination der unkorrelierten Signale aus ATLAS- und CMS-Analysen deutlich verbessert werden.

Abstract

In this thesis, various methods for the precise calculation of processes at the Large Hadron Collider are explained, implemented, and carried out.

In the context of quantum chromodynamics, fixed-order calculations can be matched with parton showers using the POWHEG method. This allows for the calculation of real and virtual photon production, both of which can serve as signals for the quark-gluon plasma. Since virtual photons, measured as dileptons, cannot easily be distinguished from semileptonic decays of heavy hadrons, these must also be simulated. My calculation of a new process for POWHEG BOX V2, to generate Monte Carlo events for a photon with two jets in next-to-leading order quantum chromodynamics, is described in this thesis and compared with data from the ATLAS experiment for isolated photons with two resolved jets. The use of both Pythia and Herwig parton showers results in predictions that are consistent with next-to-next-to-leading order results.

For the investigation of electroweak supersymmetric particles at the Large Hadron Collider, the resummation of soft gluons is useful, as potentially large logarithms are taken into account. I calculate the production of a squark and an electroweakino in next-to-leading order quantum chromodynamics matched to next-to-leading logarithms. For squark masses in the tera-electronvolt range, there is an increase in the cross section by a few percentage points and a reduction in theoretical uncertainties. This process is combined with electroweakino pair and squark pair production to obtain a stronger experimental signal for supersymmetry. Furthermore, the mass exclusion limits in the minimal supersymmetric standard model can be significantly improved by combining the uncorrelated signals from ATLAS and CMS analyses.

List of Publications

Articles

- J. Fiaschi, B. Fuks, M. Klasen, A. Neuwirth: Soft gluon resummation for associated squark-electroweakino production at the LHC ([1], JHEP 06 (2022) 130, arxiv:2202.13416):

This project was initiated by MK. In my master's thesis already, I started calculating the NLO correction for squark-electroweakino production. JF did the computation of the hard matching coefficients and soft anomalous dimensions, which were cross-checked by me and BF. I executed the `Resummino` code to generate the tables and plots. I also drafted the initial version of the publication, with all authors contributing to the finalization of the draft.

- J. Fiaschi, B. Fuks, M. Klasen, A. Neuwirth: Electroweak superpartner production at 13.6 TeV with Resummino ([2], Eur.Phys.J.C 83 (2023) 8, 707, arxiv:2304.11915):

This update of the `Resummino` manual was initiated by MK and BF. I conducted cross-checks of the `Resummino` code against `MadGraph` and then ran the `Resummino` code to produce the plots and tables. I wrote the initial draft of the publication, with all authors contributing to the finalization of the draft.

- A. Andronic, T. Ježo, M. Klasen, C. Klein-Bösing, A. Neuwirth: Di-electron production at the LHC: Unravelling virtual-photon and heavy-flavour contributions ([3], JHEP 05 (2024) 222, arxiv:2401.12875):

This project was initiated by MK, with TJ proposing the idea to update the hadronic contribution to include uncertainties. I ran the POWHEG Monte Carlo and generated the plots, recast the ALICE analysis to Rivet, and performed the fit of the cocktail to the data. I wrote the initial draft of the publication, with all authors contributing to its finalization.

- A. Feike, J. Fiaschi, B. Fuks, M. Klasen, A. Neuwirth: Combination and Reinterpretation of LHC SUSY Searches ([4], JHEP 07 (2024) 122, arxiv:2403.11715):

This project was initiated by BF and formed part of AF's master's thesis. I assisted AF with running the necessary codes `LHAPDF`, `MadGraph`, `Resummino`, `TACO`, etc., and provided support with understanding the theoretical background. I also wrote the code to extract the cross sections from `Resummino`. AF drafted the initial version of the publication, with all authors contributing to its finalization.

- T. Ježo, M. Klasen, A. Neuwirth: Prompt photon production with two jets ([5], submitted to JHEP, arxiv:2409.01424):

This project was initiated by MK. I calculated and cross checked the NLO correction for prompt photon production with two jets in POWHEG. I wrote a Rivet analysis and ran the POWHEG Monte Carlo to generate the plots. I drafted the initial version of the publication, with all authors contributing to its finalization.

Software

- Alexander Puck Neuwirth: APN-Pucky/HEPi ([6], 10.5281/ZENODO.8430837):
I developed this code to automate the evaluation of **Resummino** and distribute the workload across multiple clusters.
- Alexander Puck Neuwirth: APN-Pucky/pyfeyn2 ([7], 10.5281/ZENODO.8430851):
I wrote this code to draw Feynman diagrams in Python, building on a previous version of pyfeyn.
- Alexander Puck Neuwirth: APN-Pucky/feynml ([8], 10.5281/ZENODO.8430845):
I developed this code to systematically describe Feynman diagrams in Python, building on a previous version of feynml.
- Alexander Puck Neuwirth: APN-Pucky/feynamp ([9], 10.5281/ZENODO.11091562):
I developed this code to compute Feynman diagrams in Python.

Contents

1	Introduction	1
2	Theory	3
2.1	Standard Model	4
2.1.1	Quantum electrodynamics	4
2.1.2	Electroweak Sector	6
2.1.3	Higgs sector and Yukawa interactions	7
2.1.4	Quantum chromodynamics	7
2.2	Collider physics	9
2.2.1	Factorization theorem	9
2.2.2	Parton distribution functions	10
2.2.3	Hard scattering	14
2.2.4	Heavy resonances decay	16
2.2.5	Parton shower	17
2.2.6	Fragmentation	21
2.2.7	Hadronisation	24
2.3	Heavy-ion collisions	25
2.3.1	Initial-state effects and nuclear parton distribution functions	26
2.3.2	Quark-gluon plasma	28
3	Computation methods	33
3.1	Next-to-leading order calculations	33
3.1.1	Feynman rules	33
3.1.1.1	Eikonal approximation	34
3.1.1.2	Colour lines	36
3.1.1.3	Helicity amplitudes	41
3.1.2	Regularization	41
3.1.2.1	Dimensional regularization schemes	42
3.1.2.2	Passarino-Veltman reduction	43
3.1.3	Renormalization	46
3.1.3.1	Quarks	47
3.1.3.2	Gluon	49
3.1.4	Subtraction methods	49
3.1.4.1	The FKS subtraction method	49
3.1.4.2	The Catani-Seymour formalism	51
3.1.5	On-shell resonances	54
3.1.5.1	Subtraction and removal	54

	3.1.5.2 Breit-Wigner cutoff	55
3.2	Monte Carlo methods	56
	3.2.1 Integrators	57
	3.2.2 Importance sampling	59
	3.2.3 Random number generation and sequences	61
	3.2.4 Event generation	61
	3.2.5 Shower Monte Carlo	63
	3.2.6 Full event generation	64
3.3	Jets	67
	3.3.1 Algorithms	67
	3.3.1.1 Stermann-Weinberg	67
	3.3.1.2 Cone	67
	3.3.1.3 JADE	68
	3.3.1.4 Durham	69
	3.3.1.5 k_T algorithm	69
	3.3.1.6 Cambridge/Aachen	69
	3.3.1.7 Anti- k_T algorithm	70
	3.3.2 Merging	71
	3.3.2.1 CKKW-L	71
	3.3.2.2 Differential jet rates	72
	3.3.3 Matching	72
	3.3.3.1 Madgraph5 - MC@NLO	73
	3.3.3.2 POWHEG method	75
4	Photon production with POWHEG	79
4.1	Virtual photon production	81
	4.1.1 Sampling in POWHEG	82
	4.1.1.1 Linear sampling	83
	4.1.1.2 Logarithmic sampling	84
	4.1.1.3 Optimized sampling	84
	4.1.2 Signal and background	87
	4.1.3 Simulation setup and event selection	89
	4.1.4 Our predictions	92
	4.1.4.1 The signal: direct virtual photon production	93
	4.1.4.2 The background: open charm and bottom production	95
	4.1.4.3 Combined analysis of the signal and background	98
	4.1.4.4 Initial- and final-state nuclear effects in PbPb collisions	102
4.2	Real photon production	104
	4.2.1 Prompt photon production with one jet	105
	4.2.1.1 The POWHEG method as an alternative to fragmentation functions	106
	4.2.1.2 Enhanced QED radiation	108
	4.2.1.3 Example event	109
	4.2.1.4 Forward Calorimeter	110
	4.2.2 Prompt photon production with two jets at NLO	110
	4.2.2.1 Phase space	111
	4.2.2.2 Calculation and implementation	112
	4.2.3 Isolated-prompt photons with 2 jets at 13 TeV	115

4.2.3.1	Simulation setup	115
4.2.3.2	Isolation schemes and parton showers	115
4.2.3.3	Comparison with ATLAS data	118
5	Electroweak superpartner production with Resummino	125
5.1	The Minimal Supersymmetric Standard Model	125
5.1.1	Supersymmetry	126
5.1.2	Soft breaking	127
5.1.2.1	Squarks	130
5.1.2.2	Electroweakinos	133
5.1.2.3	Gluino	134
5.1.3	Collider phenomenology	134
5.2	Threshold resummation of soft gluons	136
5.2.1	Refactorization	137
5.2.2	Hard matching coefficient	141
5.2.3	Matching and expansion	142
5.3	Threshold resummation for squark electroweakino production	144
5.3.1	Leading and next-to-leading order	145
5.3.2	Soft anomalous dimension	146
5.3.3	Hard matching coefficients	149
5.3.3.1	Mellin space \mathbf{P} operator	150
5.3.3.2	Mellin space \mathbf{K} operator	150
5.3.4	Numerical results	155
5.3.4.1	Total cross sections and their scale uncertainty	155
5.3.4.2	Parton density uncertainties of the total cross section	156
5.3.4.3	Squark and gaugino mass dependence of the total cross section	158
5.4	Precision predictions for electroweak SUSY processes in simplified models at 13.6 TeV	158
5.4.1	Slepton pair production	161
5.4.2	Higgsino pair production	163
5.4.3	Gaugino pair production	165
5.5	LHC SUSY search	168
5.5.1	Theoretical setup and hard-scattering signal simulation	169
5.5.2	Analysis setup	171
5.5.3	Results	176
6	Conclusion and outlook	181
6.1	Conclusion	181
6.2	Outlook	182
A	Appendix	183
A.1	Notations	183
A.1.1	Natural units	183
A.1.2	Einstein summation convention	183
A.1.3	Lorentz indices	183
A.1.4	Subtraction methods	184
A.1.4.1	Matrix elements	184
A.1.4.2	Colour structure	184

A.1.5	Feynman Rules	184
A.2	Feynman rules	185
A.2.1	Standard model	185
A.2.1.1	Propagators	185
A.2.1.2	Vertices	185
A.2.2	Minimal Supersymmetric Standard Model	186
A.2.2.1	Propagators	186
A.2.2.2	Vertices	186
A.3	Relations	187
A.3.1	Colour	188
A.3.1.1	Definitions	188
A.3.1.2	Fierz identity	188
A.3.2	Gamma Matrix	188
A.3.2.1	Gamma trace relations	188
A.3.2.2	D -dimensional Gamma Matrix	188
A.3.3	P-operators	189
A.3.4	K-operator	189
A.4	Distributions	191
A.4.1	Dirac delta distribution	192
A.4.2	Heaviside step function	192
A.4.3	Plus distribution	192
A.5	Bonus Material	193
A.5.1	SISCone jet algorithm	193
A.5.2	MLM jet merging	193
A.5.3	FxFx jet merging	194
A.5.4	Jet observables	194
A.6	Files	195
A.6.1	POWHEG-BOX-V2	195
A.6.2	Resummino	196

Chapter 1

Introduction

Quantum chromodynamics (QCD), the fundamental theory describing the strong interactions between quarks and gluons, has achieved remarkable successes over the course of several decades. Despite its non-perturbative nature at low energy scales, QCD's perturbative description of high-energy particle collisions has been highly accurate. This precision has been made possible through factorization theorems, which separate non-perturbative and perturbative components of an observable. The continuous development of particle colliders, such as the Large Hadron Collider (LHC) and Relativistic Heavy Ion Collider (RHIC), has facilitated increasingly precise measurements of QCD processes. These improvements have necessitated higher-order corrections to QCD processes, extending beyond leading-order (LO) and next-to-leading-order (NLO), as the precision and statistics of the experiments improve. The most accurate comparison between theory and experiments is achieved by Monte Carlo (MC) simulations, which combine fixed-order calculations with higher-order soft and collinear emissions.

One of the most significant advancements in heavy-ion collisions is the study of the quark-gluon plasma (QGP), a state of QCD matter formed at high energy densities, such as in the early Universe. High-energy photons produced in all stages of heavy-ion collisions are important probes for determining QCD properties such as the temperature of the QGP. A useful probe for understanding the formation of the QGP are di-electrons, which arise from virtual photon decays. Unlike prompt photons, virtual photons can have a measurable invariant mass, which serves as an effective means of differentiating between collision stages and is unaffected by the blueshift due to the expansion of the medium. As electromagnetic probes, prompt photons also offer a relatively clean way to assess nuclear parton distribution functions (nPDFs), particularly at low Bjorken- x , where the gluon density increases significantly, and gluon saturation effects may come into play. However, distinguishing prompt photons arising from the hard process and photons originating from other sources becomes increasingly challenging at lower transverse momentum. This is because non-perturbative processes, such as fragmentation and hadron decays, generate more photons, making the use of isolation cones necessary. Instead of relying on fragmentation functions (FFs) to model the fragmentation of partons into photons, we use the Positive Weight Hardest Emission Generator (POWHEG) method to match the fixed-order calculation to a parton shower (PS).

Despite its successes, the Standard Model (SM) is incomplete, failing to account for phenomena like dark matter or the matter-antimatter asymmetry. Extensions like the Minimal Supersymmetric Standard Model (MSSM) aim to address these shortcomings

by introducing new particles and symmetries, such as supersymmetry (SUSY). SUSY is a compelling framework for new physics, with the LHC serving as the primary experimental avenue for searching for supersymmetric particles. These searches have focused on both strong production of squarks and gluinos and weak production of sleptons, neutralinos, and charginos. Although no direct evidence for SUSY has yet been observed, experimental limits continue to push the mass bounds of these particles higher. As the masses approach the production threshold, large logarithmic terms emerge due to the emission of multiple soft gluons, and these terms must be resummed to enhance the accuracy of theoretical predictions. The production of squarks in association with electroweak gauginos is of particular interest, as it provides a production mechanism at LHC energies that is mostly unaffected by the stringent gluino limits, and completes the set of processes found in `Resumino`. Additionally, combining different simplified SUSY model production channels with various experimental analyses is essential to achieve the most comprehensive exclusion bounds and extend them further.

The structure of this thesis is as follows. First, in chapter 2 we introduce the theoretical framework of the SM of particle physics. The necessary computational methods are discussed in chapter 3 and lay the foundation for the following studies of photon production in nucleon collisions in chapter 4. In chapter 5, threshold resummation is presented in the context of the MSSM, with the aim of improving theoretical predictions of the ongoing search for SUSY particles at the LHC. We conclude this thesis with an outlook on future research directions in chapter 6.

Chapter 2

Theory

Before diving into particle physics and the SM, it's important to first clarify what a particle is. In high-energy physics, a particle is a fundamental or composite object that exhibits wave-particle duality and can be described by quantum field theory (QFT). Particles are generally categorized based on their properties like mass, charge, spin, and interactions. Fundamental particles are not known to be made of any smaller constituents. Examples include quarks, leptons (like electrons and neutrinos), and gauge bosons (like photons, W and Z bosons, and gluons). These particles are the basic building blocks of matter and force carriers, respectively. Composite particles are made of two or more fundamental particles bound together. Examples include protons, neutrons and mesons which are made of quarks.

A more mathematical definition of a particle is that it transforms under the irreducible unitarity representation of the Poincaré group, which is the symmetry group of Minkowski spacetime that combines translations, rotations, and boosts while preserving spacetime intervals. It is defined by its generators, the energy-momentum operator P^μ , which generates translations, and the angular momentum operator $M^{\mu\nu}$, which generates Lorentz transformations

$$[P_\mu, P_\nu] = 0, \quad (2.0.1)$$

$$[M_{\mu\nu}, P_\nu] = i(g_{\nu\rho}P_\mu - g_{\mu\rho}P_\nu), \quad (2.0.2)$$

$$[M_{\mu\nu}, M_{\rho\sigma}] = -i(g_{\mu\rho}M_{\nu\sigma} + g_{\nu\sigma}M_{\mu\rho} - g_{\mu\sigma}M_{\nu\rho} - g_{\nu\rho}M_{\mu\sigma}). \quad (2.0.3)$$

Particles possess properties like mass and spin, and under Poincaré transformations, only their momenta and spin projections change. The representations in which these states transform are crucial for describing particle behaviour. Unitary representations ensure the preservation of probabilities in quantum mechanics, a requirement for computing Poincaré-invariant quantities, such as matrix elements. However, not all representations of the Poincaré group are unitary. Only specific infinite-dimensional ones are relevant for physical theories. These unitary irreducible representations are labelled by mass and spin and form the foundation for describing particles. Embedding these representations into space-time objects like scalar, vector, spinor and tensor fields, one can construct Lagrangians that describe the interactions of particles. [10]

The usual components of the Lagrangian include fields representing particles or mediators of forces, their derivatives and constants which parametrize masses and couplings. As in classical mechanics the action $S = \int d^4x \mathcal{L}$ is extremized to obtain the equations

of motion, the fields are quantized by promoting them to operators and the Lagrangian is used to derive the Feynman rules for the interactions between the fields. The full Lagrangian is separated into free and interaction parts, $\mathcal{L} = \mathcal{L}_0 + \mathcal{L}_{\text{int}}$. For the free part, the probability of a particle transitioning between two points is represented by the Green's function $D_F(x - y)$, which, in momentum space, is given by its Fourier transform $D_F(p)$. For a scalar field $\phi(x)$ this is the Klein-Gordon equation [11, 12]

$$\mathcal{L}_0 = \frac{1}{2}\partial_\mu\phi\partial^\mu\phi - \frac{1}{2}m^2\phi^2 \quad \Longrightarrow \quad (\partial_\mu\partial^\mu + m^2)\phi = 0 \quad \Longrightarrow \quad D_\phi(p) = \frac{i}{p^2 - m^2 + i\epsilon}, \quad (2.0.4)$$

and for spinors $\psi(x)$ the Dirac equation [13]

$$\mathcal{L}_0 = \bar{\psi}(i\gamma^\mu\partial_\mu - m)\psi \quad \Longrightarrow \quad (i\gamma^\mu\partial_\mu - m)\psi = 0 \quad \Longrightarrow \quad D_\psi(p) = \frac{i}{\gamma^\mu p_\mu - m + i\epsilon}, \quad (2.0.5)$$

where the Feynman prescription $i\epsilon$ is used to ensure the poles of the propagator do not violate causality.

2.1 Standard Model

The SM of particle physics is given by the quantum field theory based on the gauge group $\text{SU}(3)_C \times \text{SU}(2)_L \times \text{U}(1)_Y$. The full Lagrangian density is given by

$$\mathcal{L}_{\text{SM}} = \mathcal{L}_{\text{gauge}} + \mathcal{L}_{\text{fermion}} + \mathcal{L}_{\text{Higgs}} + \mathcal{L}_{\text{Yukawa}}, \quad (2.1.1)$$

$$\mathcal{L}_{\text{gauge}} = -\frac{1}{4}G_{\mu\nu}^a G^{a,\mu\nu} - \frac{1}{4}W_{\mu\nu}^a W^{\mu\nu,a} - \frac{1}{4}B_{\mu\nu} B^{\mu\nu}, \quad (2.1.2)$$

$$\mathcal{L}_{\text{fermion}} = \sum_{\substack{\text{generations,} \\ \Psi \in (Q_L, U_R, D_R, L_L, E_R)}} \bar{\Psi} i \not{D} \Psi, \quad (2.1.3)$$

where \not{D} is the Feynman slash notation for the covariant derivative D_μ contracted with a gamma matrix γ^μ (cf. Sec. A.3.2). Q_L, U_R, D_R, L_L and E_R represent left-handed doublet and right-handed singlet quarks and leptons, respectively. The strong $\text{SU}(3)_C$, weak $\text{SU}(2)_L$ and hypercharge $\text{U}(1)_Y$ gauge fields are denoted by $G_{\mu\nu}^a, W_{\mu\nu}^a$ and $B_{\mu\nu}$, respectively. Tab. 2.1 shows the different multiplets in the SM with their gauge group.

In the following sections, we will describe the different components of the SM Lagrangian.

2.1.1 Quantum electrodynamics

The quantum electrodynamics (QED) Lagrangian describes the interaction between electrically charged particles and the photon. As a fundamental part of the SM, it is written as

$$\mathcal{L}_{\text{QED}} = -\frac{1}{4}F_{\mu\nu}F^{\mu\nu} + \bar{\psi}(i\gamma^\mu D_\mu - m)\psi. \quad (2.1.4)$$

The first term represents the dynamics of the electromagnetic field, with $F_{\mu\nu} = \partial_\mu A_\nu - \partial_\nu A_\mu$ being the electromagnetic field strength tensor. The second term consists of

Multiplet	Name	$S = 0$	$S = \frac{1}{2}$	$S = 1$	SM group	
fermion	quarks	Q_L	-	(u_L, d_L)	-	$(\mathbf{3}, \mathbf{2}, \frac{1}{6})$
	(3 generations)	U_R	-	u_R^\dagger	-	$(\bar{\mathbf{3}}, \mathbf{1}, -\frac{2}{3})$
		D_R	-	d_R^\dagger	-	$(\bar{\mathbf{3}}, \mathbf{1}, \frac{1}{3})$
		leptons	L_L	-	(ν, e_L)	-
	(3 generations)	E_R	-	e_R^\dagger	-	$(\mathbf{1}, \mathbf{1}, 1)$
		higgs	Φ	(ϕ_+, ϕ_0)	-	-
gauge	gluon	$G^{\mu\nu}$	-	-	g	$(\mathbf{8}, \mathbf{1}, 0)$
	W boson	$W^{\mu\nu}$	-	-	(W^\pm, W^0)	$(\mathbf{1}, \mathbf{3}, 0)$
	B boson	$B^{\mu\nu}$	-	-	B^0	$(\mathbf{1}, \mathbf{1}, 0)$

Table 2.1: Multiplets in the SM, where S denotes the spin. The transformation properties under the SM gauge group $SU(3)_C \times SU(2)_L \times U(1)_Y$ are presented in the last column.

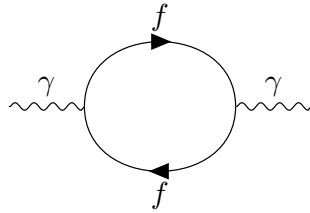


Figure 2.1: Feynman diagram of the photon propagator with a fermion loop.

the Dirac spinor field ψ representing the electron (or any charged fermion) and its adjoint $\bar{\psi}$ and the mass term m . The covariant derivative $D_\mu = \partial_\mu + ieA_\mu$ ensures that the Lagrangian is invariant under local $U(1)$ gauge transformations and includes the electromagnetic interaction through the electromagnetic four-potential A_μ , and the gamma matrices γ^μ . Expanding D_μ results in the interaction term between a photon and an electron $\mathcal{L}_{\text{inter}} = e\bar{\psi}\gamma^\mu A_\mu\psi$. Here e is still the bare electromagnetic coupling constant. In Sec. 3.1.3, we will see that an ultraviolet (UV) pole is absorbed into a redefinition of the coupling constant, giving the finite coupling e_R . As a consequence, it becomes dependent on a renormalization scale μ_R with $\alpha = \alpha(\mu_R) = e_R^2/(4\pi)$ and the renormalization group equation (RGE)

$$\frac{de_R}{d \log \mu_R} = \beta(\alpha) = \frac{4\pi}{e_R} \frac{d\alpha}{d \log \mu_R^2} = \frac{e_R^3}{12\pi^2} + \mathcal{O}(e_R^5), \quad (2.1.5)$$

linked to the one loop correction to the photon propagator as in Fig. 2.1. This gives us the well known one loop running of the electromagnetic coupling constant

$$\alpha(\mu^2) = \frac{\alpha(\mu_0^2)}{1 - \frac{\alpha(\mu_0^2)}{3\pi} \log\left(\frac{\mu^2}{\mu_0^2}\right)} = \frac{\alpha(\mu_0^2)}{1 + \frac{\beta_0^{\text{EM}}}{4\pi} \alpha(\mu_0^2) \log\left(\frac{\mu^2}{\mu_0^2}\right)}, \quad (2.1.6)$$

where $\beta_0^{\text{EM}} = -\frac{4}{3} \sum_f Q_f^2 = -\frac{4}{3}$ for a single fermion generation and a reference scale μ_0 . In Fig. 2.2, the measurement of the running electromagnetic coupling constant α

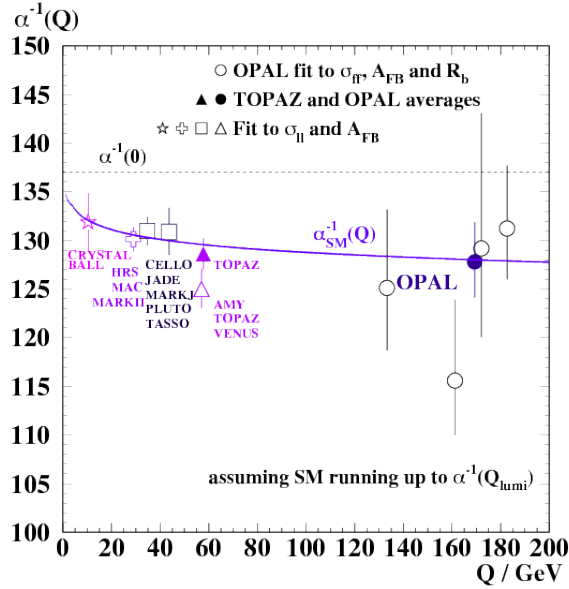


Figure 2.2: Measurement of the running of the electromagnetic coupling [14].

is depicted, illustrating only a minor dependence on the scale $\mu = Q$ within the range accessible to colliders. State-of-the-art SM calculations of the coupling include hadronic and weak effects [15].

2.1.2 Electroweak Sector

The electroweak (EW) sector of the Standard Model is responsible for the unification of the electromagnetic and weak nuclear forces. The EW Lagrangian is given by

$$\mathcal{L}_{\text{EW}} = -\frac{1}{4}W_{\mu\nu}^a W^{\mu\nu,a} - \frac{1}{4}B_{\mu\nu}B^{\mu\nu}, \quad (2.1.7)$$

where $W_{\mu\nu}^a$ and $B_{\mu\nu}$ are the field strength tensors for the weak isospin and weak hypercharge gauge fields, respectively. The electroweak unification is a fundamental aspect of the Standard Model of particle physics, which merges the electromagnetic force and the weak nuclear force into a single theoretical framework. At high energy levels, such as those produced in particle accelerators, the electromagnetic and weak forces become indistinguishable, and the electroweak theory describes this unified interaction. This is expressed through the mixing of the hypercharge gauge boson $|B^0\rangle$ and the neutral component of the weak isospin gauge boson $|W^0\rangle$, resulting in the physical photon $|\gamma\rangle$ and the Z boson $|Z^0\rangle$ states. The relationships between these states are given by

$$|\gamma\rangle = +\cos\theta_W|B^0\rangle + \sin\theta_W|W^0\rangle, \quad (2.1.8)$$

$$|Z^0\rangle = -\sin\theta_W|B^0\rangle + \cos\theta_W|W^0\rangle, \quad (2.1.9)$$

where θ_W is the Weinberg angle. This angle is crucial in the electroweak theory, as it is the only free parameter that determines the mixing of the gauge bosons, and it is

related to the masses of the W and Z bosons through the relation $\cos \theta_W = \frac{M_W}{M_Z} = (0.876\,76 \pm 0.000\,02)$ [15]. The uncertainty is dominated by the uncertainty in the mass of the W boson, which is more difficult to determine experimentally and topic of current research [16, 17]. Similarly, the electric charge e is related to the Weinberg angle through the relation $e = g \sin \theta_W$, where g is the weak isospin coupling constant.

2.1.3 Higgs sector and Yukawa interactions

While the QED Lagrangian (2.1.4) includes a mass term, the fermion sector of the SM in Eq. (2.1.3) does not. The Higgs sector of the SM is responsible for the generation of masses for the electroweak gauge bosons and fermions. It is described by the Higgs Lagrangian

$$\mathcal{L}_{\text{Higgs}} = (D_\mu \Phi)^\dagger (D_\mu \Phi) - V(\Phi), \quad (2.1.10)$$

where $\Phi = (\phi_+, \phi_0)$ is the Higgs field doublet and $V(\Phi)$ is the Higgs potential, given by

$$V(\Phi) = \mu^2 \Phi^\dagger \Phi + \lambda (\Phi^\dagger \Phi)^2. \quad (2.1.11)$$

The interaction between the Higgs field and the fermions is given by the Yukawa Lagrangian

$$\mathcal{L}_{\text{Yukawa}} = - \sum_{i,j} (y_{ij}^d \bar{q}_{iL} \Phi d_{jR} + y_{ij}^u \bar{q}_{iL} \tilde{\Phi} u_{jR} + y_{ij}^e \bar{\ell}_{iL} \Phi e_{jR} + \text{H.c.}), \quad (2.1.12)$$

where y_{ij}^d , y_{ij}^u , and y_{ij}^e are the Yukawa coupling matrices for down-type quarks, up-type quarks, and charged leptons, respectively, and $\tilde{\Phi} = i\sigma_2 \Phi^*$.

2.1.4 Quantum chromodynamics

QCD differs from QED due to the non-Abelian nature of its gauge group $SU(3)$ and the presence of gluons, which carry colour charge, making it a Yang-Mills theory [18]. The Lagrangian density for QCD is defined as [19]

$$\begin{aligned} \mathcal{L}_{\text{QCD}} = & \\ & - \frac{1}{4} G_{\mu\nu}^a G^{a,\mu\nu} + \sum_f \bar{\psi}_f (i\gamma^\mu D_\mu - m_f) \psi_f + \frac{1}{2\zeta} (\partial_\mu A^\mu)^2 + \partial_\mu \bar{c}_a (\partial^\mu c + g_S f^{abc} A_c^\mu c_b), \end{aligned} \quad (2.1.13)$$

where A , ψ , and c represent the gluon, quark, and Faddeev-Popov ghost fields respectively. The covariant derivative is given by $D_\mu = \partial_\mu - ig_S A_\mu^a T^a$ and $G_{\mu\nu}^a = \partial_\mu A_\nu^a - \partial_\nu A_\mu^a + g_S f^{abc} A_\mu^b A_\nu^c$ is the field strength tensor, f^{abc} are the structure constants of the $SU(3)$ group, and T^a are the generators of the $SU(3)$ group in the fundamental representation. The ζ term is a gauge-fixing parameter, which eliminates redundant degrees of freedom. Incorporating the Becchi-Rouet-Stora-Tyutin (BRST) symmetry [20] through ghosts ensures that the quantized theory remains gauge invariant. Fig. 2.3 shows the self-energy of the gluon, where the non-Abelian nature shows in the self coupling of the gluon. The added combinatorial complication of additional Feynman diagrams involving ghosts, especially for processes involving many gluons, can however be avoided by directly requiring external gluons to be only have their physical degrees of freedom through a modified polarization sum, which we will be using through this thesis.

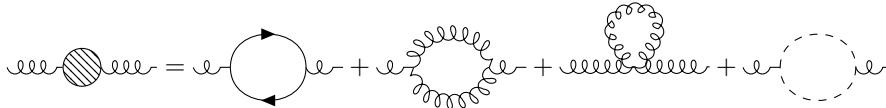


Figure 2.3: Feynman diagrams of the self-energy of the gluon.

After introducing the QCD Lagrangian, we delve into one of the most profound properties of QCD: asymptotic freedom. This property, discovered in 1973 [21, 22], was rewarded with the Nobel Prize in Physics in 2004. Asymptotic freedom is a phenomenon where the strength of the strong interaction between quarks and gluons decreases as they come closer together or, equivalently, at higher energy scales.

The key to understanding asymptotic freedom lies in the behaviour of the running coupling constant $\alpha_S(\mu) = g_S^2(\mu)/(4\pi)$ as a function of the energy scale μ . The change of α_S with μ is governed by the RGE

$$\mu \frac{d\alpha_S(\mu)}{d\mu} = \frac{d\alpha_S(\mu)}{d \log(\mu)} = \beta(\alpha_S), \quad (2.1.14)$$

where $\beta(\alpha_S)$ is the QCD beta function. At one-loop level, the beta function for QCD is [23]

$$\mu^2 \frac{\partial}{\partial \mu^2} \frac{\alpha_S}{4\pi} = \beta(\alpha_S) = - \left(\frac{\alpha_S}{4\pi} \right)^2 \sum_{n=0} \left(\frac{\alpha_S}{4\pi} \right)^n \beta_n \approx - \frac{\beta_0}{16\pi^2} \alpha_S^2, \quad (2.1.15)$$

with

$$\beta_0 = 11 - \frac{2}{3}n_f, \quad (2.1.16)$$

$$\beta_1 = 102 - \frac{38}{3}n_f, \quad (2.1.17)$$

$$\beta_2 = \frac{2857}{2} - \frac{5033}{18}n_f - \frac{325}{54}n_f^2, \quad (2.1.18)$$

...

where n_f is the number of active quark flavours and where the usual constants $C_A = N_C = 3$, $C_F = 4/3$ and $T_R = T_F = 1/2$ have already been substituted. By now, the beta terms are known up to five loops [24, 25]. The negative sign of the beta function coefficient β_0 is crucial. For $n_f \leq 16$ (the physical case has $n_f = 6$ for up, down, strange, charm, bottom, and top quarks), β_0 is positive, making the beta function negative. This implies that α_S decreases as μ increases. More explicitly, integrating the RGE, we get the strong coupling

$$\alpha_S(\mu^2) \approx \frac{4\pi}{\beta_0 \log(\mu^2/\Lambda_{\text{QCD}}^2)} \xrightarrow{\mu \rightarrow \infty} 0, \quad (2.1.19)$$

where Λ_{QCD} is the QCD scale parameter, typically around a few hundred MeV. The essence of asymptotic freedom can be seen in the limit of very high energies, where quarks and gluons interact less, allowing perturbative techniques to be applied effectively. In Fig. 2.4 some experimental measurements of α_S are shown, confirming the asymptotic freedom of QCD across several scales, processes and experiments.

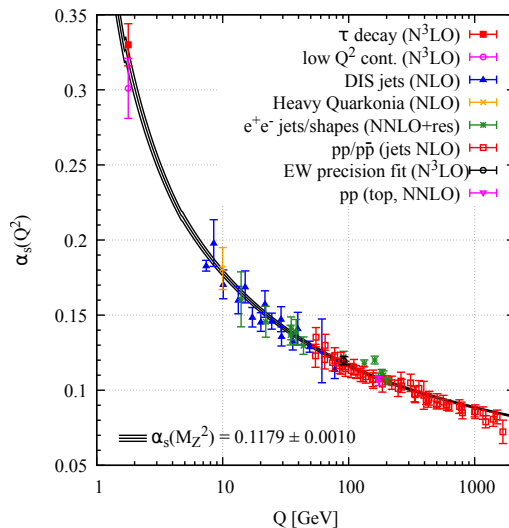


Figure 2.4: $\alpha_s(M_Z^2)$ measurements taken from the Particle Data Group (PDG) [26].

2.2 Collider physics

First we will go through the basic concepts of collider physics roughly following the stages of a collision. We will introduce the basic terminology, the kinematics of the processes we are interested in and the concept of factorization.

2.2.1 Factorization theorem

The *factorization theorem* is a fundamental concept in QCD that facilitates the separation of short-distance (hard, perturbative) and long-distance (soft, non-perturbative) effects in high-energy processes involving hadrons. This separation simplifies the complex interactions in QCD by breaking them down into more manageable parts, making it possible to apply perturbative techniques to certain aspects of the computation while relying on empirical data for others.

The proof of the factorization theorem is only well-established for processes such as the deep inelastic scattering (DIS) and Drell-Yan (DY) process. These proofs demonstrate that the cross section of these processes can be factorized into a convolution of parton distribution functions (PDFs) and a hard scattering cross section, which is calculable using perturbative quantum-chromodynamics (pQCD) [27]. This separation is crucial as it allows the complex, non-perturbative dynamics inside the hadron to be encapsulated in the PDFs. Factorization is central to most calculations in pQCD and can be understood intuitively. Assume a virtual photon probes the hadron with a scale $Q^2 = -q^2 = (k - k')^2 \gg \Lambda_{\text{QCD}}^2$, with k the incoming electron's four momentum and k' outgoing. The interaction between the virtual photon γ^* and the parton inside the hadron is characterized by a timescale $\tau_{\text{hard}} \sim 1/Q$. Conversely, the dynamics inside the hadron, described by the PDF, are characterized by a timescale $\tau_{\text{soft}} \sim 1/\Lambda_{\text{QCD}}$, where partons are confined and hadronise to form baryons or mesons [28]. Thus, the significant difference in timescales $\tau_{\text{soft}} \gg \tau_{\text{hard}}$ allows us to treat the two events as occurring independently, with the larger timescale QCD dynamics inside the hadron are

not influencing the interaction.

This intuitive picture of the DIS process can be extended to hadron-hadron collisions. Because of the asymptotic freedom of QCD and the high energy scale of the process, the partons inside the hadrons can be treated as approximately free particles moving collinear to the hadron. As the QCD coupling decreases at higher energy scales, a parton has approximate momenta xP , where $x \in (0, 1)$ and P is the hadron momentum. Consequently, when two hadrons collide, at first order the partons behave as if scattering off each other. The total cross section is then the convolution of the partonic cross section with the PDFs that describe the parton distribution inside the hadrons. The hadronic cross section is defined as

$$\sigma^h(P_A, P_B)_{cd} = \sum_{a,b} \int_0^1 \int_0^1 dx_a dx_b f_{a/A}(x_a, \mu_F) f_{b/B}(x_b, \mu_F) \sigma_{ab \rightarrow cd}(x_a P_A, x_b P_B), \quad (2.2.1)$$

where μ_F connects the long and short range physics up to subleading terms of the hard scale $\mathcal{O}(m_{A,B}/Q) \approx \mathcal{O}(\Lambda_{\text{QCD}}/Q)$, *i.e.* decreasing with collision energy [10, 29].

In the following section, we will focus on PDFs.

2.2.2 Parton distribution functions

PDFs are fundamental tools in high-energy physics, particularly in QCD, which describe the probability of finding a specific parton (*e.g.* quark or gluon) carrying a certain fraction of the proton's momentum at a given resolution scale Q^2 . However, this interpretation as a probability density strictly holds only at LO in the QCD-improved parton model, as PDFs can become negative at higher-orders. These functions are essential for making predictions in high-energy hadron collisions, such as those occurring in particle colliders like the LHC. Throughout this thesis we will use $f_{p/H}(x, \mu^2)$ to denote the PDF of parton p with momentum fraction x at scale μ^2 inside a hadron H . As of now, the PDFs can not be obtained reliably from a priori calculations, but they can be evolved from one scale to another once they are obtained at a single scale [30]. The universality of PDFs arises from the fact that the parton distribution functions are independent of the specific hard scattering process as already shown in Eq. (2.2.1). This means that once the PDFs are determined by experiments, such as DIS, the same PDFs should apply to a wide variety of other high-energy processes, including proton-proton (pp) collisions, like the DY processes, and more.

We want to derive them now in a more slightly rigorous way. In NLO QCD calculations, we encounter soft, collinear, and soft-collinear divergences. According to the Kinoshita-Lee-Nauenberg (KLN) theorem [31], soft and collinear divergences are cancelled when summing over all initial and final degenerate (experimentally indistinguishable) states. The rationale is that we cannot distinguish between a single particle and a narrow jet of collinear particles, nor can we detect soft gluons with energy below the detector's resolution. This requires adding the contributions from soft and collinear real emissions to the corresponding virtual corrections. Looking at an incoming parton with momentum p as in Fig. 2.5, we can write in the collinear limit for the real emission from a quark [32, 33]

$$d\sigma_{\text{R}}(p) = \frac{\alpha_S}{2\pi} \int \frac{dk_T^2}{k_T^2} dz \bar{P}_{qq}(z) d\sigma_B(zp) \quad (2.2.2)$$

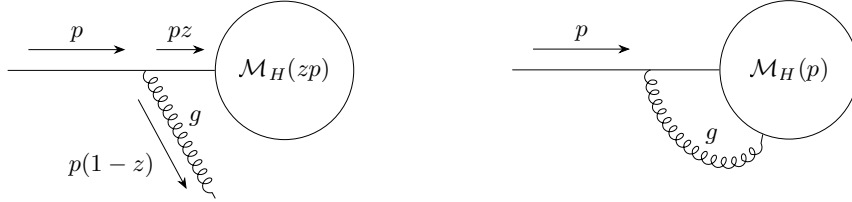


Figure 2.5: The diagram on the left illustrates a schematic Feynman diagram for real collinear emission, while the diagram on the right shows a virtual correction involving a collinear emitted virtual gluon. In both cases, after the real emission or virtual correction, the quark participates in a hard scattering process, represented by \mathcal{M}_H . Within the hard scattering, the virtual gluon interacts with another coloured particle.

and for the virtual contribution

$$d\sigma_V(p) = -\frac{\alpha_S}{2\pi} \int \frac{dk_T^2}{k_T^2} dz \bar{P}_{qq}(z) d\sigma_B(p). \quad (2.2.3)$$

The variables appearing are the transverse momentum k_T of the gluon with respect to the emitter, the fraction z of the emitter's momentum carried by the gluon, and the Altarelli-Parisi (AP) splitting function \bar{P}_{ij} with $i, j \in \{q, g\}$.

In Eq. (2.2.2) and Eq. (2.2.3) soft divergences appear in the splitting functions as $z \rightarrow 1$ and collinear divergences for $k_T \rightarrow 0$. Adding the real and virtual contributions, the soft divergences cancel, but collinear divergences remain. It can be compressed using the plus prescription (cf. Sec. A.4.3)

$$d\sigma_R(p) + d\sigma_V(p) = \frac{\alpha_S}{2\pi} \int \frac{dk_T^2}{k_T^2} dz [\bar{P}_{qq}]_+(z) d\sigma_B(zp) = \frac{\alpha_S}{2\pi} \int \frac{dk_T^2}{k_T^2} dz P_{qq}(z) d\sigma_B(zp), \quad (2.2.4)$$

with the AP splitting functions P_{ij} at LO [34]

$$P_{qq}(z) = C_F \left(\frac{1+z^2}{[1-z]_+} + \frac{3}{2} \delta(1-z) \right), \quad (2.2.5)$$

$$P_{qg}(z) = C_F \frac{1+(1-z)^2}{z}, \quad (2.2.6)$$

$$P_{gq}(z) = T_R (z^2 + (1-z)^2), \quad (2.2.7)$$

$$P_{gg}(z) = 2C_A \left(\frac{z}{[1-z]_+} + \frac{1-z}{z} + z(1-z) \right) + \delta(1-z)\beta_0. \quad (2.2.8)$$

For NLO splitting functions see [35, 36] and next-to-next-to-leading-order (NNLO) see [37, 38].

In order to separate long and short distance effects the factorization scale μ_F is introduced as

$$d\sigma_R(p) + d\sigma_V(p) = \frac{\alpha_S}{2\pi} \int_{\mu_0^2}^{\mu_F^2} \frac{dk_T^2}{k_T^2} \int_0^1 dz P_{qq}(z) d\sigma_B(zp) + \frac{\alpha_S}{2\pi} \int_{\mu_F^2}^{k_{T,\max}^2} \frac{dk_T^2}{k_T^2} \int_0^1 dz P_{qq}(z) d\sigma_B(zp), \quad (2.2.9)$$

where the first term contains the collinear divergence $\mu_0 \rightarrow 0$ and the process dependent $k_{T,\max}$ is explicit. Then we can define a parton-in-parton distribution function loosely describing the probability density of finding a quark of momentum zp in a quark of momentum p as

$$\phi_{qq}(z, \mu_F^2) = \delta(1-z) + \frac{\alpha_S}{2\pi} \int_{\mu_0^2}^{\mu_F^2} \frac{dk_T^2}{k_T^2} P_{qq}(z) \quad (2.2.10)$$

for a given resolution scale μ_F . The same probability applies after picking a quark q from a hadron H

$$\begin{aligned} f_{q/H}(x, \mu_F^2) &= \int dx dz \phi_{qq}(z, \mu_F^2) f_{q/H}(y, \mu_F^2) \delta(x-yz) \\ &= \int_x^1 \frac{dz}{z} \phi_{qq}(z, \mu_F^2) f_{q/H}\left(\frac{x}{z}, \mu_F^2\right). \end{aligned} \quad (2.2.11)$$

While this redefinition technically absorbs the collinear divergence, the actual divergence cancels against the hard process. Hence, it is recommended to use the same order and scheme in the PDF and the hard process to avoid contributions from mismatched cancellations. This is the origin of the universal and process independent collinear counterterms needed in NLO calculations involving hadron initial-states. The hadronic cross section now reads

$$d\sigma^{(h)}(P) = \sum_q \int_0^1 dx f_{q/H}(x, \mu_F^2) d\sigma_q(xP, \mu_F^2), \quad (2.2.12)$$

where partonic cross section $\sigma_q^{(h)}(xP)$ only includes short distance effects. Higher-order PDF computations will not introduce a cutoff on the integration over k_T but rather use more convenient dimensional regularization, which will be discussed later in Sec. 3.1.2. Another simplification in the above procedure lies in the assumption of on-shell (OS) partons, however they can be off-shell up to μ_F^2 [39].

The Dokshitzer-Gribov-Lipatov-Altarelli-Parisi (DGLAP) equations are a set of integro-differential equations that describe the scale dependence and evolution of PDFs with respect to Q^2 [34, 36, 40, 41]. They are obtained from taking the derivative on Eq. (2.2.11)

$$\mu_F^2 \frac{d}{d\mu_F^2} f_i(x, \mu_F^2) = \sum_j \frac{\alpha_S}{2\pi} \int_x^1 \frac{dz}{z} P_{ij}(z) f_j(z, \mu_F^2), \quad (2.2.13)$$

where i and j run over all partons up to flavour n_f , *i.e.* q, \bar{q}, g . Similarly, these evolution equations can be obtained from requiring the invariance of cross section σ on the factorization scale μ_F in Eq. (2.2.12) (cf. Sec. 5.2). As a consequence of the factorization theorem this even generalizes to higher-orders [27]

$$\mathcal{P}_{ij} = \sum_{n=1}^{\infty} \left(\frac{\alpha_S}{2\pi}\right)^n P_{ij}^{(n)}, \quad (2.2.14)$$

$$\frac{d}{d \log \mu_F^2} f_i(x, \mu_F^2) = \sum_j [\mathcal{P}_{ij} \otimes f_j](x, \mu_F^2). \quad (2.2.15)$$

The measurements of PDFs are obtained from a global fit to experimental data, which cover a wide range of kinematic variables, such as the Bjorken x and the squared

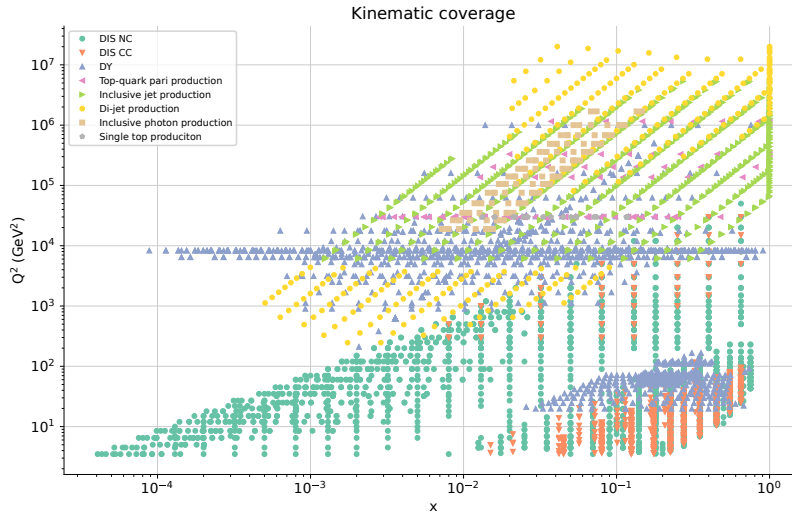


Figure 2.6: Kinematic coverage datasets in x and Q^2 labelled by different processes that are used in the NNPDF4.0 [42] global PDF fits [43]. The y-axis is offset to enhance the visual comparison of the distributions.

momentum transfer $\mu_F^2 = Q^2$. They cover a wide range of processes such as DIS, DY processes, and hadron collider data as show in Fig. 2.6.

In Fig. 2.7 the evolution of up, down, gluon, and charm quark PDFs as a function of x and Q^2 is shown. At low scales we see a peak in up and down quarks at $x \approx 1/3$ with the up peak height being approximately double the down peak height. This is due to the valence quark content of the proton and typical proton composition of two up quarks and one down quark. While gluons and sea quarks (here strange) are less prominent at low scales, they become more important at higher scales. The rise in low values of x also smears out the peak in the valence quarks. All PDFs converge to zero at $x \rightarrow 1$. At very small x , the gluon density is expected to become very large until it reaches saturation, at which point the assumptions underlying factorization may break down. This will be discussed more in Sec. 2.3.

The uncertainties of the PDF have a significant impact on precision predictions, especially towards the tails of the distribution in x , where the PDFs are less constrained by the data. The resulting uncertainties are typically defined as described in the reference [46]. These uncertainties can be computed by performing calculations for a set of PDFs that represent the uncertainty in the fit, and then recombining the results using the built-in methods of LHAPDF [45]. There are two common types of PDF uncertainties, those derived from Hessian eigenvectors and those based on MC replicas.

For uncertainties based on eigenvectors, experimental uncertainties are parametrized by orthogonal Hessian eigenvector sets of PDFs. The uncertainty in the cross section, $\Delta\sigma_{\text{PDF}\pm}$, is calculated using

$$\Delta\sigma_{\text{PDF}\pm} = \sqrt{\sum_{i=1}^n [\max(\pm\sigma_{+i} \mp \sigma_0, \pm\sigma_{-i} \mp \sigma_0, 0)]^2}, \quad (2.2.16)$$

where σ_0 is the central value and $\sigma_{\pm i}$ are related to directional eigenvectors to allow for

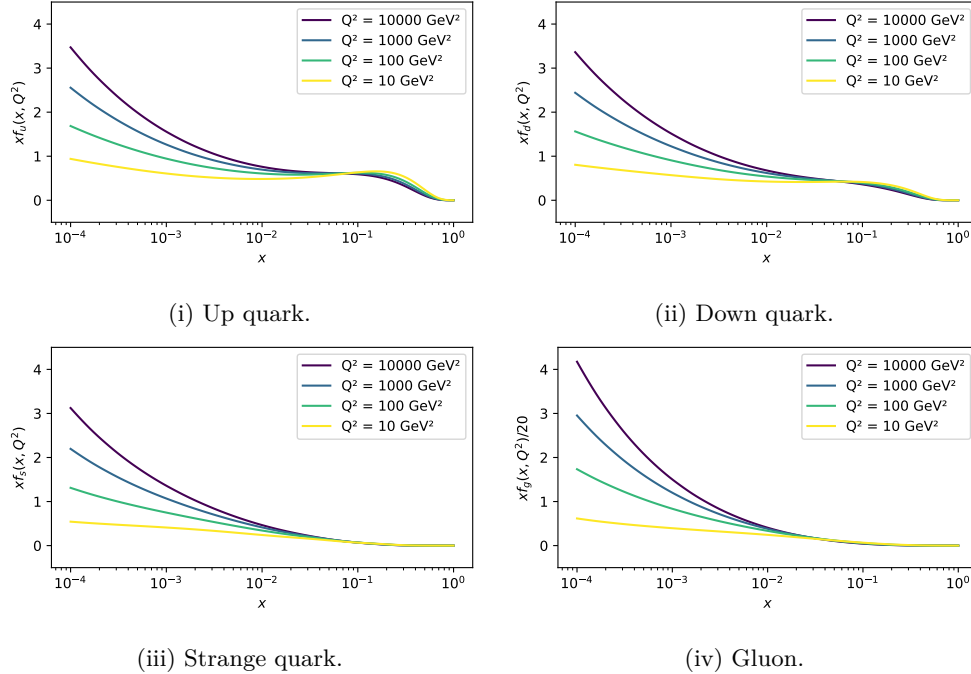


Figure 2.7: MSHT20n1o_as118 [44] PDFs through LHAPDF 6 [45] of the up quark, down quark, strange quark and gluon as a function of x and Q^2 . Note that the gluon for the gluon a division by 20 is applied to enhance the visual comparison.

asymmetric uncertainties. This method is typically employed in parametrized fits, such as those found in PDF sets like CT18 [47], MSHT20 [44], and others.

For uncertainties based on replicas, MC PDF sets come with multiple replicas, which are combined to give a statistical symmetric uncertainty. The uncertainty in the cross section, $\Delta\sigma_{\text{PDF}\pm}$, is computed as

$$\Delta\sigma_{\text{PDF}\pm} = \sqrt{\frac{1}{n-1} \sum_{i=1}^n [\sigma_i - \langle\sigma\rangle]^2}, \quad (2.2.17)$$

where the central value $\langle\sigma\rangle$ is the mean, defined as $\langle\sigma\rangle = \frac{1}{n} \sum_{i=1}^n \sigma_i \approx \sigma_0$. This method is commonly used in neural networks, for example in NNPDF4.0 [42].

2.2.3 Hard scattering

In high-energy physics, the study of hard scattering processes is fundamental for understanding the interactions at the level of quarks and gluons. These processes involve collisions where the momentum transfer is sufficiently high, typically characterized by large negative values of the square of the four-momentum transfer, $-q^2 = Q^2$. When Q^2 is large enough, pQCD becomes applicable, allowing for a systematic expansion in the strong coupling constant α_S , which is small at high energies due to asymptotic freedom [21, 22, 48] (cf. Sec. 2.1.4). The partonic cross section is calculable within pQCD and is

typically computed to a certain order in α_S , often at NLO or NNLO. These calculations are essential for making precise predictions that can be compared with experimental results [49].

The partonic cross section, $\sigma_{ab \rightarrow cX}$ quantifies the probability that two partons a and b will scatter and produce an outgoing parton c , along with other possible particles represented by X . To describe these processes, it is essential to introduce the Mandelstam variables, which are a set of kinematic variables that simplify the expression of the scattering amplitude in terms of the four-momenta of the involved particles. The Mandelstam variables s , t , and u are defined as:

- $s = (p_a + p_b)^2$ represents the square of the centre-of-mass energy of the incoming partons a and b .
- $t = (p_a - p_c)^2$ represents the square of the four-momentum transfer between the initial parton a and the final parton c .
- $u = (p_b - p_c)^2$ represents the square of the four-momentum transfer between the initial parton b and the final parton c .

These variables satisfy the relation $s + t + u = \sum_i m_i^2$, where the sum is over the squared masses of all particles involved in the scattering process (including m_X^2). In many cases, especially in high-energy collisions where the masses of the particles are negligible compared to their momenta, this simplifies to $s + t + u = 0$ [50]. For processes involving more than two particles in the final-state, additional Mandelstam variables can be defined to describe the kinematics of the scattering process. These variables are usually $s_{ij} = (p_i + p_j)^2$ and $t_{ij} = (p_i - p_j)^2$ for each pair of particles i and j in the final-state.

The S-matrix, or scattering matrix, is a central object in QFT that encodes the transition probabilities between different quantum states due to a scattering process. It relates the initial-state to the final-state and is used to calculate observables such as cross sections and decay rates. The elements of the S-matrix, often called transition amplitudes, are computed using perturbation theory and provide the probability amplitude for a particular scattering process to occur [51].

Matrix elements (MEs) play a crucial role in calculating the transition probabilities between different quantum states in scattering processes. In perturbative QCD, these matrix elements correspond to the Feynman diagrams that describe the interactions of quarks and gluons. The importance of matrix elements lies in their ability to capture the dynamics of the interaction, including quantum mechanical interference effects between different diagrams. The square of the matrix element gives the transition probability, which is then used to compute the cross section.

The cross section σ can generally be calculated from the invariant matrix element \mathcal{M} through an integration over the phase space of the n particles in the final-state [52]

$$d\sigma = \frac{1}{F} \langle |\mathcal{M}|^2 \rangle d\Phi_n. \quad (2.2.18)$$

Here, $F = 4\sqrt{(p_a p_b)^2 - (m_a m_b)^2} \xrightarrow{s \gg m_a^2, m_b^2} 2s$ is the flux factor in the centre-of-mass frame. For a general n -particle final-state, the phase space element is given by

$$d\Phi_n = \prod_{i=3}^{n+2} \left(\frac{d^4 p_i}{(2\pi)^4} (2\pi) \delta(p_i^2 - m_i^2) \theta(p_i^0) \right) \cdot (2\pi)^4 \delta^{(4)} \left(p_1 + p_2 - \sum_{i=3}^{n+2} p_i \right), \quad (2.2.19)$$

where we integrate over every final-state particle four momentum and require them to be on-shell with a positive energy. The final delta function enforces energy-momentum conservation. This expression involves a $4n$ integrations, reduced by the $4 + n$ delta functions, resulting in $3n - 4$ independent Mandelstam variables to describe a $2 \rightarrow n$ process. As the phase space increases in dimension with the number of final-state particles, the matrix element also has to change its dimensionality for the resulting cross section to be physical.

In high-energy particle physics experiments, hard scattering events are typically identified by the production of high-energy jets. These jets are narrow cones of hadrons and other particles that result from the fragmentation and hadronisation of outgoing quarks and gluons. The identification and analysis of jets are crucial for understanding the underlying parton-level interactions that occurred in the collision.

Jets serve as key signatures in particle detectors, allowing to reconstruct the hard scattering process. By studying the distribution and properties of jets, one can test predictions of the Standard Model, such as the running of the strong coupling constant, and search for signs of new physics beyond the Standard Model, such as supersymmetry or extra dimensions [53].

2.2.4 Heavy resonances decay

The PDG defines resonances as poles of the S-matrix, whether in scattering, production, or decay matrix elements [15, 54]. Such resonances are characterized by a peak in the cross section, which is a result of going OS, *i.e.* the momentum in the denominator of the propagator cancels against the mass. They can be viewed as a two-step process $A + B \rightarrow R \rightarrow C_1 + \dots + C_n$, where the resonance is produced and then decays into particles. The lifetime of the resonance R is connected to its width Γ_R through the uncertainty principle, expressed as $\Delta E \Delta t \sim \hbar$. As a result, resonances with a broad width correspond to a short lifetime, and vice versa. We will sketch the concept of resonances in the context of the most prominent example the Z^0 . Considering the propagator with mass m_Z and width Γ_Z

$$\frac{-i(g_{\mu\nu} - \frac{q_\mu q_\nu}{m_Z^2})}{q^2 - m_Z^2 + im_Z \Gamma_Z}, \quad (2.2.20)$$

the squared matrix element for the decay like $e^+e^- \rightarrow Z^0 \rightarrow f\bar{f}$ is

$$|\mathcal{M}|^2 \sim \frac{1}{(q^2 - m_Z^2)^2 + m_Z^2 \Gamma_Z^2}. \quad (2.2.21)$$

The added width in the denominator prohibits the propagators from going to infinity and the cross section can be expressed as a Breit-Wigner (BW) distribution

$$\sigma \sim \frac{1}{(s - m_Z^2)^2 + m_Z^2 \Gamma_Z^2}. \quad (2.2.22)$$

As a result of the decay width being additive

$$\Gamma_Z = \sum_{f \in (u, c, d, s, b, e, \mu, \tau, \nu_e, \nu_\mu, \nu_\tau)} \Gamma_{Z \rightarrow f\bar{f}}, \quad (2.2.23)$$

the number of light neutrino families can be determined to be 3 from the Z^0 BW like distribution as shown in Fig. 2.8. The branching ratio of a process is determined by its contribution to the total width, expressed as $\text{Br}_f = \Gamma_{Z \rightarrow f\bar{f}} / \Gamma_Z$.

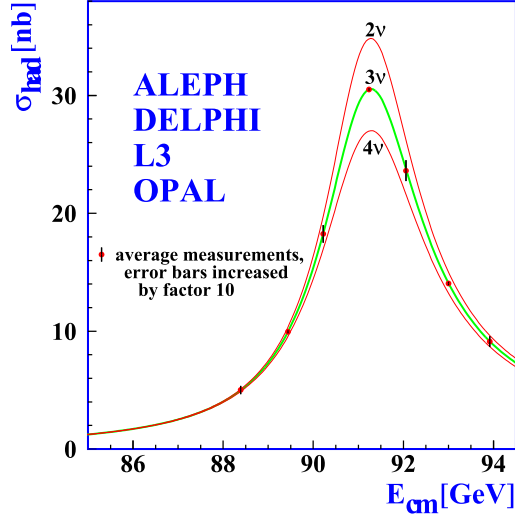


Figure 2.8: Determination of the number of neutrino families from the Z^0 decay width [55].

2.2.5 Parton shower

Parton showers are essential in high-energy physics simulations, modelling the evolution of quarks and gluons into hadrons. This process captures the infrared (IR) and collinear divergences inherent in QCD. The parton shower's dynamics are described by the AP splitting kernels, which govern the probability of a parton splitting into two or more partons. The AP splitting probability in the soft ($k_T \rightarrow 0$) and collinear ($\theta \rightarrow 0$ or π) approximations can be expressed as

$$d\mathcal{P}_{a \rightarrow bc}^{\text{FSR}}(z, Q^2) = \frac{\alpha_S(Q^2)}{2\pi} \frac{dQ^2}{Q^2} P_{a \rightarrow bc}(z) dz, \quad (2.2.24)$$

$$d\mathcal{P}_{a \rightarrow bc}^{\text{ISR}}(z, Q^2) = \frac{dQ^2}{Q^2} \frac{\alpha_S(Q^2)}{2\pi} \int \frac{dx}{x} \frac{f_{a/A}(\frac{z}{x}, Q)}{f_{i/A}(x, Q)} P_{a \rightarrow bc}(x), \quad (2.2.25)$$

where α_S is the strong coupling constant, Q^2 is the virtuality of the splitting, and $P_{a \rightarrow bc}(z)$ is the splitting function dependent on the momentum fraction z carried by one of the daughter partons [56]. Where the initial-state radiation (ISR) includes a reweighting factor to account for the PDFs of the incoming partons in accordance to the DGLAP Eq. (2.2.13) [57]. For simplicity, we will focus on the final-state radiation (FSR) in the following.

From an emission probability \mathcal{P}_{em} we can compute the probability \mathcal{P}_{no} that there is

no emission between times 0 and T as

$$\begin{aligned}
\mathcal{P}_{\text{no}}(0 \leq t < T) &= \lim_{n \rightarrow \infty} \prod_{i=0}^{n-1} \mathcal{P}_{\text{no}}(T_i \leq t < T_{i+1}) \\
&= \lim_{n \rightarrow \infty} \prod_{i=0}^{n-1} (1 - \mathcal{P}_{\text{em}}(T_i \leq t < T_{i+1})) \\
&= \exp \left(- \lim_{n \rightarrow \infty} \sum_{i=0}^{n-1} \mathcal{P}_{\text{em}}(T_i \leq t < T_{i+1}) \right) \\
&= \exp \left(- \int_0^T \frac{\mathcal{P}_{\text{em}}(t)}{dt} dt \right).
\end{aligned} \tag{2.2.26}$$

Inverting this relation we can compute the probability of the first emission at time T as

$$\mathcal{P}_{\text{first}}(T) = 1 - \mathcal{P}_{\text{no}}(T) \implies d\mathcal{P}_{\text{first}}(T) = d\mathcal{P}_{\text{em}}(T) \exp \left(- \int_0^T \frac{\mathcal{P}_{\text{em}}(t)}{dt} dt \right). \tag{2.2.27}$$

However, in momentum space the time variable t is replaced by $t \sim 1/Q$ according to the Heisenberg uncertainty principle. More rigorously, the no emission probability between scales q^2 and Q^2 , called Sudakov factor $\Delta(Q^2, q^2)$ is given by

$$\Delta(Q^2, q^2 + \Delta q^2) = \Delta(Q^2, q^2) + \Delta(Q^2, q^2 + \Delta q^2) \Delta P_{\text{em}}(q^2), \tag{2.2.28}$$

where the left-hand side no emission probability down to $q^2 + \Delta q^2$ is the sum of the probabilities that no emission happens between earlier $q^2 + \Delta q^2$ down to later q^2 and that there is an emission at q^2 . For small Δq^2 this becomes an ordinary differential equation (ODE)

$$\frac{d\Delta(Q^2, q^2)}{dq^2} = \Delta(Q^2, q^2) \frac{\alpha_s(q^2)}{2\pi} \frac{1}{q^2} \int dz P(z), \tag{2.2.29}$$

solved by

$$\Delta(Q^2, q^2) = \exp \left(- \int_{q^2}^{Q^2} \frac{d\hat{q}^2}{\hat{q}^2} \int dz \frac{\alpha_s(\hat{q}^2)}{2\pi} P(z) \right). \tag{2.2.30}$$

Its boundary conditions

$$\Delta(Q^2, Q^2) = 1 \tag{2.2.31}$$

correspond to the case of no emission since no phase space is available and

$$\Delta(Q^2, 0) = 0 \tag{2.2.32}$$

due to the logarithmic divergence at $\hat{q}^2 = 0$, which can be understood as guaranteed radiation after long enough times, a correspondence to colour confinement as $\alpha_s(\Lambda_{\text{QCD}}) \gtrsim 1$. Therefore, the parton shower can not continue below Λ_{QCD} . One crucial property of the parton shower is that it does not alter the normalization of a process, *i.e.* it is unitary. This can be seen from looking at a large sample and summing the probabilities of no radiation, one radiation, two radiations, *etc.*

$$\begin{aligned} & \Delta(Q^2, \Lambda_{\text{QCD}}^2) + \int_{\Lambda_{\text{QCD}}^2}^{Q^2} dq_1^2 \frac{d\Delta(Q^2, q_1^2)}{dq_1^2} \Delta(q_1^2, \Lambda_{\text{QCD}}^2) \\ & + \int_{\Lambda_{\text{QCD}}^2}^{Q^2} dq_1^2 \int_{\Lambda_{\text{QCD}}^2}^{q_1^2} dq_2^2 \frac{d\Delta(Q^2, q_1^2)}{dq_1^2} \frac{d\Delta(Q^2, q_2^2)}{dq_2^2} \Delta(q_2^2, \Lambda_{\text{QCD}}^2) + \dots \end{aligned} \quad (2.2.33)$$

$$= \sum_{i=0}^{\infty} \left(\prod_{j=0}^{i-1} \int_{\Lambda_{\text{QCD}}^2}^{q_j^2} dq_{j+1}^2 \frac{d\Delta(q_j^2, q_{j+1}^2)}{dq_{j+1}^2} \right) \Delta(q_i^2, \Lambda_{\text{QCD}}^2) \quad (2.2.34)$$

$$= \Delta(Q^2, \Lambda_{\text{QCD}}^2) \sum_{i=0}^{\infty} \prod_{j=0}^{i-1} \int_{\Lambda_{\text{QCD}}^2}^{q_j^2} dq_{j+1}^2 \frac{d\mathcal{P}_{\text{em}}(q_{j+1}^2)}{dq_{j+1}^2} \quad (2.2.35)$$

$$= \Delta(Q^2, \Lambda_{\text{QCD}}^2) \sum_{i=0}^{\infty} \frac{1}{i!} \left(\int_{\Lambda_{\text{QCD}}^2}^{Q^2} dq^2 \frac{d\mathcal{P}_{\text{em}}(q^2)}{dq^2} \right)^i \quad (2.2.36)$$

$$= \Delta(Q^2, \Lambda_{\text{QCD}}^2) \exp \left(\int_{\Lambda_{\text{QCD}}^2}^{Q^2} dq^2 \frac{d\mathcal{P}_{\text{em}}(q^2)}{dq^2} \right) \quad (2.2.37)$$

$$= 1. \quad (2.2.38)$$

This unitarity also shows that the Sudakov factor approximately resums virtual corrections to cancel real corrections [58–61]. The unitarity can also be understood as PSs not altering the normalization of a process. For instance, approximating a two-jet cross section by a $2 \rightarrow 2$ tree-level cross section will yield the same total dijet cross section as the $2 \rightarrow 2$ plus parton shower result. Each generated radiation effectively multiplies the cross section by the radiation probability. In a sufficiently large sample, cases with no radiation, one radiation, or multiple radiations will occur, but the inclusive cross section remains unchanged, demonstrating the unitarity of the parton shower. However, differential cross sections can benefit significantly from parton shower corrections, adding realistic jet shapes and distributions.

Different evolution variables, such as transverse momentum, angle, or virtuality, can be used in parton showers. The choice of evolution variable impacts the shower algorithm and the resulting simulated events. Angular ordering ensures that each successive emission occurs at a smaller angle relative to the previous one. This method maintains colour coherence and accurately reproduces the angular distribution of emissions, with the ordering variable given by

$$Q^2 = E_a^2 \theta_{a \rightarrow bc}^2. \quad (2.2.39)$$

On the other hand, transverse-momentum ordering prioritizes emissions based on the transverse momentum k_T relative to the parent parton, effective for resumming large logarithms and accurately accounting for emissions with large transverse momenta

$$Q^2 = k_T^2. \quad (2.2.40)$$

Each method has advantages: angular ordering naturally incorporates colour coherence, while k_T ordering is adept at handling wide-angle emissions and large logarithms. Fig. 2.9 illustrates the differences between the two approaches in a Lund diagram, showing the regions of phase space where emissions are most likely to occur. As shown in

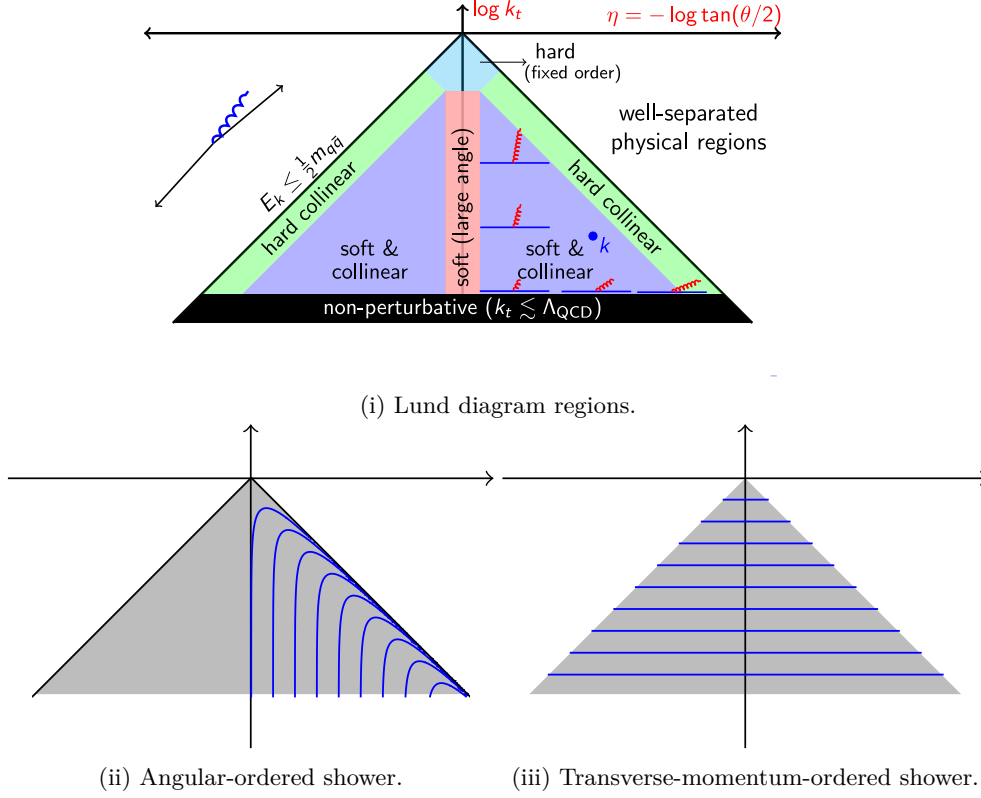


Figure 2.9: Lund diagrams for parton showers.

Fig. 2.9i it spans the axis between k_T and η . The hard process is located at the axis intersection and the non-perturbative regime begins at the bottom $k_T \sim \Lambda_{\text{QCD}}$. The parton shower connects them through the soft and collinear regime in between. Represented as ordered slices where the emission occur, Fig. 2.9ii shows the angular order and Fig. 2.9iii the transverse momentum ordering.

Defining a shower as \mathcal{S}

$$\mathcal{S}(Q^2) = \Delta(Q^2, \Lambda_{\text{QCD}}^2) + \int_{\Lambda_{\text{QCD}}^2}^{Q^2} dq^2 dz \Delta(Q^2, q^2) \frac{\alpha_s(q^2)}{2\pi q^2} P(z) \mathcal{S}(z^2 q^2) \mathcal{S}((1-z)^2 q^2), \quad (2.2.41)$$

where the first term corresponds to no emission, the second to splitting in two recursive showers of z and $1-z$ fractions of the parent parton. The standard vetoed shower expression is

$$\begin{aligned} \mathcal{S}(Q^2) = & \Delta(Q^2, \Lambda_{\text{QCD}}^2) \\ & + \int_{\Lambda_{\text{QCD}}^2}^{Q^2} dq^2 dz \Delta(Q^2, q^2) \frac{\alpha_s(q^2)}{2\pi q^2} P(z) \mathcal{S}(z^2 q^2) \mathcal{S}((1-z)^2 q^2) \theta(g(z, q^2)) \\ & + \int_{\Lambda_{\text{QCD}}^2}^{Q^2} dq^2 dz \Delta(Q^2, q^2) \frac{\alpha_s(q^2)}{2\pi q^2} P(z) \mathcal{S}(q^2) (1 - \theta(g(z, q^2))), \end{aligned} \quad (2.2.42)$$

with a constraint function $g(z, q^2)$ applied to the branching process. A branching is created if $g(z, q^2) > 0$ otherwise it is rejected and the search for a new branching is started again from q^2 . The Eq. (2.2.41) is recovered with $P(z) \rightarrow P(z)\theta(g(z, q^2))$ [62, 63]

$$\begin{aligned} \mathcal{S}(Q^2) = & \Delta'(Q^2, \Lambda_{\text{QCD}}^2) \\ & + \int_{\Lambda_{\text{QCD}}^2}^{Q^2} dq^2 dz \Delta'(Q^2, q^2) \frac{\alpha_s(q^2)}{2\pi q^2} P(z) \mathcal{S}(z^2 q^2) \mathcal{S}((1-z)^2 q^2) \theta(g(z, q^2)), \end{aligned} \quad (2.2.43)$$

where Δ' is the Sudakov factor with the veto applied

$$\Delta'(Q^2, q^2) = \exp \left(- \int_{q^2}^{Q^2} \frac{d\hat{q}^2}{\hat{q}^2} \int dz \frac{\alpha_s(\hat{q}^2)}{2\pi} P(z) \theta(g(z, q^2)) \right). \quad (2.2.44)$$

The form of a vetoed shower has computational advantages, that will become clear in Sec. 3.2.5 and Sec. 3.3.3.2.

We have seen that MEs provide fixed-order calculations accurate for hard jets, including all terms up to a given order in α_s . These are valid for high p_T^2 but are computationally expensive and limited to a few emissions. In contrast, parton showers can handle any number of emissions and remain finite, though they are only valid in the soft/collinear regions. Combining matrix elements with parton showers through NLO matching (cf. Sec. 3.3.3) or multi-jet merging (cf. Sec. 3.3.2) harnesses the strengths of both methods, with hard emissions modeled by fixed-order calculations and subsequent emissions handled by the parton shower.

One detail omitted in above discussion is the handling of colour in parton showers. Going to the large- N_c limit is convenient, since gluons, which for $N_c = 3$ carry the irreducible colour-octet representation, can be replaced by a colour-anticolour pair. This simplifies the colour flow in Feynman diagrams, allowing for unambiguous colour assignment to partons. This method eliminates interference terms between different colour structures, which are higher-order corrections in $1/N_c$. The large- N_c limit results in planar colour flows, making it easier to implement colour-based models in Shower Monte Carlo (SMC) generators. Their details are postponed to Sec. 3.1.1.2 and Sec. 3.2.5.

2.2.6 Fragmentation

In Sec. 2.2.1 we introduced the concept of factorization leading to the definition of PDFs. Now we introduce the concept of FFs which are the analogue of PDFs for the fragmentation of partons into for instance hadrons or photons. They include the long-distance non-perturbative effects in the final-state of a hard scattering process.

Eq. (2.2.1) can be extended straightforward to include the fragmentation of partons. For a process $AB \rightarrow CX$ involving hadrons A , B , and C , with X denoting the undetected remains, a factorized cross section can then be written as

$$\begin{aligned} d\sigma_{AB \rightarrow CX}(p_A, p_B, p_C) = & \sum_{a,b,c} \int_0^1 dx_a dx_b dz f_{a/A}(x_a, \mu_{F_i}) f_{b/B}(x_b, \mu_{F_i}) \\ & d\hat{\sigma}_{ab \rightarrow cX}(x_a p_A, x_b p_B, \frac{p_C}{z}, \mu_R, \mu_{F_i}, \mu_{F_f}) D_{C/c}(z, \mu_{F_f}). \end{aligned} \quad (2.2.45)$$

Here one sums over the intermediate initial and final-state partons and convolves the PDFs $f_{a/A}$, picking parton a from hadron A , and FFs $D_{\gamma/c}$, fragmenting parton c to a photon, with the partonic cross section $d\hat{\sigma}_{ab \rightarrow cX}$. The pieces are connected through the renormalization scale μ_R and factorization scale in the initial-state μ_{F_i} and final-state μ_{F_f} . The partonic cross section $\hat{\sigma}$ is not IR safe for identified partons however the factorization theorems cancel these universal collinear divergences [27]. In the fragmentation process, the evolution of FFs is described by evolution equations, analogous to those governing PDFs.

In the following we will focus on the fragmentation of partons into photons, $C = \gamma$.

The photon fragmentation functions evolve according to equations similar to the DGLAP Eq. (2.2.13). Specifically, this involves replacing the gluon-related Casimir operators in the splitting kernels Eqs. (2.2.5) to (2.2.8) with those appropriate for photons $C_A \rightarrow 0$ and the quark-related Casimir operator by the electromagnetic charge of the quark $C_F \rightarrow Q_i^2$. The photon splitting kernels for quarks and gluons at LO are

$$P_{\gamma q}(z) = Q_q^2 \frac{1 + (1-z)^2}{z}, \quad (2.2.46)$$

$$P_{\gamma g}(z) = 0. \quad (2.2.47)$$

At NLO, the evolution equations become more complex, involving additional terms from gluon fragmentation. The general form of the evolution equations for photon fragmentation functions includes convolutions of the splitting functions with the FFs, integrating over the momentum fraction z

$$\frac{dD_{\gamma/i}(\mu_F^2)}{d \log \mu_F^2} = \frac{\alpha}{2\pi} D_{\gamma/\gamma}(\mu_F^2) \otimes P_{\gamma i} + \frac{\alpha_S(\mu_F^2)}{2\pi} \times [D_{\gamma/q}(\mu_F^2) \otimes P_{qi} + D_{\gamma/g}(\mu_F^2) \otimes P_{gi}], \quad (2.2.48)$$

where $i \in \{q, g, \gamma\}$ and P_{ij} are time-like AP splitting functions [64].

Using $D_{\gamma/\gamma}(z, \mu_F) = \delta(1-z)$ at electromagnetic (EM) LO thus

$$\mu_F^2 \frac{d}{d\mu_F^2} D_{\gamma/c}(z, \mu_F) = \frac{\alpha}{2\pi} P_{\gamma c}(z) \quad (2.2.49)$$

gives

$$D_{\gamma/q}(z, \mu_F) = \frac{\alpha}{2\pi} P_{\gamma q}(z) \log \left(\frac{\mu_F^2}{\mu_s^2} \right) + D_{\gamma/q}^{\text{measured}}(z, \mu_s), \quad (2.2.50)$$

$$D_{\gamma/g}(z, \mu_F) = \text{const.} = 0, \quad (2.2.51)$$

where the constant value of $D_{\gamma/g}$ is zero, since it must also take that value at $z = 1$, where the photon remains a photon.

Solving these equations requires a starting scale μ_s , from which the FFs evolve. The choice of this starting scale can affect the results, and it often involves assumptions about the initial conditions, such as the minimal transverse momentum between partons.

Similar to PDFs the FFs first need to be determined from experimental data such as prompt photon production in e^+e^- collisions [65, 66], in hadronic collisions [67] as well as in vector meson production, where the photon is assumed to fluctuate into hadronic states [68]

$$D_{\gamma,i}^{\text{had}}(z, \mu_s) = \sum_{V=\rho,\omega,\phi} \frac{4\pi\alpha}{f_V^2} D_{V/i}(z, \mu_s). \quad (2.2.52)$$

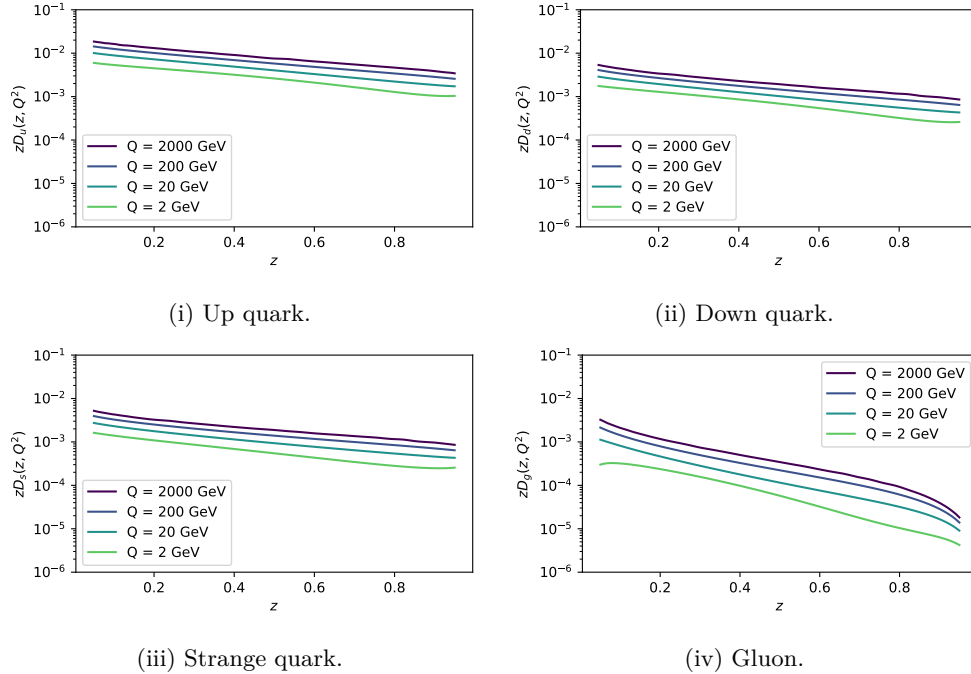


Figure 2.10: BFG I [69] FFs through JetPhox [70–72] of the up quark, down quark, strange quark and gluon as a function of z and Q^2 .

In Fig. 2.10 the FF of some partons and scales Q are shown. The largest contribution comes from the up quark while the down and strange quark contributions are roughly the same. The gluon contribution is the lowest, as expected, since it only plays a significant role beyond LO. As the scale increases, there is a higher probability that a parton fragments into a photon as expected from Eq. (2.2.50).

For prompt-photon production, the fragmentation contributions are significant, especially at low transverse momentum, which typically chosen as the scale $Q = p_T$ as shown in Fig. 2.11. This is a result of purely strong jet production becoming dominant at low scales, due to increased α_S and gluon-gluon initial-states, outpacing the reduction in the FFs as the scale decreases. In order to partially eliminate the phenomenological less interesting fragmentation contributions one introduces the concept of isolation.

In the study presented in Ref. [74], three distinct photon isolation schemes are defined and compared, namely the fixed-cone, the smooth-cone, and the hybrid isolation. These can all be described by a single equation, which is then used to calculate the hadronic activity around the photon and to compare against the isolation energy

$$\sum_i^{\Delta R_i < \epsilon R} p_T^i \left(\frac{\epsilon R}{r} \right)^{2n} \leq E_T^{\max} = p_T^{\text{iso}}, \quad (2.2.53)$$

where $(n = 0, \epsilon = 1)$ corresponds to the fixed-cone isolation, $(n = 1, \epsilon = 1)$ to the smooth-cone isolation, and the hybrid isolation requires both $(n = 1, \epsilon = 0.1)$ and $(n = 0, \epsilon = 1)$ to be satisfied. A graphical representation of the three isolation schemes is shown in Fig. 2.12. The fixed-cone isolation is the most common isolation scheme

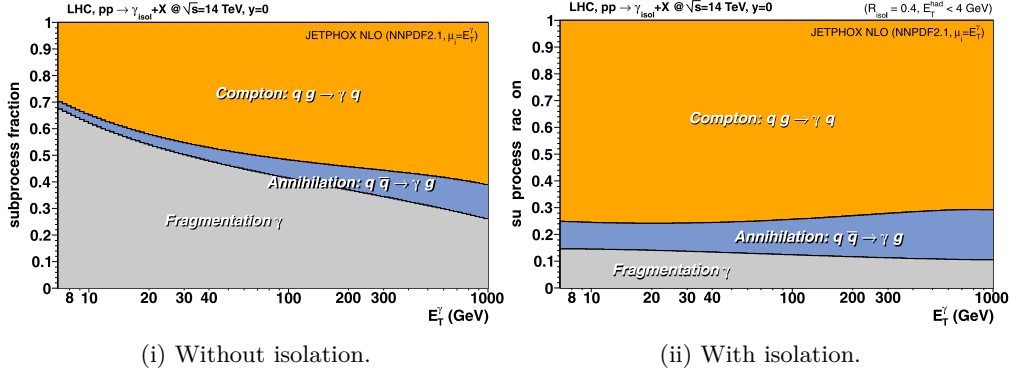


Figure 2.11: Prompt photon production prediction at LHC energies of $\sqrt{s} = 14$ TeV. The contributions are separated into the two leading order processes Compton and annihilation as well as fragmentation contribution. Figure taken from [73].

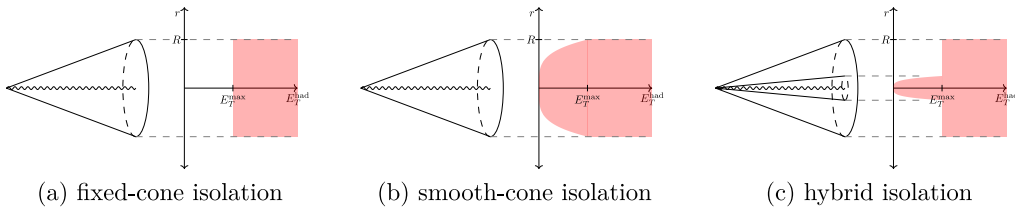


Figure 2.12: Graphical depiction of different isolation cones. The x-axis represents the hadronics activity in the isolation cone and the y-axis the radial distance. When the energy exceeds the isolation energy, the event is no longer isolated (red shaded area). Figure taken from [74].

used in experimental analyses, as it is simple to implement and has a clear physical interpretation. To consistently eliminate the fragmentation contributions, one must exclude collinear parton-photon configurations without disrupting the cancellation of infrared singularities from soft gluon emissions [75]. While straightforwardly vetoing the collinear configurations, as in the fixed cone approach, is not infrared-collinear (IRC) safe, suppressing them maintains the necessary cancellation. This method is known as smooth-cone isolation. The proof of infrared safety is similar to that of jet definitions, where analogous cone algorithms are also sensitive to IRC safety [76]. Typically, theoretical tools use the smooth-cone isolation as it has the advantage that it does not get contributions from the parton-to-photon fragmentation functions [75]. The hybrid isolation is a compromise between the two, as it is more restrictive than the fixed-cone isolation, but less restrictive than the smooth-cone isolation [77, 78]. Fig. 2.11 shows the impact of the isolation cone on the hadronic activity around the photon and how it reduces the fragmentation contribution especially towards low p_T .

2.2.7 Hadronisation

Hadronisation is the intricate process by which quarks and gluons, liberated during high-energy particle collisions, transform into hadrons. This process is fundamentally

tied to the principle of confinement in QCD, which posits that quarks cannot exist in isolation but must combine to form colour-neutral particles, such as mesons and baryons. The complexity of hadronisation arises from the non-perturbative nature of QCD in this regime, which prevents a precise first-principles calculation of the transition from quarks and gluons to hadrons. As such, the detailed mechanism of hadronisation remains beyond the reach of pQCD, necessitating the use of phenomenological models to describe the process. Two primary models have been developed to simulate hadronisation: the Lund string model and the cluster model.

The Lund string model [79, 80], utilized by the event generator PYTHIA [61, 81–83], conceptualizes the colour field between quarks as a string that stretches and eventually breaks as the quarks move apart. This breaking of the string results in the formation of new quark-antiquark pairs, which then hadronise, producing a cascade of hadrons. This model effectively captures the jet structure observed in high-energy collisions, where hadrons are distributed along the paths of the original quarks, as well as between the jets due to the fragmentation of the string.

On the other hand, the cluster model [84], implemented in event generators like HERWIG [85–89] and Sherpa [90, 91], operates on the principle of preconfinement [92]. In this model, after the parton shower phase, first gluons are split into quark antiquark pairs, then the quarks coalesce into colour-neutral clusters through colour reconnection. These clusters subsequently decay into hadrons, a process that involves the creation of additional quark-antiquark pairs. The cluster model simplifies the hadronisation process by treating these clusters as intermediate states that decay into final-state hadrons, offering a different approach to modelling hadronisation compared to the string model.

Both models are essential tools in high-energy physics, enabling the simulation of hadronisation in particle collision experiments. Since the process cannot be calculated directly from QCD, these models are calibrated using experimental data such as hadron correlations, ensuring their predictions align with observed results. The Lund string model, with its intuitive picture of colour flux tubes breaking into hadrons, and the cluster model, with its focus on preconfinement and cluster decay, represent the best available descriptions of a fundamentally complex and non-perturbative process [81, 86]. The improvement of these models continues along with modern techniques such as machine learning [93–95].

2.3 Heavy-ion collisions

Over a century ago, one of the earliest and most significant experiments in heavy-ion collisions, the Rutherford experiment, led to the discovery of the atomic model, revealing a dense nucleus surrounded by orbiting electrons [96]. Since that discovery, the field of heavy-ion physics has advanced significantly. For instance the development of high-energy accelerators such as the LHC and the RHIC has opened the door to exploring the properties of the QGP [97]. To compare theoretical predictions with experimental results, much like our earlier examination of the proton’s structure, we first focus on understanding the constituents of heavy-ions.

2.3.1 Initial-state effects and nuclear parton distribution functions

The initial-state of hadronic collisions plays a crucial role in determining the particle production and overall dynamics of nucleus-nucleus (AA) events. A key difference between AA and pp collisions is the amount of produced entropy, reflected in the significantly higher number of particles in the final-state of the former. In heavy-ion collisions, the majority of the entropy is generated during the early stages after the collisions, meaning that the initial conditions are fundamental before any hydrodynamic evolution of the QGP occurs [97]. This is especially true for soft particles with low transverse momentum ($p_T \lesssim 1$ GeV), where the initial conditions directly impact particle multiplicity and collision geometry [98]. The production of hard probes, which are sensitive to parton-parton scattering with large momentum transfer, is also influenced by the nPDFs of the incoming particles. This is critical because changes in the initial-state can mimic the signals expected from QGP-induced modifications, complicating the interpretation of observables such as the nuclear modification factor, R_{AA} .

Since a nucleus is a larger and more complex structure compared to a proton, analysing collisions requires a way to measure the overlap between the two nuclei, as not all nucleons may be involved in the collision. The centrality c of an event is defined as

$$c = \frac{\int_0^{b'} \frac{d\sigma}{db} db}{\int_0^\infty \frac{d\sigma}{db} db}, \quad (2.3.1)$$

with the impact parameter b , which is the distance between the centres of the colliding ions. But as experiments do not measure the impact parameter b , the centrality is instead approximated as the percentile of the hadronic cross section in which the produced energy or multiplicity exceeds a certain threshold [99, 100]. This definition leads to the counterintuitive result that the most central or head-on collisions are associated with low centrality values, while ultra-peripheral collision (UPC), where the nuclei do not “overlap”, correspond to high centrality values. The Glauber model is a theoretical framework used to describe and calculate the geometric aspects of nuclear collisions [101–103]. The model assumes that nucleons move independently, and that interactions can be treated probabilistically. It allows for the estimation of the number of participating nucleons N_{part} and the number of binary nucleon-nucleon collisions N_{coll} based on the overlap geometry of the colliding nuclei. An example of this geometric configuration is illustrated in Fig. 2.13.

In pp collisions, the partonic substructure is well-described using PDFs obtained through fits to experimental data. However, extending this approach to heavy-ion collisions by considering the nucleus as a mere superposition of free proton and neutron PDFs does not sufficiently describe the observed data. DIS experiments in the 1980s revealed that parton momentum distributions within bound nucleons are different from those in free protons, necessitating the use of nPDFs [105]. Written as an inequality, the nuclear modification of a parton distribution function can not be expressed as

$$A f_{i/A}(x, \mu) \neq Z f_{i/p}(x, \mu) + N f_{i/n}(x, \mu), \quad (2.3.2)$$

with $N = A - Z$, where A is the atomic number of the nucleus, and Z and N are the number of protons and neutrons, respectively. Thus, in nPDF a dependence on A is introduced. EPPS16 [106] accounts for nuclear effects by modifying the free proton PDF

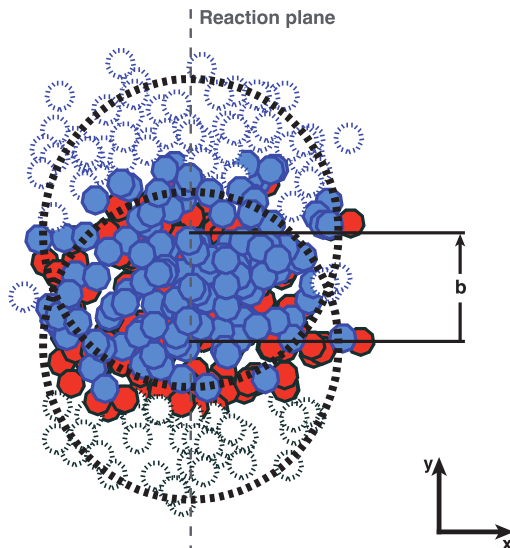


Figure 2.13: The number of participating nucleons N_{part} (filled circles) and binary collisions N_{coll} is determined by the overlap geometry of the colliding nuclei through the Glauber model. Figure taken from [104].

is by a factor R_i^A

$$f_{i/p/A}(x, \mu) = R_i^A(x, \mu) f_{i/p}(x, \mu). \quad (2.3.3)$$

Alternatively, nCTEQ15 [107] adds a dependence on the atomic number A by introducing

$$A f_{i/A}(x, \mu) = Z f_{i/p/A}(x, \mu, A) + N f_{i/n/A}(x, \mu, A), \quad (2.3.4)$$

where the isospin symmetry $f_{d/n/A} = f_{u/p/A}$ and $f_{d/p/A} = f_{u/n/A}$ holds and the momentum fraction is $x \in (0, A)$ with values above 1 negligible. The bound proton PDF $f_{i/p/A}$ differs from the free proton PDF $f_{i/p}$ due to nuclear effects encoded by the A dependence in the fit parameters. The fit results are shown in Fig. 2.14 for different ions, where no nuclear effects (*i.e.* proton) would correspond to a flat line. It shows nuclear effects like shadowing, anti-shadowing, the European Muon Collaboration (EMC) effect, but not Fermi motion, which is only relevant at high- x . These nuclear phenomena vary across different momentum fractions. For example, shadowing is a depletion of parton densities at low- x , that can be attributed to multiple scattering within the extended nuclear environment, leading to shielding by outer nuclei. This is a consistent explanation with the fact that heavier nuclei show stronger shadowing effects than lighter ones. At intermediate- x (~ 0.1 to 0.2), anti-shadowing is observed, where the parton densities are enhanced compared to free protons. This effect is attributed to the interference of multiple scattering amplitudes, leading to a constructive interference in the nuclear environment. The EMC effect, observed at mid- x (~ 0.2 to 0.8), historically sparked a significant debate, with various models proposing changes in nucleon structure or enhanced pion presence as possible explanations [110, 111]. At high- $x \sim 1$, a steep rise in parton densities is linked to Fermi motion, where the intrinsic momentum of nucleons inside the nucleus adds to the parton momentum distribution [105], but also due to the fact that the proton PDF needs to go to zero at $x = 1$. Despite the progress made in

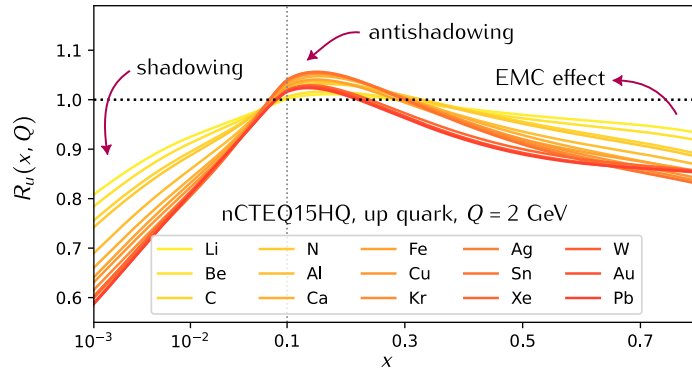


Figure 2.14: nCTEQ15HQ [108] nPDF for different nuclei, showing the difference to free-proton PDFs due to nuclear effects. Figure taken from [109].

developing nPDFs, considerable uncertainties remain, especially in the gluon sector at low- x , where experimental data is scarce.

In the previous discussion of PDFs, we found that the gluon density gets increasingly dominant at low- x values (see Fig. 2.7). This increase occurs because linear evolution equations, such as DGLAP and its counterpart Balitsky-Fadin-Kuraev-Lipatov (BFKL) [112], primarily account for parton splitting processes. However, it becomes evident that this growth cannot continue indefinitely without eventually encountering physical limitations. At very low- x , the gluon density becomes so high that the probability of gluon fusion becomes significant, leading to saturation effects. This regime can then be described by the non-linear Balitsky-Kovchegov (BK) [113] and Jalilian-Marian-Iancu-McLerran-Weigert-Leonidov-Kovner (JIMWLK) [114] equations. The Color Glass Condensate (CGC) framework offers a theoretical model for this regime, which influences the initial conditions for the evolution of the collision system, impacting properties like the shear viscosity of the QGP [98]. The theoretical saturation scale Q_s at which the splitting processes are in equilibrium takes the form

$$Q_s^2(x) \sim x^{-\lambda} A^{\frac{1}{3}} Q_{s,0}^2, \quad (2.3.5)$$

where $\lambda \approx 0.3$ and $Q_{s,0}$ is the saturation scale of a single nucleon. This is displayed in Fig. 2.15. Experimental studies focusing on saturation phenomena, particularly in proton-nucleus (pA) collisions, are crucial since these environments provide a cleaner probe of initial-state effects without significant QGP-induced final-state interactions. This has motivated the development of detectors like the Forward Calorimeter (FoCal) [116] for A Large Ion Collider Experiment (ALICE), which aims to enhance sensitivity to low- x phenomena by focusing on measurements at forward rapidities. The sensitivity of current and future experiments is shown in Fig. 2.16 where the saturation scales of heavier ions are closer to the experimental regimes.

2.3.2 Quark-gluon plasma

One of the key objectives of the LHC physics program is to understand the high-energy density and temperature conditions in ultra-relativistic heavy-ion collisions. These collisions lead to the creation of a QGP, a state of matter in which quarks and gluons,

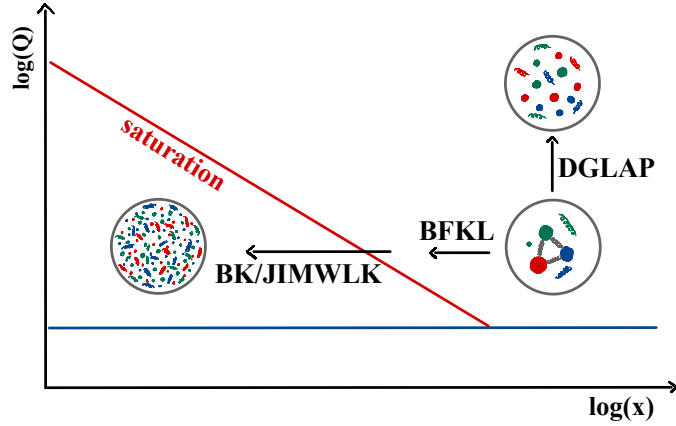


Figure 2.15: QCD evolution of the PDF along Q by DGLAP and along x by BFKL. The transition over the saturation scale Q_s is governed by the BK/JIMWLK equations. Figure taken from [115].

usually confined within protons and neutrons, become deconfined and interact freely. This deconfined state, with restored chiral symmetry [117], is believed to have existed in the early Universe shortly after the Big Bang and is predicted by QCD calculations on the lattice [118]. The QGP occurs at extremely high temperatures and energy densities, such as those recreated in high-energy heavy-ion collisions. In this phase, the interaction strength between quarks and gluons is reduced due to asymptotic freedom, where the strong force weakens at large momentum transfers [97]. In the high-temperature and low baryochemical potential μ_B region of the QCD matter phase diagram in Fig. 2.17, the QGP is reached in a smooth crossover, while at low temperatures and high baryochemical potentials, it is expected to be reached through a first-order phase transition with a discontinuity in the thermodynamic variables [119].

Understanding the properties of QGP is crucial for mapping the phase diagram of QCD matter, which includes regions where different phases of matter exist based on temperature and baryon density. The QGP formed in heavy-ion collisions provides a unique opportunity to study this phase transition, mirroring the early universe's evolution as it cooled and formed protons, neutrons, and other hadrons. The exploration of this phase transition at low baryochemical potential has been well-studied in LHC and RHIC collisions, where the matter produced is nearly baryon-symmetric [123].

Experiments at facilities like the LHC and the RHIC have successfully created QGP by colliding heavy-ions such as gold and lead at nearly the speed of light. The space-time evolution of two colliding nuclei is illustrated in Fig. 2.18. Contrary to pp collisions the majority of the energy gets deposited in the soft processes, leading to the pre-equilibrium phase, where the matter is not in thermal equilibrium. Once thermalization occurs, the QGP initially forms in a state resembling a nearly perfect fluid with low viscosity, as indicated by comparisons of hydrodynamic models with experimental data. Although QGP is short-lived, decaying within about 1×10^{-22} s, its presence can be inferred through indirect probes. These include the measurement of thermal photons produced by the plasma, jet quenching (a reduction in the momentum of jets passing through the QGP), and suppressed back-to-back correlations of high-momentum particles. Especially photons are important probes of the QGP as they do not interact much with

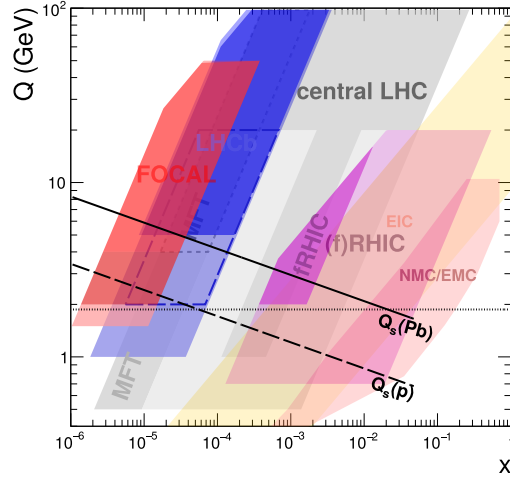


Figure 2.16: Kinematic coverage in x and Q for various existing (such as RHIC, LHC, LHC beauty (LHCb)) and future experiments (Electron Ion Collider (EIC), FoCal). It contains both EM and DIS (less transparent) as well as hadronic and UPC measurements (more transparent). The original figure [116] has been adapted.

the hot medium. The differences between heavy-ion collision results and those from proton-proton collisions, where QGP is not expected to form, further highlight the distinct properties of this exotic state [97]. The system then expands and rapidly cools, eventually transitioning back into ordinary hadronic matter as it undergoes a crossover phase transition at a critical temperature of approximately 155 MeV [122, 124, 125]. In the subsequent hadron gas phase, the difference between chemical freeze-out and kinetic freeze-out is that chemical freeze-out marks the point where inelastic collisions stop, while kinetic freeze-out represents the final stage when elastic collisions also cease.

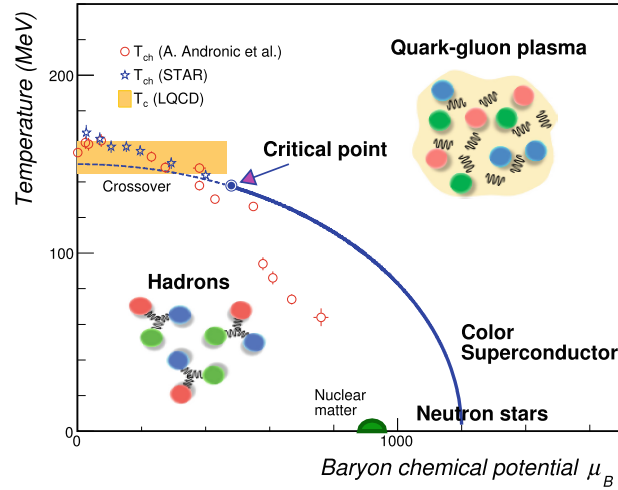


Figure 2.17: A sketch of the QCD phase diagram is presented, showing its dependence on temperature T_{ch} and baryon chemical potential μ_B . The diagram includes conjectured phase boundaries, represented by solid and dashed lines, as well as a possible critical point, marked by a solid circular point. Additionally, the extracted values of T_{ch} and μ_B from a statistical model [120, 121] are also plotted on the diagram. Figure taken from [122].

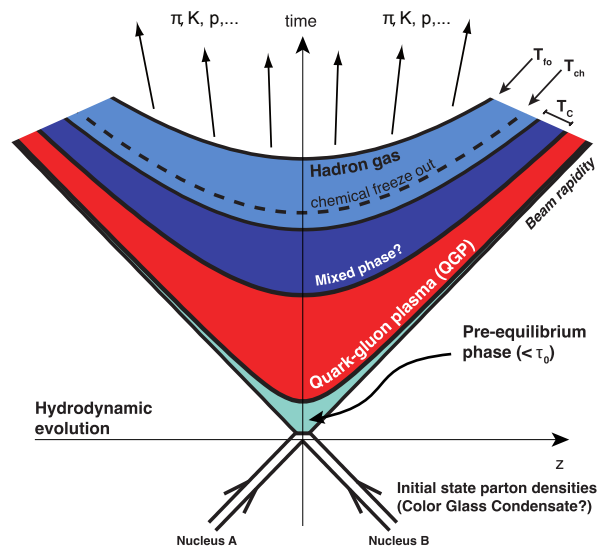


Figure 2.18: QGP evolution in heavy-ion collisions. Figure taken from [104].

Chapter 3

Computation methods

Now it is time to look into the computation of aforementioned quantities. There are several methods addressing the arising complications of the actual calculation, and we can only present a subset here.

3.1 Next-to-leading order calculations

The pure NLO cross section is defined as

$$\Delta\sigma_{\text{NLO}} = \int_{n+1} d\sigma^{\text{R}} + \int_n d\sigma^{\text{V}}. \quad (3.1.1)$$

The integration over the n -particle phase space of the real corrections $d\sigma^{\text{R}}$ turns out to be problematic due to IR divergences, meaning very small momenta in denominators. From the KLN theorem [31, 126] it is known that these soft and/or collinear divergences cancel against the IR divergences from the virtual corrections $d\sigma^{\text{V}}$. When we compute the virtual corrections, will encounter integration over unconstrained loop momenta. They will give rise to UV divergences, meaning very large momenta. UV divergences will be absorbed into counterterms during renormalization. In the end a measurable inclusive quantity will have no more divergences.

To calculate the next-to-leading order we must introduce several methods and formalisms. We start with introducing the several Feynman rules in Sec. 3.1.1. Then, in Sec. 3.1.2 we explain the regularization of divergences, followed by a description of the OS renormalization in Sec. 3.1.3. We start with introducing the Frixione-Kunst-Signer (FKS) and Catani-Seymour (CS) formalism in Sec. 3.1.4.

3.1.1 Feynman rules

Before we can start calculating cross sections and decay rates, we need to establish the Feynman rules for the SM. They can be derived from the Lagrangian of the SM and the rules we will be needing are given in Sec. A.2.1. Further we will need to introduce some alternative Feynman rules, namely the eikonal approximation, the colour lines and the helicity amplitudes.

Type	incoming q	incoming \bar{q}	incoming g	outgoing \tilde{g}	outgoing \tilde{q}
Δ	+	-	+	+	+
δ	-	-	-	+	+
\mathbf{T}^j	T^a	T^a	$-if^{abc}$	$-if^{abc}$	T^a

Table 3.1: Signs and colour operators for eikonal Feynman rule for emitting a soft gluon. In the case of absorbing a gluon or switching incoming and outgoing, the sign δ changes to $-\delta$.

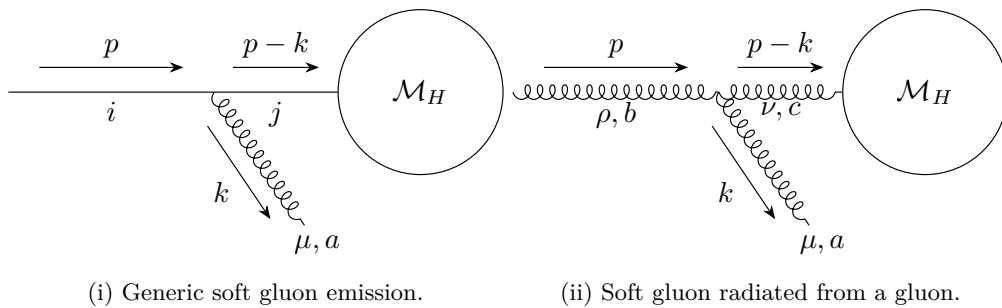


Figure 3.1: Feynman diagrams illustrating eikonal approximation of the emission of a soft gluon

3.1.1.1 Eikonal approximation

Eikonal Feynman rules are a specialized set of rules in QFT designed to handle high-energy scattering processes, particularly in situations where the interaction occurs over long distances or involves small momentum transfers. In such cases, the scattering amplitudes can be simplified using the eikonal approximation, which assumes that the trajectory of the particles is nearly straight and the effects of the interactions are accumulated gradually. The generic form of the eikonal Feynman rule for a process involving two particles scattering off each other is given by

$$\Gamma_{\text{eik}}^\mu = g_S \mathbf{T}^j \frac{\Delta_i v^\mu}{\delta_i v \cdot k + i\epsilon}, \quad (3.1.2)$$

where $v^\mu = p^\mu \sqrt{2/s}$. The signs Δ , δ and the colour operators \mathbf{T}^j are to be used according to Tab. 3.1.

Verifying the eikonal Feynman rule for a soft gluon radiated from a quark is straightforward for a generic underlying hard scattering process \mathcal{M}_H

$$\mathcal{M}_q = \mathcal{M}_H \frac{i(\not{p} - \not{k} + m)}{(p-k)^2 - m^2 + i\epsilon} (-ig_S \gamma^\mu T^a) \varepsilon_\mu^{a*} u(p) \quad (3.1.3)$$

$$\approx \mathcal{M}_H \frac{i(\not{p} + m)}{-2p \cdot k + i\epsilon} (-ig_S \gamma^\mu T^a) \varepsilon_\mu^{a*} u(p), \quad (3.1.4)$$

where we have used the soft limit $k \rightarrow 0$, $p^2 = m^2$. Next we (anti-)commutate the gamma matrices $\not{p}\gamma^\mu = -\gamma^\mu\not{p} + 2p^\mu$ and use the Dirac Eq. (2.0.5) $(-\not{p} + m)u(p) = 0$ to

obtain

$$\mathcal{M}_q = \mathcal{M}_H \frac{2p^\mu}{-2p \cdot k + i\epsilon} (g_S T^a) \varepsilon_\mu^{a*} u(p) \quad (3.1.5)$$

$$= \mathcal{M}_H \Gamma_{\text{eik}}^\mu \varepsilon_\mu^{a*}. \quad (3.1.6)$$

The calculation is even simpler for a gluon radiated from a squark

$$\mathcal{M}_{\bar{q}} = \mathcal{M}_H \frac{i}{(p-k)^2 - m^2 + i\epsilon} i g_S T^a (-2p^\mu + k^\mu) \varepsilon_\mu^{a*} \quad (3.1.7)$$

$$\approx \mathcal{M}_H \frac{+2p^\mu}{-2p \cdot k + i\epsilon} g_S T^a \varepsilon_\mu^{a*} \quad (3.1.8)$$

$$= \mathcal{M}_H \Gamma_{\text{eik}}^\mu \varepsilon_\mu^{a*}, \quad (3.1.9)$$

where the sign δ is different to Tab. 3.1 due to the squark being incoming in our calculation. For a soft gluon being emitted by a gluon the procedure is similar. Starting from the diagram in Fig. 3.1ii we can calculate the eikonal Feynman rule. We write the general expression for this diagram using the usual Feynman rules

$$\mathcal{M}_g = \mathcal{M}_H^\nu \frac{-i g_S f^{bac}}{(p-k)^2 + i\epsilon} [g^{\rho\mu} (p+k)^\nu + g^{\mu\nu} (-k+p-k)^\rho + g^{\nu\rho} (-p+k-p)^\mu] \varepsilon_\rho^b \varepsilon_\mu^{*a} \quad (3.1.10)$$

$$= \mathcal{M}_H^\nu \frac{1}{-2p \cdot k + i\epsilon} (-i f^{abc}) g_S (2g^{\nu\rho} p^\mu - g^{\rho\mu} p^\nu - g^{\mu\nu} p^\rho) \varepsilon_\rho^b \varepsilon_\mu^{*a}, \quad (3.1.11)$$

where in the numerator we have used the soft limit $k \rightarrow 0$, $p^2 = m^2 = 0$ and the antisymmetry of f^{abc} . We can now use a procedure that follows what is presented in [127, eq. (16.16)], which consists of temporarily replacing $\varepsilon_\mu^{*a}(k) \rightarrow k_\mu$. This way, the last two terms contract a metric tensor with the momentum k , leaving just the momentum

$$\mathcal{M}_g = \mathcal{M}_H^\nu \frac{1}{-2p \cdot k + i\epsilon} (-i f^{abc}) g_S (2g^{\nu\rho} p^\mu k_\mu - k^\rho p^\nu - k^\nu p^\rho) \varepsilon_\rho^b \quad (3.1.12)$$

$$= \mathcal{M}_H^\nu \frac{1}{-2p \cdot k + i\epsilon} (-i f^{abc}) g_S (2g^{\nu\rho} p^\mu k_\mu + (k-p)^\rho (k-p)^\nu - k^\rho k^\nu - p^\rho p^\nu) \varepsilon_\rho^b, \quad (3.1.13)$$

where the last three terms vanish due to the soft limit, transverse polarizations of the external gluons $\varepsilon(p)^\mu p^\mu = 0$ and the Ward-Takahashi identity [128, 129]. Making now the inverse substitution $k_\mu \rightarrow \varepsilon_\mu^{*a}(k)$, we obtain

$$\mathcal{M}_g = \mathcal{M}_H^\nu \frac{1}{-2p \cdot k + i\epsilon} (-i f^{abc}) g_S (2p^\mu) \varepsilon_\nu^b \varepsilon_\mu^{*a}. \quad (3.1.14)$$

We can write this results in the general form of an eikonal vertex as

$$\mathcal{M}_g = \mathcal{M}_H \Gamma_{\text{eik.}}^\mu \varepsilon_\mu^{*a}, \quad (3.1.15)$$

where

$$\mathcal{M}_H = \mathcal{M}_H^\nu \varepsilon_\nu^b \quad (3.1.16)$$

and

$$\Gamma_{\text{eik.}}^\mu = \frac{2p^\mu}{-2p \cdot k + i\epsilon} g_S (-i f^{abc}) = g_S \mathbf{T}^j \frac{\Delta_i v^\mu}{\delta_i v \cdot k + i\epsilon}, \quad (3.1.17)$$

again with $v^\mu = p^\mu \sqrt{2/s}$, $\Delta_i = +1$, $\delta_i = -1$ and $\mathbf{T}^j = (-i)f^{abc}$. These signs and colour factors match what presented in Tab. 3.1 for a soft gluon radiated from an incoming gluon. For the other cases the procedure is analogous [130].

3.1.1.2 Colour lines

In this chapter we will introduce the concept of colour lines, also known as colour-flow decomposition, following along [131, 132].

The colour-flow decomposition offers several compelling advantages for analysing and computing QCD amplitudes. It provides an alternative to the fundamental-representation decomposition, extending naturally to all multi-parton amplitudes. The approach is particularly well-suited for calculations involving large numbers of external particles, where it significantly reduces computational complexity. For example, using colour-flow decomposition, the amplitude for a process involving 12 gluons can be calculated approximately 60 times faster than with traditional methods. This increased efficiency stems from the intuitive alignment of the colour-flow decomposition with the physical flow of colour charge within a scattering process, offering a straightforward interpretation of QCD dynamics that directly relates to the underlying particle interactions. Moreover, this method is highly compatible with Monte Carlo simulations, seamlessly integrating with parton shower algorithms and hadronisation models, which are essential for generating realistic event samples at collider experiments [132].

The colour-flow decomposition addresses this challenge by expressing the colour structure of QCD in terms of reducible tensor products of the fundamental representation and its conjugate. This allows the entire scattering amplitude, including sums over multiple Feynman diagrams, to be efficiently represented as weighted sums of Kronecker delta functions, known as colour flows. The decomposition leverages the isomorphism between the adjoint representation of the gauge group and the tensor product of fundamental representations, simplifying the colour representation. This approach connects naturally with 't Hooft's double-line notation [133], where each gluon is represented by a pair of quark and antiquark lines, providing a visual and computational framework for evaluating colour factors. In the large N_c limit, planar Feynman diagrams, where double lines do not cross, become the leading contributions to scattering amplitudes.

Beyond computational efficiency, the colour-flow representation has broader implications. It aligns closely with models of QCD fragmentation, parton showers, and hadronisation, all of which depend on an accurate representation of colour flow in partonic processes [134–136]. All in all, the method is instrumental in Monte Carlo event generators that simulate the full evolution of particle collisions, from hard scattering to the formation of hadrons.

To derive Feynman rules we start from a $SU(N)$ gauge theory

$$\mathcal{L} = \frac{1}{2g_S^2} \text{Tr} F^{\mu\nu} F_{\mu\nu} + \bar{\psi}(i \not{D} - m)\psi, \quad (3.1.18)$$

where

$$D_\mu = \partial_\mu - ig_S A_\mu, \quad (3.1.19)$$

$$F_{\mu\nu} = [D_\mu, D_\nu], \quad (3.1.20)$$

as we already saw in Sec. 2.1.4. Next the gluon field A_μ is decomposed in the fundamental representation matrices T

$$(A_\mu)_j^i = A_\mu^a (T^a)_j^i \quad (3.1.21)$$

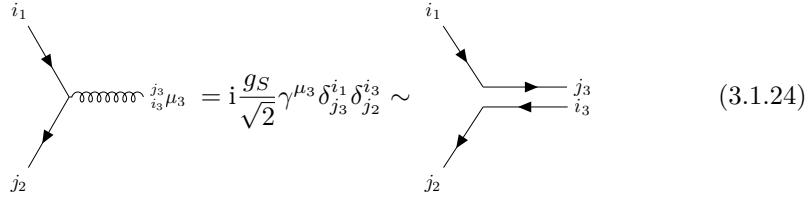
and with the relation $f^{abc} = -i \text{Tr}(T^a T^b T^c - T^a T^c T^b)$ amplitudes can be decomposed into traces of fundamental representation of matrices T [137]. The Lagrangian is given in Ref. [132] as

$$\mathcal{L} = -\frac{1}{4}(F^{\mu\nu})_j^i (F_{\mu\nu})_i^j + i\bar{\psi}_i \gamma^\mu (\delta_j^i \partial_\mu + i\frac{g_S}{\sqrt{2}}(A_\mu)_j^i) \psi^j - m\bar{\psi}_i \psi^i, \quad (3.1.22)$$

with

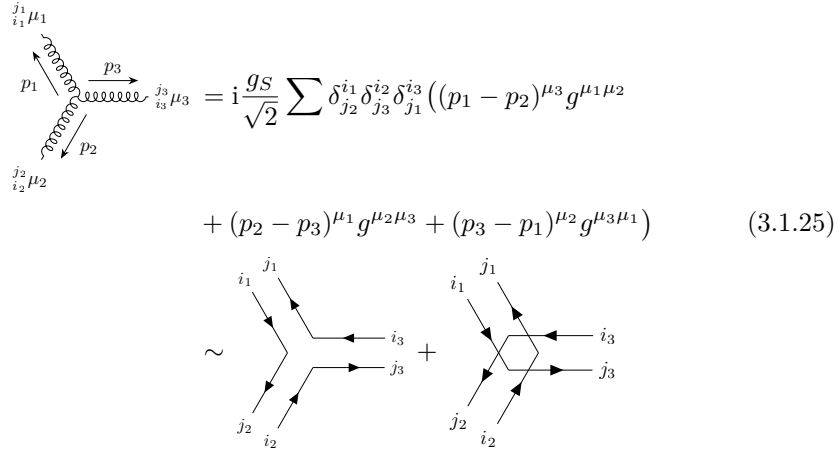
$$(F_{\mu\nu})_j^i = \partial_\mu (A_\nu)_j^i - \partial_\nu (A_\mu)_j^i + i\frac{g_S}{\sqrt{2}}(A_\mu)_k^i (A_\nu)_j^k - i\frac{g_S}{\sqrt{2}}(A_\nu)_k^i (A_\mu)_j^k. \quad (3.1.23)$$

The resulting Feynman rules are



$$\text{Diagram} = i\frac{g_S}{\sqrt{2}} \gamma^{\mu_3} \delta_{j_3}^{i_1} \delta_{j_2}^{i_3} \sim \text{Diagram} \quad (3.1.24)$$

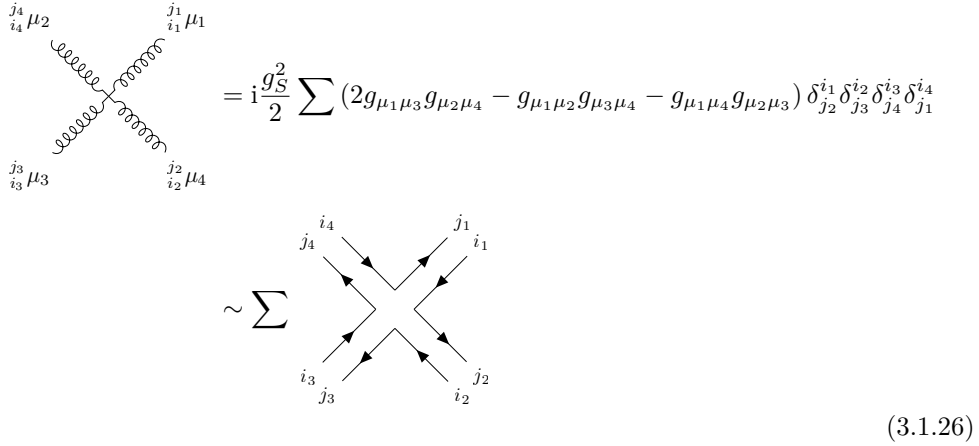
for the quark-gluon vertex,



$$\text{Diagram} = i\frac{g_S}{\sqrt{2}} \sum \delta_{j_2}^{i_1} \delta_{j_3}^{i_2} \delta_{j_1}^{i_3} ((p_1 - p_2)^{\mu_3} g^{\mu_1 \mu_2} + (p_2 - p_3)^{\mu_1} g^{\mu_2 \mu_3} + (p_3 - p_1)^{\mu_2} g^{\mu_3 \mu_1}) \quad (3.1.25)$$

$$\sim \text{Diagram} + \text{Diagram}$$

for the three-gluon vertex and



$$\text{Diagram} = i\frac{g_S^2}{2} \sum (2g_{\mu_1 \mu_3} g_{\mu_2 \mu_4} - g_{\mu_1 \mu_2} g_{\mu_3 \mu_4} - g_{\mu_1 \mu_4} g_{\mu_2 \mu_3}) \delta_{j_2}^{i_1} \delta_{j_3}^{i_2} \delta_{j_4}^{i_3} \delta_{j_1}^{i_4} \quad (3.1.26)$$

$$\sim \sum \text{Diagram}$$

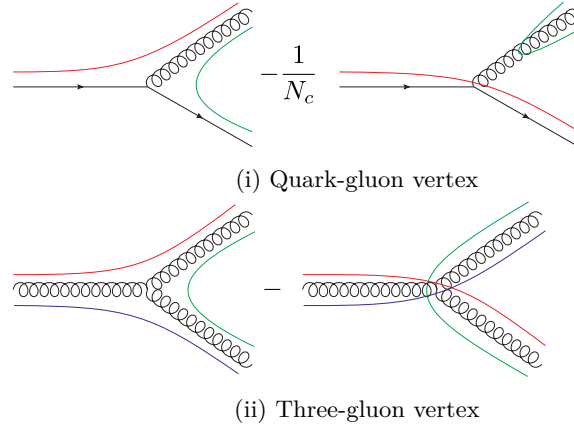


Figure 3.2: Colour flows in conventional Feynman rules [138].

for the four-gluon vertex, where arrows represent the flow of colour. For the three-gluon vertex, the sum covers the two non-cyclic permutations of (1, 2, 3), while in the four-gluon vertex, it includes the six non-cyclic permutations of (1, 2, 3, 4). When calculating a partial amplitude, only a single term of the sum is relevant for a particular colour flow, so that the remaining terms can be neglected. In the colour flow basis the gluon propagator is proportional to

$$\langle (A_\mu)_{j_1}^{i_1} (A_\nu)_{j_2}^{i_2} \rangle \propto \delta_{j_2}^{i_1} \delta_{j_1}^{i_2} - \frac{1}{N} \delta_{j_1}^{i_1} \delta_{j_2}^{i_2} \quad (3.1.27)$$

instead of the usual δ^{ab} as in the conventional Feynman rules, while the quark keeps its colour δ^{ij} . Going to the large N limit, the second term vanishes and the gluon propagator simplifies.

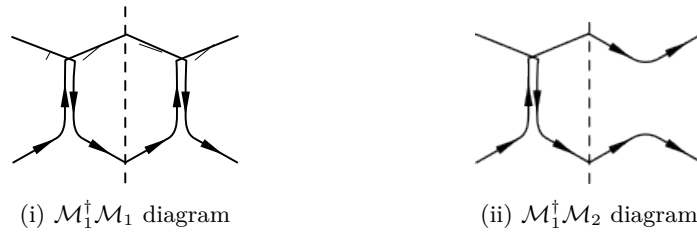
An alternative approach to the colour flow decomposition is given in Fig. 3.2. The quark-gluon vertex in Fig. 3.2i can be understood from

$$T_{ij}^a T_{kl}^a = \frac{1}{2} \left(\delta_{il} \delta_{jk} - \frac{1}{N} \delta_{ij} \delta_{kl} \right), \quad (3.1.28)$$

where one T comes from the vertex and one from the gluon field. Similarly, the three-gluon vertex in Fig. 3.2ii corresponds to contracting the three gluon fields with the vertex' structure constant f^{abc}

$$f^{abc} T_{ij}^a T_{kl}^b T_{mn}^c = (\delta_{il} \delta_{kn} \delta_{mj} - \delta_{in} \delta_{ml} \delta_{kj}). \quad (3.1.29)$$

Since many automated tools for computing amplitudes are based on the conventional Feynman rules, we can adapt them to colour-flow decomposition. The idea behind the following simplified decomposition is to use the fact that in the large N limit, only the diagram combinations with the most closed loops contribute. This is due to each closed colour flow loop contributing a factor of N . Unfortunately, the 4 gluon vertex mixes colour and Lorentz structures which prohibits a simple factorization of the colour and thus decomposition as outlined below. Looking at the diagrams of $qq \rightarrow qq$ in Fig. 3.3, we observe that there are two possible colour flows. At large N , the first diagram connects q_1 with q_4 through the gluon (CL1), while the second connects q_1 with q_3 (CL2). They

Figure 3.3: Example of conventional Feynman diagrams for a $qq \rightarrow qq$ process.Figure 3.4: Example of a colour flow diagram for a $qq \rightarrow qq$ process. The dashed lines in the middle symbolize the phase space integration with the conjugated diagram on the right side. Figures adapted from [131].

are depicted in Fig. 3.4. Following the colour flow through the diagram and the adjoint diagram, we observe that the interference term has one closed loop less

$$\mathcal{M}_1^\dagger \mathcal{M}_1 \sim N^2, \quad (3.1.30)$$

$$\mathcal{M}_2^\dagger \mathcal{M}_2 \sim N^2, \quad (3.1.31)$$

$$\mathcal{M}_1^\dagger \mathcal{M}_2 \sim N. \quad (3.1.32)$$

Since we know that $\mathcal{M}^\dagger \mathcal{M}$ must be the same regardless of using the colour flow or conventional calculation this will also hold in the large N limit. Therefore, we can write

$$\mathcal{M}_1^\dagger \mathcal{M}_1 = a_{11} \mathcal{M}_{11, \text{CL1}}^2 + b_{11} \mathcal{M}_{11, \text{CL2}}^2 + c_{11} 2 \text{Re}(\mathcal{M}_{11, \text{CL1}}^\dagger \mathcal{M}_{11, \text{CL2}}), \quad (3.1.33)$$

$$\mathcal{M}_2^\dagger \mathcal{M}_2 = a_{22} \mathcal{M}_{22, \text{CL1}}^2 + b_{22} \mathcal{M}_{22, \text{CL2}}^2 + c_{22} 2 \text{Re}(\mathcal{M}_{22, \text{CL1}}^\dagger \mathcal{M}_{22, \text{CL2}}), \quad (3.1.34)$$

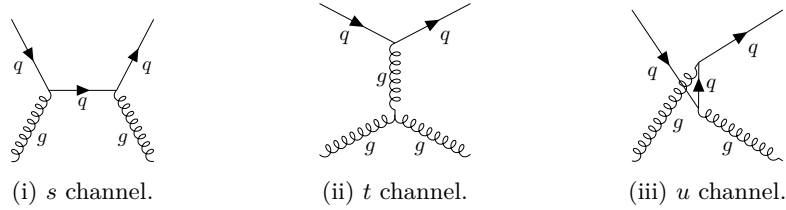
$$2 \text{Re}(\mathcal{M}_1^\dagger \mathcal{M}_2) = a_{12} \mathcal{M}_{12, \text{CL1}}^2 + b_{12} \mathcal{M}_{12, \text{CL2}}^2 + c_{12} 2 \text{Re}(\mathcal{M}_{12, \text{CL1}}^\dagger \mathcal{M}_{12, \text{CL2}}), \quad (3.1.35)$$

where the amplitude calculated in the colour flow is $\mathcal{M}_{\text{CL1}} = \sum a_{ij} \mathcal{M}_{ij, \text{CL1}}^2$. The coefficients a , b and c can be seen as components of a basis transformation matrix. Since we are looking at the large N limit, we can already neglect the interference terms in the colour flow $c \rightarrow 0$. From comparing the conventional diagram with the colour line diagram we can see that only

$$a_{11} = 1 \quad \text{and} \quad b_{22} = 1 \quad (3.1.36)$$

are non-zero. Then, we have

$$\mathcal{M}_{\text{CL1}}^2 = \frac{4}{9} g_s^4 \frac{s^2 + u^2}{t^2}, \quad (3.1.37)$$

Figure 3.5: Example of conventional Feynman diagrams for a $qq \rightarrow qq$ process.

$$\mathcal{M}_{\text{CL2}}^2 = \frac{4}{9}g_S^4 \frac{s^2 + t^2}{u^2}, \quad (3.1.38)$$

in agreement with [134] and does not include the higher N order suppressed term $-8u^2/(27st)$ as in Ref. [49, tab. (7.1)]. In Fig. 3.5 we see an example of a $qq \rightarrow qq$ process which now involves a ggg -vertex. The possible colour flows can be read of the diagrams 1 and 3 since starting from the incoming quark the line has to enter the gluon. Therefore, the colour flow either goes from q_1 to g_2 (CL1) or from q_1 to g_4 (CL2). Then,

$$\mathcal{M}_1^\dagger \mathcal{M}_1 = a_{11} \mathcal{M}_{11, \text{CL1}}^2, \quad (3.1.39)$$

$$\mathcal{M}_2^\dagger \mathcal{M}_2 = a_{22} \mathcal{M}_{22, \text{CL1}}^2 + b_{22} \mathcal{M}_{22, \text{CL2}}^2, \quad (3.1.40)$$

$$\mathcal{M}_3^\dagger \mathcal{M}_3 = b_{33} \mathcal{M}_{33, \text{CL2}}^2, \quad (3.1.41)$$

$$2 \text{Re}(\mathcal{M}_1^\dagger \mathcal{M}_2) = a_{12} \mathcal{M}_{12, \text{CL1}}^2, \quad (3.1.42)$$

$$2 \text{Re}(\mathcal{M}_1^\dagger \mathcal{M}_3) = 0, \quad (3.1.43)$$

$$2 \text{Re}(\mathcal{M}_2^\dagger \mathcal{M}_3) = b_{23} \mathcal{M}_{23, \text{CL2}}^2, \quad (3.1.44)$$

where the triple gluon vertex contains both flows equally $\mathcal{M}_2 \sim (\mathcal{M}_{\text{CL1}} - \mathcal{M}_{\text{CL2}})/\sqrt{2}$ and their interference drops in the large N limit resulting in $a_{22} = b_{22} = 1/2$. Similarly, $\mathcal{M}_1^\dagger \mathcal{M}_2$ and $\mathcal{M}_2^\dagger \mathcal{M}_3$ become projection-like and give a single colour flow in the large N limit and $a_{11} = a_{33} = a_{12} = b_{23} = 1$. Hence,

$$\mathcal{M}_{\text{CL1}}^2 = \mathcal{M}_1^\dagger \mathcal{M}_1 + \mathcal{M}_2^\dagger \mathcal{M}_2 / 2 + 2 \text{Re}(\mathcal{M}_1^\dagger \mathcal{M}_2) = \frac{4}{9}g_S^4 \left(2 \frac{u^2}{t^2} - \frac{u}{s} \right), \quad (3.1.45)$$

$$\mathcal{M}_{\text{CL2}}^2 = \mathcal{M}_3^\dagger \mathcal{M}_3 + \mathcal{M}_2^\dagger \mathcal{M}_2 / 2 + 2 \text{Re}(\mathcal{M}_2^\dagger \mathcal{M}_3) = \frac{4}{9}g_S^4 \left(2 \frac{s^2}{t^2} - \frac{s}{u} \right), \quad (3.1.46)$$

satisfying the crossing relation $u \leftrightarrow s$ corresponding to swapping the external gluon legs as in Ref. [134]. Comparing against [49, Tab. (7.1)]

$$\mathcal{M}^2 = g_S^4 \left(\frac{u^2 + s^2}{t^2} - \frac{4}{9} \frac{s^2 + u^2}{su} \right) \quad (3.1.47)$$

we see that the error is just $(u^2 + s^2)/(9t^2)$ reassuring us that the colour of a particle can be assigned reasonably well in the large N limit.

We have demonstrated that it is possible to compute the colour lines using the conventional Feynman rules as long as there is no four-gluon vertex. These colour lines allow us to probabilistically assign a leading colour to each particle in the large N limit

for a given phase space point of the hard process by their relative strength. Practically, a random $r \in (0, 1)$

$$r < \min_M \left(\frac{\sum_k^M \mathcal{M}_{\text{CL}k}^2}{\sum_i^N \mathcal{M}_{\text{CL}i}^2} \right) \quad (3.1.48)$$

decides which colour flow M out of N possibilities is chosen, such that in a large sample the events follow the correct colour flow distribution.

3.1.1.3 Helicity amplitudes

In automated computations, following the analytic steps of squaring the amplitude and performing trace operations over gamma matrices become impractical, especially for processes involving many final-state particles. The number of contributing diagrams scales factorially with the number of particles, and processes involving multiple gluons produce particularly large analytic expressions due to the structure of the ggg and $gggg$ vertices in conventional Feynman rules. In such cases, the expressions become exceedingly lengthy and only simplify after substantial algebraic manipulation.

A more efficient approach is to directly evaluate the external particle's wave-functions for specific phase space points. Fermions and vector particles can be represented by six-dimensional vectors of complex numbers that encode full momentum, helicity, and spin information. These wave-functions are then combined according to the vertices in the Feynman diagram. However, care must be taken with the order in which the Feynman rule vertices are applied. For example, in the process $e^+e^- \rightarrow \mu^+\mu^-$, the $ee\gamma$ vertex generates the wave-function for the photon, which is then contracted with the $\gamma\mu\mu$ vertex to yield the amplitude. The result is a single complex number, \mathcal{M}_i , for each diagram's amplitude, which can be summed and squared to obtain $|\mathcal{M}|^2$ for a given helicity configuration. In a process like $e^+e^- \rightarrow \gamma, Z, H \rightarrow \mu^+\mu^-$, the interference terms of the amplitudes are reduced to summing complex numbers

$$\mathcal{M} = \mathcal{M}_\gamma + \mathcal{M}_Z + \mathcal{M}_H. \quad (3.1.49)$$

This approach is particularly advantageous when many diagrams contribute to the same process, such as when many external legs or gluons are involved. The squared matrix element is then summed over all possible helicity configurations to obtain the final cross section.

At tree level, this can be efficiently accomplished using the HELAS [139] formalism, which provides a set of Fortran routines for evaluating matrix elements for specific processes. Similar methods are employed in popular tools like MadGraph [140], Whizard [141, 142], and FormCalc [143], and have been extended to NLO in HELAC-NLO [144]. One drawback of this numerical approach is the need for high precision, especially when significant cancellations occur between terms in the amplitudes.

3.1.2 Regularization

A proper treatment of the divergences requires them to be regularized. The following methods are motivated by the fact that changing the number of dimensions affects the divergence of an integral, *e.g.*

$$\int_a^\Lambda \frac{1}{r^2} d^3r \sim \mathcal{O}(\Lambda), \quad \int_a^\Lambda \frac{1}{r^2} d^2r \sim \mathcal{O}(\log \Lambda), \quad \int_a^\Lambda \frac{1}{r^2} d^1r \sim \mathcal{O}(1), \quad (3.1.50)$$

for a large cutoff scale Λ . Transitioning to a $D = 4 - 2\epsilon$ dimensional momentum integral

$$\int d^4l \rightarrow \mu^{4-D} \int d^Dl \quad (3.1.51)$$

regularizes the divergence through poles in ϵ with a renormalization scale μ to conserve mass-dimensions. There are two types of poles IR and UV. UV poles are always simple poles and arrive from $D \rightarrow 4^-$, *i.e.* $\epsilon > 0$. IR poles can be simple or double poles corresponding to a soft and collinear divergence as $D \rightarrow 4^+$, *i.e.* $\epsilon < 0$. While in a final result all poles must cancel within their type, it is common to not treat $\epsilon_{\text{IR}}^{-1}$ and $\epsilon_{\text{UV}}^{-1}$ poles separately, but just as ϵ^{-1} . [127, 145]

3.1.2.1 Dimensional regularization schemes

We will look briefly at different Dimensional Reduction (DRED) schemes. They differ in their treatment of the vector field regularization, *i.e.* the gluon. Since these schemes use different spaces, we list them here:

- 4-dimensional Minkowski space ($\mathbf{S}_{[4]}$)
- quasi- d -dimensional space ($\mathbf{QS}_{[d]}$) is infinite dimensional and as a consequence it is a superspace of $\mathbf{S}_{[4]} \subset \mathbf{QS}_{[d]}$.
- quasi-4-dimensional space ($\mathbf{QS}_{[d_s]}$) is closely related to $\mathbf{S}_{[4]}$ but $\mathbf{QS}_{[d]} \subset \mathbf{QS}_{[d_s]} = \mathbf{QS}_{[d_s]} \oplus \mathbf{QS}_{[n_\epsilon]}$ must hold to sustain gauge invariance. Thereby, $d_s \equiv d + n_\epsilon = 4 - 2\epsilon + n_\epsilon$.

The index in brackets $[d]$ refers to the dimension of the space. From here we can look at the consequences for the metric tensors and gamma matrices

$$g_{[d_s]}^{\mu\nu} = g_{[d]}^{\mu\nu} + g_{[n_\epsilon]}^{\mu\nu}, \quad g_{[\text{dim}]}^{\mu\mu} = \text{dim}, \quad g_{[d]}^{\mu\nu} g_{[n_\epsilon]}^{\nu\rho} = 0, \quad (3.1.52)$$

$$\gamma_{[d_s]}^\mu = \gamma_{[d]}^\mu + \gamma_{[n_\epsilon]}^\mu, \quad \{\gamma_{[\text{dim}]}^\mu, \gamma_{[\text{dim}]}^\nu\} = 2g_{[\text{dim}]}^{\mu\nu}, \quad \{\gamma_{[d]}^\mu, \gamma_{[n_\epsilon]}^\nu\} = 0. \quad (3.1.53)$$

The ordering of these spaces implies the projections relations to be

$$g_{[d_s]}^{\mu\nu} g_{[d]}^{\nu\rho} = g_{[d]}^{\mu\rho}, \quad g_{[d_s]}^{\mu\nu} g_{[4]}^{\nu\rho} = g_{[4]}^{\mu\rho}, \quad g_{[d]}^{\mu\nu} g_{[4]}^{\nu\rho} = g_{[4]}^{\mu\rho}, \quad (3.1.54)$$

meaning that we take the subspace upon contractions with a different space.

After settling these formalities, we move on to the regularization. Regardless of the scheme the momentum integration is done in d dimensions. We will call singular gluons **internal**, meaning those in collinear/soft emissions or loops, and the remaining gluons **external**. Divergences only appear with internal ones, so regularization of external gluons is optional. Four prominent regularization schemes are:

- **Conventional Dimensional Regularization (CDR)**: Both internal and external gluons are treated d -dimensional. This makes this scheme appealing for automatized calculations.
- **'t Hooft Veltman (tHV)**: The internal gluons are d -dimensional, but the external ones are 4-dimensional.
- **DRED**: Both internal and external gluons are quasi-4-dimensional.

- **Four Helicity Dimension (FHD):** The internal gluons are quasi-4-dimensional, but the external ones are 4-dimensional. This scheme is used in `MadGraph` since it allows using a helicity formalism through `HELAS`.

For DRED and FHD d_s is usually 4 or equivalently $n_\epsilon = 2\epsilon$.

Methods for converting different schemes can be found in Refs. [146–148] and more details and examples are available in Refs. [149–152]. The application of γ^5 in D dimensions must also be reconsidered. We will stick to the naive handling by keeping its anticommutation relation $\{\gamma_5, \gamma_\mu\} = 0$ and dropping the trace relation $\text{Tr}[\gamma^\mu \gamma^\nu \gamma^\rho \gamma^\sigma \gamma_5] = i4\epsilon^{\mu\nu\rho\sigma}$ [153]. By convention the trace is evaluated to $\text{Tr}[\mathbb{1}] = 4$.

3.1.2.2 Passarino-Veltman reduction

To evaluate a divergent loop integral in $D - 2\epsilon$ dimensions the Passarino-Veltman (PV) reduction is very useful. A general N -loop integral is depicted in Fig. 3.6 written in the following in an algebraic form

$$T_{\mu_1, \dots, \mu_M}^N(p_1, \dots, p_M, m_1, \dots, m_M) = \frac{\mu^{4-D}}{i\pi^{D/2} r_\Gamma} \int d^D l \frac{l_{\mu_1} \dots l_{\mu_M}}{\mathcal{D}_1 \dots \mathcal{D}_N}, \quad (3.1.55)$$

with the prefactor

$$r_\Gamma = \frac{\Gamma(1-\epsilon)^2 \Gamma(1+\epsilon)}{\Gamma(1-2\epsilon)} = 1 - \gamma_E \epsilon + \left(\frac{\gamma_E^2}{2} - \frac{\pi^2}{12}\right) \epsilon^2 + \mathcal{O}(\epsilon^3) \quad (3.1.56)$$

and denominators

$$\mathcal{D}_1 = l^2 - m_1^2, \quad (3.1.57)$$

$$\mathcal{D}_2 = (l + p_1)^2 - m_2^2, \quad (3.1.58)$$

$$\vdots \quad (3.1.59)$$

$$\mathcal{D}_N = \left(l + \sum_{i=1}^N p_i\right)^2 - m_N^2. \quad (3.1.60)$$

Alternative definitions factorize $1/\Gamma(1+\epsilon)$ giving differences of order $\mathcal{O}(\epsilon)$

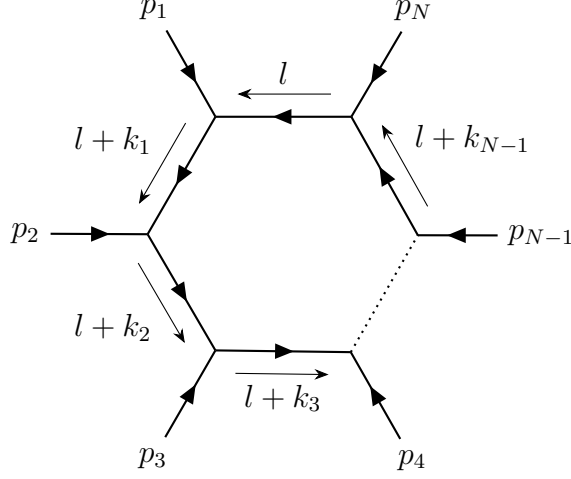
$$\frac{\Gamma(1+\epsilon)}{\Gamma(1-\epsilon)^2 \frac{\Gamma(1+\epsilon)}{\Gamma(1-2\epsilon)}} = 1 + \frac{\pi^2}{6} \epsilon^2 + \mathcal{O}(\epsilon^3) \quad (3.1.61)$$

resulting in shifted finite (ϵ^0) contributions when double poles (ϵ^{-2}) appear. In accordance with the conventions of `LoopTools` [143] we introduce the notation

$$\Delta = \frac{1}{\epsilon} - \gamma_E + \log 4\pi \quad (3.1.62)$$

and use the definition of the momenta

$$k_n = \sum_{i=1}^n p_i. \quad (3.1.63)$$

Figure 3.6: Momentum conventions for general N -loop diagrams.

Of special importance are the scalar integrals ($M = 0$). We will need them with up to five particles in the loop

$$T^1 = A_0(m_1^2) = \frac{\mu^{4-D}}{i\pi^{D/2} r_\Gamma} \int d^D l \frac{1}{\mathcal{D}_1} =: \int_l \frac{1}{\mathcal{D}_1}, \quad (3.1.64)$$

$$T^2 = B_0(p_1^2, m_1^2, m_2^2) = \int_l \frac{1}{\mathcal{D}_1 \mathcal{D}_2}, \quad (3.1.65)$$

$$T^3 = C_0(p_1^2, p_2^2, (p_1 + p_2)^2, m_1^2, m_2^2, m_3^2) = \int_l \frac{1}{\mathcal{D}_1 \mathcal{D}_2 \mathcal{D}_3}, \quad (3.1.66)$$

$$T^4 = D_0(p_1^2, p_2^2, p_3^2, p_4^2, (p_1 + p_2)^2, (p_2 + p_3)^2, m_1^2, m_2^2, m_3^2, m_4^2) = \int_l \frac{1}{\mathcal{D}_1 \mathcal{D}_2 \mathcal{D}_3 \mathcal{D}_4}. \quad (3.1.67)$$

They were first calculated by 't Hooft and Veltman in Ref. [154]. The tensor reduction proposed by Passarino and Veltman avoids solving more complicated integrals by recycling the scalar integrals [155].

The Lorentz covariance of the integrals allows for the decomposition of the tensor integrals into tensors formed from the external momenta p_i and the metric tensor $g_{\mu\nu}$, with totally symmetric coefficient functions $T_{i_1 \dots i_P}^N$. To express the terms involving $g_{\mu\nu}$ more compactly, we introduce a momentum p_0 formally. This leads to

$$T_{\mu_1 \dots \mu_P}^N(p_1, \dots, p_{N-1}, m_0, \dots, m_{N-1}) = \sum_{i_1, \dots, i_P=0}^{N-1} T_{i_1 \dots i_P}^N k_{i_1 \mu_1} \dots k_{i_P \mu_P}. \quad (3.1.68)$$

From this expression, the correct $g_{\mu\nu}$ terms can be obtained by discarding all terms containing an odd number of k_0 's and replacing products of even numbers of k_0 's with the corresponding tensors constructed from $g_{\mu\nu}$, for instance

$$k_{0\mu_1} k_{0\mu_2} \rightarrow g_{\mu_1 \mu_2}, \quad (3.1.69)$$

$$k_{0\mu_1} k_{0\mu_2} k_{0\mu_3} k_{0\mu_4} \rightarrow g_{\mu_1 \mu_2} g_{\mu_3 \mu_4} + g_{\mu_1 \mu_3} g_{\mu_2 \mu_4} + g_{\mu_1 \mu_4} g_{\mu_2 \mu_3} \quad (3.1.70)$$

and written explicitly

$$B^\mu = k_1^\mu B_1, \quad (3.1.71)$$

$$B^{\mu\nu} = g^{\mu\nu} B_{00} + k_1^\mu k_1^\nu B_{11}, \quad (3.1.72)$$

$$C^\mu = k_1^\mu C_1 + k_2^\mu C_2, \quad (3.1.73)$$

$$C^{\mu\nu} = g^{\mu\nu} C_{00} + k_1^\mu k_1^\nu C_{11} + (k_1^\mu k_2^\nu + k_2^\mu k_1^\nu) C_{12} + k_2^\mu k_2^\nu C_{22}, \quad (3.1.74)$$

\vdots

Since four-dimensional space is spanned by four Lorentz vectors, terms involving $g_{\mu\nu}$ should be excluded for $N \geq 5$. In such cases, the decomposition should involve no more than four Lorentz vectors

$$T_{\mu_1 \dots \mu_P}^N(p_1, \dots, p_{N-1}, m_0, \dots, m_{N-1}) = \sum_{i_1, \dots, i_P=1}^4 T_{i_1 \dots i_P}^N k_{i_1 \mu_1} \dots k_{i_P \mu_P}. \quad (3.1.75)$$

By applying the Lorentz decomposition of the tensor integrals as in Eq. (3.1.68), the invariant functions $T_N^{i_1 \dots i_P}$ can be iteratively reduced to the scalar integrals T_N^0 [156–159]. Using

$$l^\mu k_k^\mu = \frac{1}{2}(k_k + l)^2 - l^2 - k_k^2 = \frac{1}{2}(\mathcal{D}_k - \mathcal{D}_1 - f_k), \quad (3.1.76)$$

$$f_k = k_k^2 - m_k^2 + m_1^2, \quad (3.1.77)$$

$$g^{\mu\nu} l^\mu l^\nu = l^2 = \mathcal{D}_1 + m_1^2, \quad (3.1.78)$$

the reduction of tensor integrals to scalar integrals is achieved by contracting the tensor integrals with a momentum

$$T_{\mu_1 \dots \mu_P}^N k_k^{\mu_P} = \frac{1}{2} \int_l \left(\frac{l_{\mu_1} \dots l_{\mu_{P-1}}}{\mathcal{D}_1 \dots \mathcal{D}_{k-1} \mathcal{D}_{k+1} \dots \mathcal{D}_N} + \frac{l_{\mu_1} \dots l_{\mu_{P-1}}}{\mathcal{D}_2 \dots \mathcal{D}_N} - f_k \frac{l_{\mu_1} \dots l_{\mu_{P-1}}}{\mathcal{D}_1 \dots \mathcal{D}_N} \right) \quad (3.1.79)$$

$$= \frac{1}{2} \left[T_{\mu_1 \dots \mu_{P-1}}^{N-1}(k) - T_{\mu_1 \dots \mu_{P-1}}^{N-1}(0) - f_k T_{\mu_1 \dots \mu_{P-1}}^N \right] \quad (3.1.80)$$

or a metric

$$T_{\mu_1 \dots \mu_P}^N g^{\mu_{P-1} \mu_P} = \frac{1}{2} \int_l \left(\frac{l_{\mu_1} \dots l_{\mu_{P-1}}}{\mathcal{D}_2 \dots \mathcal{D}_N} + m_1^2 \frac{l_{\mu_1} \dots l_{\mu_{P-2}}}{\mathcal{D}_1 \dots \mathcal{D}_N} \right) \quad (3.1.81)$$

$$= \left[T_{\mu_1 \dots \mu_{P-2}}^{N-1}(0) + m_1^2 T_{\mu_1 \dots \mu_{P-2}}^N \right]. \quad (3.1.82)$$

The argument k in the tensor integrals of the last line indicates that the propagator \mathcal{D}_k has been cancelled. It is important to note that $T_{N-1}^{\mu_1 \dots \mu_{P-1}}(0)$ contains an external momentum in its first propagator. Consequently, a shift in the integration momentum is required in this integral to bring it into the desired form of Eq. (3.1.55).

Exemplary, $B^\mu = k_1^\mu B_1 = p_1^\mu B_1$ must have that form since p_1^μ is the only available Lorentz-structure and

$$2p_1^2 B_1 = 2p_1^\mu B^\mu = \int_l \frac{2p_1^\mu l^\mu}{\mathcal{D}_1 \mathcal{D}_2} = \underbrace{\int_l \frac{(l+p_1)^2 - m_2^2}{\mathcal{D}_1 \mathcal{D}_2}}_{A_0(m_1^2)} - \underbrace{\int_l \frac{l^2 - m_1^2}{\mathcal{D}_1 \mathcal{D}_2}}_{A_0(m_2^2)} - (p_1^2 - m_2^2 + m_1^2) \underbrace{\int_l \frac{1}{\mathcal{D}_1 \mathcal{D}_2}}_{B_0} \quad (3.1.83)$$

gives B^μ in terms of scalar integrals. The reduction of the B Tensor is

$$B_1(p_1^2, m_1^2, m_2^2) = \frac{1}{2p_1^2} [A_0(m_1^2) - A_0(m_2^2) - (p_1^2 - m_2^2 + m_1^2)B_0] , \quad (3.1.84)$$

$$B_{00}(p_1^2, m_1^2, m_2^2) = \frac{1}{2(D-1)} [A_0(m_2^2) + 2m_1^2B_0 + (p_1^2 - m_2^2 + m_1^2)B_1] , \quad (3.1.85)$$

$$B_{11}(p_1^2, m_1^2, m_2^2) = \frac{1}{2(D-1)} \frac{1}{p^2} [(D-2)A_0(m_2^2) - 2m_1^2B_0 - D(p_1^2 - m_2^2 + m_1^2)B_1] , \quad (3.1.86)$$

where when no parameters are given to a function, the same parameters as on the left-hand side are used. Their divergence as listed in Tab. 3.2 can be found in Refs. [156, 160] and in the papers referenced therein.

Integral	UV divergences	$(D-4) \times \text{Integral}$
$A_0(m^2)$	$m^2 \Delta$	$-2m^2$
B_0	Δ	-2
B_1	$-\frac{1}{2} \Delta$	1
B_{00}	$-(\frac{p^2}{12} - \frac{1}{4}(m_0^2 + m_1^2)) \Delta$	$(\frac{p^2}{6} - \frac{1}{2}(m_0^2 + m_1^2))$
C_{00}	$\frac{1}{4} \Delta$	$-\frac{1}{2}$

Table 3.2: Passarino Veltman Loop integral divergences [156, 160].

For higher-order tensors combining Eq. (3.1.80), Eq. (3.1.82) and Eq. (3.1.68) results in a set of linear equations for the corresponding coefficient functions. If it can be solved the tensor integrals are expressed iteratively in terms of scalar integrals T_0^L with $L \leq N$. Depending on the momentum the linear equations can not be solved and the reduction algorithm breaks down. This usually happens at the edge of phase space where some momenta p_i become collinear. If the Gram determinant is zero, but the momenta are not linear dependent one has to use a different reduction algorithm [161–163]. For numerical evaluation the PV tensors are not necessarily ideal, since cancellations between the scalar integrals can lead to numerical instabilities. More advanced reductions to master integrals can be achieved using integration-by-parts identities, leading to a linear system that is solved using the Laporta algorithm [164, 165]. This complication and freedom in the reduction of loops is the reason for the existence of many loop (reduction) libraries. Just to name a few prominent examples: `FF` [166], `Collier` [167], `LoopTools`, `OneLoop` [168], `CutTools` [169], `QCDloop` [170], `MadLoop` [171], `Golem` [172], `Ninja` [173] and `Samurai` [174]. Now that we have established a practical framework for managing divergences, we proceed to address the necessary renormalization of our fields in the following chapter.

3.1.3 Renormalization

In order to absorb the UV-divergences appearing at one-loop level we replace the bare bosonic fields ϕ_0 with renormalized fields ϕ

$$\phi_0 = \sqrt{Z_0} \phi_0 \rightarrow \sqrt{Z_\phi} \phi = \sqrt{1 + \delta Z_\phi} \phi = (1 + \frac{1}{2} \delta Z_\phi) \phi. \quad (3.1.87)$$

Left- and right-handed fermionic fields are treated separately

$$\psi_0 = \sqrt{Z_0}\psi_0 \rightarrow \left(1 + \frac{1}{2}\delta Z_\psi^L P_L + \frac{1}{2}\delta Z_\psi^R P_R\right)\psi, \quad (3.1.88)$$

where we introduce the chirality projectors $P_{L,R} = \frac{1}{2}(1 \mp \gamma_5)$ since we are operating in the mass-eigenstates now. The L, R index notation is used to separate the two cases in analogy to the \pm notation.

Similarly, couplings λ and masses m get corrections

$$\lambda_0 \rightarrow Z_\lambda \lambda = \lambda + \delta Z_\lambda \lambda, \quad (3.1.89)$$

$$m_0 \rightarrow Z_m m = m + \delta Z_m m. \quad (3.1.90)$$

The advantage of using a renormalization constant δZ shifted from the bare coupling 1 instead of the whole multiplicative renormalization constants Z is that we reproduce our original bare Lagrangian with new counterterms

$$\mathcal{L}_0 \rightarrow \mathcal{L} + \mathcal{L}_\times. \quad (3.1.91)$$

The counterterms will then be chosen to explicitly cancel the UV-divergences encountered at one-loop level in the bare Lagrangian.

In the OS renormalization scheme the renormalized masses correspond to the physical masses and the real part of the propagator's residue is normalized to 1. This differs from the modified minimal subtraction scheme $\overline{\text{MS}}$, where one includes extra counterterms to account for the proper normalization of the residue [10]. Another advantage of the OS renormalization is that we do not have to compute loops at the legs of our Feynman diagrams. Furthermore, the cancellation of UV divergences between various vertices and wave-function renormalization functions is checked explicitly.

Since we only encounter gluons and quarks as intermediate particles at LO in our processes, we look at their renormalization first. To determine the running of the coupling we will also renormalize the gluon propagator.

3.1.3.1 Quarks

The kinetic and mass terms of the bare Lagrangian for quarks reads

$$\mathcal{L}_0 = i\bar{\psi}_0^L \not{\partial} \psi_0^L - m_0 \bar{\psi}_0^R \psi_0^L + (L \leftrightarrow R). \quad (3.1.92)$$

Here the upper indices refer to whether a quark is left- or right-handed. Replacing the bare quantities

$$\psi_0^{L,R} \rightarrow \sqrt{Z_\psi^{L,R}} \psi_{L,R} = \left(1 + \frac{1}{2}\delta Z_\psi^{L,R}\right) \psi_{L,R}, \quad (3.1.93)$$

$$m_0 \rightarrow Z_m m = (1 + \delta Z_m) m, \quad (3.1.94)$$

in the bare Lagrangian \mathcal{L}_0 yields

$$\mathcal{L} = \underbrace{i\bar{\psi}^L \not{\partial} \psi^L - m\bar{\psi}^R \psi^L}_{\mathcal{L}_0} \quad (3.1.95)$$

$$+ \underbrace{i \text{Re}[\delta Z_\psi^L] \bar{\psi}^L \not{\partial} \psi^L - m \left(\delta Z_m + \frac{1}{2}(\delta Z_\psi^{R*} + \delta Z_\psi^L) \right) \bar{\psi}^R \psi^L}_{\mathcal{L}_\times} + (L \leftrightarrow R), \quad (3.1.96)$$

without higher-order terms in δZ . The bare Lagrangian \mathcal{L}_0 gives the typical two-point Green's function by replacing the derivatives with the momenta $-ip$, formally a Fourier transformation into momentum space, and dropping the fields ψ

$$-i\Sigma_0 = i(\not{p} - m), \quad (3.1.97)$$

where we apply $P_L + P_R = 1$, after using $\bar{\psi}_R \psi_L = \bar{\psi} P_L \psi$ and $\bar{\psi}_L \gamma^\mu \psi_L = \bar{\psi} \gamma^\mu P_L \psi$. Following the same steps, the new two-point Green's function for the counterterms is obtained

$$-i\Sigma_\times = i \left(\not{p} \text{Re}[\delta Z_\psi^L] - m \left(\delta Z_m + \frac{1}{2}(\delta Z_\psi^{R*} + \delta Z_\psi^L) \right) \right) P_L + (L \leftrightarrow R). \quad (3.1.98)$$

The NLO propagator Π_ψ^{NLO} then consists of additional self-energies and counterterms

$$\Pi_\psi^{\text{NLO}} = \Pi_\psi^{\text{LO}} + \Pi_\psi^{\text{LO}}(-i\Sigma)\Pi_\psi^{\text{LO}} + \Pi_\psi^{\text{LO}}(-i\Sigma_\times)\Pi_\psi^{\text{LO}} \quad (3.1.99)$$

$$= \Pi_\psi^{\text{LO}}(1 + (-i\hat{\Sigma})\Pi_\psi^{\text{LO}}), \quad (3.1.100)$$

where Σ are the bare self-energy loop contributions. Combining the counterterms and self-energies then gives the renormalized self-energy $\hat{\Sigma}$. Splitting up the vectorial Σ_V and scalar Σ_S part allows us to rewrite

$$\hat{\Sigma} = \left(\underbrace{\not{p}(\Sigma_V - \text{Re}[\delta Z_\psi^L])}_{\hat{\Sigma}_V^L} + m \underbrace{\left(\delta Z_m + \frac{1}{2}(\delta Z_\psi^{R*} + \delta Z_\psi^L) + \frac{\Sigma_S^L}{m} \right)}_{\hat{\Sigma}_S^L} \right) P_L + (L \leftrightarrow R). \quad (3.1.101)$$

To realize OS renormalization the following two conditions must be satisfied [33, 175]. First, the real part of the propagator's pole must be the physical mass, that is

$$\text{Re} \left[\frac{1}{\Pi_\psi^{\text{NLO}}(m^2)} \right] u(p, m) = 0 \quad \xrightarrow{3.1.100} \quad \text{Re}[\hat{\Sigma}(p^2 = m^2)]u(p, m) = 0. \quad (3.1.102)$$

And second, the real part of the propagator's residue should be normalized to 1, translating to

$$\lim_{p^2 \rightarrow m^2} \text{Re}[-i(\not{p} - m)\Pi_\psi^{\text{NLO}}]u(p, m) = u(p, m) \quad \xrightarrow{3.1.100} \quad \lim_{p^2 \rightarrow m^2} \frac{\not{p} + m}{p^2 - m^2} \text{Re}[\hat{\Sigma}]u(p, m) = 0. \quad (3.1.103)$$

These conditions define how we get the OS renormalization constants δZ from the bare self-energies Σ

$$\delta Z_m = -\frac{1}{2} \text{Re} \left[\Sigma_V^L + \Sigma_V^R + \frac{\Sigma_S^L + \Sigma_S^R}{m} \right]_{p^2=m^2}, \quad (3.1.104)$$

$$\delta Z_\psi^{L,R} = \text{Re} \left[\Sigma_V^{L,R} + m^2(\dot{\Sigma}_V^{L,R} + \dot{\Sigma}_V^{R,L} + \frac{\dot{\Sigma}_S^{L,R} + \dot{\Sigma}_S^{R,L}}{m}) \right]_{p^2=m^2}, \quad (3.1.105)$$

where $\dot{\Sigma}$ is the derivative in p^2 . However, we will see in the following sections that no corrections to the quark mass are necessary, since the only particle we treat as massive is the top, which we assume to be negligible in the proton initial-state.

3.1.3.2 Gluon

The renormalization of the gluon is determined in a similar procedure to the previous squark case. But a difference lies in the vanishing longitudinal propagator due to gauge invariance

$$-i\Pi_{\mu\nu}^{ab}(p^2) = -i\delta^{ab} \left(\left(g^{\mu\nu} - \frac{p^\mu p^\nu}{p^2} \right) \Pi_t(p^2) + \frac{p^\mu p^\nu}{p^2} \Pi_l(p^2) \right). \quad (3.1.106)$$

Since the gluon is massless, its renormalization constant is solely determined by the OS condition

$$\delta Z_g = -\text{Re} \left[\frac{d\Pi_t(p^2)}{dp^2} \right]_{p^2=0}. \quad (3.1.107)$$

The resulting counterterms and the UV limit are given in [176].

3.1.4 Subtraction methods

After tackling the UV divergences by renormalization, we are left with the IR divergences. One consequence of the IR divergences is that a Monte-Carlo integration over a 3-particle phase space or larger will not give reliable results. The solution of the formalism can be written in a short equation

$$\sigma^{\text{NLO}} = \int_{n+1} [\text{d}\sigma^{\text{R}} - \text{d}\sigma^{\text{A}}]_{\epsilon=0} + \int_n [\text{d}\sigma^{\text{V}} + \text{d}\sigma^{\text{C}} + \int_1 \text{d}\sigma^{\text{A}}]_{\epsilon=0}. \quad (3.1.108)$$

An auxiliary function σ^{A} is subtracted from the real corrections and added to the virtuals. It will be chosen in such a way that it cancels all the soft and collinear divergences arising in σ^{R} . For initial-state hadrons, the collinear counterterms σ^{C} are added to the virtual corrections in consistency with the terms included in the PDF.

Several subtraction methods exist, each differing in their choice of the auxiliary function $\text{d}\sigma^{\text{A}}$ by resorting to different dipoles. We will first look at the FKS subtraction method [177–179] and then the CS dipole [180, 181] subtraction.

3.1.4.1 The FKS subtraction method

The FKS method was introduced in Ref. [177] and generalized in Ref. [179]. The fundamental idea behind is to introduce a partition function that allows to separate soft and collinear from hard regions similar to phase space slicing [182–186]. The goal is to reproduce the divergent behaviour of the real corrections, *i.e.* in the soft and collinear limits,

$$S \rightarrow \begin{cases} \infty & \text{as } E_j \rightarrow 0 \text{ or } \theta_{ij} \rightarrow 0, \\ 0 & \text{else.} \end{cases} \quad (3.1.109)$$

One parametrization of this is separating in the divergent FSR and ISR. They diverge as

$$S_{0j}^{\text{ISR}} = S_{1j} + S_{2j} = \frac{1}{E_j^2(1 - \cos^2 \theta_{1j})} \quad \text{and} \quad S_{ij}^{\text{FSR}} = \frac{E_i^2 + E_j^2}{2E_i^2 E_j^2 (1 - \cos \theta_{ij})}, \quad (3.1.110)$$

with particle indices $i, j \geq 3$ and θ_{ij} the angle between the two particles. They can be obtained from leading order dijet production limits [187]. After normalization, they read

$$\tilde{S}_{0j} = \frac{S_{ij}}{\sum_j (S_{0j} + \sum_i S_{ij})} \quad \text{and} \quad \tilde{S}_{ij} = \frac{S_{ij}}{\sum_j (S_{0j} + \sum_i S_{ij})} \frac{E_j}{E_i + E_j}, \quad (3.1.111)$$

where the ratio over the energies is introduced to raise the degeneracy between i and j . If one now probes a divergent $2 \rightarrow 3$ regime, then the non-divergent \tilde{S} vanish by construction

$$\tilde{S}_{0j,ij} \rightarrow \begin{cases} 1 & \text{as } E_j \rightarrow 0 \text{ or } \theta_{ij} \rightarrow 0, \\ 0 & \text{else.} \end{cases} \quad (3.1.112)$$

This allows us to isolate the divergent parts of the real corrections R_{ij} for given particle i and j as

$$R = \sum_{i,j} \tilde{S}_{ij} R = \sum_{i,j} R_{ij}. \quad (3.1.113)$$

In a generalized form extended to D dimensions, the phase space integral of a radiated parton i can be written as

$$\frac{d^{D-1}p_i}{(2\pi)^{D-1}2E_i} = d\xi_i dy d\Omega_{D-2} \frac{s^{1-\varepsilon}}{(4\pi)^{3-2\varepsilon}} \xi_i^{1-2\varepsilon} (1-y_{ij}^2)^{-\varepsilon}, \quad (3.1.114)$$

with $\xi_i = 2E_i/\sqrt{s} \in [0, 1]$ and $y_{ij} = \cos(\theta_{ij}) \in [-1, 1]$ and $d\Omega_{D-2}$ is the $(D-2)$ -dimensional solid-angle relative to the momentum of parton j . Next we can pick contributions from there to cancel the divergences per singular region R_{ij} in the real corrections

$$\frac{d^{D-1}p_i}{(2\pi)^{D-1}2E_i} R_{ij} = d\xi_i dy d\Omega_{D-2} \frac{s^{1-\varepsilon}}{(4\pi)^{3-2\varepsilon}} \xi_i^{-1-2\varepsilon} \frac{(1-y_{ij}^2)^{-\varepsilon}}{1-y_{ij}} \hat{R}_{ij}, \quad (3.1.115)$$

where $\hat{R}_{ij} = \xi_i^2(1-y_{ij})R_{ij}$ is divergence free as can be seen from comparing against Eq. (3.1.110). Instead of constructing the $d\sigma^A$ explicitly one uses $d\sigma^R - d\sigma^A = d\sigma^{\hat{R}}$.

We can then extract the IR divergences in ε^{-1} and ε^{-2}

$$\xi_i^{1-2\varepsilon} = -\frac{1}{2\varepsilon} \delta(\xi_i) + \left(\frac{1}{\xi_i}\right)_+ - 2\varepsilon \left(\frac{\log(\xi_i)}{\xi_i}\right)_+ + \mathcal{O}(\varepsilon^2), \quad (3.1.116)$$

$$\frac{(1-y_{ij}^2)^{-\varepsilon}}{1-y_{ij}} = (1+y_{ij})^{-\varepsilon} (1-y_{ij})^{-1-\varepsilon}, \quad (3.1.117)$$

$$(1-y_{ij})^{-1-\varepsilon} = -\frac{2^{-\varepsilon}}{\varepsilon} \delta(1-y_{ij}) + \left(\frac{1}{1-y_{ij}}\right)_+ - \varepsilon \left(\frac{\log(1-y_{ij})}{1-y_{ij}}\right)_+ + \mathcal{O}(\varepsilon^2), \quad (3.1.118)$$

where we encounter δ and plus distributions (cf. Sec. A.4.3). The poles are cancelled against the poles of the virtual corrections and the collinear counterterms. In the FKS subtraction scheme, the virtual contributions need to be provided using the CDR scheme. Within the CDR scheme, the renormalized virtual contributions \mathcal{V} can be expressed with the IR poles explicitly shown

$$\mathcal{V} = \frac{(4\pi)^\varepsilon}{\Gamma(1-\varepsilon)} \frac{\alpha_s}{2\pi} \left[\frac{1}{\varepsilon^2} aB + \frac{1}{\varepsilon} \sum_{i,j} c_{ij} B_{ij} + \mathcal{V}_{\text{fin}} \right]. \quad (3.1.119)$$

The coefficients a and c_{ij} are independent of ϵ , whereas the Born amplitude B and the colour-correlated Born amplitude B_{ij} are defined in D dimensions and thus depend on ϵ . The finite virtual corrections are then \mathcal{V}_{fin} . The coefficients c_{ij} are given in Ref. [177] for coloured legs i and j by

$$c_{ij} = (1 - \delta_{ij}) \left[-\frac{\gamma_i}{C_i} + \log \left(\frac{2p_i \cdot p_j}{\mu_R^2} \right) \right] \quad (3.1.120)$$

and a is the sum over the Casimir constants C_i

$$a = - \sum_i C_i. \quad (3.1.121)$$

The constants γ_i depend on the colour representation of the respective particle

$$\gamma_q = \gamma_{\bar{q}} = \frac{3}{2} C_F, \quad (3.1.122)$$

$$\gamma_g = \frac{11}{6} C_A - \frac{2}{3} n_f T_F. \quad (3.1.123)$$

All together, this results in the lengthy soft-virtual term $d\sigma^V + \int d_1 d\sigma^A$ in Eq. (2.99) of Ref. [188] used in the `POWHEG BOX` [63, 188, 189] implementation. In practice, `POWHEG BOX` will construct the IR subtraction terms by itself, using the Born B , colour-correlated Born B_{ij} and the spin-correlated Born $B_{\mu\nu}$ to cancel the divergences of the real corrections R_{ij} .

3.1.4.2 The Catani-Seymour formalism

The CS dipole formalism provides a convenient way of handling IR divergences. A full explanation of this method can be found in Ref. [180] for massless particles, in Ref. [190] specific for the case of photon radiation off massive fermions and in Ref. [191] for massive final-state particles. For massive initial-state particles, the method is described in Ref. [192]. The regularization scheme dependence of the dipoles is discussed in Ref. [193] and in even more generality in the references of Sec. 3.1.2. We first introduce the general method. For more details on the notation see Sec. A.1.4 or the referenced papers.

The method derives its name from the construction of σ^A by summing over different dipoles

$$d\sigma^A = \sum_{\text{dipoles}} d\sigma^B \otimes dV_{\text{dipole}} \quad (3.1.124)$$

correlated with spins and colours of the leading order σ^B . The contribution to the virtuals corrections can then be rewritten

$$\int_1 d\sigma^A = d\sigma^B \otimes \sum_{\text{dipoles}} \int_1 dV_{\text{dipole}} = d\sigma^B \otimes \mathbf{I}, \quad (3.1.125)$$

where an insertion operator \mathbf{I} is introduced. As a consequence of the KLN theorem, it will cancel the infrared divergences in the virtual corrections. In hadron collisions, there are additional contributions from the collinear remainders, expressed as \mathbf{P} and \mathbf{K}

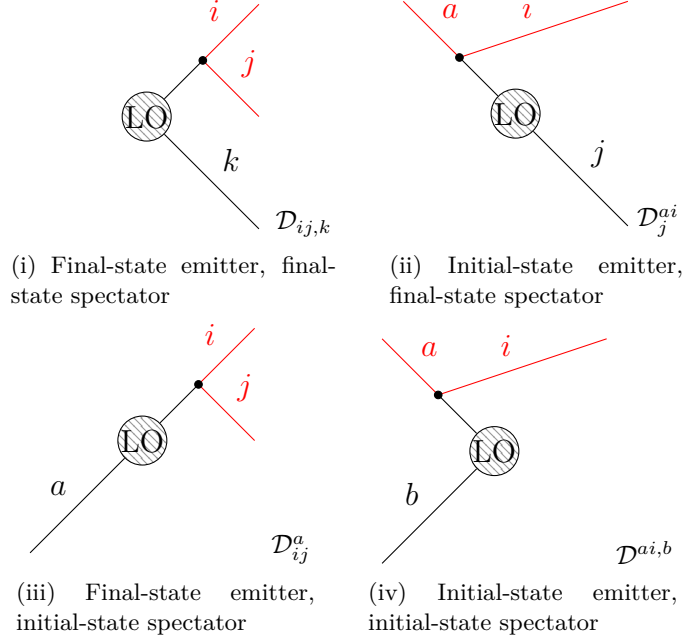


Figure 3.7: Dipole diagrams for various emitter-spectator cases. Other particles involved in the matrix element are not shown.

operators

$$\begin{aligned} \Delta\sigma^{\text{NLO}} = & \int_3 [\text{d}\sigma^{\text{R}} - \text{d}\sigma^{\text{A}}]_{\epsilon=0} + \int_2 \left[\text{d}\sigma^{\text{V}} + \int_1 \text{d}\sigma^{\text{A}} \right]_{\epsilon=0} \\ & + \int_0^1 dx \int_2 [\text{d}\sigma^{\text{B}}(xp) \otimes (\mathbf{P} + \mathbf{K})(x)]_{\epsilon=0} . \end{aligned} \quad (3.1.126)$$

The dipole factorization formula reads

$$|\mathcal{M}_{2 \rightarrow 3}^{\text{DIP}}|^2 = \sum_{i,j} \sum_{k \neq i,j} \mathcal{D}_{ij,k} + \sum_{i,j} \sum_a \mathcal{D}_{ij}^a + \sum_{a,i} \sum_{j \neq i} \mathcal{D}_j^{ai} + \sum_{a,i} \sum_{b \neq a} \mathcal{D}^{ai,b} ,$$

where the sums mean that we include all possible dipoles associated with our real correction Feynman diagrams. The dipoles are defined such that the singular regions of the real correction $2 \rightarrow 3$ matrix element are cancelled, but can also be used for processes with more than 3 final-state particles. Each dipole, \mathcal{D} , corresponds to a distinct emitter-spectator configuration, where both the emitter and spectator are coloured particles. Fig. 3.7 illustrates the four possible configurations. The general structure of all these dipoles is

$$\mathcal{D}_j^{ai}(p_1, p_2, p_3; p_a, p_b) \propto \frac{1}{p^2} {}_2 \langle \dots, j, \dots; ai, \dots | \frac{\mathbf{T}_{\text{spectator}} \mathbf{T}_{\text{interm.}}}{\mathbf{T}_{\text{interm.}}^2} \mathbf{V} | \dots, j, \dots; ai, \dots \rangle_2 , \quad (3.1.127)$$

where the division by p^2 is the origin of the IR divergence. The Casimir operator $\mathbf{T}_{\text{interm.}}^2$ is linked to the particle that enters the leading order process and is connected to two

external particles (red), the emitter ij or ai . The kernel \mathbf{V} depends on the momenta and is closely related to the AP splitting functions (Eqs. (2.2.5) to (2.2.8)) describing the collinear divergence. In order to match the divergence of the real corrections the colour-correlation needs to be taken into account through $\mathbf{T}_{\text{spectator}}\mathbf{T}_{\text{interm.}}$. The 3-particle phase space needs to be mapped to a 2-particle phase space such that the limiting behaviour is correct and momentum conservation holds.

By integrating out the soft emitted particle of the dipoles, the insertion operator \mathbf{I} can be determined. We refer to [180] for more detailed equations where these derivations are explained in depth. The integrated dipoles are defined through an insertion operator \mathbf{I} [191, Eq. (6.66)]

$$\begin{aligned} \int d\sigma^A &= {}_m \langle 1, \dots, m | \mathbf{I}_{m+a+b}(\epsilon, \mu^2, \{p_i, m_i\}) | 1, \dots, m \rangle_m = \langle \mathbf{I}_{m+a+b}(\epsilon, \mu^2, \{p_i, m_i\}) \rangle \\ &= \langle \mathbf{I}_m(\epsilon, \mu^2, \{p_i, m_i\}) + \mathbf{I}_a(\epsilon, \mu^2, \{p_i, m_i\}) + \mathbf{I}_b(\epsilon, \mu^2, \{p_i, m_i\}) \rangle \\ &- \left\langle \frac{\alpha_s}{2\pi} \frac{(4\pi)^\epsilon}{\Gamma(1-\epsilon)} \left(\frac{1}{\mathbf{T}_a^2} \mathbf{T}_a \cdot \mathbf{T}_b \left[\left(\frac{\mu^2}{\epsilon^2} \right)^\epsilon \left(\frac{\mathbf{T}_a^2}{\epsilon^2} + \frac{\gamma_a}{\epsilon} \right) - \mathbf{T}_a^2 \frac{\pi^2}{3} + \gamma_a + K_a \right] + (a \leftrightarrow b) \right) \right\rangle, \end{aligned} \quad (3.1.128)$$

with the singular terms included in \mathbf{I} [191, Eq. (6.16)]

$$\begin{aligned} \mathbf{I}_m(\epsilon, \mu_R^2; \{p_i, m_i\}) &= -\frac{\alpha_S}{2\pi} \frac{(4\pi)^\epsilon}{\Gamma(1-\epsilon)} \sum_j \frac{1}{\mathbf{T}_j^2} \sum_{k \neq j} \mathbf{T}_j \mathbf{T}_k \\ &\cdot \left[\mathbf{T}_j^2 \left(\frac{\mu^2}{s_{jk}} \right)^\epsilon \left(\nu_j(s_{jk}, m_j, m_k, m_F; \epsilon, \kappa) - \frac{\pi^2}{3} \right) \right. \\ &\left. + \Gamma_j(\mu, m_j, m_F; \epsilon) + \gamma_j(1 + \log \frac{\mu^2}{s_{jk}}) + K_j + \mathcal{O}(\epsilon) \right]. \end{aligned} \quad (3.1.129)$$

The finite constants γ_j and K_j as well as the dipole kernel functions $\nu_j = \nu_j^S + \nu_j^{NS}$ can be found in the paper [191]. The parameters change with the use of different regularization schemes [148]. However, there is no difference between CDR and tHV schemes. This is also intuitively clear since we expect the procedure to kill all remaining ϵ poles after renormalization and thereby the additional $\mathcal{O}(\epsilon)$ terms from CDR do not contribute to the finite result.

The collinear counterterms are [180, Eq. (10.23)]

$$\begin{aligned} \int d\sigma^C &= \\ &\sum_{a'} \int_0^1 dx_{m,a'b} \langle 1, \dots, m; xp_a, pb | \mathbf{K}^{a,a'}(x) + \mathbf{P}^{a,a'}(x, \mu_F^2) | 1, \dots, m; xp_a, pb \rangle_{m,a'b} \\ &+ \sum_{b'} \int_0^1 dx_{m,ab'} \langle 1, \dots, m; p_a, xp_b | \mathbf{K}^{b,b'}(x) + \mathbf{P}^{b,b'}(x, \mu_F^2) | 1, \dots, m; p_a, xp_b \rangle_{m,ab'} , \end{aligned}$$

where the operators \mathbf{K} and \mathbf{P} are finite collinear counterterms depending on the longitudinal momentum fraction x . The \mathbf{P} operator is defined in [191, Eq. (6.53)] and

(6.67)]

$$\mathbf{P}^{a,a'}(x; \mu_F^2; p_j, xp_a, pb) = \frac{\alpha_S}{2\pi} P^{aa'}(x) \left[\frac{1}{\mathbf{T}_{a'}^2} \sum_j \mathbf{T}_j \cdot \mathbf{T}_{a'} \log \frac{\mu_F^2}{xs_{ja}} + \frac{1}{\mathbf{T}_{a'}^2} \mathbf{T}_b \cdot \mathbf{T}_{a'} \log \frac{\mu_F^2}{xs_{ab}} \right] \quad (3.1.130)$$

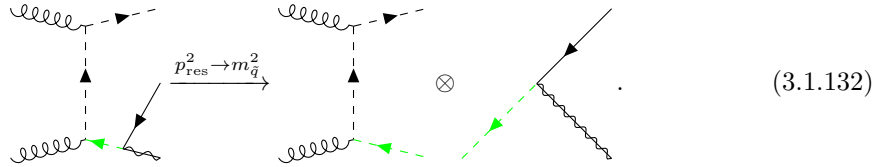
and the \mathbf{K} operator is defined in [191, Eq. (6.55) and (6.68)]

$$\begin{aligned} \mathbf{K}^{a,a'}(x; p_j, p_a, pb) &= \frac{\alpha_S}{2\pi} \left\{ \bar{K}^{aa'}(x) - K_{\text{F.S.}}^{aa'}(x) - \sum_j \mathbf{T}_j \cdot \mathbf{T}_{a'} \mathcal{K}_j^{a,a'}(x; s_{ja}, m_j) \right. \\ &\quad - \frac{1}{\mathbf{T}_{a'}^2} \sum_j \mathbf{T}_j \cdot \mathbf{T}_{a'} \left[P_{\text{reg}}^{aa'}(x) \log \frac{(1-x)s_{ja}}{(1-x)s_{ja} + m_j^2} \right. \\ &\quad \left. \left. + \gamma_a \delta^{aa'} \delta(1-x) \left(\log \frac{s_{ja} - 2m_j \sqrt{s_{ja} + m_j^2} + 2m_j^2}{s_{ja}} + \frac{2m_j}{\sqrt{s_{ja} + m_j^2 + m_j}} \right) \right] \right. \\ &\quad \left. - \mathbf{T}_b \cdot \mathbf{T}_{a'} \left[\frac{1}{\mathbf{T}_{a'}^2} P_{\text{reg}}^{aa'}(x) \log(1-x) + \delta^{aa'} \left(2 \left(\frac{\log(1-x)}{1-x} \right)_+ - \frac{\pi^2}{3} \delta(1-x) \right) \right] \right\}. \end{aligned} \quad (3.1.131)$$

All further the needed expressions for calculating these operators are given in Sec. A.3.3 and Sec. A.3.4.

3.1.5 On-shell resonances

In Sec. 2.2.4 we have seen how resonances can be described by a peak in the cross section due to the denominator of the propagator going to zero. In the following example we will consider electroweakino-squark production, where the resonances appear when the particle's momentum gets close to its mass $p_{\text{res}}^2 \rightarrow m_{\tilde{q}}^2$. Then the process splits into a leading order process with a subsequent decay. Schematically, this can be illustrated as



This process is only possible if the squark has a higher mass than the gaugino to allow a decay in its own reference frame. We do not want this contribution in our computation since it is already a part of the prediction of producing two squarks at leading order.

3.1.5.1 Subtraction and removal

In a first step we regularize the OS divergence by introducing a finite width $\Gamma_{\tilde{q}}$ to the propagator such that

$$\frac{1}{p_{\text{res}}^2 - m_{\tilde{q}}^2} \rightarrow \frac{1}{p_{\text{res}}^2 - m_{\tilde{q}}^2 + im_{\tilde{q}}\Gamma_{\tilde{q}}}. \quad (3.1.133)$$

This width will act purely as a regulator and does not need to be the physical width. If two amplitudes are combined and each has a resonant propagator we get a double resonant propagator (note the conjugation of one propagator)

$$\frac{1}{(p_{\text{res}}^2 - m_{\tilde{q}}^2)^2} \rightarrow \frac{1}{(p_{\text{res}}^2 - m_{\tilde{q}}^2)^2 + m_{\tilde{q}}^2 \Gamma_{\tilde{q}}^2}. \quad (3.1.134)$$

Our total ME splits into three pieces

$$|\mathcal{M}_{\text{tot}}|^2 = |\mathcal{M}_{nr}|^2 + 2 \text{Re}[\mathcal{M}_r \mathcal{M}_{nr}^*] + |\mathcal{M}_r|^2. \quad (3.1.135)$$

The non-resonant diagrams are part of \mathcal{M}_{nr} and the remaining resonant diagrams are included in \mathcal{M}_r .

The simplest method to exclude the large contributions is Diagram Removal (DR), where double resonance $|\mathcal{M}_r|^2$ and the interference $2 \text{Re}[\mathcal{M}_r \mathcal{M}_{nr}^*]$ are not considered (DR-I). It is also possible to only exclude the double resonant part and keep the interference (DR-II) [194]. The price one pays for such a simple method is the apparent loss of gauge invariance.

Therefore, we will instead apply Diagram Subtraction (DS). DS keeps both the single (interference) and double resonant pieces and only locally subtracts the contribution from the leading order process followed by the decay (lhs. Eq. (3.1.132)). The advantage of this method is that it respects gauge invariance for vanishing width $\Gamma_{\tilde{q}}$. Consequently, we do not just integrate $|\mathcal{M}_{\text{tot}}|^2$ over a 3-particle phase space $d\Phi_3$ but instead include a point wise subtraction

$$\left(|\mathcal{M}_{\text{tot}}|^2 - |\mathcal{M}_r(\tilde{\Phi}_3)|^2 \underbrace{\frac{m_{\tilde{q}}^2 \Gamma_{\tilde{q}}^2}{(p_{\text{res}}^2 - m_{\tilde{q}}^2)^2 + m_{\tilde{q}}^2 \Gamma_{\tilde{q}}^2}}_{\text{Breit-Wigner}} \underbrace{\theta(\sqrt{s} - m_{\tilde{q}} - m_{\tilde{q}^*})}_{\tilde{q}\tilde{q}^*\text{-production}} \underbrace{\theta(m_{\tilde{q}} - m_{\tilde{\chi}})}_{\text{decay}} \frac{d\tilde{\Phi}_3}{d\Phi_3} \right) d\Phi_3. \quad (3.1.136)$$

First, we include a BW function corresponding to the decay with given width $\Gamma_{\tilde{q}}$. For the production of $\tilde{q}\tilde{q}^*$ at leading order to be kinematically allowed there must be sufficient energy \sqrt{s} to constitute their masses. The second θ function restrains our subtraction to the cases where a subsequent decay is allowed.

We must introduce a new 3-particle phase space $\Phi_3 \rightarrow \tilde{\Phi}_3$ similar to the CS formalism to remove only contributions from $|\mathcal{M}_r|^2$ where $\tilde{p}_{\text{res}}^2 = (p_2 + p_3)^2 = m_{\tilde{q}}^2$ is OS. Please note that the BW function is still evaluated in Φ_3 as it evaluates to 1 otherwise. More details, especially on the explicit form of the Jacobian $\frac{d\tilde{\Phi}_3}{d\Phi_3}$, are given in Ref. [195] on the specific case of squark pair production.

We split the integration over the 3-particle phase space $d\Phi_3$ in a double resonant part with the diagram subtraction and the rest (non-resonant and single resonant). This allows the MC integration to converge faster by focusing on the dominating region of each part.

3.1.5.2 Breit-Wigner cutoff

MadGraph instead uses a BW cutoff $\Delta_{\text{bwcutoff}}^{\%}$ [140]. Given again a squark resonance with a physical width $\Gamma_{\tilde{q}}$, two separate processes are computed for the virtuality $m_{\tilde{q}}^* = \sqrt{p_{\text{res}}^2}$ being close to the mass pole, *i.e.* the OS region

$$|m_{\tilde{q}}^* - m_{\tilde{q}}| \leq \Delta_{\text{bwcutoff}}^{\%} \Gamma_{\tilde{q}}, \quad (3.1.137)$$

and the off-shell region

$$|m_{\tilde{q}}^* - m_{\tilde{q}}| > \Delta_{\text{bwcutoff}}^{\%} \Gamma_{\tilde{q}}. \quad (3.1.138)$$

The OS process only includes resonant diagrams, which violates gauge invariance, except for the case of vanishing width $\Gamma_{\tilde{q}}$. A consequence of the narrow-width approximation [196–198] is that there is no interference between the decay products of different resonances. Hence, the decay factorizes as expressed in `MadGraph`'s decay-chain syntax `p p > sq sq*, sq* > chi q*`¹ resembling Eq. (3.1.132) with spin correlations and off-shell effects taken into account exactly. The off-shell process includes all diagrams and is used to compute the full matrix element, `p p > sq chi q*`. While the individual processes are dependent on the BW cutoff, the sum is almost independent of it

$$d\sigma \approx d\sigma_{\text{on-shell}} + d\sigma_{\text{off-shell}}. \quad (3.1.139)$$

3.2 Monte Carlo methods

MC methods are a versatile and widely-used class of computational techniques that rely on random sampling to solve problems that are too complex to handle with direct analytical methods. The strength of MC techniques lies in their simplicity, flexibility and parallelizability, making them particularly well-suited for handling multi-dimensional integrals and stochastic processes, like the inherently statistical nature of quantum mechanics, especially in particle physics, but also across a wide range of scientific fields. In quantum systems, many processes do not have a single deterministic outcome but rather a distribution of possible outcomes that can only be understood through probabilistic reasoning. This statistical ensemble approach is intrinsic to how quantum measurements are modelled and analysed, and MC techniques offer a natural way to explore such distributions. By generating random samples according to specific probability distributions, MC simulations allow us to estimate quantities that are otherwise challenging to compute. The applications of MC methods span various domains in high-energy physics:

Monte Carlo Integrators Integrating high-dimensional functions over complex domains is a recurring problem in particle physics, especially when calculating cross sections, decay rates, or other observables. Traditional numerical integration techniques often become impractical as the dimensionality increases. MC integrators excel here because they scale efficiently with dimensionality and are straightforward to implement. Moreover, they are easily parallelizable, allowing for fast computations, and provide reliable error estimates, making them a favoured choice in simulations.

Since many programs exist we will just list a few prominent examples here. The `VEGAS` [199, 200] algorithm is a widely-used method for adaptive importance sampling, which partitions the integration domain into hypercubes and adjusts their sizes iteratively based on the function's behaviour. The `CUBA` [201, 202] library offers a collection of MC integrators, each designed with distinct strategies such as adaptive subdivision and stratified sampling to enhance the efficiency of numerical integration. Another noteworthy approach is the `FOAM` [203] algorithm, which employs a triangulation technique to divide the integration region into cells, facilitating a more refined exploration of the

¹These are not the actual particle names within `MadGraph`'s MSSM models.

space. Recently, machine learning techniques have been introduced into this area with the `i-flow` [204] framework. It uses normalizing flows, *i.e.* invertible neural networks trained to optimize the importance sampling function, thereby improving both accuracy and computational speed.

Since the transition to event generators is seamless some tools support both. The `SPRING-BASES` [205] system builds on the VEGAS algorithm [199], initially performing integration of a positive function and subsequently generating events with a probability distribution proportional to the integrand. Similarly, the `MINT` [206] program is specifically designed for adaptive MC integration and event generation, and is particularly useful in generating unweighted distributions as applied in `POWHEG BOX`.

General-Purpose Event Generators In particle physics, simulating events like collisions at the LHC is crucial for both theoretical predictions and experimental analyses. These event generators incorporate detailed models of particle interactions, including parton showers, hadronisation, and even detector effects. By generating large ensembles of events that mimic real experiments, they allow studying processes ranging from fundamental interactions to complex backgrounds. Prominent examples include `MadGraph`, `PYTHIA`, `HERWIG`, and `Sherpa`.

Monte Carlo Markov Chains While not the main focus of this thesis, Monte Carlo Markov Chain (MCMC) methods are another important subset of MC techniques. They are particularly useful in situations where a large parameter space needs to be explored efficiently, such as in lattice QCD or fitting models to data. The Metropolis algorithm, a cornerstone of MCMC methods, is recognized as one of the most significant algorithms developed in the 20th century [207].

3.2.1 Integrators

The fundamental idea behind Monte Carlo integration is the repeated sampling of random points to approximate the desired integral, allowing the approximation to converge to the exact solution as the number of samples increases. The method is closely related to the Riemann sum for approximating an integral $\int_a^b g(x), dx$ can be expressed as

$$\int_a^b g(x)dx = \lim_{N \rightarrow \infty} \frac{b-a}{N} \sum_{i=1}^N g(x_i) = (b-a)\langle g \rangle, \quad (3.2.1)$$

where x_i are evenly spaced points within the interval $(a; b)$, and $\langle g \rangle$ represents the average value of the function $g(x)$ over the interval. In Monte Carlo integration, instead of using evenly spaced points, random points $x_r \in (a; b)$ are sampled

$$\int_a^b g(x), dx = \lim_{N \rightarrow \infty} \frac{b-a}{N} \sum_{r=1}^N g(x_r) = (b-a)\langle g \rangle. \quad (3.2.2)$$

The central limit theorem ensures that the average $\langle g \rangle$ of the sampled points approaches a Gaussian distribution with a standard deviation given by [208]

$$\sigma_N(I_1) = \sqrt{\frac{V_N(I_1)}{N}}, \quad (3.2.3)$$

where $V_N(I_1)$ is the variance of the integral estimate

$$\begin{aligned} V_N(I_1) &= \frac{1}{N} \sum_{r=1}^N (W_r - \langle W_r \rangle)^2 = \frac{1}{N} \sum_{r=1}^N (W_r^2 - 2W_r \langle W_r \rangle + \langle W_r \rangle^2) \\ &= \frac{1}{N} \sum_{r=1}^N W_r^2 - \left(\frac{1}{N} \sum_{r=1}^N W_r \right)^2 = \langle W_r^2 \rangle - \langle W_r \rangle^2 \geq 0, \end{aligned} \quad (3.2.4)$$

with weights $W_r = (b-a)g(x_r)$. For all practical purposes it is sufficient to integrate over the unit hypercube, as the integral can be rescaled to the desired interval

$$\int_a^b g(x) dx = \int_0^1 (b-a)g(a+(b-a)x) dx. \quad (3.2.5)$$

One of the significant advantages of Monte Carlo integration is that its convergence rate is proportional to $1/N^{1/2}$, regardless of the dimensionality of the problem. This feature makes it particularly effective for high-dimensional integrals, where other numerical integration methods, such as the trapezoidal rule $1/N^{2/d}$, Simpson's rule $1/N^{4/d}$, or Gaussian quadrature $1/N^{(2m-1)/d}$, suffer from the curse of dimensionality [209].

For a d -dimensional integral over the region $(a_1 \leq x_1 \leq b_1, a_2 \leq x_2 \leq b_2, \dots, a_d \leq x_d \leq b_d)$, Monte Carlo integration takes the form

$$I_d = \int_{a_1}^{b_1} dx_1 \int_{a_2}^{b_2} dx_2 \cdots \int_{a_d}^{b_d} dx_d g(x_1, x_2, \dots, x_d) = \lim_{N \rightarrow \infty} \frac{\text{Vol}}{N} \sum_{r=1}^N g(x_1, x_2, \dots, x_d), \quad (3.2.6)$$

where the integration volume Vol is given by

$$\text{Vol} = \int_{a_1}^{b_1} dx_1 \int_{a_2}^{b_2} dx_2 \cdots \int_{a_d}^{b_d} dx_d = \prod_{i=1}^d (b_i - a_i). \quad (3.2.7)$$

Thus, the integral can be expressed as

$$I_d = \text{Vol} \langle g \rangle. \quad (3.2.8)$$

This method remains effective even as the dimensionality increases, the standard deviation remains proportional $1/\sqrt{N}$. This characteristic makes Monte Carlo integration an essential tool for evaluating high-dimensional integrals in areas such as quantum mechanics and statistical physics [210].

The text book example for Monte Carlo integration is the calculation of π . To calculate π , consider the area of a unit circle, which is given by $A = \pi r^2 = \pi$ for a circle with radius $r = 1$. The integral to compute this area can be expressed as $I = \int_{-1}^1 \int_{-1}^1 dx dy (1 - \theta(x^2 + y^2)) O(x, y)$, where $\theta(x^2 + y^2)$ is a step function that evaluates to 1 inside the circle and 0 outside (cf. Sec. A.4.2). For a simple Monte Carlo integration with $O = 1$, random points (x, y) are generated uniformly within the square $[-1, 1] \times [-1, 1]$ as illustrated in Fig. 3.8i. The fraction of these points that fall inside the circle (where $x^2 + y^2 \leq 1$) is then multiplied by the area of the square, 4, to estimate π . The convergence rate of this method is $\mathcal{O}\left(\frac{1}{\sqrt{N}}\right)$, where N is the number of samples. This is shown in Fig. 3.8ii.

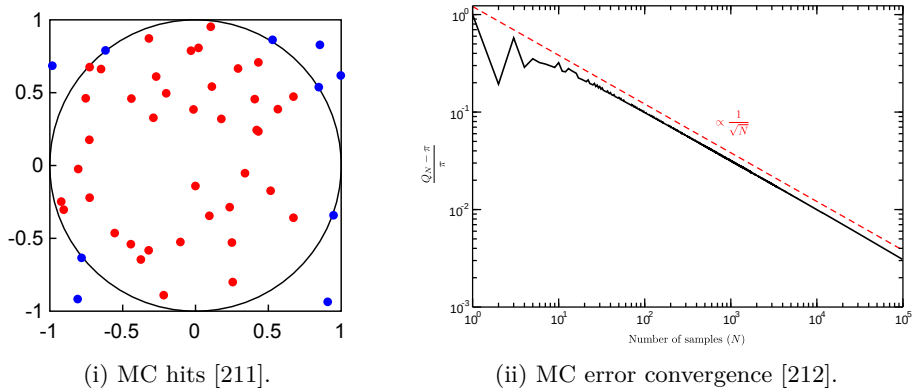


Figure 3.8: MC integration of a circle.

d	2	5	10	50	100
$\text{Vol}(S_d)/\text{Vol}(C_d)$	0.785	0.164	0.0025	1.5×10^{-28}	1.9×10^{-70}

Table 3.3: Volume of the d dimensional sphere S_d relative to the volume of the d dimensional hypercube C_d [202].

The convergence property is the primary reason Monte Carlo integration is favoured for high-dimensional problems. However, challenges arise as the dimensionality increases significantly. Consider a d -dimensional sphere S_d inscribed within a d -dimensional hypercube $C_d = [-1, 1]^d$. As the dimension d grows, the probability of randomly hitting the sphere diminishes because most of the hypercube's volume lies outside the sphere. This phenomenon is illustrated by the ratio

$$\frac{\text{Vol}(S_d)}{\text{Vol}(C_d)} = \frac{\left(\frac{\pi}{4}\right)^{\frac{d}{2}}}{\Gamma\left(1 + \frac{d}{2}\right)}, \quad (3.2.9)$$

where Γ is the gamma function. The ratio is shown for various dimensions d in Tab. 3.3. For large d , the problem resembles Monte Carlo integration over a distribution with a very narrow peak. The volume of the sphere can be more efficiently calculated by switching to spherical coordinates. This approach involves transforming the original integral, and such transformations in Monte Carlo integration are commonly referred to as Importance Sampling, which we will discuss next.

3.2.2 Importance sampling

Importance sampling is a variance reduction technique often used in MC integration. The core idea is to focus computational effort on the regions of the integration domain that contribute most to the integral. Considering again an integral of the form

$$I = \int_a^b g(x) dx. \quad (3.2.10)$$

If the function $g(x)$ is small in most of the integration region, many sampled points contribute very little to the integral, leading to inefficiency. Importance sampling addresses

this by introducing a different function $f(x)$ that resembles $g(x)$ but is easier to sample from and has a simple invertible integrated function $F(x)$. First, choose a function $f(x)$ that is similar to $g(x)$, ensuring that it is easy to sample from and that its integral can be inverted

$$y = F(x) \quad \Leftrightarrow \quad x = F^{-1}(y), \quad (3.2.11)$$

$$\frac{dy}{dx} = f(x) \quad \Leftrightarrow \quad dx = \frac{dy}{f(x)}. \quad (3.2.12)$$

This allows us to express the integral as

$$I = \int_a^b g(x)dx = \int_{F(a)}^{F(b)} \frac{g(F^{-1}(y))}{f(F^{-1}(y))} dy = \int_{F(a)}^{F(b)} g(F^{-1}(y))(F^{-1})'(y)dy, \quad (3.2.13)$$

where the final step is the inverse function rule. The advantage here is that $f(x)$ is chosen to be large where $g(x)$ is large, focusing the sampling on regions that contribute most to the integral. Ideally, this leads to a significant reduction in the variance (3.2.4) and thus reduces the Monte Carlo integration error (3.2.3). While the approach ideally solves the problem of inefficient sampling, it requires the choice of a suitable function $f(x)$. If $f(x)$ is not well-matched to $g(x)$, the performance may actually degrade, leading to longer computation times and poor convergence. Essentially, importance sampling can be viewed as a form of integration by substitution, where the variable transformation is designed to flatten the integrand and reduce the variability in the results. To make that more explicit we can substitute $F^{-1} \rightarrow h$

$$I = \int_{h^{-1}(a)}^{h^{-1}(b)} g(h(y))h'(y)dy = \int_a^b g(x)dx. \quad (3.2.14)$$

A simple example here is the integration of a BW distribution

$$I = \int_{M_{\min}^2}^{M_{\max}^2} \frac{1}{(m^2 - M^2)^2 + M^2\Gamma^2} dm^2, \quad (3.2.15)$$

where we can guess the integral of the function to behave as $m^2 = F^{-1}(\rho) = M\Gamma \tan \rho + M^2$, giving

$$I = \int_{\rho_{\min}}^{\rho_{\max}} \left| \frac{\partial m^2}{\partial \rho} \right| \frac{1}{(m^2 - M^2)^2 + M^2\Gamma^2} d\rho \quad (3.2.16)$$

$$= \int_{\rho_{\min}}^{\rho_{\max}} M\Gamma \sec^2 \rho \frac{1}{M^2\Gamma^2 \sec^2 \rho} d\rho \quad (3.2.17)$$

$$= \frac{1}{M\Gamma} \int_{\rho_{\min}}^{\rho_{\max}} d\rho. \quad (3.2.18)$$

Picking any random point in the ρ space contributes equally to the integral, making the sampling more efficient than in the original m^2 space [208]. In praxis the sampling function will not be as fitting as the one in this example, but the principle remains the same.

3.2.3 Random number generation and sequences

So far we have just assumed that we can generate random numbers. This is not trivial, since computers are deterministic machines, though hardware driven methods exist to obtain truly random numbers [213–216]. We can only generate pseudo-random numbers, which are sequences of numbers that appear random, but are actually generated by a deterministic algorithm. The algorithm is initialized with a seed, and then generates a sequence of numbers that are uniformly distributed in the interval $[0, 1]$. The sequence is periodic through application of modulo arithmetic with a Mersenne prime number, and the period is determined by the algorithm and the seed. The Mersenne Twister is a popular pseudo-random number generator that has a long period of $2^{19937} - 1$ and good statistical properties. It is suitable for most general-purpose simulations and computations.

The Koksma-Hlawka inequality [217] provides a powerful bound for numerical integration when using low-discrepancy sequences, which are sequences designed to fill the integration domain more uniformly than random sampling. For a function f defined on the d -dimensional unit cube $[0, 1]^d$, the inequality is given by

$$\left| \frac{1}{N} \sum_{j=1}^N f(x_j) - \int_{[0,1]^d} f(x) dx \right| \leq D_N V(f). \quad (3.2.19)$$

The quantity $V(f)$ is the variation of the function f , capturing the function's sensitivity to changes across the domain. Here, D_N represents the discrepancy of the sequence $\{x_1, x_2, \dots, x_N\}$, which quantifies how uniformly the points are distributed by comparing the number of points within any axis-aligned box $[0, t]$ to the volume of that box. Specifically, D_N is defined as

$$D_N = \sup_{t \in [0,1]^d} \left| \frac{1}{N} \sum_{j=1}^N \chi_{[0,t]}(x_j) - \prod_{k=1}^d t_k \right|, \quad (3.2.20)$$

where $\chi_{[0,t]}(x)$ is the characteristic function that indicates whether a point x lies within the box $[0, t] = [0, t_1] \times [0, t_2] \times \dots \times [0, t_d]$. This inequality highlights the advantage of using low-discrepancy sequences, as they typically achieve convergence rates of $\mathcal{O}\left(\frac{\log^{d-1} N}{N}\right)$, which is significantly better than the $\mathcal{O}\left(\frac{1}{\sqrt{N}}\right)$ rate associated with standard Monte Carlo methods.

One example of such quasi random number sequences is the Sobol sequence [218], which is designed to be well-distributed across the space and avoid clustering of points. Since it avoids clustering, it is particularly beneficial for subdividing algorithms, where clustering can lead to inaccuracies in the results. The difference between pseudo-random and quasi-random sequences is displayed in Fig. 3.9. It demonstrates that quasi-random numbers distribute across the plane more uniformly than pseudo-random numbers.

3.2.4 Event generation

Event generators play a crucial role in particle physics simulations, allowing us to produce events according to a given probability distribution. Instead of merely integrating over a probability distribution to obtain cross sections or observables, Monte Carlo techniques enable us to generate a set of events directly. This approach allows us to create

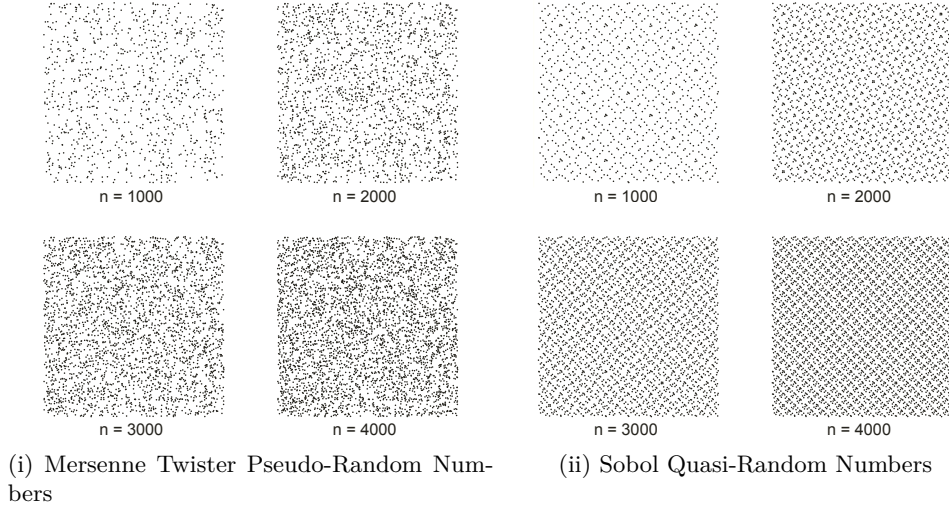


Figure 3.9: Comparison of random numbers by taking n pairs of random values and plotting them in a 2D space, thus showing how they probe the space [202].

realistic event samples that can be reused for different analyses, enhancing the efficiency and flexibility of our studies.

Monte Carlo event generation begins with the collection of a set of phase space points, each corresponding to a potential event. Since an event corresponding to a single phase space point with fixed momenta has a vanishing probability and therefore does not significantly contribute to the integral, it is the collective sample of events that carries physical relevance. The core challenge lies in assigning weights to these events according to the underlying distribution. In general, the weights represent the probability of each event occurring based on the model being simulated. However, processing events with very small weights can be wasteful since they contribute minimally to further calculations. Therefore, ideally we would like to generate events with uniform weights, simplifying the analysis and making the sample more manageable.

A common approach to unweighting is the *hit-or-miss* method. This technique relies on selecting phase space points and accepting them with a probability proportional to their weight. The procedure can be summarized as follows:

1. During the integration phase, determine and store the maximum value of the distribution, denoted as f_{\max} . This value is used for normalization and calculating the total cross section $\langle f \rangle$.
2. Randomly sample phase space points x . Each point is accepted with a probability given by $f(x)/f_{\max}$, where $f(x)$ is the value of the distribution at that phase space point. This is illustrated in Fig. 3.10.
3. Accepted events are assigned a uniform weight of $\langle f \rangle$, effectively generating an unweighted sample.

The distribution information is now encoded in the number of events, rather than varying weights, making the sample easier to analyse and suitable for direct use in further simulations or studies.

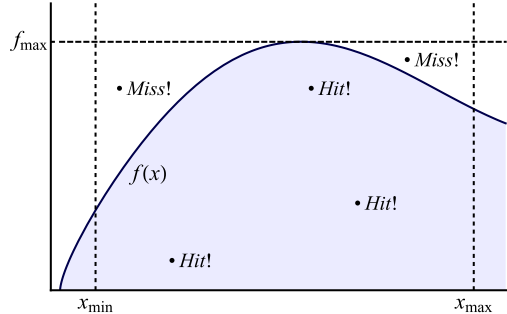


Figure 3.10: Illustration of the hit-or-miss method for event generation. Phase-space points are sampled, and events are accepted or rejected based on the value of the distribution at each point relative to f_{\max} . The figure can be found in Ref. [219].

One potential problem with the hit-or-miss method that has been omitted in the above description is how negative values of f are handled. Since the probability of an event cannot be negative, negative weights are not physically meaningful, but can practically be used as long as there are not too many. The folding procedure is a technique commonly used in particle physics simulations to address the problem of negative-weight events, which can arise during the unweighting process when calculating cross sections that are not positive-definite in certain radiative phase spaces. This issue is mitigated by averaging over multiple “folds”, which are sets of integration variables typically linked to the radiated particles (η , y and ξ), allowing local negative contributions to be efficiently balanced out before performing unweighting. That such a factorization can improve the negative weight ratio was first noted in Ref. [220], formalized in Ref. [206] and later implemented in POWHEG BOX. However, the computational cost of this method increases significantly with the number of folds, as runtime scales approximately with the product of the folding factors. While this approach can reduce the occurrence of negative weights, making it computationally advantageous in scenarios involving overheads like detector simulation and storage, the net benefit may not always justify the additional central processing unit (CPU) time, depending on the complexity and requirements of the simulation [221, 222].

3.2.5 Shower Monte Carlo

In Sec. 2.2.5 the mathematical formalism of parton showers was introduced. Now we map the parton shower evolution to a Monte Carlo algorithm. From Eq. (2.2.43) we want to generate a splitting according to

$$f(x)\Delta(h(x)), \quad (3.2.21)$$

with

$$\Delta(h) = \exp\left(-\int dx f(x)\theta(h(x)-h)\right) \quad (3.2.22)$$

and f and h non-negative functions and $\Delta(0) = 0$ since f diverges. From the derivative of the Sudakov factor

$$d\Delta(h) = \int dx dh \delta(h-h(x))f(x)\Delta(h) = dx f(x)\Delta(h(x)), \quad (3.2.23)$$

we see that distributing dx is uniform in $\Delta(h)$. Therefore, one picks a uniform random number $r_i \in (0, 1)$ and solves $\Delta(H) = r_1$ for H . Next, H can be used to generate the x variables using $\int dx \delta(H - h(x)) f(x) = r_2$. Since solving these equations numerically is difficult, using the following veto method is more practical.

Given a simpler upper bounding function $F(x) \geq f(x)$ the Sudakov factor can be written as

$$\Delta_F(h) = \exp \left(- \int dx F(x) \theta(h(x) - h) \right). \quad (3.2.24)$$

First a random number r_1 is drawn and H is solved from $\Delta_F(H)/\Delta_F(H_{\max}) = r_1$, where $\Delta_F(H_{\max})$ is 1 in the beginning. Next, an x is constructed following $F(x)\theta(h(x) - H)$. The splitting is accepted if a new random number $r_2 < f(x)/F(x)$ otherwise $H_{\max} = H$ and the procedure is repeated. The proof that this procedure generates the correct distribution is given in Ref. [223]. For a transverse momentum ordered shower $h(x) = p_T(x)$ and $f(x) = P(x)$ are the AP-splittings and terminates when the scale reaches Λ_{QCD} .

The procedure can be generalized for multiple possible splitting through the highest- p_T bid procedure

$$f_k(x_k) \prod_i \Delta_i(h_k(x_k)) dx_k^d, \quad (3.2.25)$$

where

$$\Delta_i(h) = \exp \left(- \int d^d x_i f_i(x_i) \theta(h_i(x_i) - h) \right) \quad (3.2.26)$$

as shown in Ref. [188]. Generating x_k as before with a probability

$$f_k(x_k) \Delta_i(h_k(x_k)) dx_k^d \quad (3.2.27)$$

the k value of largest h_k is selected. The probability of the $h_k(x_k)$ being the largest is given by the probability that no other emission occurs before

$$\prod_{i \neq k} \Delta_i(h_k(x_k)), \quad (3.2.28)$$

which reproduces Eq. (3.2.25) multiplied with its own probability in Eq. (3.2.27).

3.2.6 Full event generation

The full generation of a physical event is a multistep process, where several distinct stages contribute to the simulation of a realistic event. Each of the following steps is visualized in Fig. 3.11. They mostly correspond to the discussed stages in Sec. 2.2

1. **Hard process generation:** Pick a phase space following hit-or-miss method. (Sec. 5.2.2)
2. **Heavy resonance decay:** Heavy resonances with narrow widths are decayed before the parton shower. (Sec. 2.2.4)
3. **PDF and parton shower:** Any charged (QCD/QED) initial or final parton/-particle can radiate. (Sec. 2.2.2 and Sec. 2.2.5)

4. **Multiple parton interactions:** Secondary interactions between partons within the colliding hadrons, modelled as QCD $2 \rightarrow 2$ interactions, are generated. (Sec. 2.3)
5. **Hadronisation and hadron decays:** In the cluster model, clusters are formed and hadrons are produced. Unstable hadrons are subsequently decayed. (Sec. 2.2.7)

After generating many full events, the next step can be a detector simulation the response, followed by further analysis steps such as applying selection criteria and extracting physical observables. Alternatively, the events can be compared against experimental data, where detector effects have been removed through unfolding techniques.

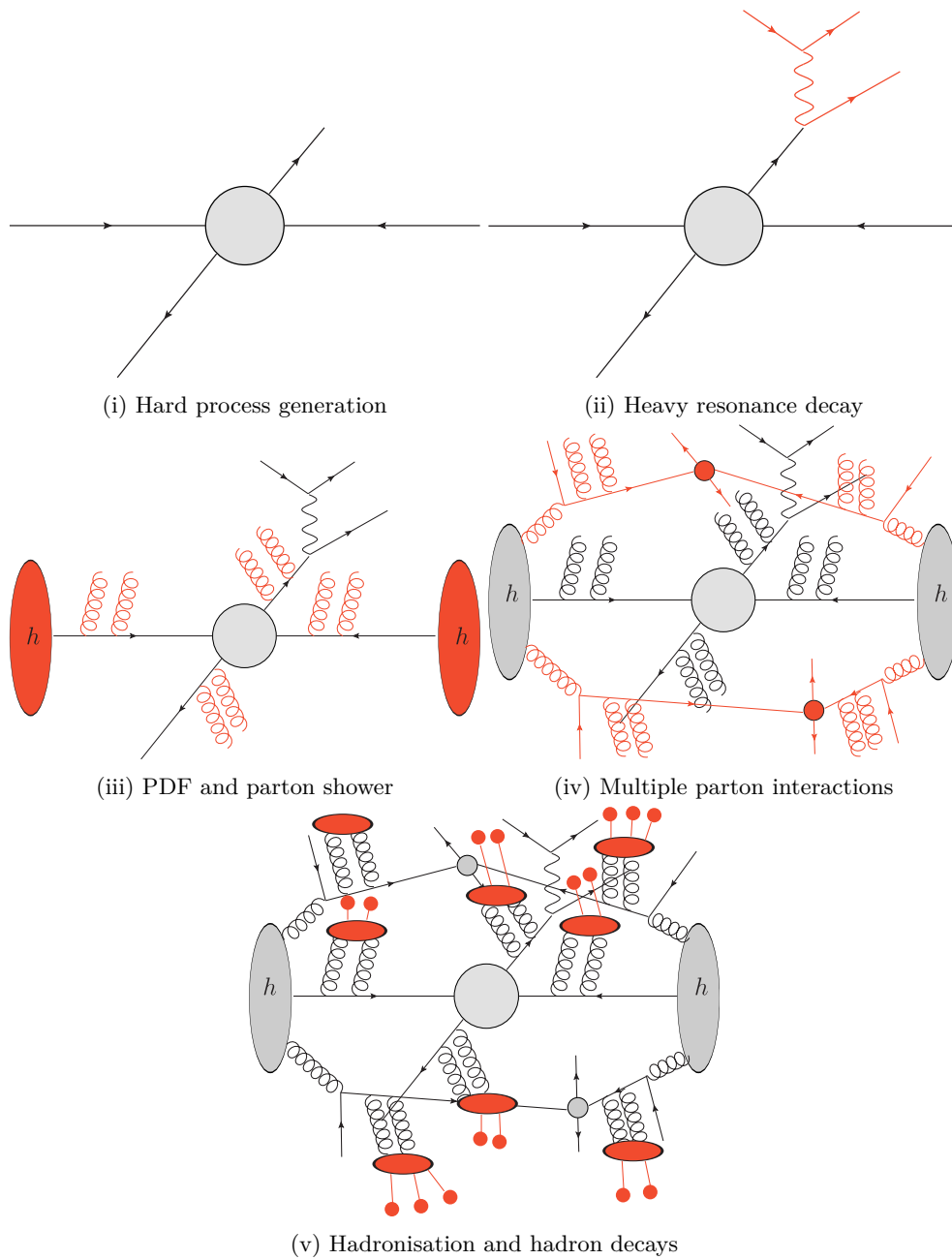


Figure 3.11: Different stages of event generation [208].

3.3 Jets

In order to analyse the generated events and extract physical observables, we need to identify and reconstruct jets. Interestingly, this is phenomenologically reversing the parton shower process.

3.3.1 Algorithms

Any robust jet algorithm must meet several essential criteria to ensure its efficiency and reliability. Firstly, it must be fully defined, leaving no ambiguities in its application. Secondly, the algorithm must be practical and applicable in both experimental and theoretical contexts, ensuring that it can be universally utilized across various studies. Most critically, to maintain the accuracy and consistency of cross section calculations at any perturbative order, the algorithm must be IRC safe. An observable is considered infrared safe if, for any n -parton configuration, the addition of an infinitely soft parton does not impact the observable in any way. An observable is collinear safe if, for any n -parton configuration, replacing any massless parton with an exactly collinear pair of massless partons has no effect on the observable.

The definition of jets is very important for the study of QCD processes. It not only allows to compare theoretical predictions with experimental data, but also to study the properties of the strong force and jet substructure. Further, higher-order corrections such as the merging of different event samples, as will be discussed in Sec. 3.3.2, require the definition of jets. We will explain the most prominent algorithms and discuss them in historical order.

3.3.1.1 Stermann-Weinberg

In 1977, Sterman and Weinberg provided the first algorithmic definition of a jet, aimed at describing 2-jet-like events [224]. They calculated the cross section $\sigma(e^+e^- \rightarrow q\bar{q})$ at the Born level and related it to the unresolved 3-jet cross section $\sigma^{\text{NLO}}(e^+e^- \rightarrow qq, \epsilon, \delta)$. The unresolved third parton is either soft (with an energy less than ϵE) or collinear (inside either of the jet cones of half-angle δ). The fraction f of all events which have all but a fraction ϵ of their energy in the opposite cones of size δ is

$$f = \frac{\sigma^{\text{NLO}}(e^+e^- \rightarrow q\bar{q}, \epsilon, \delta)}{\sigma^{\text{Born}}(e^+e^- \rightarrow qq)} \quad (3.3.1)$$

$$= \frac{\sigma^{\text{Born+Virt}}(e^+e^- \rightarrow q\bar{q}) + \sigma^{\text{Real}}(e^+e^- \rightarrow q\bar{q}g, \epsilon, \delta)}{\sigma^{\text{Born}}(e^+e^- \rightarrow qq)} \quad (3.3.2)$$

$$= 1 - (g_E^2/3\pi^2)(3 \log \delta + 4 \log \delta \log 2\epsilon + \pi^2/3 - 7/4). \quad (3.3.3)$$

As the renormalized QCD gauge coupling constant $g_E^2 = 24\pi^2/25 \log(E/\Lambda_{\text{QCD}})$ gets small with large energies E , the two-jet probability f approaches 1 even for small ϵ and δ . Now one can require 70% of the events to have 80% of their energy in the two jet cones of angular radius $\delta(E, f = 0.7, \epsilon = 0.2)$.

3.3.1.2 Cone

Cone algorithms are the simplest jet algorithm and have existed since the early 1980's [225, 226]. In the $\eta - \phi$ space a cone of radius $R_j = \sqrt{(\phi_i - \phi_j^C)^2 + (\eta_i - \eta_j^C)^2}$ is defined

around a center (η_j^C, ϕ_j^C) . Every parton that falls into this cone of $R_j \leq R$ is clustered together to form a jet.

To find a stable cone the Snowmass scheme [227] starts with a trial axis (η_0^C, ϕ_0^C) and computes the weighted centre of partons within the cone

$$\eta_{j+1}^C = \frac{\sum_{i \in R_j} E_i \eta_i}{\sum_{i \in R_j} E_i} \quad \text{and} \quad \phi_{j+1}^C = \frac{\sum_{i \in R_j} E_i \phi_i}{\sum_{i \in R_j} E_i}. \quad (3.3.4)$$

This is repeated until the axis converges to find a single jet. Their straight forward mapping to an experimental setup and ease of implementation made them popular in the early days of jet physics. However, the cone algorithms are typically not IRC safe. The problem of collinear safety is connected to the problem of identifying the correct jet axis, *i.e.* the seed (η_0^C, ϕ_0^C) . If a jet's parton were to split into two partons, the cone algorithm could cluster them into two separate jets violating collinear safety. Further a soft parton can change the jet axis and clustering significantly, which is not physical [228].

In order to obtain more than one jet the above stable cone finding has to be repeated. These schemes are called iterative cone (IC) algorithms and there are two common types: collinear unsafe IC progressive removal (IC-PR) and infra-red unsafe IC split-merge (IC-SM) [76]. IC-PR starts with the hardest parton as seed and removes all partons within the found stable cone. Then the next hardest parton is taken as seed and the process is repeated until no partons are left. IC-SM instead finds all cones above a certain threshold E_{cut} without removing them. Depending on the summed k_T of the overlapping partons, the resulting overlap of cones is treated either by merging them to one jet or splitting them into two separate jets. In the splitting procedure the ambiguous partons get included in the jet with the closer axis. A modern IRC safe cone algorithm Seedless Infrared-Safe Cone (SIScone) is sketched in Sec. A.5.1.

3.3.1.3 JADE

The first 3-jet events were measured in 1979 at Deutsches Elektronen-Synchrotron (DESY) [229] and further identified as spin 1 gluons [230]. The JADE algorithm is named after one of the detectors at PETRA [231, 232]. Contrary to the Sterman-Weinberg jet this algorithm clusters partons together to form jets. To do so, we first introduce the notion of a protojet, which is a parton or a cluster of partons. The clusters are constructed as follows:

1. Compute $y_{ij} = M_{ij}^2/Q^2 = (p_i + p_j)^2/Q^2 \stackrel{\text{massless}}{=} 2E_i E_j (1 - \cos \theta_{i,j})/Q^2$ for all protojets i, j where Q is the total energy of an event.
2. Find the two protojets i and j with the smallest y_{ij} .
3.
 - If $y_{ij} < y_{\text{cut}}$, combine them into a new protojet ij carrying the summed four momenta $p_{ij} = p_i + p_j$ and go to step 1,
 - else stop and assign all protojets to jets.

The algorithm is infrared and collinear safe, *i.e.* it is insensitive to a low-energy or a small-angle splitting of a parton. However, one shortcoming of the JADE algorithm is that multiple soft emissions of back-to-back partons can be clustered into another jet, which is not physical [233].

3.3.1.4 Durham

The Durham algorithm [234] is a very similar to the JADE algorithm, but replaces the invariant mass M_{ij} by the transverse momentum $k_{T,ij} = 2 \min(E_i^2, E_j^2)(1 - \cos \theta_{ij})$ giving an alternative measure of the distance between protojets

$$y_{ij} = 2(1 - \cos \theta_{ij}) \min(E_i^2, E_j^2)/Q^2. \quad (3.3.5)$$

The added minimization resolves the shortcoming of the JADE algorithm. The Durham algorithm does not cluster soft emissions together if there is a hard emission with a smaller distance in θ_{ij} , as $\min(E_i^2, E_j^2)$ will be equally small for every combination [233].

3.3.1.5 k_T algorithm

The k_T algorithm [235] is a successive recombination algorithm. It proceeds similar to previous algorithms by computing the distance between all protojets, however without a direct dependence on the total event energy or scale Q . The algorithm consists of multiple steps:

1. Compute the distance of protojet i to the beam

$$d_{iB} = k_{ti}^2 \quad (3.3.6)$$

and between all protojets

$$d_{ij} = d_{ji} = \min(k_{ti}^2, k_{tj}^2) \frac{R_{ij}^2}{R^2}, \quad (3.3.7)$$

where $R_{ij}^2 = (\eta_i - \eta_j)^2 + (\phi_i - \phi_j)^2$ is a distance in the $\eta - \phi$ plane. The desired radius R of the jet enters as a parameter of typical size $R = 0.3$ to 0.7 .

2. Find the smallest distance d_{\min} in d_{ij} or d_{iB} .
3. • If d_{\min} is a d_{ij} , then merge the protojets i and j into a new protojet ij with the following kinematics

$$k_{T,ij} = k_{T,i} + k_{T,j}, \quad \eta_{ij} = \frac{k_{T,i}\eta_i + k_{T,j}\eta_j}{k_{T,ij}}, \quad \phi_{ij} = \frac{k_{T,i}\phi_i + k_{T,j}\phi_j}{k_{T,ij}}. \quad (3.3.8)$$

- If d_{\min} is a d_{iB} , then the protojet i is removed and promoted to a jet.

4. Go to step 2 until all protojets are clustered.

3.3.1.6 Cambridge/Aachen

The Cambridge/Aachen algorithm [233, 236] can be formulated identical to the k_T algorithm with simplified distance measures

$$d_{ij} = d_{ji} = \frac{R_{ij}^2}{R^2} \quad \text{and} \quad d_{iB} = 1. \quad (3.3.9)$$

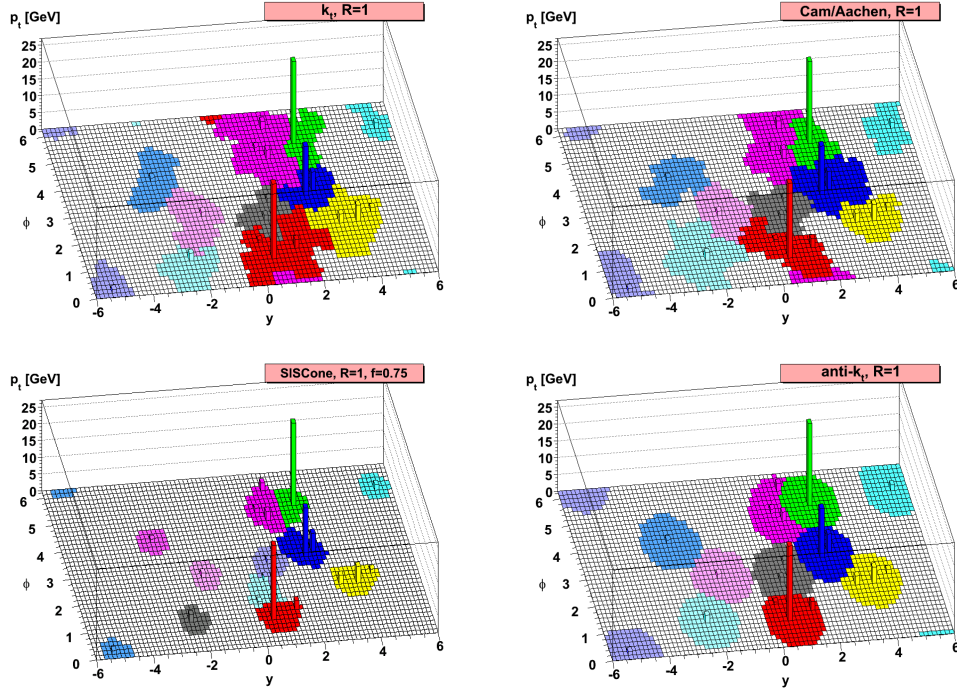


Figure 3.12: Comparison of the jet cluster definition of four different algorithms on a parton-level event: k_T (upper left), Cambridge/Aachen (upper right), SIScone (lower left) and anti- k_T (lower right) [237].

3.3.1.7 Anti- k_T algorithm

The anti- k_T [237] algorithm again uses a modified distance measure

$$d_{ij} = d_{ji} = \min\left(\frac{1}{k_{ti}^2}, \frac{1}{k_{tj}^2}\right) \frac{R_{ij}^2}{R^2} \quad \text{and} \quad d_{iB} = \frac{1}{k_{ti}^2}. \quad (3.3.10)$$

Interestingly, the k_T , Cambridge/Aachen and anti- k_T algorithms can be combined into a single expression

$$d_{ij} = d_{ji} = \min(k_{ti}^{2p}, k_{tj}^{2p}) \frac{R_{ij}^2}{R^2} \quad \text{and} \quad d_{iB} = k_{ti}^{2p}, \quad (3.3.11)$$

where p is a parameter that can be set to -1 for the anti-kt algorithm, 1 for the k_T algorithm and 0 for the Cambridge/Aachen.

In Fig. 3.12 the results jet cluster definition of four different algorithms is compared. Here, the anti- k_T algorithm produces the “roundest” jet clusters, especially around the high- p_T objects (red, green and dark blue). The roundness of a jet shows a strong similarity to the cone algorithms and is what one would statistically expect from many single hard partons. Hence, the anti- k_T algorithm is often used for the identification of hard objects in an event. The listed algorithms and many more are implemented in FastJet [238].

3.3.2 Merging

In order to get an accurate description of the hadronic activity in events with a final-state featuring a high jet multiplicity, it is essential to rely on the combination of hard-scattering matrix elements of different jet multiplicities. Consistency in this combination is crucial to avoid double counting the QCD emissions generated from the matrix elements (final-states with a fixed number of jets, inclusive of soft emissions) and from parton showers (explicitly including the soft emissions, describing exclusive final-states in the number of jets). The general idea behind multi-jet merging is to solve the double counting issue by dividing the phase space into a hard region, where the matrix element is used to describe the QCD radiation, and a soft region, where the parton shower is used. This requires a merging scale Q_{ms} to cut off divergences. Each generated n -jet sample is then reweighted (by Sudakov form factor, α_S and PDF ratios) to resemble how a parton shower would have generated the same event. Below the merging scale the normal parton shower can proceed as usual. There remain however some issues, such as the merging scale dependence and the breaking of unitarity of the shower.

In a simplified example of generating a $t\bar{t}$ event with up to $n = 2$ jets it would follow the following steps [239]:

1. Compute the cross section and generate events for each of the parton multiplicities $t\bar{t}$, $t\bar{t}j$ and $t\bar{t}jj$ up to the cutoff.
2. Pick one of the 3 multiplicities based on their relative integrated cross sections.
3. Adjust the weight by the probability that a parton shower will not attach an emission that would already be covered by the other matrix element level multiplicities.
4. Continue the shower such that either of the multiplicities obtain soft emissions, without an overlap in the hard region.

In the following we will discuss the Catani-Krauss-Kuhn-Webber-Lönnblad (CKKW-L) algorithm in detail, while outlines of Michelangelo-L.-Mangano (MLM) and Frederix-Frixione (FxFx) merging can be found in Secs. A.5.2 to A.5.3.

3.3.2.1 CKKW-L

A popular merging algorithm is the CKKW-L algorithm [240–242]. The algorithm starts from a hard-scattering event and generates a sequence of dipole emissions resembling the structure emerging from the showered event. If the configuration of any of the dipole emissions falls into the phase space region that should be described by the matrix element, the event is rejected. This ensures that the hardest emissions are always described by matrix elements and the softer ones by parton showers. Analogously, this results in re-weighting the event by the associated Sudakov form factor (*i.e.* the probability that there is no further emission once we start from the matrix element configuration). Each dipole emission in the sequence is thus accepted as long as its scale does not exceed a predefined merging scale Q_{MS} , that describes the transition between the regime in which QCD radiation is described by matrix elements and that in which it is described by parton showers. In a step by step description, the CKKW-L algorithm proceeds as follows:

1. Generate events and calculate the cross section up to a cutoff Q_{MS} with a maximum parton multiplicity N .

2. Randomly select a parton multiplicity n with a probability proportional to its integrated cross section at fixed strong coupling α_S .
3. Construct a full cascade history, *i.e.* a set of intermediate states (S_2, S_3, \dots, S_n) where S_2 corresponds to the $2 \rightarrow 2$ process, S_n to the n -parton final-state and ρ_i is the scale where S_{i-1} transitions to S_i . This is achieved by selecting branchings proportional to their probability.
4. Reweight the events with $\prod_{i=3}^n \alpha_S(\rho_i)/\alpha_S^{n-2}$.
5. For each state S_i ensure that no emission happens between ρ_i and ρ_{i+1} , otherwise reject the event, as there is an overlap between the hard and soft regime. This rejection procedure becomes equivalent to reweighting by the Sudakov $\prod_{i=2}^{n-1} \Delta_{S_i}(\rho_i, \rho_{i+1})$ for large samples.
6. Finally,
 - If $n < N$, reject the event if there is an emission between ρ_n and Q_{MS} , else accept it and continue the shower cascade from Q_{MS} .
 - If $n = N$, shower the event from the last branching scale ρ_n .

3.3.2.2 Differential jet rates

Differential jet rate (DJR), also known as Durham Jet Resolution, distributions play an important role in validating the choice of parameters relevant for the merging prescription, particularly the value of the merging scale Q_{MS} to which they are highly sensitive. A suitable choice ensures a smooth transition between an event topology with n final-state hard jets and a topology with $n + 1$ final-state hard jets, without any bumps, peaks or abrupt transitions in the DJR spectra. Plotted is the cross section of every jet multiplicity state and their sum against the logarithm of the minimized distance measure $d_{n,n+1}$ between two protojets as computed by the jet algorithm. Fig. 3.13 shows an example of a smooth inverted parabola in the DJR distribution between two 0 and 1 jet samples. A large value of d_{ij} indicates that the two protojets are well separated and thus likely to be reconstructed as two separate jets. Hence, the sample generated with more jets should have a larger cross section at large d_{ij} values. The lower jet multiplicity samples also give some contributions to the high d_{ij} values, due to the attached parton shower.

3.3.3 Matching

In the preceding sections, we have explored merging techniques used to improve the accuracy of cross section predictions in General-Purpose Event Generators (GPEGs). Typically, GPEGs rely on a LO approximation for the hard process, which is subsequently enhanced by a parton shower. This approach, however, often results in significant discrepancies between the generated cross sections and higher-order theoretical predictions. One common method to address this discrepancy is the application of a K-factor, which scales the parton shower results to better match higher-order calculations. Nevertheless, parton showers inherently employ approximations over a broad range of scales, where precise higher-order calculations would be more appropriate.

For instance, when the first radiation occurs at a high scale, just below the hard process scale, it is preferable to generate this radiation using a tree-level amplitude

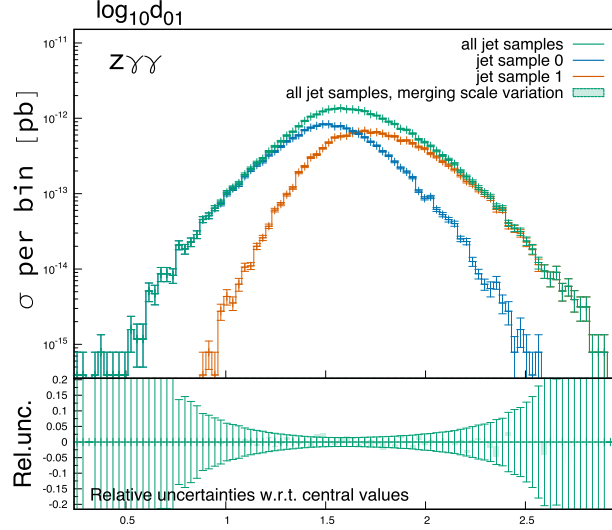


Figure 3.13: Example of a smooth transition in the DJR distribution between 0 and 1 jets in $Z\gamma\gamma$ production with MLM merging at the High Luminosity LHC (HL-LHC) [243].

with an additional parton, rather than relying on the collinear approximation. In the preceding section we saw that this issue is mitigated by merging tree-level results with different numbers of partons in the final-state. An alternative and more comprehensive solution involves the showering of full NLO results, or beyond. This approach not only improves the normalization of the total cross section but also enhances the accuracy of the first radiation distribution.

3.3.3.1 Madgraph5 - MC@NLO

Achieving NLO accuracy cannot be accomplished merely by replacing LO amplitudes with NLO amplitudes for the hard process in combination with a parton shower, due to the risk of double-counting real and virtual corrections. A NLO observable \mathcal{O} comprises contributions from both n -particle and $n+1$ -particle states

$$\begin{aligned}
 \langle \mathcal{O} \rangle &= \int d\Phi_n (B_n + V_n) \mathcal{O}_n(\Phi_n) \sim \text{hard final state} + \text{virtual radiation (loop)} \\
 &+ \int d\Phi_{n+1} B_{n+1} \mathcal{O}_{n+1}(\Phi_{n+1}) \sim \text{real radiation} .
 \end{aligned} \tag{3.3.12}$$

The divergences between B_{n+1} and V_n can be handled with universal FKS subtraction terms as in **MadGraph**. Writing the local IR counterterms as D_1 and their integrated form as I_1 the NLO observable becomes

$$\langle \mathcal{O} \rangle = \int d\Phi_n (B_n + V_n + B_n \otimes I_1) \mathcal{O}_n(\Phi_n) \sim \text{hard final state} + \text{virtual radiation (loop)} + \int \text{counter terms}$$

$$+ \int d\Phi_{n+1} (B_{n+1} \mathcal{O}_{n+1}(\Phi_{n+1}) - B_n \otimes D_1 \mathcal{O}_n(\Phi_{n+1})) \sim \text{diagram with real radiation} - \text{diagram with counter terms}, \quad (3.3.13)$$

where soft and collinear gluons are coloured in blue. In our graphical notation attaching an emission to the B_n by the PS overlaps with real radiation

$$\text{PS}_n \sim \text{diagram 1} + \text{diagram 2}. \quad (3.3.14)$$

Consequently, an event generator must determine whether to generate an n -particle or an $n+1$ -particle hard event initially. This decision is made by selecting the hard event with a probability proportional to its respective contribution, ensuring that these contributions are made finite by appropriate subtraction techniques. Thus double counting between NLO and PS can be avoided with additional parton shower counterterms \bar{P}_{n+1} [244, 245]

$$\begin{aligned} \langle \mathcal{O} \rangle &= \int d\Phi_n (B_n + V_n + B_n \otimes I_1) \text{PS}_n(\mathcal{O}_n, \Phi_n) \sim \text{diagram 1} + \text{diagram 2} + \int \text{diagram 3} \\ &+ \int d\Phi_{n+1} (B_{n+1} - B_n \bar{P}_{n+1}) \text{PS}_{n+1}(\mathcal{O}_{n+1}, \Phi_{n+1}) \sim \text{diagram 4} - \text{diagram 5} \\ &+ \int d\Phi_{n+1} (B_n \bar{P}_{n+1} - B_n \otimes D_1) \text{PS}_n(\mathcal{O}_n, \Phi_{n+1}) \sim \text{diagram 6} - \text{diagram 7}. \end{aligned} \quad (3.3.15)$$

The last line shows that the dipole D and parton shower counterterms may cancel each other. The PS has to start at respective emissions

$$\text{PS}_n \sim \text{diagram 8} + \text{diagram 9} + \dots, \quad (3.3.16)$$

$$\text{PS}_{n+1} \sim \text{diagram 10} + \dots \quad (3.3.17)$$

The MC@NLO method regulates the low transverse momentum region and provides a smooth transition between lower and higher scales as can be seen in Fig. 3.14. It shows a top quark pair simulation by `MadGraph`, a well-known code that uses MC@NLO. At large transverse momenta $p_T^{t\bar{t}}$ the fixed NLO calculation gives reliable results, while at low transverse momenta the PS is more accurate. However, the drawbacks of this method are that it requires a shower implementation with the correct counterterms and can lead to many events with negative weights, which make a probability interpretation impossible. This can be rectified by generating events with probabilities proportional to the absolute values of the two contributions and assigning a negative weight to events that would have had a negative probability. Since the focus is on large samples of events, such as when computing distributions, this approach poses no problem because the sum of both contributions is always positive (except in cases where the NLO calculation fails). Nonetheless, a large fraction of negative weighted events will reduce statistical power leading to longer computation times. This has prompted the recent development of MC@NLO- Δ matching [221], which reduces the number of negative weights through the construction of Δ term, similar to the Sudakov form factor, to separate hard from soft and collinear regions.

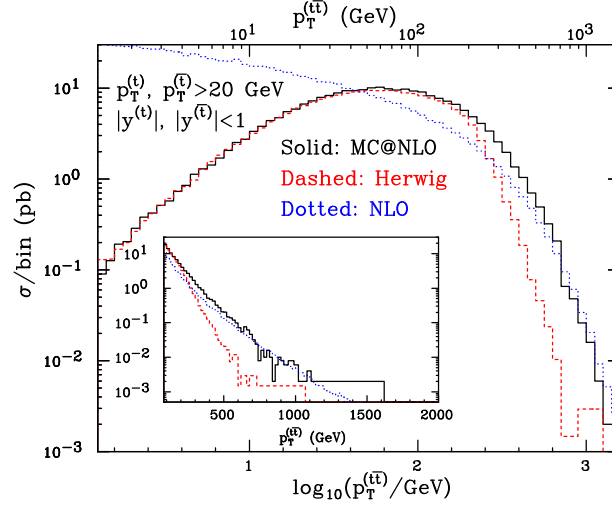


Figure 3.14: Transverse momentum distribution of the top quark pair at the LHC with acceptance cuts. Shown in Refs. [58, 246].

3.3.3.2 POWHEG method

The Positive Weight Hardest Emission Generator (POWHEG) method [63, 188], as the name suggests, aims to solve the MC@NLO problem of negative weights. The method starts with three key observations about the nature of emissions:

1. The hardest emission aligns with the hardest line in the shower.
2. Configurations with non-soft emissions before the hardest emission are collinear subleading.
3. The ordering along the hardest line has $Q^2 \lesssim p_T^2$.

They also hold for angular ordered parton showers [63]. The POWHEG method is based on generating the hardest emission first, using the ratio of the real to the Born matrix elements as the splitting probability. After this initial splitting, the parton shower is then applied, but only after the first emission has been generated.

Again, an observable \mathcal{O} can be written as

$$\langle \mathcal{O} \rangle = \int d\sigma \mathcal{O} = \int d\Phi_B (B(\Phi_B) + V(\Phi_B)) \mathcal{O}(\Phi_B) + \int d\Phi_R R(\Phi_R) \mathcal{O}(\Phi_R), \quad (3.3.18)$$

where $\Phi_B = \Phi_n$ and $\Phi_R = \Phi_{n+1}$ are the Born and real phase spaces respectively. They can be mapped to each other by the radiation of an extra parton

$$d\Phi_R = d\Phi_B d\Phi_{\text{rad}}, \quad (3.3.19)$$

where the real phase spaces matches the Born kinematics in the soft and collinear limits. This is similar to the phase space 3.1.114 seen in the FKS subtraction.

Instead of generating both n and $n+1$ particle final-states, only the n particle state is generated. Through a modified Sudakov factor, the first emission is attached to the n

particle state in such a way that the NLO accuracy is preserved. This means that there are no negative weights², as the emission is attached with the right NLO probability, and the parton shower can take care of following emissions. In the description of the FKS and CS subtraction methods we have already seen that an $n + 1$ phase space can be mapped to an n phase space and vice versa. Then,

$$\begin{aligned} \bar{B}(\Phi_B) &= B(\Phi_B) + V(\Phi_B) + \int d\Phi_{\text{rad}} R_s(\Phi_R(\Phi_B, \Phi_{\text{rad}})) \\ &+ \int d\Phi_{\text{rad}} (R(\Phi_R(\Phi_B, \Phi_{\text{rad}})) - R_s(\Phi_R(\Phi_B, \Phi_{\text{rad}}))), \end{aligned} \quad (3.3.20)$$

where R_s describes the singular behaviour of the real cross section in the soft and collinear limits. Thus, the first integral represents the integrated subtraction terms, while the second integral takes into account the divergence subtracted real correction and integrates out the radiation. The POWHEG-Sudakov factor can then be defined in analogy to Eq. (2.2.44) as

$$\Delta_R(\Phi_B, p_T) = \exp \left[- \int d\Phi_{\text{rad}} \frac{R(\Phi_R)}{B(\Phi_B)} \theta(k_T(\Phi_R) - p_T) \right], \quad (3.3.21)$$

where mappings between the Born and real phase spaces are implicit $\Phi_R = \Phi_R(\Phi_B, \Phi_{\text{rad}})$. The interpretation of Δ_R as a Sudakov no emission probability can be seen from the singular behaviour as $R \rightarrow \infty$ where the resulting no emission probability goes to 0. Instead of a AP splitting functions the NLO accurate ratio of real to Born cross sections R/B is used. Then the resulting cross section is

$$d\sigma = \bar{B} d\Phi_B \left\{ \Delta_R(\Phi_B, p_T^{\text{min}}) + \Delta_R(\Phi_B, k_T(\Phi_R)) \frac{R(\Phi_R)}{B(\Phi_B)} \theta(k_T(\Phi_R) - p_T^{\text{min}}) d\Phi_{\text{rad}} \right\}, \quad (3.3.22)$$

with $p_T^{\text{min}} \sim \Lambda_{\text{QCD}}$ and reproduces Eq. (2.2.43) at small k_T . The first term corresponds to the n particle event generation and the second term to the $n + 1$ particle event generation. That this produces the first radiation to NLO accuracy can be seen from expanding the expression to NLO. That is, \bar{B} from Eq. (3.3.20) times the expanded Sudakov factor $\Delta_R(\Phi_B, p_T^{\text{min}})$ cancels the real contributions³ and reproduces $B + V + I$ as expected from the events without an attached emission. Alternatively, by analogy to the unitarity of a parton shower we see that the terms in the curly brackets must sum up to one, *i.e.* either one or no emission is attached. The first emission is consequently already ordered in p_T and the parton shower has to generate radiation only from below the scale k_T . An angular ordered parton shower has to employ a veto algorithm to avoid radiations above k_T .

The method generalizes for multiple flavour structures f_b and singular regions α_r for a given flavour structure $\{\alpha_r | f_b\}$ to

$$\begin{aligned} d\sigma &= \sum_{f_b} \bar{B}^{f_b}(\Phi_B) d\Phi_B \left\{ \Delta^{f_b}(\Phi_B, p_T^{\text{min}}) \right. \\ &+ \left. \sum_{\alpha_r \in \{\alpha_r | f_b\}} \Delta^{f_b}(\Phi_B, k_T) \frac{R(\Phi_R^{\alpha_r})}{B^{f_b}(\Phi_B)} \theta(k_T(\Phi_R^{\alpha_r}) - p_T) d\Phi_{\text{rad}} \right\}, \end{aligned} \quad (3.3.23)$$

²There are still occasional negative weighted events, *e.g.* from negative PDF values, but significantly less than in MC@NLO.

³Up to scale p_T^{min} .

with the Sudakov factor

$$\Delta^{f_b}(\Phi_B, p_T) = \exp \left\{ - \sum_{\alpha_r \in \{\alpha_r | f_b\}} \int d\Phi_{\text{rad}} \frac{R(\Phi_R^{\alpha_r})}{B f_b(\Phi_B)} \theta(k_T(\Phi_R^{\alpha_r}) - p_T) \right\}, \quad (3.3.24)$$

where $\Phi_R^{\alpha_r} = \Phi_R(\Phi_B, \Phi_{\text{rad}}(\alpha_r))$ such that flavour structure of α_r agrees with f_b . Picking the kinematics, singular region and flavour structure of the first emission is done by the highest- p_T bid procedure as outlined in Sec. 3.2.5.

The outlined method has several analogies to the CKKW-L merging of Sec. 3.3.2.1. However, one difference we want to highlight here is that the CKKW-L method reconstructs the matrix elements as parton shower, while the POWHEG method uses a truncated shower, *i.e.* it starts after the hardest emission. We leave the practical implementation of a process in the POWHEG-BOX to the following Sec. 4.2.2.

Chapter 4

Photon production with POWHEG

To study the properties of the QGP, various hadronic observables are typically analysed. However, while hadrons are primarily produced during the freeze-out phase, photons are emitted throughout all stages of the collision. Unlike hadrons, photons can traverse the medium without significant interaction due to their large mean free path compared to the system size. This unique feature allows photons to offer a direct glimpse into the medium, providing insights into earlier stages and higher temperatures that are inaccessible through hadronic measurements. Hence, photons are widely regarded as indispensable probes of heavy-ion collisions. Understanding the connection between photon production and medium properties requires examining the processes responsible for their emission. There are many sources of photons in proton-proton and heavy-ion collisions. Generated throughout all stages of the collision process, they originate either from decays of light- and heavy-flavour hadrons or are produced directly from hard-scattering processes like the quark-gluon Compton scattering and quark-anti-quark annihilation. In addition to these sources, the hot medium produced in heavy-ion collisions may emit thermal radiation, commonly grouped together with the direct production. Unaffected by the strong interaction, the photons pass through the dense medium without undergoing any final-state interactions. Fig. 4.1 shows how they can be grouped. The majority of photons observed in such collisions arise from the decay of particles like the π^0 . Photons that do not originate from hadron decays are termed direct photons, which can be further categorized based on their emission sources. [248, 249]

Thermal photons arise when a medium is sufficiently hot and dense, leading to frequent scatterings between its constituents, resulting in photon emission. In heavy-ion collisions, for example, these constituents are partons in the QGP and later the hadrons in the hadron gas after hadronisation. If the QGP is not fully equilibrated, the emitted photons are termed pre-equilibrium photons; otherwise, they are classified as thermal photons.

One of the expected signals of a QGP is the radiation of thermal photons, with a particular transverse momentum spectrum reflecting its temperature [117, 250]. In an equilibrated medium with a given temperature T , the emission rate $N_\gamma^{\text{thermal}}$ of thermal photons depends exponentially on the photon energy E . Specifically, the rate follows

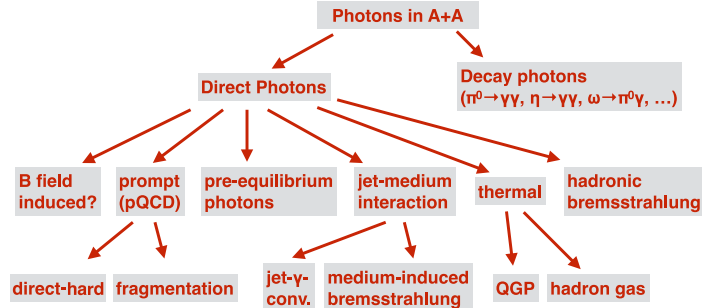


Figure 4.1: Disambiguation of photon sources in proton-proton and heavy-ion collisions. Figure adapted from [247].

the relation

$$E \frac{dN_{\gamma}^{\text{thermal}}}{d^3 p}(E, T) \sim T^2 e^{-E/T}. \quad (4.0.1)$$

This behaviour suggests that direct photons provide critical insight into the temperature of the medium [251–253].

In the hadron gas phase, photons can be emitted through various mechanisms, such as interactions between mesons (*e.g.* $\pi^{\pm} + \rho^0 \rightarrow \pi^{\pm} + \gamma$), reactions involving baryons, radiative decays, or hadronic Bremsstrahlung resulting in an approximately exponential spectrum at low p_T [251, 254–257].

At higher p_T , the direct photon spectrum is dominated by prompt photons, which are characterized by a power-law shape, in contrast to the exponentially distributed thermal photons that dominate at lower p_T ($\lesssim 3 \text{ GeV}/c$) [257]. Consequently, experimental measurements of direct photons can be particularly useful in distinguishing thermal photon production at low p_T and prompt photon production at high p_T .

Pre-equilibrium photons are emitted by the medium before it reaches thermal equilibrium following a heavy-ion collision. The medium during this pre-equilibrium phase can be described by the Glasma framework [258, 259], a state characterized by strong colour fields after the collision and before full thermalization occurs. The importance of pre-equilibrium photons lies in their sensitivity to the early stages of medium evolution, potentially allowing them to probe the conditions even before the QGP fully forms. In particular, studies like those referenced in [260] show that the contribution of these pre-equilibrium photons can be comparable to that of the thermal photons produced in later stages.

We focus on prompt photon production, meaning photons that are prompt-direct, produced in the hard collisions, computed in perturbative non-thermal QCD, as well as fragmentation photons originating from quark and gluon fragmentation. Fragmentation photons, instead, are produced when a high-energy parton undergoes radiation, leading to a photon that is accompanied by other hadronic activity [261, 262]. The distinction between these two types is critical and is often maintained through isolation criteria in experimental setups. Isolation techniques are also implemented to separate prompt photons from those produced in hadronic decays. This involves restricting the hadronic activity around a photon candidate, ensuring the hadronic energy in a cone around the photon is below a certain threshold [70, 74, 263]. These criteria help to minimize the

contamination from fragmentation photons. This allows for a clearer interpretation of direct photon production. The effect of the isolation cone on the parton-to-photon fragmentation contribution has been thoroughly examined, for example, using `JetPhox` [72, 73]. Especially, in the low transverse momentum regime, the isolation cone is crucial to suppress the dominant fragmentation contribution compared to the photons originating in the hard process. To consistently eliminate the fragmentation contributions, one must exclude collinear parton-photon configurations without disrupting the cancellation of infrared singularities from soft gluon emissions [75]. While straightforwardly vetoing the collinear configurations, as in the fixed cone approach, is not IRC safe, suppressing them maintains the necessary cancellation. This method is known as smooth-cone isolation. The proof of infrared safety is similar to that of jet definitions, where analogous cone algorithms are also not IRC safe [76].

Thermal photons produced in QGP can be obtained by subtracting the rate of prompt photons from the rate of direct photons

$$dN_{\gamma}^{\text{thermal}} = dN_{\gamma}^{\text{direct}} - dN_{\gamma}^{\text{prompt}} \quad (4.0.2)$$

neglecting other contributions. The photons are detected either directly, *e.g.* in the electromagnetic calorimeter, or indirectly by conversion via low invariant-mass e^+e^- pairs. In the following sections we will explore the direct-hard production of virtual photons in Sec. 4.1 and real photons in Sec. 4.2 using the POWHEG method.

4.1 Virtual photon production

In contrast to real photons, virtual photons ($\gamma^* \rightarrow e^+e^-$) carry a mass (m_{ee}), unaltered by the radial flow, that can act as an approximate clock, allowing for the separation of different collision stages. The pre-equilibrium effects become evident around $m_{ee} \gtrsim 2$ GeV, followed by the expected formation of the QGP in the range $1 \text{ GeV} \lesssim m_{ee} \lesssim 2$ GeV, and finally the hadronic phase at later emission stages with $m_{ee} \lesssim 1$ GeV [264, 265]. They can therefore provide valuable insight into the entire time evolution and dynamics of the hot system. However, measurements of the thermal photon signal in heavy-ion collisions face some considerable challenges, such as a small production cross section due to the electromagnetic coupling and significant combinatorial and physical backgrounds from hadron decays.

In pp collisions, the di-electron low and intermediate mass spectrum can be well described by a combination of expected hadronic sources, the so-called cocktail [266–270]. The low-mass region (LMR) ($m_{ee} < 1.1$ GeV) is dominated by light-flavoured vector meson decays, whereas the intermediate-mass region (IMR) ($1.1 \text{ GeV} < m_{ee} < 2.7$ GeV) receives contributions mostly from semileptonic decays of charm and bottom hadrons correlated through flavour conservation. Despite the overwhelming backgrounds, significant enhancements of direct real or low-mass virtual photons have been observed in heavy-ion collisions at the Super Proton Synchrotron (SpS), RHIC and LHC [267, 271–281]. The enhancements are well described by exponential distributions in $p_{T,\gamma}$ and are thus indicative of thermal radiation consistent with average (effective) temperatures in the range of 200 – 300 MeV [277, 280, 281]. In the intermediate-mass window, an excess over decay di-electrons has so far been observed only at the SpS [275, 276, 282, 283]. In order to discern the characteristics of the subtle thermal photon signal in this range at the LHC, that promises increased sensitivity to QGP thermal radiation, it is crucial

to understand the di-electron yield originating from the hard production of photons as well as from heavy-flavour particle decays.

In this section, we report on theoretical advances in describing the di-electron mass spectrum in the intermediate-mass region in setups similar to those used in the ALICE experimental analyses. First, we calculate the contribution to the direct photon production signal originating from the hard scattering. This component is usually extracted from the data [284], assuming the invariant mass shape from the Kroll-Wada prescription [285] with additional constraints from real direct photon measurements, and must be subtracted from the total direct photon signal for reliable temperature estimates [281, 286], especially in the intermediate transverse momentum region. Here, for the first time, we obtain a prediction for the di-electron invariant mass spectrum based on a first-principles calculation using the DY process in association with an extra jet at NLO QCD accuracy matched to parton showers. Second, we perform a thorough analysis of the dominant decay backgrounds with a variation of perturbative scales and PDFs, also taking into account cold nuclear effects through nPDFs. Such uncertainties can have an appreciable impact on the systematic uncertainty estimates in the measured di-electron spectrum baseline in pp as well as heavy-ion collisions. Studying this process is also of broader interest, as it offers a means to test pQCD calculations and MC event generators at the limits of perturbativity. In heavy-ion collisions it can be used in studies of energy loss, levels of thermalisation of charm and bottom quarks within the medium, and mechanisms of heavy-quark hadronisation [287–290]. The distribution of correlated e^+e^- pairs stemming from charm-hadron decays provides information about kinematic correlations between charm and anticharm quarks, shedding light on the production mechanisms and offering sensitivity to soft heavy-flavour production [291–293] and thermalisation, in lead-lead (PbPb) collisions. In recent experimental analysis efforts the distance of closest approach (DCA) method [284] has been employed to separate prompt di-electrons ($\text{DCA}_{ee} < 0.5\sigma$) from non-prompt di-electrons ($\text{DCA}_{ee} > 2\sigma$) reducing the impact of heavy-quark di-electrons on the signal.

An overview of the different contributions to an invariant mass spectrum and the DCA_{ee} impact are shown in Fig. 4.2.

This section is based on our publication [3] and organised as follows. We first discuss the phase space and improve the importance sampling in POWHEG BOX V2 for the DY process in Sec. 4.1.1. We first present general theoretical considerations and define our signal and background in the di-electron observables in the kinematic region of interest in Sec. 4.1.2. Next, we provide an explanation of our simulation setup, which includes our workflow and the event selection in Sec. 4.1.3. In Sec. 4.1.4 we present our results for virtual photon and heavy flavour production combined into a new prediction for the “hadronic cocktail”.

4.1.1 Sampling in POWHEG

Since we are interested in dilepton pairs of low invariant mass and transverse momentum, we need to improve the importance sampling in POWHEG BOX V2. The following steps are for the DY process, but can be adapted to other processes especially the DY process with an extra jet of interest. For each transformation we track also its derivative, *i.e.* the Jacobian determinant, since it practically is a form of importance sampling (see Sec. 3.2.2).

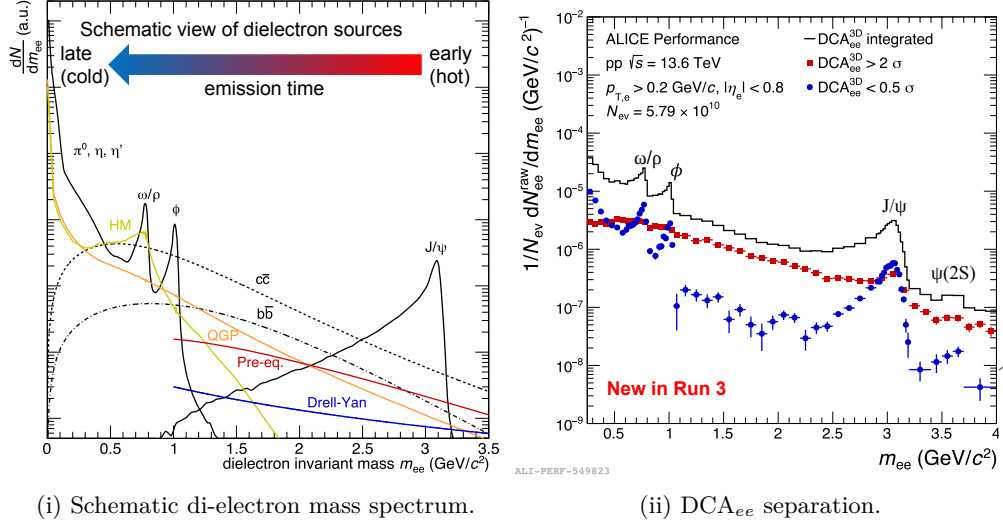


Figure 4.2: Di-electron mass spectrum and DCA_{ee} separation [294].

4.1.1.1 Linear sampling

In the POWHEG BOX implementation of NLO Z [295] production the phase space is parametrized as

$$\begin{aligned} d\Phi_2 &= dx_+ dx_- (2\pi)^2 \delta^4(k_+ + k_- - k_1 - k_2) \frac{d^3 k_1}{(2\pi)^3 2k_1^0} \frac{d^3 k_2}{(2\pi)^3 2k_2^0} \\ &= \frac{1}{S} \frac{1}{16\pi} dM^2 dY d\cos\theta_l \frac{d\phi_l}{2\pi}, \end{aligned} \quad (4.1.1)$$

where the suffix l indicates that the angles are to be understood between the leptons. The new integration variables are the invariant mass M

$$M^2 = (k_1 + k_2)^2 \quad (4.1.2)$$

and rapidity

$$Y = \frac{1}{2} \log \frac{(k_1 + k_2)^0 + (k_1 + k_2)^3}{(k_1 + k_2)^0 - (k_1 + k_2)^3}. \quad (4.1.3)$$

The relation between these Born parametrizations is

$$x_+ = \sqrt{\frac{M^2}{S}} e^Y \quad \text{and} \quad x_- = \sqrt{\frac{M^2}{S}} e^{-Y}. \quad (4.1.4)$$

The implementation of the code uses a linear sampling on M^2 if the Z peak is not included in the user supplied integration limits M_{\min} and M_{\max} , that is

$$M^2 = M_{\min}^2 + x_1 (M_{\max}^2 - M_{\min}^2) \quad \text{and} \quad \frac{dM^2}{dx_1} = (M_{\max}^2 - M_{\min}^2). \quad (4.1.5)$$

By using a random $x_i \in (0, 1)$ the necessary scaling of the Jacobian determinant from the substitution is $\frac{dM^2}{dx}$. Similarly, after picking a value for M^2

$$Y = -\frac{(1 - 2x_2)}{2} \log \frac{M^2}{S} \quad \text{and} \quad \frac{dY}{dx_2} = \log \frac{M^2}{S} \quad (4.1.6)$$

such that the boundary cases correspond to $x_+ = 1$ and $x_- = 1$. And the final third variable is

$$\cos \theta = \frac{3}{2} \left((1 - 2x_3) - \frac{(1 - 2x_3)^3}{3} \right) \quad \text{and} \quad \frac{d \cos \theta}{dx_3} = \frac{3}{2} (-2 + 2(1 - 2x_3)^2), \quad (4.1.7)$$

which is optimized to produce more θ values close to 0 or π and less between.

`POWHEG BOX` uses an adaptive MC integration routine, namely `MINT`, with 50 bins per dimension. The quality of the integration and importance sampling can be monitored by inspecting the `.top`-plot files generated¹. In these plots the x-axis is the x_1 value from 0 to 1 and corresponds to an integration variable. The y-axis is the relative contribution to the cross section projected on given bin. The curve is monotonous since the contribution at *e.g.* $x = 0.5$ is the combination of all bins from 0 to 0.5. The vertical lines in the plot illustrate `POWHEG BOX`'s decision for the adaptive bins. Ideally each bin contains the same contribution to the total cross section such that the curve is a straight line with slope 1. Divergences are often visible at $x = 0$ and $x = 1$, depending on the phase space parametrization. The other integration variable also indirectly suffer from the bad convergence in one variable since the sampling and therefore also the projection becomes unreliable.

In this case the sampling converges badly at low M up to the point where `POWHEG BOX` gives unreliable/negative NLO cross sections. This behaviour is shown in Fig. 4.3i with the full input parameters given in file A.1. In this case, we observe that most bins are concentrated at low x_1 , making the vertical binning lines nearly indistinguishable.

4.1.1.2 Logarithmic sampling

We have seen that the linear sampling prefers the low M region. Hence, we want to emphasize the low M region by a logarithmic sampling

$$M^2 = M_{\max}^2 \left(\frac{M_{\min}^2}{M_{\max}^2} \right)^{x_1} \quad \text{and} \quad \frac{dM^2}{dx_1} = M^2 \log \left(\frac{M_{\max}^2}{M_{\min}^2} \right). \quad (4.1.8)$$

We notice an improvement in the binning in Fig. 4.3ii and a better statistical convergence in Tab. 4.1.

4.1.1.3 Optimized sampling

`POWHEG BOX` shows the grids and binning as normalized integrated cross section

$$\frac{\int_0^z dx \frac{d\sigma}{dx}}{\int_0^1 dx \frac{d\sigma}{dx}} = F(z). \quad (4.1.9)$$

To optimize the sampling we choose the inverse of this curve

$$\text{inverse} \frac{\int_0^z dx \frac{d\sigma}{dx}}{\int_0^1 dx \frac{d\sigma}{dx}} = F^{-1}(z), \quad (4.1.10)$$

¹To draw these files we recommend <https://github.com/APN-Pucky/pytopdrawer>.

which exists since the curve is monotonous. This is optimal since using the inverse function rule gives

$$1 = \left[\frac{d \int_0^y dx \frac{d\sigma}{dx}}{dy \int_0^1 dx \frac{d\sigma}{dx}} \right]_{y=F^{-1}(z)} (F^{-1})'(z), \quad (4.1.11)$$

where the first bracket corresponds to the importance sampled cross section and the second to the Jacobian determinant. The equality of its derivative to one means that every point in y is now of equal weight. Expressed in similarity to the importance sampling in Eq. (3.2.13)

$$\sigma(z) = \int_0^z dx \frac{d\sigma}{dx}(x) = \int_{F(0)}^{F(z)} dy \frac{d\sigma}{dx}(F^{-1}(y))(F^{-1})'(y) \quad (4.1.12)$$

the slope $d\sigma/dy$ with respect to the new variable y is always constant. Practically, this corresponds to importance sampling the function by itself, however we are only looking at one projected integration variable.

We can use any fit function that is invertible to determine F . Next computing the inverse of a monotonous function in Eq. (4.1.10) is significantly easier than solving the differential equation in Eq. (4.1.11). The new importance sampling is then given by F^{-1} . If this sampling does not give satisfying results it can be repeated on the importance sampled cross section.

The fitting is demonstrated in Fig. 4.4 the straight line on the left is due to the last point (0,0) on a logarithmic scale. It comes as no surprise that the derivative of the guessed fit function F

$$F(x) = \frac{a+1}{\frac{a}{x}+1}, \quad F^{-1}(x) = \frac{ax}{a-x+1}, \quad (F^{-1})'(x) = \frac{a(a+1)}{(a-x+1)^2}, \quad (4.1.13)$$

resembles the divergence of the photon pole regulated by the mass window cuts. We choose $a = M_{\min}^2/M_{\max}^2$ such that we obtain an a of the same order as in the fit. Finally, the optimized sampling F^{-1} with some abbreviations is

$$a = \frac{M_{\min}^2}{M_{\max}^2}, \quad d = (M_{\max}^2 - M_{\min}^2), \quad (4.1.14)$$

$$M^2 = \frac{ax_1d}{(1-x_1+a)} + M_{\min}^2, \quad \frac{dM^2}{dx_1} = \frac{a(a+1)d}{(1-x_1+a)^2}. \quad (4.1.15)$$

We observe a major improvement in the binning in Fig. 4.3iii where all bins are same sized as desired. In the comparison between the different samplings in Tab. 4.1 we see that the fitted sampling gives the best convergence and the lowest computation time. Furthermore, the NLO computation with the improved sampling does no longer return negative cross sections.

Finally, note that the Z production POWHEG BOX codes were not original designed for low p_T studies. Probing close to the photon pole is blocked, and this filter has to be removed from the code. Furthermore, the parameters `alphas_from_pdf 1` and `pdf_cutoff_fact 0.01d0` allowed us to stretch into even lower p_T regimes, without loosing stability.

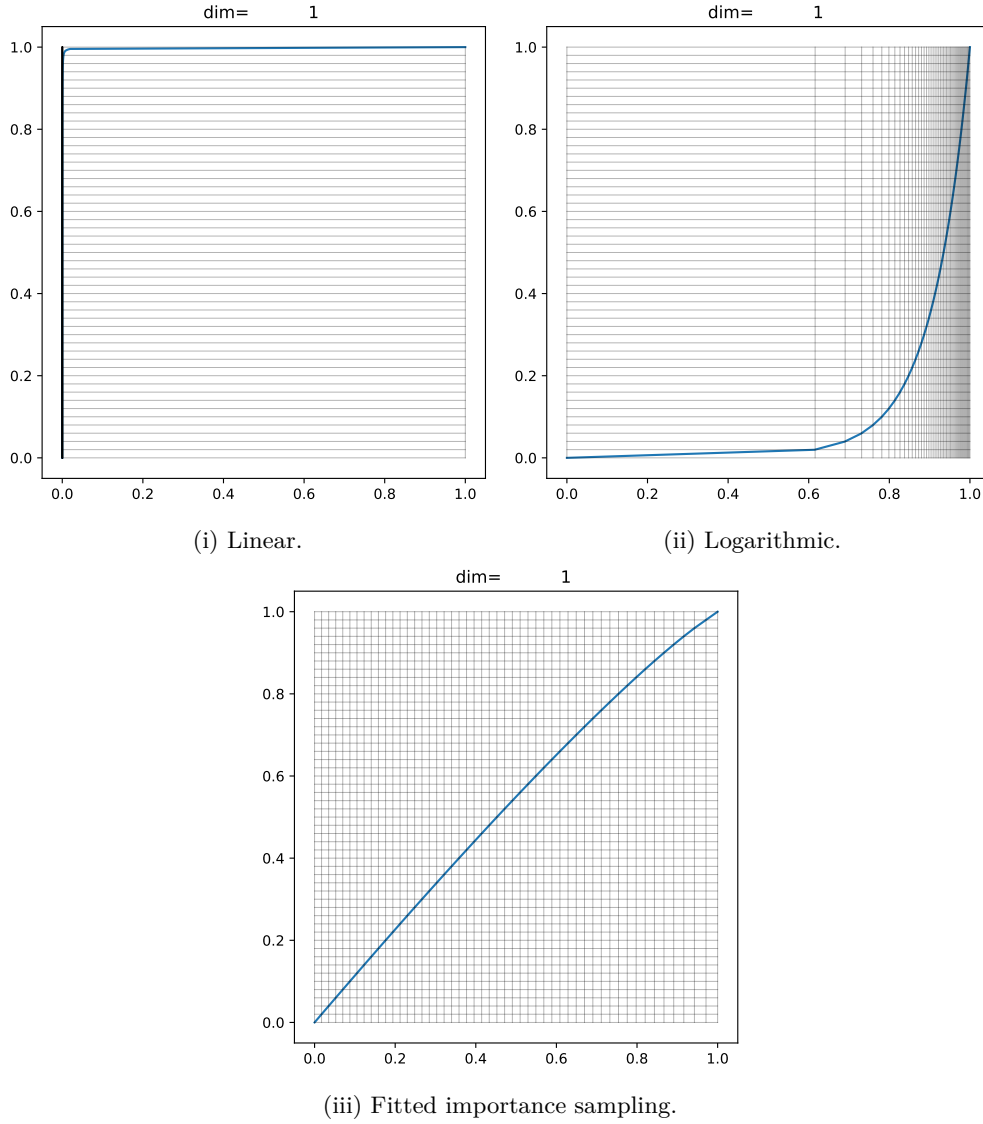


Figure 4.3: Importance sampling in POWHEG BOX.

Sampling	cross section [pb]	cross section stat. [pb]	btide time [pb]
Linear	24 334 890	$\pm 96\,432$	2.8
Logarithmic	24 208 610	$\pm 13\,635$	0.5
Fitted	24 207 000	$\pm 10\,697$	0.4

Table 4.1: LO comparison of the importance samplings.

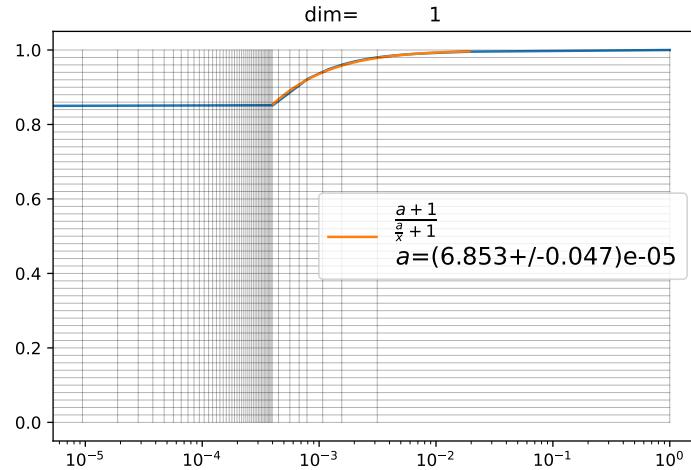


Figure 4.4: Linear importance sampling on a logarithmic scale with a fit.

4.1.2 Signal and background

The intermediate mass window region in measurements of di-electron spectra is characterized by a lepton pair with a relatively low invariant mass, between roughly 1 GeV to 3 GeV, and a relatively small transverse momentum, below 10 GeV. In addition to the thermal photon signal, there are two dominant production modes in this kinematic regime. One of them is direct photon production, which involves the conversion of photons into di-electrons. In the following, we will refer to this contribution as the signal. The second contribution is the production of heavy-flavoured hadrons followed by a decay into a pair of electrons.² We will call this contribution the background.

The signal is the direct production of photons with non-zero virtuality that decay into di-electrons, this is the DY process. The DY process is described at tree level by the partonic process $q\bar{q} \rightarrow \gamma^* \rightarrow l^+l^-$ and is of the order $\mathcal{O}(\alpha^2)$ in the perturbative expansion of the electromagnetic coupling constant. In the absence of any other particles, the e^+e^- pair is produced back-to-back and the system carries no transverse momentum and falls out of the kinematic region of our interest. To circumvent this problem, one must produce a pair of di-electrons in association with one jet at order $\mathcal{O}(\alpha^2\alpha_S)$ in the simultaneous expansions of the electromagnetic and strong couplings constants. Fig. 4.5i shows one such LO Feynman diagram. At this order, one obtains contributions not only from the $q\bar{q}$ channel, but also from the qg channel and therefore acquires a sensitivity to the gluon density. Additionally, the NLO QCD corrections, $\mathcal{O}(\alpha^2\alpha_S^2)$, can also be gluon-gluon initiated. Note that this process also receives contributions from the topology where the photon is replaced by the Z boson and from the corresponding $\gamma - Z$ interference, both of which we include, but their contributions are negligible in the invariant mass regime far below the mass of the Z -boson. We simulate our signal with NLO QCD precision, *i.e.* including real and virtual higher-order corrections up to $\mathcal{O}(\alpha^2\alpha_S^2)$, using the Zj [296] process from the POWHEG BOX V2 package, which is now also available in multi scale improved NLO (MiNLO) [297] and NNLO (multi scale improved

²The light-flavoured hadron production with di-electron decay dominates the invariant mass spectrum below 1 GeV, but is rather suppressed above.

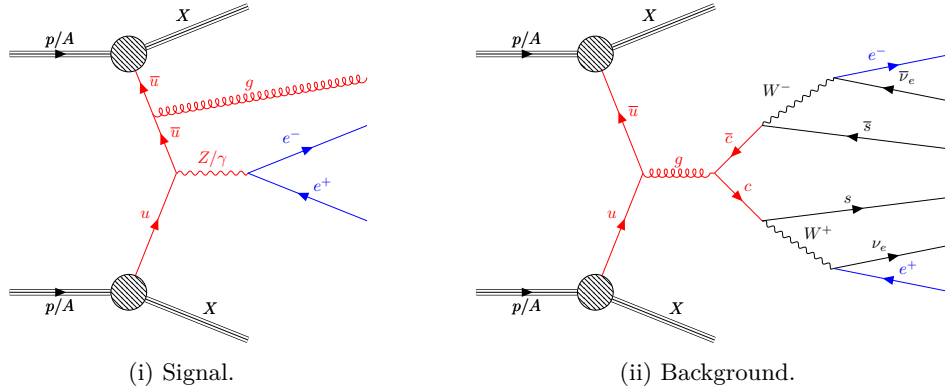


Figure 4.5: Exemplary LO Feynman diagrams for dilepton production via a virtual photon/ Z boson (signal, left) and heavy quarks (HQs) (background, right). The LO hard process is coloured in red, while the dileptons are coloured in blue. The diagrams were generated with [7].

NNLO (MiNNLO)) [298, 299] precisions.

In the limit of zero di-electron virtuality, real direct photon production is restored at $\mathcal{O}(\alpha\alpha_S)$, where the photon is produced OS and does not decay into di-electrons. Similarly to the fragmentation of jets into photons in direct real photon production, contributions from the fragmentation of jets into di-electrons are possible. In analogy to our calculation of real direct photons [300] within the POWHEG framework, the Zj process includes this fragmentation contribution, which is partially generated by parton shower emissions of the photon. In contrast to real photons, in virtual photon production there is no explicit divergence that has to be absorbed in fragmentation functions, but the divergence is regulated by the photon virtuality [65, 301]. Nevertheless, the resulting logarithms $\log(m_{ee}/p_{T,ee})$ arising per order of α_S could in principle become large and spoil the convergence of the perturbation series. We keep track of the ratio $m_{ee}/p_{T,ee}$ and find that it varies mostly from 10^{-1} to 10^1 , with a peak around 1. This is illustrated in Fig. 4.6, with the details behind the creation of the plot deferred to Sec. 4.1.3. We therefore expect our predictions to be stable with respect to such higher-order effects in the kinematic range of our interest.

We now proceed to the discussion of the background, which can be further divided into the open production of charm and bottom quarks [264, 302]. Although photon-induced or DY-like production of HQs is possible, it is usually sufficient to consider only the QCD production due to the ratio of the coupling strengths $\alpha^2/\alpha_S^2 \lesssim 0.5\%$ [303, 304]. This means that heavy-flavour partons are only produced from a subset of the QCD Feynman diagrams for the production of light-flavours, namely where the heavy quarks in the final-state are connected by a fermion line and thus belong to the same flavour generation independently of the partons in the initial-state. One of the Feynman diagrams is shown in Fig. 4.5ii. The HQs then hadronise predominantly into D - and B -mesons, which further decay into electrons in a correlated manner. This results in correlated electron pairs stemming from two different hadrons that originate from the same hard process. To simulate our background with NLO QCD accuracy ($\mathcal{O}(\alpha_S^3)$), we use the hvq [305] process in POWHEG BOX V2.

Both simulations, of the signal and of the background, are then interfaced with

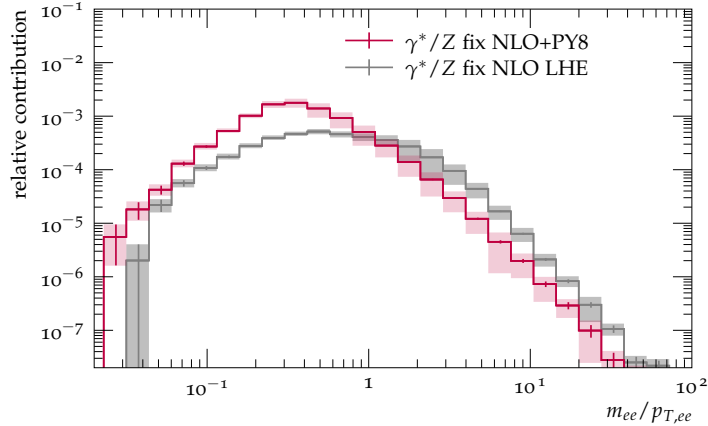


Figure 4.6: Relative contribution to the cross section of $m_{ee}/p_{T,ee}$ constellations in the signal process for pp.

PYTHIA 8.3.08. In the case of the signal, it only provides higher-order QCD and QED corrections in the soft-collinear approximation via PSs, while in the case of the background we rely on it also for the hadronisation and the heavy-flavoured hadron decays.

4.1.3 Simulation setup and event selection

In this section we focus on the production of di-electrons, open charm and bottom pairs in pp, proton-lead (pPb) and PbPb collisions at the LHC with $\sqrt{s} = 5.02$ TeV (per nucleon pair). The experimental pp and pPb data of the corresponding ALICE measurement [306] are available in HEPdata [307]. The ALICE data in PbPb were recently published [308], but the numerical values were not available in HEPdata at the time of this work. Unless otherwise stated in this chapter, we use MSHT20n1o [44] PDFs for the proton and nCTEQ15HQ [108] nPDFs for lead as given by LHAPDF6 with the corresponding value of $\alpha_S(M_Z)$.

We generate the Les Houches Event (LHE) samples with POWHEG BOX V2 and shower them using PYTHIA 8 piloted by the main-PYTHIA83-1hef executable, which is in turn coupled to Rivet 3.1.7 [309–311] and is based on the Rivet 2 interface originally developed in Ref. [312] and later updated for Rivet 3 in Ref. [313]. The relevant physical input parameters are chosen from Ref. [314] with

$$\alpha = 1/128.89, \quad m_c = 1.27 \text{ GeV}, \quad m_b = 4.18 \text{ GeV}.$$

While these are the $\overline{\text{MS}}$ values, technically the pole mass should be used in POWHEG BOX. The difference between the masses is quite significant, but flat and consistent within the uncertainties, as shown in Fig. 4.7. However, since we will later in Sec. 4.1.4.3 fit our distributions to the data the normalization does not matter. For the production of HQs, the renormalization and factorization scales are dynamically chosen as $\mu_r = \mu_f = \sqrt{p_T^2 + m_q^2}$, where $p_T \neq p_{T,ee}$ is the transverse momentum of the heavy quark and q denotes its flavour. For $c\bar{c}$ a three-flavour scheme is used, while for $b\bar{b}$ we use a four-flavour scheme. The corresponding running of α_S is calculated using internal

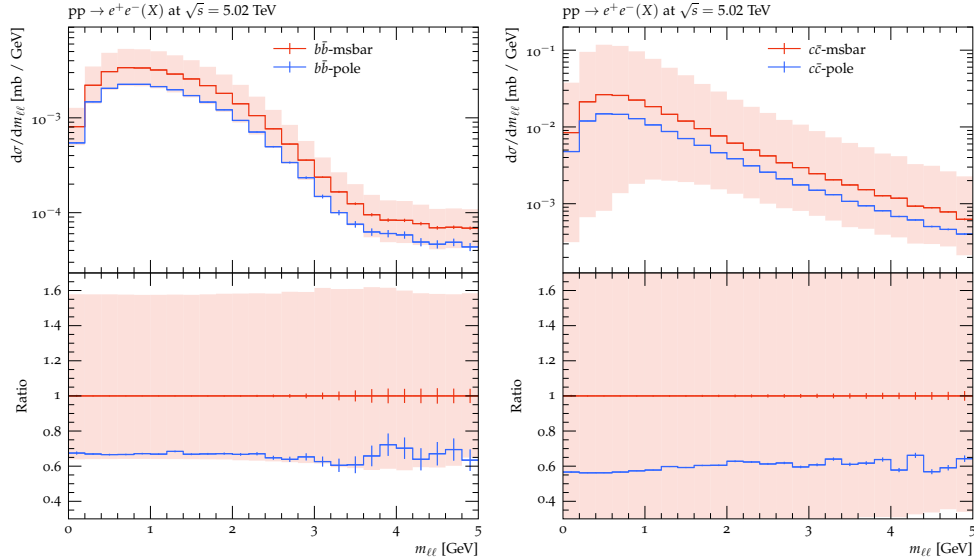


Figure 4.7: The pole mass m_{pole} and the $\overline{\text{MS}}$ mass $m_{\overline{\text{MS}}}$ of the charm and bottom quarks.

POWHEG BOX subroutines. For the DY process, we instead set the value of the renormalization and factorization scales to $\mu_r = \mu_f = \max\left(2 \text{ GeV}, \sqrt{p_{T,\gamma}^2 + p_\gamma^2}\right)$ with its minimum value frozen at 2 GeV and use a five-flavour scheme. In both cases, we calculate perturbative scale uncertainties using the standard factor-two seven-point μ_r, μ_f scale variation method, excluding relative factors of four. By freezing the scale at 2 GeV we can approach kinematics down to the lowest considered value of $\sqrt{p_{T,\gamma}^2 + p_\gamma^2} = 1 \text{ GeV}$, *i.e.* down to the point where perturbativity may break down. For very small photon virtualities, $p_{ee}^2 \sim p_\gamma^2 \rightarrow 0$, di-electron production can be related to prompt photon production through a FF [65] or the Kroll-Wada approach [285].

In PYTHIA8 we leave parton showers, hadronisation and multiple parton interactions (MPI) activated. Hadron decays are only enabled for our background predictions to avoid decay photons in our signal. Similarly, in heavy flavour production we turn off the QED shower, but leave it on for the production of virtual photons in order to generate the fragmentation contribution. To match to POWHEG, we use the standard procedure in which shower evolution starts unrestricted, but shower emissions are vetoed using `PowhegHooks`. In Tab. 4.2 we list the values of the PYTHIA8 parameters selected for each process.

Our event selection and histogramming of the observables is done by a Rivet analysis created, which mimics the analysis of Ref. [306]. We select all electrons and positrons that satisfy the acceptance cuts of $0.2 \text{ GeV} < p_{T,e} < 10 \text{ GeV}$ and $|\eta_e| < 0.8$ required by the central barrel geometry of ALICE. We then use the electron and the positron to construct the transverse momentum and virtuality of the pair, $p_{T,ee}$ and m_{ee} . As in the ALICE analysis, we consider the transverse momentum and invariant mass ranges $0 \text{ GeV} < p_{T,ee} < 8 \text{ GeV}$ and $0.5 \text{ GeV} < m_{ee} < 1.1 \text{ GeV}$ or $1.1 \text{ GeV} < m_{ee} < 2.7 \text{ GeV}$ for the di-electron pair. For the invariant mass spectra, we also consider the range $0 \text{ GeV} < m_{ee} < 7 \text{ GeV}$, which extends upon the ALICE measurement, which only available in the

PYTHIA setting	Zj	hvq
PartonLevel:ISR	on	on
PartonLevel:FSR	on	on
PartonLevel:MPI	on	on
PartonLevel:Remnants	on	on
PartonShowers:model	1	1
SpaceShower:pTmaxMatch	2	2
TimeShower:pTmaxMatch	2	2
POWHEG:veto	1	1
POWHEG:pTdef	1	1
SpaceShower:QEDshowerByL	on	off
SpaceShower:QEDshowerByQ	on	off
TimeShower:QEDshowerByGamma	on	off
TimeShower:QEDshowerByL	on	off
TimeShower:QEDshowerByOther	on	off
TimeShower:QEDshowerByQ	on	off
HadronLevel:Hadronize	on	on
HadronLevel:Decay	off	on

Table 4.2: Parameters used in PYTHIA for the different processes. Values that deviate from the default are highlighted in bold.

range $0 \text{ GeV} < m_{ee} < 3.5 \text{ GeV}$.

We remove the combinatorial background using the same-sign approximation, as in Ref. [269], where the raw pair signal S is obtained with the formula

$$S = \underbrace{(N_{+-})}_{\text{opposite-sign}} - R_{\text{acc}} \underbrace{(N_{++} + N_{--})}_{\text{same-sign}}, \quad (4.1.16)$$

where we estimate the number of same-sign pairs with an arithmetic mean, which is more suitable than a geometric mean when considering a contribution to the spectrum due to a single process, and where we set the relative acceptance correction factor, $R_{\text{acc}} \approx 1$. Furthermore, N_{+-} is the number of pairs with opposite sign and N_{++} , N_{--} are the numbers of positron-positron and electron-electron pairs in the signal region. Assuming that the same-sign pairs are uncorrelated, the subtracted term will correspond to the uncorrelated opposite-sign pairs at the high statistical limit. This gives the raw pair signal S with unwanted uncorrelated contributions removed.

To isolate the continuum contribution to open heavy flavour production from the HQ POWHEG BOX+PYTHIA8 sample, we classify electrons according to their origin. In Fig. 4.8 we show di-electron invariant mass spectra from $pp \rightarrow c\bar{c}(X)$ and $pp \rightarrow b\bar{b}(X)$ production. In both cases, below 1 GeV the spectrum receives contributions from heavy to light flavoured hadron cascade decays: $\pi^0, \rho^0, \eta, \omega, \eta', \phi$. Above 1 GeV, only the J/ψ peak at about 3 GeV is visible, while in between, in the IMR, the continuum dominates.

This inspires our definition of the continuum contribution to the hadronic cocktail as

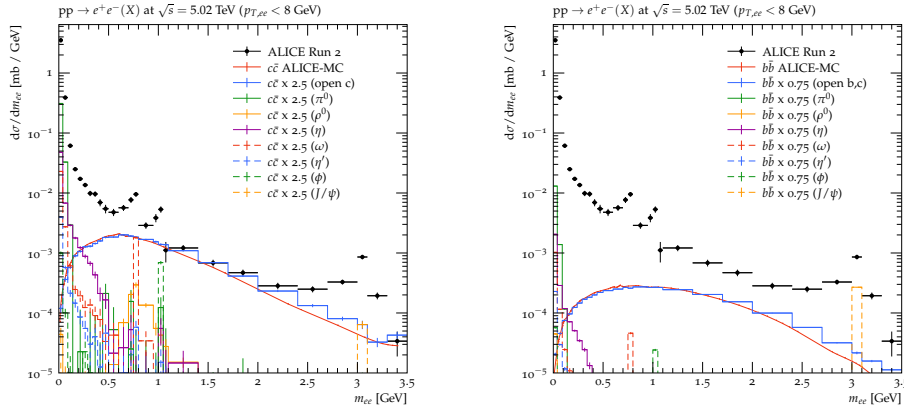


Figure 4.8: Di-electron mass spectra for the production of $pp \rightarrow c\bar{c}(X)$ (left) and $pp \rightarrow b\bar{b}(X)$ (right), decomposed into open heavy-flavour continuum and the resonance production in the LMR and IMR. All the contributions were normalized as in [306].

the POWHEG BOX+PYTHIA 8 subsample with electrons from light hadron and J/ψ decays filtered away. Practically speaking, we require that all leptons to have a parent particle that is either a hadron of flavour b or c by inspecting the HepMC [315, 316] event record in Rivet. It is worth noting that this implies that the hadron decay chains $b \rightarrow c \rightarrow e$ are not filtered out.³

This is meant to align with the definition used in ALICE, where contributions removed by filtering based on origin are instead obtained using the Monte Carlo Event Generator (MCEG) EXODUS [267]. Our predictions (blue histograms) reproduce very well the predictions of ALICE extracted from Ref. [306], $c\bar{c}(b\bar{b})$ ALICE-MC, which were obtained with POWHEG BOX+PYTHIA 6 and CTEQ6.6 [317] PDFs (red curves). We note that our predictions were normalized such that the area under the curve of our “open c ” and “open b ” predictions match the area under the “ $c\bar{c}$ ALICE-MC” and “ $b\bar{b}$ ALICE-MC” curves, respectively. This scaling procedure results in factors $f_{c\bar{c}} = 2.5$ and $f_{b\bar{b}} = 0.75$.

4.1.4 Our predictions

In Refs. [269, 270, 306] the production of di-electron pairs (e^+e^-) in pp collisions at $\sqrt{s} = (5.02, 7, 13) \text{ TeV}$ was measured with the ALICE detector at the LHC. The studies focused on the invariant mass and transverse momentum distributions of the e^+e^- pairs. The data was compared to a hadronic cocktail composed of expected di-electron distributions of known three dominant hadronic sources: light-flavour (LF) decays, the J/ψ resonance, and open heavy-flavour (HF) decays. A good agreement between the data and the hadronic cocktail was observed over the entire mass range ($m_{ee} < 3.5 \text{ GeV}$). However, the extracted total cross sections for charm and beauty depend strongly on details of the theoretical modelling (*e.g.* PYTHIA 6 vs. POWHEG BOX+PYTHIA 6). The same measurement was also performed for pPb collisions at $\sqrt{s_{NN}} = 5.02 \text{ TeV}$ [306]. Again, good agreement with the cocktail was found assuming the HF cross sections scale with the atomic mass number A of the lead nucleus in pPb-collisions with respect to the pp

³The source code of the analysis named after the HEPdata entry number is available at https://gitlab.com/APN-Pucky/rivet-ALICE_2020_I1797621.

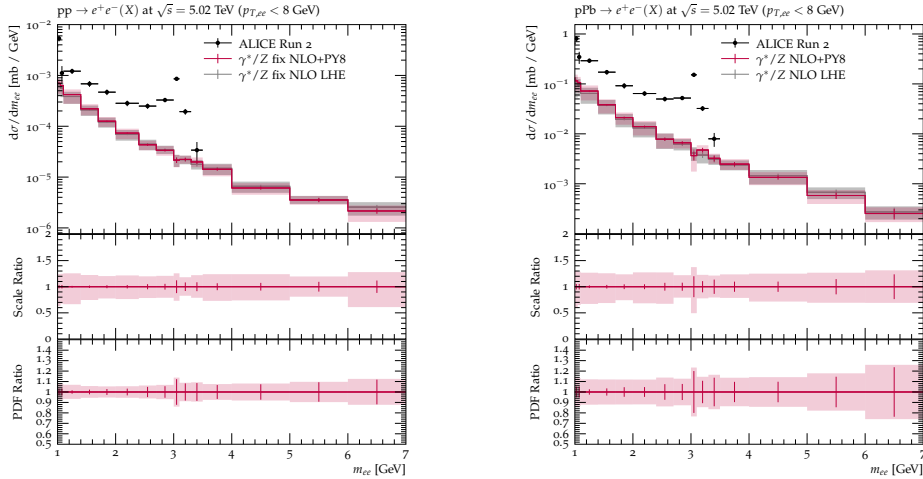


Figure 4.9: Di-electron pair invariant mass spectrum from virtual photon production in association with at least one jet at NLO+PS for pp (left) and pPb (right) obtained with POWHEG+Pythia8 using MSHT20n1o and nCTEQ15HQ PDFs for p and Pb. The uncertainty band combines scale and PDF uncertainties in quadrature. The second and third ratio panels respectively show the relative scale and PDF uncertainties independently.

reference. The measured ratio R_{pPb} , corrected for such A -scaling, is consistent with unity within uncertainties in the IMR, with most of the e^+e^- pairs originating from correlated open HF hadron decays. Therefore, the uncertainties on the measured $p_{T,ee}$ dependence of R_{pPb} are still too large to draw conclusions on the nuclear modification of HF production in pPb collisions. For PbPb collisions, ALICE has measured the e^+e^- spectra at $\sqrt{s_{\text{NN}}} = (2.76, 5.02)$ TeV [284, 308], but the former measurement is statistically limited. Also, here the cocktail with an additional scaling by $R_{\text{PbPb}}^{b,c \rightarrow e}$ due to final-state medium effects is in reasonable agreement with the data, despite neglecting the cold nuclear matter effects.

In this section we study two predictions that enter those analyses. First we present our predictions for the prompt component of the di-electron spectrum due to direct virtual photon production in Sec. 4.1.4.1. This contribution has so far not been considered in the ALICE measurements. Second we show our predictions for the open charm and bottom production, including a careful analysis of uncertainties from scale and PDF variations in Sec. 4.1.4.2. In Sec. 4.1.4.3 we analyse all our predictions together and assemble them into a new prediction for the hadronic cocktail with realistic uncertainties. Finally, Sec. 4.1.4.4 is dedicated to our predictions for PbPb collisions and a discussion on initial- and final-state matter effects.

4.1.4.1 The signal: direct virtual photon production

Fig. 4.9 shows the invariant mass spectra of the di-electron system, which originate from virtual photons produced in association with at least one jet in 5.02 TeV pp and pPb in collisions at NLO+PS in red and at the NLO LHE level in grey. The precision NLO LHE corresponds to a NLO prediction supplemented by the Sudakov form factor of

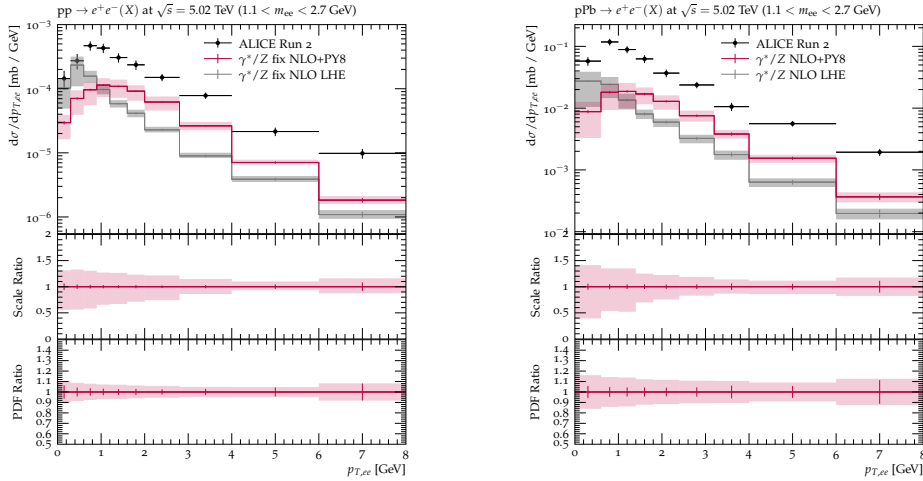


Figure 4.10: Di-electron pair transverse momentum spectrum from virtual photon production in association with at least one jet at NLO+PS for pp (left) and pPb (right) obtained with POWHEG+Pythia8 using MSHT20nlo and nCTEQ15HQ PDFs for p and Pb. The uncertainty band combines scale and PDF uncertainties in quadrature. The second and third ratio panels respectively show the relative scale and PDF uncertainties independently.

the NLO emission as described in Sec. 3.3.3.2. If one goes below an invariant mass of $m_{ee} = 1$ GeV, the cross section becomes less reliable due to the photon pole at $m_{ee} = 0$. It is therefore not surprising that the invariant mass spectrum increases continuously towards lower masses, see the top panels. The total uncertainties combined in quadrature are dominated by the variation of scales and are about $\pm 25\%$ across the whole invariant mass range, but up to $\pm 50\%$ in the low tail of the transverse momentum spectra (see below). In contrast, the PDF uncertainties are roughly $\pm 10\%$ for pp collisions and only a few percent more for pPb, see the third and the fourth panels. Note that the PDF uncertainty band beyond $m_{ee} > 3$ GeV likely overestimates the true PDF uncertainty, because this kinematic regime is difficult to populate with MC events and is therefore dominated by statistical uncertainties (shown as error bars). The difference between the sizes of the cross section of the different initial-states is a relative increase by $A = 208$ from pp to pPb. For the p_T spectrum in Fig. 4.10 we observe that the parton shower emissions beyond $\mathcal{O}(\alpha_S)$ soften the low tail and harden the high tail of the $p_{T,ee}$ spectrum (NLO LHE vs. NLO+Py8). Such a transformation into a more physical distribution is expected from matching to parton showers.

The virtual photon production is a subleading but not a negligible contribution to the di-electron pair production in this kinematic regime. It reaches fractions up to 45% in the range of 1.2 GeV to 3 GeV of the invariant mass spectrum, where the depletion at 3 GeV is due to the J/ψ contribution in the measured spectrum. Similarly, in the transverse momentum spectrum it contributes up to 40% in the intermediate p_T range of 1 GeV to 4 GeV. Note that our choice of scale, appropriate for this kinematic regime, enhances the virtual photon production cross section appreciably. With the inappropriate choice $\mu_f = \mu_r = m_Z$, this contribution would be only at about 5% with

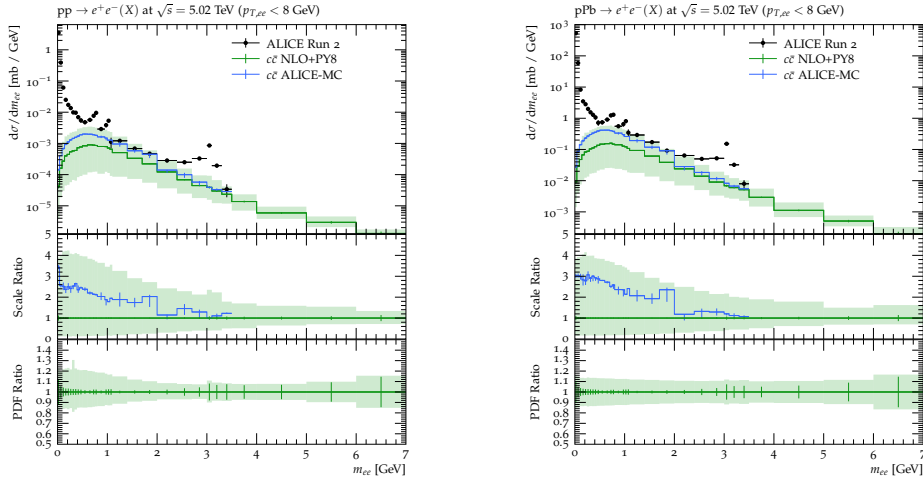


Figure 4.11: Invariant di-electron mass spectra in open charm production $pp, p\text{Pb} \rightarrow c\bar{c}(X)$ obtained with POWHEG BOX+PYTHIA 8 and MSHT20n1o and nCTEQ15HQ PDFs for p and Pb. The second row shows the scale and the third row the PDF uncertainties.

very similarly shaped distributions.

4.1.4.2 The background: open charm and bottom production

Next, we present our predictions for open charm and bottom production, again in pp and pPb collisions at $\sqrt{s} = 5.02$ TeV. The first rows of Figs. 4.11 and 4.12 respectively show the absolute predictions for the invariant mass and the transverse momentum spectra of di-electrons from open charm at NLO+PS in green. In the second rows we show the perturbative scale variations and generally observe very large uncertainties, presumably due to large logarithms related to the charm quark mass, which can exceed a factor of three regardless of the collision system. For di-electrons from open bottom production the situation is under much better control and the scale uncertainties drop under $^{+60\%}_{-40\%}$, see Figs. 4.13 and 4.14. The third rows in Figs. 4.11 to 4.14 show that the PDF uncertainty is small relative to the scale band and under $\pm 20\%$ ($\pm 10\%$) for the open charm (bottom) channel for both pp and pPb collisions throughout. Comparing the pp and pPb PDF uncertainties they increase slightly from pp to pPb in open bottom but not in the open charm production. This suggests that very low- x gluons in the nPDF fit (nCTEQ15HQ) have a smaller uncertainty than in the proton PDF fit (MSHT20n1o). A realistic estimate of the PDF uncertainty in pPb collisions should of course include both the proton and the nuclear uncertainty dimension, which is however not available in the nCTEQ15HQ fit.

We also compare our predictions with the calculations of POWHEG BOX+PYTHIA 6 (ALICE-MC), in blue, and data from ALICE [306], in black. The HF production is subleading in the LMR, but in the region in $m_{ee} \in [1, 2]$ GeV the open charm production almost saturates the data. The two predictions generally agree well. There are differences both in normalization and shape, but they agree within the scale uncertainty band of our prediction for both the open charm and open bottom channel, except for the tails of m_{ee} . The remaining differences in the shapes of the invariant mass distributions

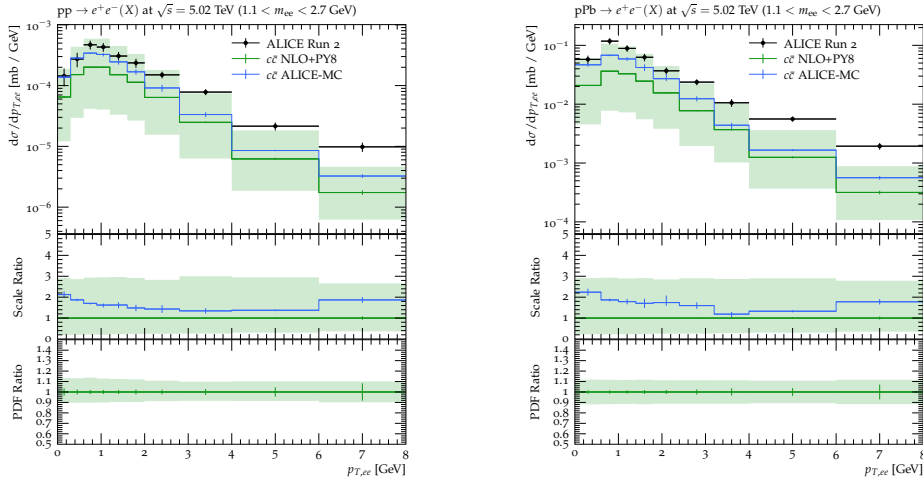


Figure 4.12: Di-electron transverse momentum spectra in open charm production $pp, p\text{Pb} \rightarrow e^+e^-(X)$ obtained with POWHEG BOX+PYTHIA 8 and MSHT20n1o and nCTEQ15HQ PDFs for p and Pb. The second row shows the scale and the third row the PDF uncertainties.

can be explained by the different hadronisation model in PYTHIA version 6 vs. version 8 and the use of different, in the case of our predictions, more modern PDF sets.

In the measurements of the di-electron spectra, the total $c\bar{c}$ and $b\bar{b}$ production cross sections are determined from the data. The normalization component of the uncertainty must thus not necessarily be taken into account. If we were to fix the normalization of each of the predictions in the scale or PDF variation bands, we would expect the uncertainty due to normalization to drop out and the uncertainty bands to shrink. The extent to which this happens will be examined in the next section.

We find that PYTHIA8 hadronises the charm quarks mainly to D^\pm (50%), D_0 (39%) and D_s^\pm (7%) hadrons, while the immediate parent particles of the electrons in open bottom production are mainly D^\pm (23%), D^0 (23%), B_0 (22%), B^\pm (20%), D_s^\pm (7%) and B_s^\pm (4%) hadrons.

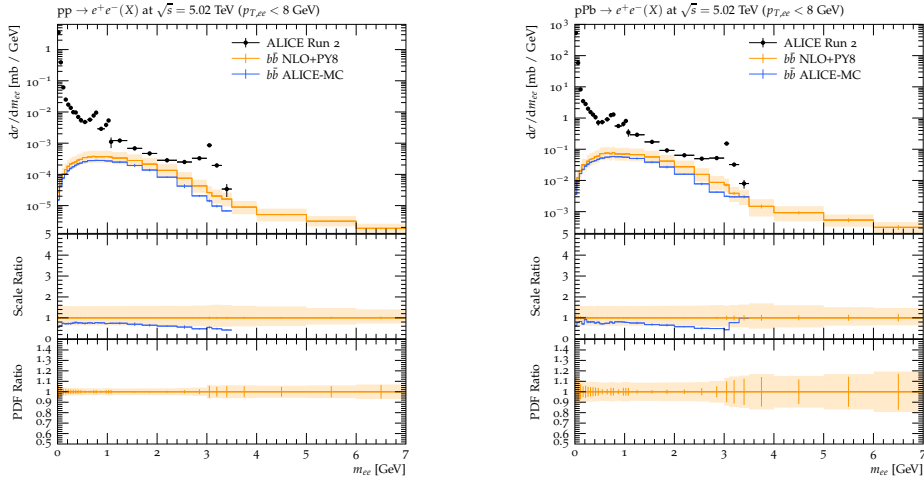


Figure 4.13: Invariant di-electron mass spectra in open bottom production $pp, p\text{Pb} \rightarrow b\bar{b}(X)$ obtained with POWHEG BOX+PYTHIA 8 and MSHT20n1o and nCTEQ15HQ PDFs for p and Pb. The second row shows the scale and the third row the PDF uncertainties.

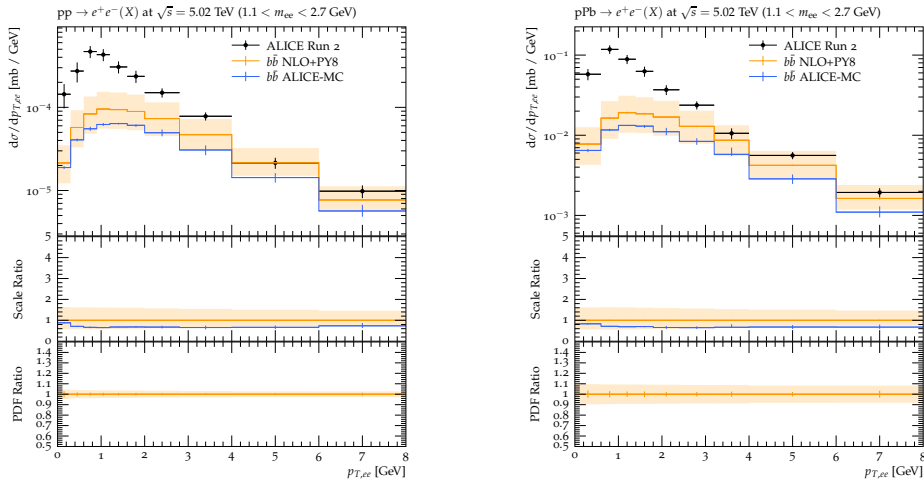


Figure 4.14: Di-electron transverse momentum spectra in open bottom production $pp, p\text{Pb} \rightarrow b\bar{b}(X)$ obtained with POWHEG BOX+PYTHIA 8 and MSHT20n1o and nCTEQ15HQ PDFs for p and Pb. The second row shows the scale and the third row the PDF uncertainties.

4.1.4.3 Combined analysis of the signal and background

In this section, we consider our new prediction for the virtual photon and the revised predictions for open HF production together. The first rows on both panels in Fig. 4.15 show our absolute predictions for virtual photon production in purple, $b\bar{b}$ in yellow and $c\bar{c}$ in green, while the third rows show their ratio to the largest channel ($c\bar{c}$). The normalization of the HF continuum is typically determined via double differential fits in m_{ee} and $p_{T,ee}$ in the intermediate mass regime [306] or via the measured and extrapolated total cross section [270, 318]. In this section, thus, we also normalize our predictions to the same cross sections that ALICE does, [306], by multiplying by the two overall normalizations factors, $f_{c\bar{c}}$ and $f_{b\bar{b}}$, for open charm and open bottom production respectively. We determine those factors to be $f_{c\bar{c}} = 2.5$ and $f_{b\bar{b}} = 0.75$. Similarly, we normalize the virtual photon contribution by a factor $f_{\gamma/Z} = 0.06$. This value will be explained in what follows. Such a normalization procedure also impacts our predictions for uncertainties. In fact, one needs to normalize each of our predictions in the seven-point scale or PDF variations individually. This means that the uncertainty due to normalization cancels out and only that due to change of shape remains. We observed that the different error sets of the PDF do not give a different shape and thus nearly vanish when normalized such that PDF uncertainties can be neglected. The $c\bar{c}$ contribution dominates across the whole m_{ee} and $p_{T,ee}$ range, with $b\bar{b}$ coming in second reaching up to 30% in the bin at 2 GeV in the invariant mass and up to 100% in the high tail of the transverse momentum spectrum. The virtual photon contributes under 10% across the whole range. The $c\bar{c}$ production yields an appreciably softer transverse momentum spectrum, dominating the low p_T region, as compared to the $b\bar{b}$ which starts to contribute significantly at around 2 GeV and eventually matches the $c\bar{c}$ channel. The shapes of the invariant mass spectra for the two heavy flavour production modes, instead, are relatively similar, except below $m_{ee} = 1.5$ GeV, where the bottom spectrum flattens out whereas the charm does not. Both the invariant mass and the transverse momentum spectra of the virtual photon contribution are relatively flat, as compared to those of open charm production. Thanks to our normalization procedure, the uncertainty bands are now significantly reduced, compared to Figs. 4.11 to 4.14. However, the remaining *shape* uncertainty, dominated by the scale variation, is still considerable especially in the $c\bar{c}$ channel where it goes from about $\pm 10\%$ at $m_{ee} = m_c$ to about $\pm 150\%$ in the high tail. This shape uncertainty is actually considerably larger than the statistical and systematic uncertainty as well as the uncertainty on the branching ratios into electrons for $c\bar{c}$ production, respectively, which were found to be 11%, 5% and 22% in a previous study by ALICE.

We now want to combine our predictions for the production of virtual photons and open HFs into a new prediction for the hadronic cocktail. To this end we start by isolating the contributions from LF and J/ψ from ALICE cocktail from Ref. [306], simply by subtracting the $c\bar{c}$ and $b\bar{b}$ ALICE-MC predictions bin-by-bin. We then sum all the contributions together, optionally including virtual photons, with a normalization for each contribution left as a free parameter, and perform several fits to all publicly available ALICE data in which we extract the values of $f_{c\bar{c}}$, $f_{b\bar{b}}$, $f_{LF+J/\psi}$ and $f_{\gamma/Z}$. Our fit results are summarized in Tab. 4.3. In the first column we report the results of the original ALICE fit, using the ALICE-MC predictions. The fit determines $f_{c\bar{c}} = 2.5$ and $f_{b\bar{b}} = 0.75$ and describes the data well with $\chi^2/\text{ndf} = 0.9$. We repeat this fit twice, first with all the data points in the LMR and in the IMR (*i.e.* one invariant mass spectrum in its full range and two transverse momentum spectra for each pp and pPb collisions)

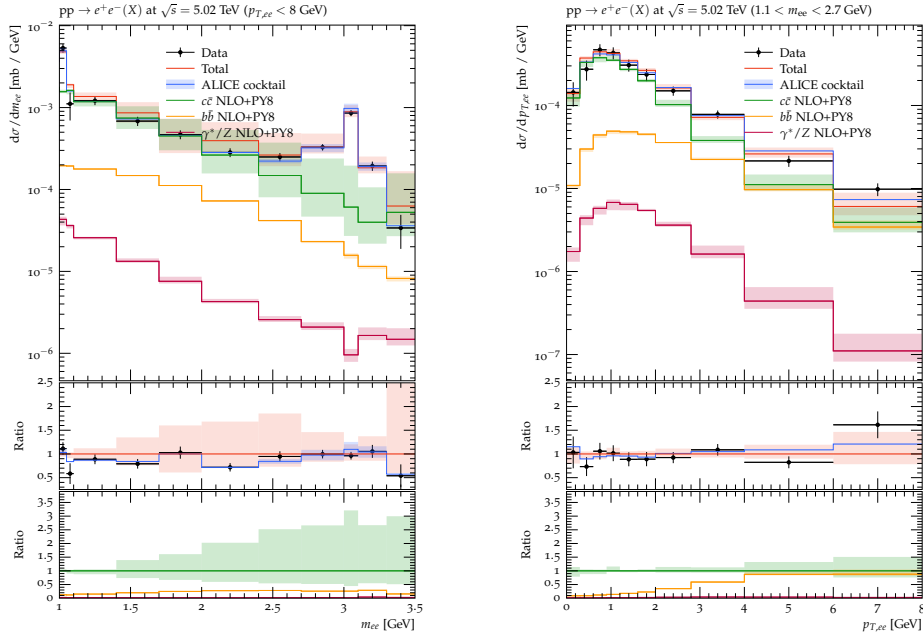


Figure 4.15: Comparison of the cocktail used by ALICE against our new cocktail including the DY process with an extra jet. The shaded band is the scale shape uncertainty. The blue shaded band on the cocktails is the uncertainty given by ALICE collaboration on their cocktail. The red shaded band combines scale shape and ALICE uncertainties.

we had access to (npts = 89 as compared to npts = 123 in the ALICE fit) and only our predictions for the background, and then the second time only in the IMR (npts = 53, *i.e.* one invariant mass spectrum in a reduced range and one transverse momentum spectrum for each pp and pPb collisions) but now also with our prediction for the virtual photons. Each time we offer two alternatives, one in which the shape uncertainties are not considered (“central”, $\chi^2 = \sum_i (x_i - m_i)^2 / \Delta m_i^2$) and one in which they are considered in a fully uncorrelated manner (“shape”, $\chi^2 = \sum_i (x_i - m_i)^2 / (\Delta m_i^2 + \Delta x_i^2)$). The uncertainties on the normalization coefficients f , reported in round brackets in columns 2 to 5 of Tab. 4.3, are the Hesse errors obtained from the χ^2 minimization by `iminuit` [319, 320]. The uncertainty on $\sigma_{c\bar{c}}$ and $\sigma_{b\bar{b}}$ in the first column, also reported in round brackets, are instead obtained by combining all uncertainties from Table 3 of Ref. [306] in quadrature. Correspondingly, the uncertainties on $\sigma_{c\bar{c}}$ and $\sigma_{b\bar{b}}$ in columns 2 to 5 are obtained by rescaling the uncertainty in column 1 by the ratio of the newly extracted cross section to that of column 1. In our first fit in columns 2 and 3, we get a very good data description with χ^2/ndf equal to 0.95 and 0.74, respectively. The normalization coefficient $f_{c\bar{c}}$ increases which in turn leads to an increase of extracted values of the $c\bar{c}$ cross sections from $756 \mu\text{b} \rightarrow 788 \mu\text{b}$ and to $888 \mu\text{b}$, respectively. The normalization coefficient $f_{b\bar{b}}$ is instead slightly decreased. The relative fit uncertainties on the normalization coefficients are small ($\sim 5\%$) as compared to the uncertainty on the total extracted cross section reported by ALICE ($\sim 25\%$) for the $c\bar{c}$ channel, but not for $b\bar{b}$ ($\sim 18\%$ to 25% vs. $\sim 14\%$). In our second fit in columns 4 and 5, the addition

of the virtual photon contribution pulls the fit back in the direction of the original fit in column 1 reducing the factor $f_{c\bar{c}}$ and increasing $f_{b\bar{b}}$. The fit prefers a smaller value of the virtual photon normalization of 23% and 6% that is however still compatible with 1.0 within 3σ , in particular in view of the fact that in this kinematic region with very small values of photon virtuality and transverse momentum, the dependence of the cross section on the choice of the factorization and renormalization scales is significant. Thus, the sensitivity to the virtual photon contribution is limited and strongly dependent on the uncertainties of the background contributions. All our fits prefer a reduced fraction of the light flavour and J/ψ contributions, more notably in fits that include the virtual photon contribution. Ultimately, however, the fact whether the *shape* scale uncertainty is included in the fit or not plays a more important role. All in all, the light flavour and J/ψ contribution is compatible with 1.0 within 2 standard deviations and in agreement with previous studies. Owing to the large branching ratio uncertainty the extracted charm and bottom cross sections are also compatible within one sigma across all five fits. In general, the inclusion of shape uncertainties increases these uncertainties for every fitting parameter, but most significantly, as expected, for $f_{c\bar{c}}$. The best description of the data, *i.e.* the smallest χ^2/ndf , is obtained in the fit that takes into account both the virtual photon and the shape uncertainties.

In Fig. 4.15, we compare our best prediction for the hadronic cocktail (corresponding to fit 2), denoted by Total and shown in red, with the hadronic cocktail from ALICE in blue, and with data in black. Our prediction for the hadronic cocktail agrees with the previous prediction from ALICE and describes the measurement well. Our central fit describes the data less well than the central fit from ALICE, deviating from the data by up to 30%, however only one point is more than 1σ away, not considering the theoretical uncertainties. However, our hadronic cocktail deviates from the one by ALICE considerably when it comes to uncertainties. Whereas ALICE's uncertainties are well below $\pm 5\%$ in the low tail increasing to about $\pm 10\%$ in the high tail, our uncertainties reach up to $\pm 50\%$ and almost never drop under $\pm 10\%$. This striking difference is due to the perturbative scale shape uncertainties in the $c\bar{c}$ production, which were not considered in the ALICE analysis. Including the contribution of the virtual photons does not significantly change the shape of the total result relative to the data uncertainties.

Finally, in Fig. 4.16, we show the ratios of our pPb and pp compared to those of ALICE and the data. Both ratios were obtained by simply dividing the pPb prediction by the pp prediction after appropriate rebinning. The R_{pPb} predictions agree very well across the entire range of the m_{ee} and $p_{T,ee}$ spectra, except in the first transverse momentum bin where our prediction is closer to the data. In the intermediate range of the invariant mass spectrum, our prediction has considerably larger uncertainties as a result of the open charm production scale shape uncertainties not completely cancelling in the ratio.

dataset	ALICE cocktail	LF+ J/ψ + $b\bar{b}$ + $c\bar{c}$		LF+ J/ψ + $b\bar{b}$ + $c\bar{c}$ + γ/Z	
	pp & pPb	pp & pPb		pp & pPb (no LMR)	
uncertainty	central	central	shape	central	shape
$f_{c\bar{c}}$	2.50	(2.61 ± 0.16)	(2.93 ± 0.19)	(2.35 ± 0.24)	(2.86 ± 0.31)
$f_{b\bar{b}}$	0.75	(0.60 ± 0.11)	(0.48 ± 0.12)	(0.63 ± 0.13)	(0.57 ± 0.15)
$f_{LF+J/\psi}$	1.0	(0.96 ± 0.03)	(0.93 ± 0.03)	(0.91 ± 0.06)	(0.88 ± 0.08)
$f_{\gamma/Z}$	-	-	-	(0.23 ± 0.17)	(0.06 ± 0.20)
χ^2/ndf	110.9/123	84.2/89	65.9/89	47.7/49	33.3/49
	0.90	0.95	0.74	0.97	0.68
$\frac{d\sigma_{c\bar{c}}}{dy} _{y=0}$ [μb]	(756 ± 188)	(788 ± 196)	(888 ± 221)	(709 ± 176)	(866 ± 215)
$\frac{d\sigma_{b\bar{b}}}{dy} _{y=0}$ [μb]	(28 ± 5)	(22 ± 3)	(22 ± 3)	(24 ± 3)	(21 ± 3)

Table 4.3: Different normalization parameters f , χ^2/ndf and HQ cross sections for the different combinations of processes contributing to di-electron production obtained from a fit with `iminuit` [319, 320].

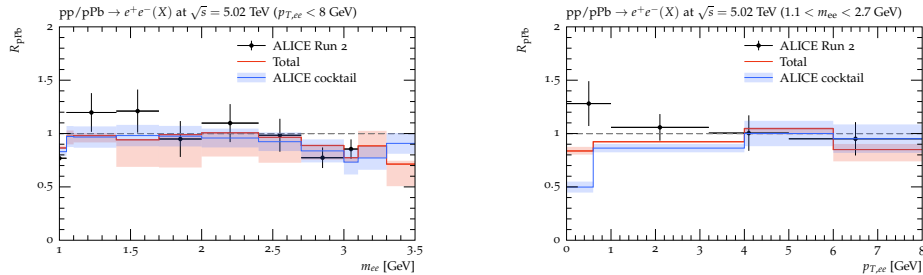


Figure 4.16: R_{pPb} in invariant mass (left) and transverse momentum (right) for the total cocktail. For the total curve the uncertainty band are correlated scale uncertainties of the $c\bar{c}$, $b\bar{b}$ and Zj process. The uncertainty band of the ALICE cocktail is computed solely from the lead uncertainty given by ALICE in the nominator of the ratio.

4.1.4.4 Initial- and final-state nuclear effects in PbPb collisions

In this section we focus on PbPb collisions at 5.02 TeV. We start by comparing our predictions for open heavy flavour production to ALICE-MC predictions and data in Figs. 4.17 and 4.18 for di-electron invariant mass and transverse momentum spectra. Whereas in the previous sections we compared measured cross sections to cross section predictions, here we compare yields to cross section predictions, because a cross section measurement is thus far not available. Instead of dividing by N_{coll} obtained from the Glauber model as we did in Ref. [3], we normalize our predictions to the ALICE-MC predictions in PbPb collisions from Ref. [308].

As before our predictions for open charm agree with ALICE-MC within the uncertainties, but those for open bottom don't, because the scale uncertainties, now stripped off the normalization component, are significantly smaller. Note that the shape difference between the two predictions may be exaggerated because our prediction does not take into account potential kinematic dependence of the detector acceptance. While the normalized scale uncertainties are very similar to those in pp and pPb collisions, replacing both proton beams by lead markedly increases the PDF uncertainties, as one would expect. The resulting nuclear PDF uncertainty of about $\pm 30\%$ ($\pm 20\%$) is no longer the subleading in the open bottom production. Finally, we also note that in the last bin of the transverse momentum spectrum of PbPb collisions in Fig. 4.14 both predictions exceed the ALICE data.

The excess of our predictions over the data in the high p_T region point to further nuclear effects. In fact there is another important correction to the processes $\text{PbPb} \rightarrow c\bar{c}(X), b\bar{b}(X)$, namely in Ref. [321] a suppression of hadronic decays involving transitions $c \rightarrow e$ and $b \rightarrow e$ was measured relative to pp collisions, *i.e.* $R_{AA}^{c/b \rightarrow e}(p_T) < 1$ [322]. This correction depends on the centrality and can give a reduction of up to 50% in collisions of centrality 0% to 10% and 30% to 50% and the effects disappear in collisions of centrality 60% to 80%. The inclusion of this final state effect is multiplicative and due to the dependence on p_T it does not only affect the normalization but also the shape of the distribution. Similar effects for R_{pA} are possible, but have not yet been measured with sufficient precision [321]. Fig. 4.19 shows the effect of including this nuclear modification factor $R_{AA}^{b,c \rightarrow e}$ on $b\bar{b}$ production in 0% to 10% centrality collisions. The resulting p_T spectra no longer exceed the data for large p_T , while the relative shape uncertainty remains almost unchanged. The correction by a factor of 2 to 3 is well above the largest source of uncertainty so far, which are the PDFs, as we have seen in the PbPb case in Fig. 4.18. The inclusion of such a factor and its uncertainty is therefore necessary to obtain a reliable prediction for the $b\bar{b}$ production in PbPb collisions, especially if the normalization is to be determined by a fit.

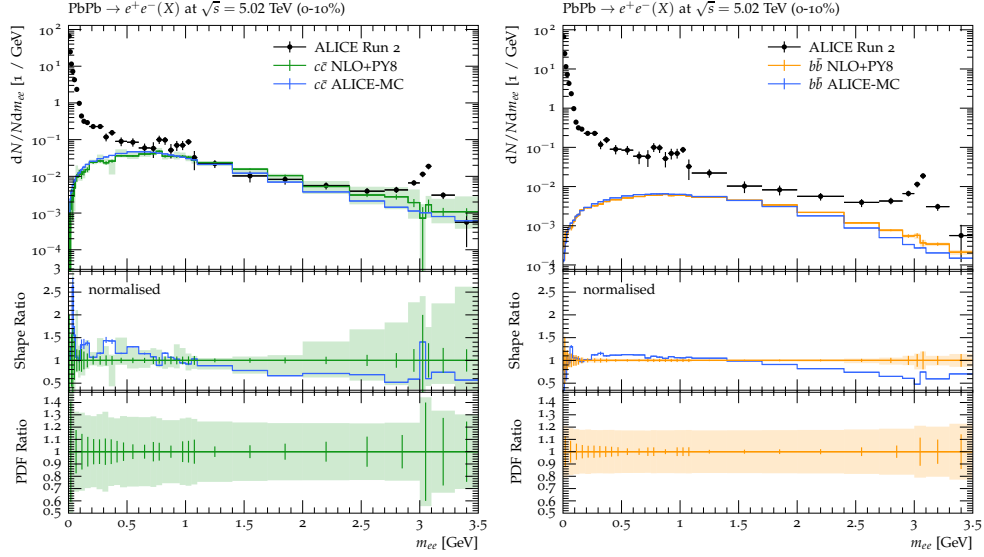


Figure 4.17: Invariant mass spectrum to open charm production $\text{PbPb} \rightarrow c\bar{c}(X), b\bar{b}(X)$ using POWHEG BOX and PYTHIA with nCTEQ15HQ as PDFs. The area of the green and orange curves is normalized to the ALICE-MC prediction. The second row is scale shape uncertainty and the third row is normal PDF uncertainty.

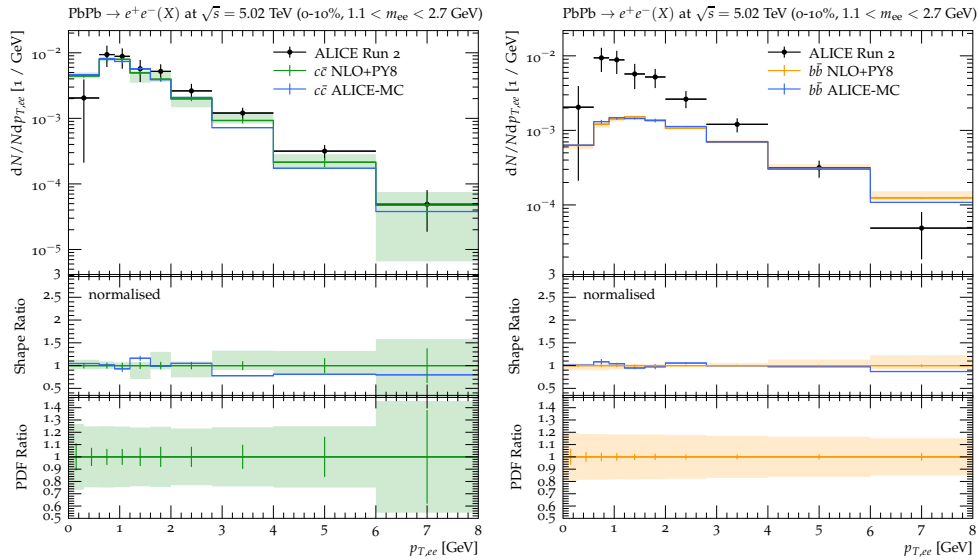


Figure 4.18: Transverse momentum spectrum in the intermediate invariant mass region to open charm production $\text{PbPb} \rightarrow c\bar{c}(X), b\bar{b}(X)$ using POWHEG BOX and PYTHIA with nCTEQ15HQ as PDFs. The area of the red curve is normalized to the ALICE-MC prediction. The second row is scale shape uncertainty and the third row is normal PDF uncertainty.

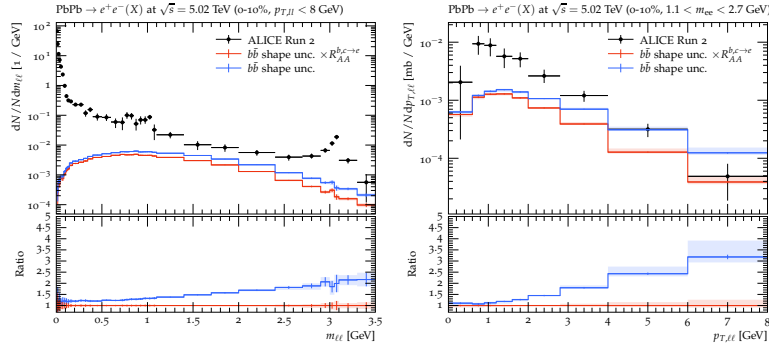


Figure 4.19: Open bottom production $\text{PbPb} \rightarrow e^+e^-(X)$ with and without including a $R_{AA}^{b,c \rightarrow e}$ factor. Both curves use a different normalization to ALICE-MC predictions. The lead nPDF in use is nCTEQ15HQ.

4.2 Real photon production

If we omit the splitting of the photon into an e^+e^- pair, the Feynman diagram in Fig. 4.5i becomes the annihilation process in Fig. 4.20 and the final-state contains a prompt on-shell photon. Processes involving prompt photons, such as their production in association with jets, provide a unique opportunity to study the distribution of gluons in nuclei due to their production mechanism via quark-gluon Compton scattering ($gq \rightarrow \gamma q$) [286, 323]. The gluon density becomes especially large at low values of Bjorken- $x \sim 2p_T^2/\sqrt{s}$ and scale $Q \sim p_T^2$, where at some point saturation may occur [324, 325]. The knowledge of precise distributions of parton momenta within a nucleon, described in the framework of collinear factorization by PDFs, is crucial for precise simulations of high-energy collisions.

Early prompt photon calculations were performed at the next-to-leading-logarithmic (NLL) accuracy without the inclusion of fragmentation [326] and later at NLO in the small-cone approximation [327] relying on MC methods. Following them, a new calculation released under the name of **JetPhox** [70–72] was published improving on the aforementioned shortcomings by including the direct and fragmentation contributions without any approximations. NNLO calculations for direct photon production have been performed in MCFM [328–331] and NNLOJET [78, 332] but are unfortunately not yet publicly available.

Complementary to the above calculations, the NLO **POWHEG BOX** implementation in Ref. [300] does not rely on fragmentation functions but instead consistently attaches a PS to the generated events, allowing for more realistic studies of photon-jet correlations and photon fragmentation. Additionally, merging techniques, such as those used in the **Sherpa** framework, have advanced the accuracy of isolated photon simulations by incorporating multiple parton emissions described by exact matrix elements [90, 91]. **Sherpa** achieves NLO QCD matched to PS precision for the $2 \rightarrow 3$ production process of a photon with two jets. Recently, even higher-order corrections to γjj production at NNLO has been achieved, further enhancing the precision of theoretical predictions [333].

There have been many experimental studies of isolated prompt photon production at the Super Proton-antiproton Synchrotron (Spps), Tevatron, RHIC and the LHC as

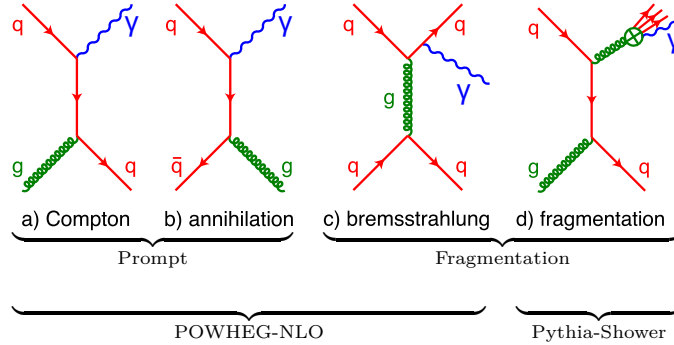


Figure 4.20: Feynman diagrams for direct photon production. Figure adapted from [116].

outlined in Ref. [115]. In Fig. 4.21 we see that also the transverse momentum distribution of direct photons separate the different phases in a heavy-ion collision. The prompt photons describe the initial hard scattering at high p_T and the thermal photons the later stages of the collision at low p_T . The pre-equilibrium photons contribute most inbetween. With current models there is however still an excess at low p_T . Pioneering High Energy Nuclear Interaction eXperiment (PHENIX) [336] and ALICE [337] not only measure low transverse momenta ($\lesssim 100$ GeV) direct photons, but they also study low invariant mass dilepton pairs originating from virtual photons [267, 269]. Typically, the yield of di-electrons with $m_{ee} \leq 1$ GeV has been computed by applying the Kroll-Wada prescription to real photon production [285]. A Toroidal LHC Apparatus (ATLAS) [338] and Compact Muon Solenoid (CMS) [339] extend their search up to the TeV scale. We will also compare our new predictions with the ATLAS measurement of isolated-photon plus two-jet production in pp collisions at $\sqrt{s} = 13$ TeV [340].

This section is structured as follows. We first discuss the POWHEG method and its application to prompt photon production in association with one jet at NLO in Sec. 4.2.1. Then it is extended to the production of a photon in association with two jets at NLO in Sec. 4.2.2 based on the publication [5]. Then we present our simulation setup and discuss the results of our calculations in Sec. 4.2.3.

4.2.1 Prompt photon production with one jet

In Fig. 4.20 exemplary Feynman diagrams for direct photon production with at least one jet are shown. The prompt photons also come from either Compton and annihilation processes and fragmentation photons from bremsstrahlung or gluon/quark fragmentation. As can be seen from the figure, going beyond leading order the definition of fragmentation photons becomes ambiguous as the splitting $q \rightarrow q\gamma$ can also be attributed to the real correction. Tab. 4.4 orders prompt photon production by the couplings and shows which processes are included in the calculation highlighted in grey.

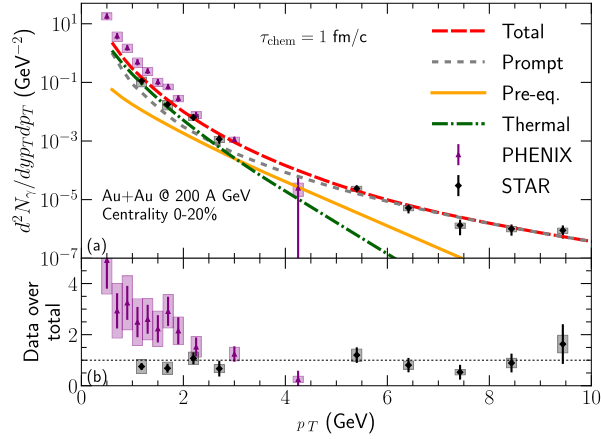


Figure 4.21: Direct photons in gold-gold (AuAu) in central events at RHIC [280, 334]. The data is compared against different theoretical contributions [335].

Born	$pp \rightarrow \gamma j \sim \mathcal{O}(\alpha\alpha_S)$		$pp \rightarrow jj \sim \mathcal{O}(\alpha_S^2)$	
Virtual	$\mathcal{O}(\alpha\alpha_S) \cdot \mathcal{O}(\alpha)$	$\mathcal{O}(\alpha\alpha_S) \cdot \mathcal{O}(\alpha_S)$	$\mathcal{O}(\alpha_S^2) \cdot \mathcal{O}(\alpha)$	$\mathcal{O}(\alpha_S^2) \cdot \mathcal{O}(\alpha_S)$
Real	$pp \rightarrow \gamma\gamma j \sim \mathcal{O}(\alpha^2\alpha_S)$	$pp \rightarrow \gamma jj \sim \mathcal{O}(\alpha\alpha_S^2)$		$pp \rightarrow jjj \sim \mathcal{O}(\alpha_S^3)$

Table 4.4: Processes contributing to prompt photon production in association with one jet at NLO. Only the greyed out processes are included in the calculation.

4.2.1.1 The POWHEG method as an alternative to fragmentation functions

In Sec. 2.2.6 we have seen that the factorized photon-hadron production cross section with untagged final-state X reads

$$\begin{aligned}
 d\sigma_{AB \rightarrow \gamma X}(p_A, p_B, p_\gamma) &= \sum_{a,b,c} \int_0^1 dx_a dx_b dz f_{a/A}(x_a, \mu_{F_i}) f_{b/B}(x_b, \mu_{F_i}) \\
 &\quad d\hat{\sigma}_{ab \rightarrow cX}(x_a p_A, x_b p_B, \frac{P_\gamma}{z}, \mu_R, \mu_{F_i}, \mu_{F_f}) D_{\gamma/c}(z, \mu_{F_f}),
 \end{aligned}
 \tag{4.2.1}$$

where one sums over the intermediate initial and final-state partons and convolves the PDFs $f_{a/A}$, picking parton a from hadron A , and FFs $D_{\gamma/c}$, fragmenting parton c to a photon, with the partonic cross section $d\hat{\sigma}_{ab \rightarrow cX}$. The pieces are connected through the renormalization scale μ_R and factorization scale in the initial-state μ_{F_i} and final-state μ_{F_f} . The partonic cross section $\hat{\sigma}$ is not IR safe for identified partons however the factorization theorems cancel these universal collinear divergences [27]. Alternatively one can use a parton shower to model the fragmentation, which is the path we pursue in this work. Advantages of the parton shower include more flexibility, customized tuning for QGP effects like jet quenching and energy loss and simulations beyond just the transition to the final-state photon.

In NLO calculations within the framework of perturbative quantum field theory, the amplitude for a given process includes contributions from n -particle states, comprising both the Born contribution and the virtual corrections, as well as $n + 1$ -particle states

due to real emission processes. The POWHEG method effectively integrates the first radiation emission into the n -particle state. This integration is achieved by employing a modified Sudakov form factor, $\Delta_R(p_T)$, which is defined as follows

$$\Delta_R(p_T) = \exp \left[- \int d\Phi_R \frac{R(\Phi_B, \Phi_R)}{B(\Phi_B)} \theta(k_T(\Phi_B, \Phi_R) - p_T) \right], \quad (4.2.2)$$

of Eq. (3.3.21) where the integration spans the real emission $n + 1$ phase space Φ_R , and the ratio of the real emission correction to the Born amplitude, $R(\Phi_B, \Phi_R)/B(\Phi_B)$, stands in for the emission probability modulated by a Heaviside step function θ prohibiting emissions below the transverse momentum scale p_T . To maintain NLO accuracy with this modified factor, one must ensure that the subsequent PS generates radiation only below the established scale p_T . In the LHE standard [341] this scale of the hard process is defined as the `SCALUP` parameter and the PS uses it as starting point to attach softer emissions [61]. In a p_T -ordered parton shower, this is achieved by starting at a given scale, while in angular-ordered PS, a veto algorithm is employed [63].

In POWHEG, the process of attaching an emission to a leading-order contribution is managed through a probabilistic method involving the transverse momentum of the emission, in analogy to SMCs in Sec. 3.2.5. The procedure starts with the determination of p_T via a randomly selected value $r \in (0, 1)$, which is used to compute

$$\log \Delta^U(p_T) = \log(r), \quad (4.2.3)$$

where $\Delta^U(p_T)$ represents the lower bound of the Sudakov form factor from Eq. (4.2.2). The lower bound is obtained by replacing the ratio of Real and Born $f \sim \frac{R}{B}$ by an upper bounding function U . The emission at given p_T is then subjected to an acceptance probability $P_{\text{acc}} = \frac{f}{U}$. Should the emission not meet the acceptance criteria, it is rejected with a probability of $1 - \frac{f}{U}$, and the procedure is repeated for a decreased p_T value. This iterative process continues until either the emission is accepted or the threshold defined as Λ_{QCD} is reached.

The POWHEG method in junction with a PS can also be used as an alternative to the FF approach. The NLO real photon production at $\mathcal{O}(\alpha\alpha_s^2)$ in POWHEG comprises two primary contributions: events with an underlying photon and a parton, and events with underlying two partons. The first category represents the true direct photon contribution, which includes the $q\bar{q} \rightarrow \gamma g$ (annihilation) or $gq \rightarrow \gamma q$ (Compton scattering) processes. The second category involves the dijet process, which contributes to the fragmentation component. NLO events are generated from these two contributions in the following ways. For the direct photon contribution, POWHEG may attach a gluon, setting the `SCALUP` to the transverse momentum of the gluon. Alternatively, it may split a gluon into a quark-antiquark pair, with the `SCALUP` set to the p_T of one of the quarks, or attach nothing, setting the `SCALUP` to a value of perturbative cutoff at approximately 1 GeV. It is important to note that $\gamma \rightarrow q\bar{q}$ splitting remove photons from the final-state, thus affecting observables that tag photons only at higher-orders, particularly if the photon is regenerated through QED showers. For the dijet contribution, POWHEG may attach a photon, setting the `SCALUP` to the photon's p_T . QCD radiation on top of dijet events, which do not initially include photons, contributes at higher-orders if the photon is regenerated through QED showers. We do not include such QCD real corrections to the underlying QCD Born events. The inclusion of underlying dijet events is solely for the purpose of subtracting the collinear singularity

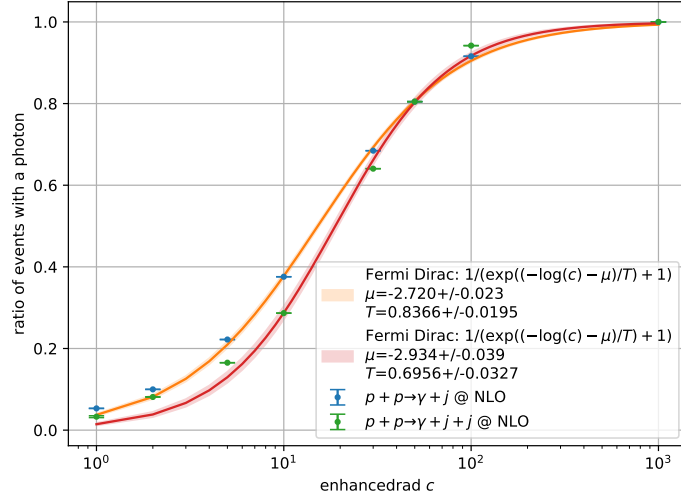


Figure 4.22: Ratio of events with a photon at the LHE level, *i.e.* before the parton shower, for different values of the `| enhancedrad |` parameter c .

and is not intended for a fragmentation function-like convolution. The remainder of the fragmentation contributions is included by the PS.

4.2.1.2 Enhanced QED radiation

Above treatment has a caveat, as attaching a photon to a parton is suppressed by the electromagnetic coupling constant α , this will happen at a very small rate. Consequently, most of the events generated will be dijet-like events, with few events containing photons in the final-state. Therefore, in Ref. [300] the `enhancedrad` parameter c was introduced to increase the ratio of generated events with photons. As the same problem remains for the process with one extra jet we repeat the same procedure again in analogy to [342] and similar to PYTHIA's `Enhance` -options [343]. The probability of attaching a photon is increased by modifying Eq. (4.2.3) to

$$\log \Delta^{cU}(p_T) = \log(r) \quad \Leftrightarrow \quad \log \Delta^U(p_T) = \frac{\log(r)}{c}, \quad (4.2.4)$$

where a constant c , $c > 1$, is introduced to increase the probability of attaching a photon. Finally, the event's weight has to be adjusted for all previous n rejected emissions

$$w_n = \frac{1}{c} \prod_{i=1}^n \frac{1 - \frac{f_i}{cU_i}}{1 - \frac{f_i}{U_i}}. \quad (4.2.5)$$

This allows us to increase the ratio of photons in typical events from $\approx 5\%$ at $c = 1$ to $\approx 30 - 40\%$ at $c = 10$ up to 90% at $c = 100$ in exchange for reduced weights. In Fig. 4.22 the ratio of photons in the final-state is shown for different values of c which showed a Fermi-Dirac like behaviour.

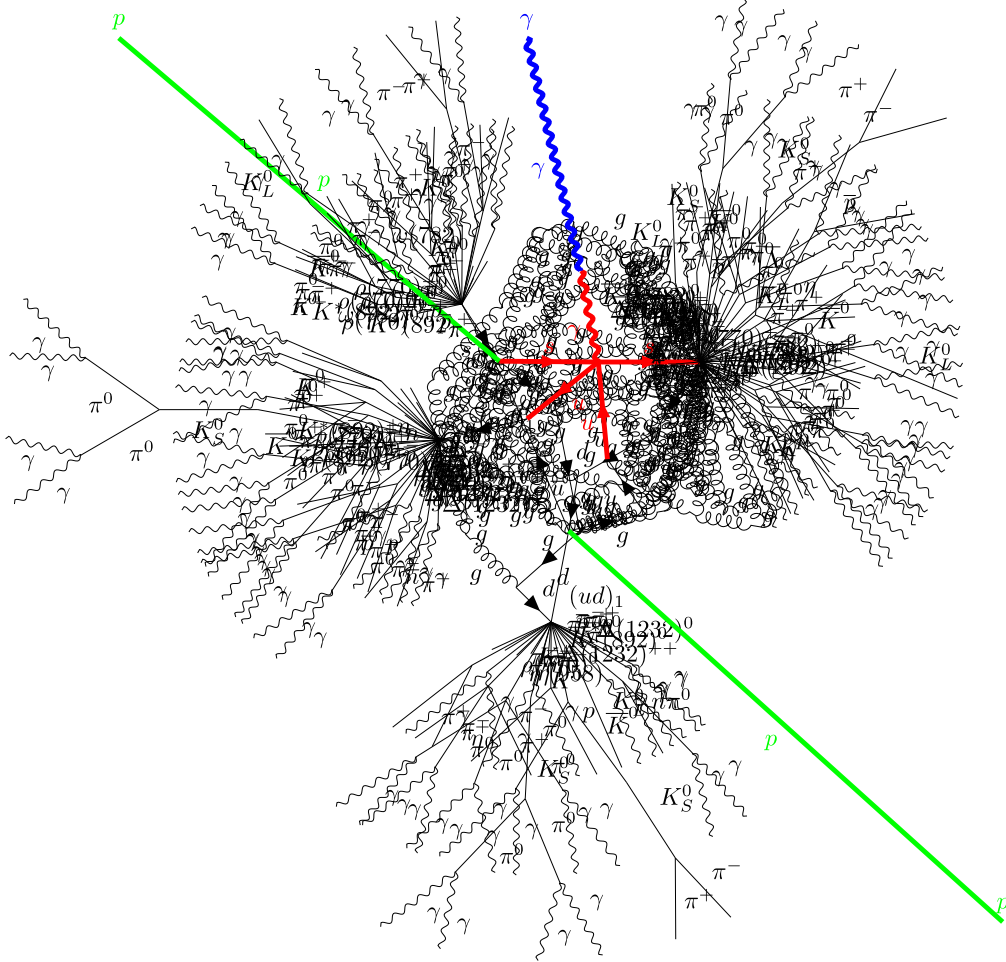


Figure 4.23: Exemplary generated POWHEG BOX NLO event with PYTHIA as PS. Figure generated with [7].

4.2.1.3 Example event

The Feynman diagram in Fig. 4.23 illustrates a fully generated pp event, incorporating parton shower effects and hadron decays. In this event, the colliding partons are represented in green, while the hard process, which is the primary high-energy interaction, is depicted in red and compressed into a single vertex⁴ (a $2 \rightarrow 3$ NLO event). A real photon, generated from the interaction, is coloured in blue. The transition from the red photon to the blue photon is due to PYTHIA's momentum rebalancing. Additionally, the event features numerous π^0 meson decays originating from the jets, which subsequently decay into even more photons, contributing to the complexity of the particle cascade. These photons are not easy distinguishable within the detector, blending into the overall

⁴This is the LHE output generated by POWHEG BOX. Since it integrates over the Feynman diagrams contributing to a specific final-state they can not be discerned. It is also not possible to display the interference of diagrams in a single event-like picture.

photon distribution. Although these photons do not originate from fragmentation processes, they are still filtered by isolation criteria typically used to separate signal photons from background contributions. This visualization highlights the intricate nature of particle interactions and the resulting shower of particles and decay products following a high-energy collision. The Feynman diagram representation does not consider momenta or clustering effects. Interestingly however, just a 2D-graph spring tension minimisation between the vertices to visualize the event already shows jet like formations. In this visualization, the ISR is evident since the green proton is not directly linked to the red hard process. The splits into an up quark entering the hard process and beam remnant $(ud)_1$.

4.2.1.4 Forward Calorimeter

As an example application of the direct photon code we will look at the FoCal experiment. The FoCal is a cutting-edge detector that will be installed in the ALICE experiment during the Long Shutdown 3 of the LHC [116]. Designed to explore the frontier of QCD, FoCal aims to measure the gluon density in protons and nuclei at very small values of the Bjorken scaling variable x and the squared momentum transfer Q^2 . At these small x values, where the gluon density becomes extremely high, interesting nonlinear QCD phenomena, such as gluon saturation, are expected to occur. These measurements are crucial for understanding the behaviour of strongly interacting matter under extreme conditions, such as those found in the early universe and inside neutron stars. FoCal's ability to study ultraperipheral collisions, long-range correlations, and the transition to the QGP makes it an essential tool for probing the fundamental aspects of QCD.

FoCal consists of two main components: first the thinner electromagnetic calorimeter and then the larger hadronic calorimeter. These detectors will be located approximately 7 meters from the interaction point of ALICE, providing unique capabilities for studying forward physics, where particles are produced at small angles relative to the beam direction.

Similarly to Sec. 4.1.1 a customized phase space sampling helps to generate events with a photon in the forward region. Within POWHEG BOX this is equivalent to optimizing the `bornsuppression` routine. Predictions for isolated prompt photons in the FoCal experiment at $\sqrt{s} = 14$ TeV are shown in Fig. 4.24. The cuts applied on the photon are $3.4 < \eta^\gamma < 5.8$ with a fixed isolation cone of $R_{\text{iso}} = 0.4$ and $E_T^{\text{iso}} = 5$ GeV. Generating such forward events in either requires simulating many events (most of which get discarded by the cuts) or modifying the phase space generation/born suppression in the POWHEG BOX code. The mixed production channel qg outweighs the qq and gg channel, but gg rises faster towards small p_T^γ . Further, the LO PYTHIA calculation underestimates the gg channel compared to NLO POWHEG BOX. The combination of POWHEG BOX+PYTHIA increases the cross section in the low p_T^γ regime by a few percent, but this effect is overshadowed by the numeric uncertainties as shown by the vertical bars. Fig. 4.25 shows the distribution of x_g and Q for the same process and confirms that the forward region of FoCal's prompt photons probes low x and Q .

4.2.2 Prompt photon production with two jets at NLO

Next, we present a new calculation of prompt photon production with two jets at NLO QCD matched to PSs using the POWHEG method [63, 188]. Extending the existing

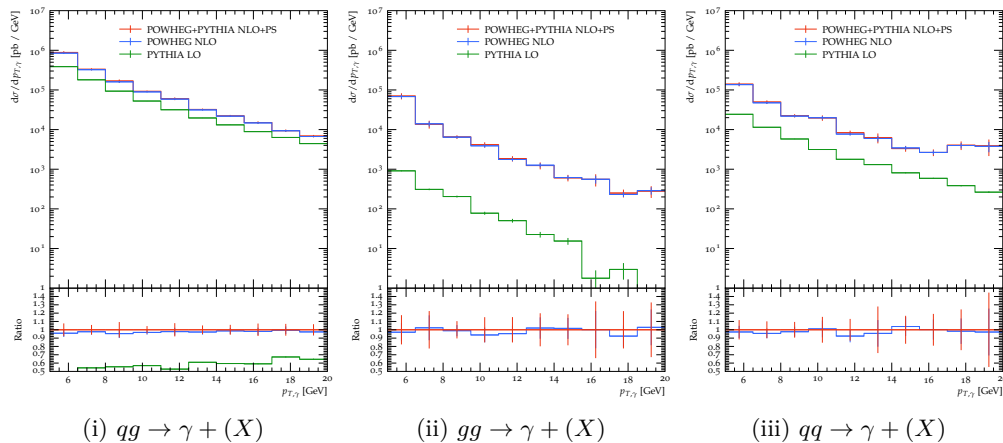


Figure 4.24: Predictions for isolated prompt photons in the FoCal experiment at $\sqrt{s} = 14$ TeV. The cuts applied on the photon are $3.4 < \eta^\gamma < 5.8$ with a fixed isolation cone of $R_{\text{iso}} = 0.4$ and $E_T^{\text{iso}} = 5$ GeV. The vertical bars represent the numerical uncertainties.

POWHEG BOX [189] direct photon calculation [300] by one jet is a significant advancement for several reasons. Firstly, incorporating the second jet at NLO improves the accuracy of the photon plus jet calculations by providing a more precise depiction of the event, reducing theoretical uncertainties. It also enables the study of jet-jet correlations within this process, offering new insights into the dynamics between jets in the presence of a direct photon. Moreover, the simulation allows for a detailed analysis of scenarios where a photon traverses a jet, including cases where the photon lies within the jet cone, which is crucial for understanding jet-photon interactions and isolation criteria. Lastly, this calculation enhances the capability to examine the ratio of Z +jets to γ +jets, thus improving background estimations in searches for new physics in $Z \rightarrow \nu\bar{\nu}$ decays [344].

Building upon our previous work on prompt photon production in association with a single jet at NLO [300] in the POWHEG BOX V2 framework, we now perform the calculation of the process with an additional jet. The concepts and methods used in the calculation are similar to the ones used in the single jet case, however, the complexity of the calculation increases with the number of final-state particles. In the subsequent sections, we will review the concept of the POWHEG method, detail the calculation of the process $pp \rightarrow \gamma jj$ at NLO, and describe the implementation of this calculation in POWHEG BOX V2. Particular attention will be given to differences with respect to our previous calculation.

4.2.2.1 Phase space

For the definition of the phase space, we adopted the multi-channel phase space construction from the topologically similar `trijet` [187] process in POWHEG BOX V2. This in turn builds on the phase space of the POWHEG BOX for the production of two jets `dijet` [345], which has already been adapted for the use in `directphoton` [300]. This method provides independent importance sampling in the 6 divergent FSR and 3 ISR.

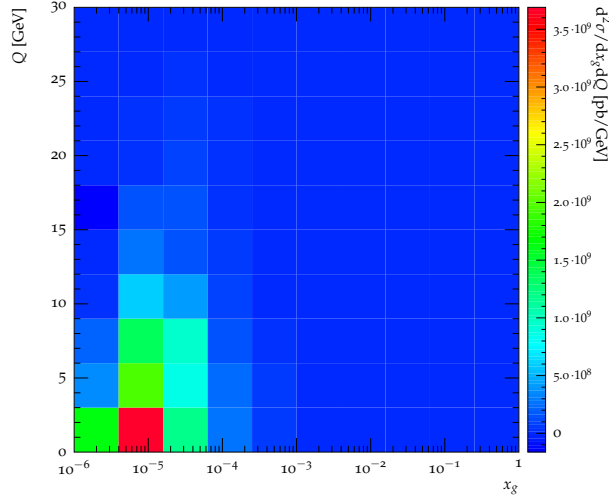


Figure 4.25: Distribution of x_g and Q for isolated prompt photons in the FoCal experiment at $\sqrt{s} = 14$ TeV. The cuts applied on the photon are $3.4 < \eta^\gamma < 5.8$ with a fixed isolation cone of $R_{\text{iso}} = 0.4$ and $E_T^{\text{iso}} = 5$ GeV.

They diverge as

$$S_{0j}^{\text{ISR}} = S_{1j} + S_{2j} = \frac{1}{E_j^2(1 - \cos^2 \theta_{1j})} \quad \text{and} \quad S_{ij}^{\text{FSR}} = \frac{E_i^2 + E_j^2}{2E_i^2 E_j^2 (1 - \cos \theta_{ij})}, \quad (4.2.6)$$

with $i, j \geq 3$ and can be normalized

$$\tilde{S}_{0j} = \frac{S_{ij}}{\sum_j (S_{0j} + \sum_i S_{ij})}, \quad \tilde{S}_{ij} = \frac{S_{ij}}{\sum_j (S_{0j} + \sum_i S_{ij})} \frac{E_j}{E_i + E_j}, \quad (4.2.7)$$

as we already saw in Sec. 3.1.4.1. Starting from a $2 \rightarrow 2$ massless phase space ($\Phi_{2 \rightarrow 2}$) and it is constructed as $d\Phi_B = \sum_{kj} \tilde{S}_{kj} d\Phi_{2 \rightarrow 3, kj}$, where $d\Phi_{2 \rightarrow 3, kj}$ is $d\Phi_{2 \rightarrow 2}$ with the emission kj added through POWHEG BOX's $n + 1$ phase space construction routines [63, 188, 189]. If one now probes a divergent $2 \rightarrow 3$ regime then the non-divergent \tilde{S} vanish by construction

$$\tilde{S}_{0j, ij} \rightarrow \begin{cases} 1 & \text{as } E_j \rightarrow 0 \text{ or } \theta_{ij} \rightarrow 0 \\ 0 & \text{else} \end{cases}. \quad (4.2.8)$$

Thus, the phase space sampling is guaranteed to pick the $d\Phi_{2 \rightarrow 3, kj}$ that works well despite the soft and/or collinear divergences. The $2 \rightarrow 2$ phase space generation in `directphoton`, `dijet` and `trijet` corresponds to Eq. (4.1.1) with different importance sampling options.

4.2.2.2 Calculation and implementation

In Fig. 4.26 exemplary Feynman diagrams for direct photon production with at least two jets are shown. Since the addition of a jet to the direct photon process is straightforward

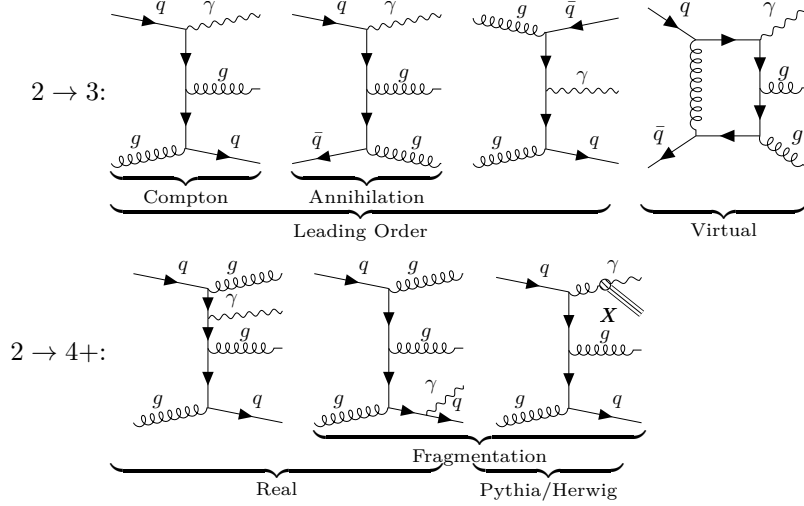


Figure 4.26: Schematic representation of the different contributions to prompt photon production in association with two jets at NLO+PS. This extended disambiguation is inspired by [116].

Born	$pp \rightarrow \gamma jj \sim \mathcal{O}(\alpha\alpha_S^2)$		$pp \rightarrow jjj \sim \mathcal{O}(\alpha_S^3)$	
Virtual	$\mathcal{O}(\alpha\alpha_S^2) \cdot \mathcal{O}(\alpha)$	$\mathcal{O}(\alpha\alpha_S^2) \cdot \mathcal{O}(\alpha_S)$	$\mathcal{O}(\alpha_S^3) \cdot \mathcal{O}(\alpha)$	$\mathcal{O}(\alpha_S^3) \cdot \mathcal{O}(\alpha_S)$
Real	$pp \rightarrow \gamma\gamma jj \sim \mathcal{O}(\alpha^2\alpha_S^2)$	$pp \rightarrow \gamma jjj \sim \mathcal{O}(\alpha\alpha_S^3)$		$pp \rightarrow jjjj \sim \mathcal{O}(\alpha_S^4)$

Table 4.5: Processes contributing to prompt photon production in association with two jets at NLO. Only the greyed out processes are included in the calculation.

the prompt photons also come from either Compton and annihilation processes and fragmentations photons from bremsstrahlung or gluon/quark fragmentation. The main conceptual differences to the direct photon production with one jet is that already at leading order there is a gluon-gluon initiated process. As can be seen from the figure, going beyond leading order the definition of fragmentation photons becomes again ambiguous as the splitting $q \rightarrow q\gamma$ can also be attributed to the real correction. Tab. 4.5 orders prompt photon production by the couplings and shows which processes are included in the calculation highlighted in grey. Using the POWHEG method as an alternative to FFs for process $pp \rightarrow \gamma j$ at NLO as explained in Sec. 4.2.1.1 can be straightforwardly extended to the process $pp \rightarrow \gamma jj$ at NLO.

The numerical implementation of the NLO calculation for the process $pp \rightarrow \gamma jj$ was performed using the POWHEG BOX V2 framework. Usually, the required ingredients for a new process are the Born amplitudes and their colour- and spin-correlated counterparts, the Born phase space, a decomposition of the amplitudes in the colour flow basis, the finite part of the virtual corrections, and the real correction amplitudes. For this process however we will also reuse the modifications, *e.g.* the Sudakov weight Eq. (4.2.5), to the core POWHEG BOX functionality introduced in Ref. [300].

The usual leading order, virtual and real corrections were computed with FormCalc

in a five-flavour scheme. The required leading order components for $pp \rightarrow jjj$ have been reused from the `trijet` process [187]. The UV divergences are handled by the constrained differential renormalization [346]. Whereas the IR divergences are treated using the FKS subtraction in `POWHEG BOX V2` (cf. Sec. 3.1.4.1), which combines the colour- and spin-correlated amplitudes to reproduce and treat the divergent behaviour. The colour-correlated Born amplitudes were obtained from `FormCalc` by injecting the colour charge operators into the amplitudes in the Mathematica code

$$B_{ij} = -N \sum_{\substack{\text{spins} \\ \text{colors}}} \mathcal{M}_{\{c_k\}} \mathcal{T}_{c_i, c'_i}^a \mathcal{T}_{c_j, c'_j}^a [\mathcal{M}_{\{c_k\}}^\dagger]_{c_i \rightarrow c'_i, c_j \rightarrow c'_j}. \quad (4.2.9)$$

Here the averaging factors are included in N , $\{c_k\}$ are the sets of colour indices of the external particles and \mathcal{T} represents the structure constants f^{abc} for gluons or $\pm T_{\alpha\beta}^a$ for quarks (cf. Sec. A.1.4.2). The colour-correlation is automatically checked at runtime by requiring that $\sum_{i,i \neq j} B_{ij} = C_{f_j} B$ where C_{f_j} is the Casimir constant of the parton j . Similarly to the colour-correlations, in the expression for the spin-correlation

$$B_j^{\mu\nu} = N \sum_{\substack{\text{spins} \\ \text{colors}}} \mathcal{M}_{\{s_k\}} \epsilon_{s_j}^{\mu*} \epsilon_{s'_j}^\nu [\mathcal{M}_{\{s_k\}}^\dagger]_{s_j \rightarrow s'_j} \quad (4.2.10)$$

the identity between spins s_j and s'_j has been replaced by the polarization vectors $\epsilon_{s_j}^\mu$. As `FormCalc`'s exported Fortran code uses the spinor helicity formalism [347] to compute the matrix elements, it is possible to query individual polarized and averaged helicity amplitudes. Thus, one obtains the spin-correlations between the photon and the partons by taking all but one external particle as unpolarized. The four combination of $s_j \times s'_j$ are scaled by the corresponding numeric values of the polarization vectors and then summed. A trivial cross-check is to verify $g_{\mu\nu} B_j^{\mu\nu} = -B$ for all j , which `POWHEG BOX V2` also does at runtime. Furthermore, the required tree diagrams and correlations can be computed analytically in our newly developed code [9], which glues `FORM` [348–350] and `SymPy` [351] together.

The inclusion of colour flow information is necessary to enable the parton shower to properly manage colour correlations beyond the hard process and we perform the colour flow decomposition as outlined in Sec. 3.1.1.2.

In the course of our study, several computational tools and frameworks were employed to ensure the reliability and accuracy of our results in prompt photon production calculations. To cross-verify the computational precision of our NLO QCD calculations, we compared to multiple automatic matrix element generators. The virtual corrections were validated against `MadGraph5_aMC@NLO`, `OpenLoops 2` [352] and `Recola 2` [353] whereas the real corrections were checked with `FormCalc` and `OpenLoops 2`. This comprehensive cross-check confirms the consistency across different tools. After evaluating the performance and numerical quality of the FKS subtraction of the various computations, `OpenLoops 2` was selected for the final implementation and numerical computations in the remainder of this chapter. During the process of comparing different calculations we also developed an interface between `MCFM` and `Rivet/YODA` [309–311], that also allows for direct comparison against experimental analyses.

4.2.3 Isolated-prompt photons with 2 jets at 13 TeV

4.2.3.1 Simulation setup

The events from POWHEG BOX V2 in the LHE format are showered both by PYTHIA 8 or HERWIG 7, and then analysed by Rivet 3. In our recent developments, significant updates have been made to the POWHEG-RIVET-PYTHIA [3, 5]⁵ interface to enhance its compatibility with the latest versions of HepMC 3, Rivet 3 and PYTHIA 8. Originally designed to work seamlessly with earlier versions [312, 354], the interface required an overhaul to align with the updates in these widely used simulation tools. Additionally, we have expanded the flexibility of our interface by exposing several meta parameters, such as toggles for QCD and QED showers, to the users through the `powheg.input` file. This advancement allows for an enriched user experience by providing options that were previously accessible only through customized settings. Mirroring this enhanced configurability, a new interface for HERWIG 7 has also been developed. This new interface incorporates similar user-exposed options, thereby standardizing the setup across different parton showers and making it easier for users to transition between tools without reconfiguring their parameters extensively. The complexity of keeping PYTHIA 8 and HERWIG 7 in sync can be seen in the appendix of [5].

We set the renormalization and factorization scale equal to the transverse momentum of the photon, $E_T^\gamma = p_T^\gamma$, and the PDF in use is MSHT20n1o through LHAPDF 6 whereas the running of α_S is calculated internally by POWHEG BOX. In all the following figures in Sec. 4.2.3.2 and Sec. 4.2.3.3 the vertical error bars represent the statistical uncertainties, while the bands represent the scale uncertainties. The scale uncertainties are estimated by the standard factor-two seven-point variation of the renormalization and factorization scales by a factor of two around the central value while excluding relative factors of four. As the computations involves both tree level diagrams of $pp \rightarrow \gamma jjj$ and $pp \rightarrow jjj$ this takes a significant amount of CPU hours. In order to speed up the process, we only enabled the virtual corrections in the final reweighting step, instead of generating equal weighted events for all processes. Due to the inclusion of the Sudakov reweighting factor Eq. (4.2.5), the events are already not equally weighted thus this is not a significant loss.

4.2.3.2 Isolation schemes and parton showers

In Sec. 2.2.6 we discussed the fragmentation of partons into photons and how isolation schemes are used to separate the prompt photons from the fragmentation photons. In the following we will demonstrate and discuss the effect of the different isolation schemes on the prompt photon production in association with two jets. Naturally, the hybrid isolation must result in cross sections that are lower than the fixed cone isolation. This will only be barely visible in our setup (see below), however, and the hybrid isolation mostly results in the same prediction as the fixed cone isolation. Thus, it satisfies its purpose of addressing theoretical issues while remaining close to the experimentally motivated fixed-cone isolation. Figs. 4.27 to 4.29 show our predictions for the different isolation schemes in PY8 (left) and HW7 (right). The parameters entering the analysis are the jet radius $R_j = 0.4$ for the anti- k_T algorithm [237], the isolation radius $R_I = 0.4$ and the isolation energy $p_T^{\text{iso}} = 2$ GeV. Contrary to experimental analysis, as [340], there is neither a p_T scaling of the isolation energy nor do we include a hadronic background subtraction and are only interested the hardest photon (γ) and hardest jet (j_1). An

⁵Our interface will be made publicly available in the near future within another publication.

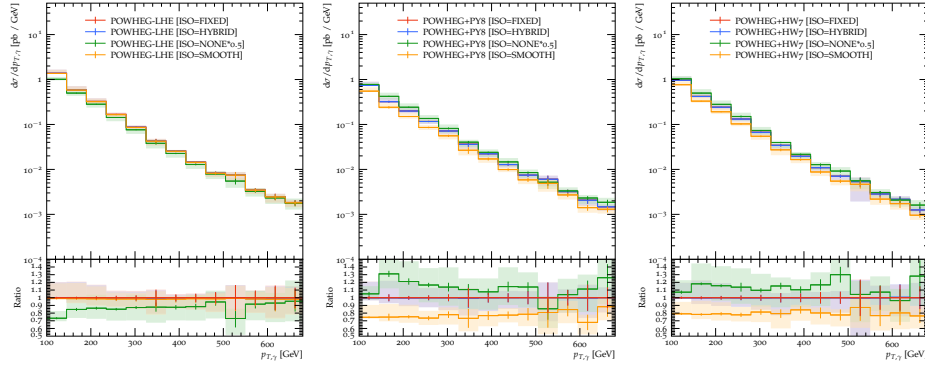


Figure 4.27: Transverse momentum distribution of the photon for different isolation schemes with no PS (left), PYTHIA (center) and HERWIG (right) parton showers.

implementation of our event selection in a Rivet analysis is available in the ancillary files accompanying Ref. [5].⁶

Fig. 4.27 shows the distribution of the photon’s transverse momentum. The red, yellow and blue curves correspond to the fixed-cone, smooth-cone, and hybrid isolation schemes, respectively. Additionally, in green the non-isolated contribution is shown and scaled by a factor of 1/2, to facilitate the comparison of shapes. The change of shape as seen in the ratio panel between the non-isolated and fixed-cone isolation suggests that the isolation suppresses low p_T photons more. For the smooth-cone isolation this is even more pronounced and above parameters result in generally smaller cross sections than a fixed-cone isolation. There is however no significant difference in shape between the different isolation schemes, only the smooth isolation is about 20% lower than the fixed and hybrid isolation. Both parton showers reduce the cross section in comparison to their input, the unshowered events. Further the LHE prediction shows no difference between the different isolation schemes. This can be explained by the fact that there are only single hard partons in the final-state instead of a broader jet. Then the event is mostly either isolated if a parton is close to the photon or non-isolated otherwise. With a parton shower however the parton spreads its energy into a cone-like jet with an increased probability to populate the photon’s isolation cone continuously. The parton shower’s reduction in the cross section is then partly due to the fact that fewer photons are isolated.

Next, in Fig. 4.28 we show how the different isolation schemes affect the separation between the photon and the hardest jet, j_1 . Comparing the non-isolated with the isolated curves one prominent difference in shape is the effective suppression above $\pi < \Delta R_{\gamma j_1} = \sqrt{(\Delta\eta)^2 + (\Delta\phi)^2}$. It is likely that even though the photon and the hardest jet are produced back-to-back, the photon is not isolated as the remaining jets can still become collinear with the photon. Then in the regime of $0.5 < \Delta R_{\gamma j_1} < \pi$ the isolation reduces the cross section less. When the hardest jet is close to the isolation cone around the photon $\Delta R_{\gamma j_1} < 0.5$ the isolation eliminates most of the cross section. Again, no difference in shape between the different isolation schemes is visible, only the smooth isolation is about 20% to 30% lower than the fixed and hybrid isolation. The

⁶Alternatively, the source code is available at https://gitlab.com/APN-Pucky/rivet-POWHEG_2023_DIRECTPHOTON.

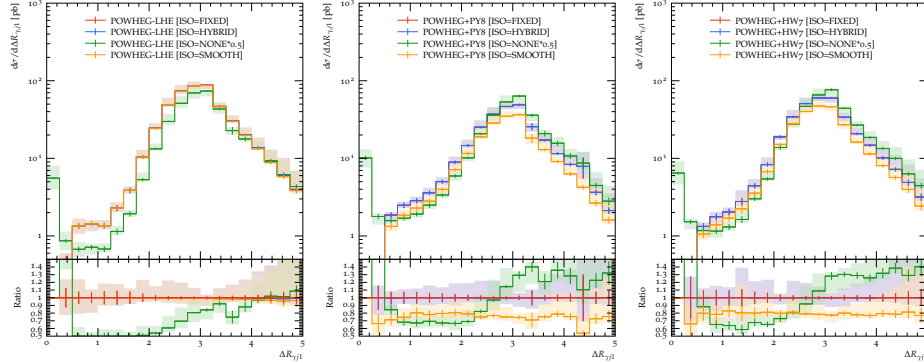


Figure 4.28: $\Delta R_{\gamma j_1}$ distribution of the photon for different isolation schemes using no PS (left), PYTHIA (center) and HERWIG (right).

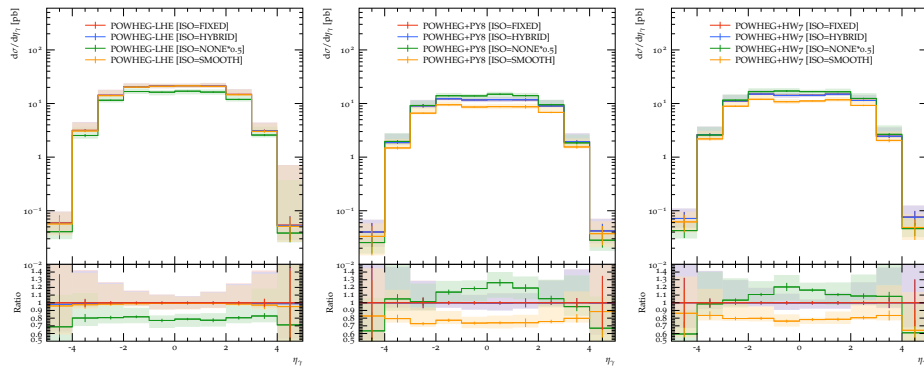


Figure 4.29: Rapidity distribution of the photon for different isolation schemes with no PS (left), PYTHIA (center) and HERWIG (right).

production of soft emissions is visible in the increase in the low ΔR region between the no PS and parton shower figures. A visible difference between the isolation schemes again exists only with the parton showers enabled.

In Fig. 4.29 the rapidity distribution of the photon is shown. The interesting feature here is that both PY8 and HW7 show a suppression towards rapidities of $y_\gamma \approx 0$ with the fixed and hybrid cone isolation. This trend is slightly more pronounced in the smooth-cone isolation. The effect is completely absent without a parton shower hinting at increased soft emission activity towards low rapidities. Comparing PY8 and HW7 across the three plots there is next to no difference in shape, which is to an extent expected since they are given the same POWHEG BOX events as input. A small difference is that HW7 predicts a marginally larger cross section than PY8 regardless of the isolation scheme. Further HW7's results come with barely smaller numerical uncertainties therefore smaller fluctuations than PY8's.

The x - Q distribution before and after the PS is shown in Fig. 4.30. Both values are used to evaluate the PDFs and are not expected to be modified significantly by a naive PS. However, minor differences can appear due to reweighting between different hard

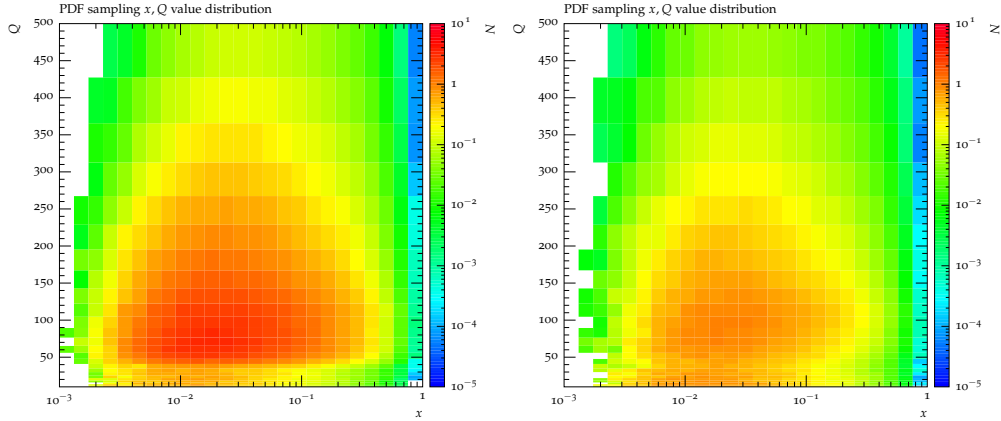


Figure 4.30: x - Q distribution in a.u. after LHE (left) and PYTHIA (right) with a fixed-cone isolation.

and parton shower internal PDFs as in Eq. (2.2.25) or the isolation fixed-cone isolation criteria applied in the analysis. The only directly visible difference is that PYTHIA reduces the cross section in the dominant centre compared to LHE. This suppression effect will be discussed more in the following section.

As mentioned in Sec. 3.3.3.2, the first and hardest emission in the underlying event is attached using the POWHEG method. Since our process is mixed in QCD and QED the underlying $2 \rightarrow 3$ event can be either a trijet (QCD) or photon plus two jets event (QED). In Fig. 4.31 the transverse momentum distribution is split between the QCD and QED underlying events. Comparing the curves without isolation (green) the pure QCD contribution dominates, but after applying the isolation cuts the QED contribution becomes more important (yellow, red and blue). Starting from a QCD event attaching a photon to one of the three jets is likely to be non-isolated. In contrast, photon plus two jet events rarely experience QCD emissions near the photon, allowing it to remain isolated. This is consistent with understanding the QCD underlying event as analogous to the FF contribution. Although using `enhancedrad` increases the ratio of QED events, it still exhibits larger numerical uncertainties. However, the scale uncertainties are smaller compared to the QCD contribution.

In general, we find that the shapes of the predictions do not depend significantly on the isolation criterion, but that the results for smooth-cone isolation lie below those for fixed-cone and hybrid isolation. The latter two as well as PYTHIA and HERWIG agree in general quite well.

4.2.3.3 Comparison with ATLAS data

The following figures show results of the new calculation for an isolated photon plus two-jet in the context of an analysis performed by ATLAS in pp collisions at 13 TeV [340]. On top of the cuts defined by the ATLAS detector dimensions, the analysis uses an isolation cone of $R_I = 0.4$ and isolation energy of $E_T^{\text{iso}} = 10 \text{ GeV} + 0.0042 p_T^\gamma + \pi R_I^2 \rho_j^{p_T}(\eta)$. The jet density $\rho_j^{p_T}(\eta)$ describes the hadronic activity by averaging the transverse momenta of the jets for given rapidity η obtained from a k_T -algorithm. In consequence the photon can be less isolated if it has a large p_T or if there are many jets. After jets are identified

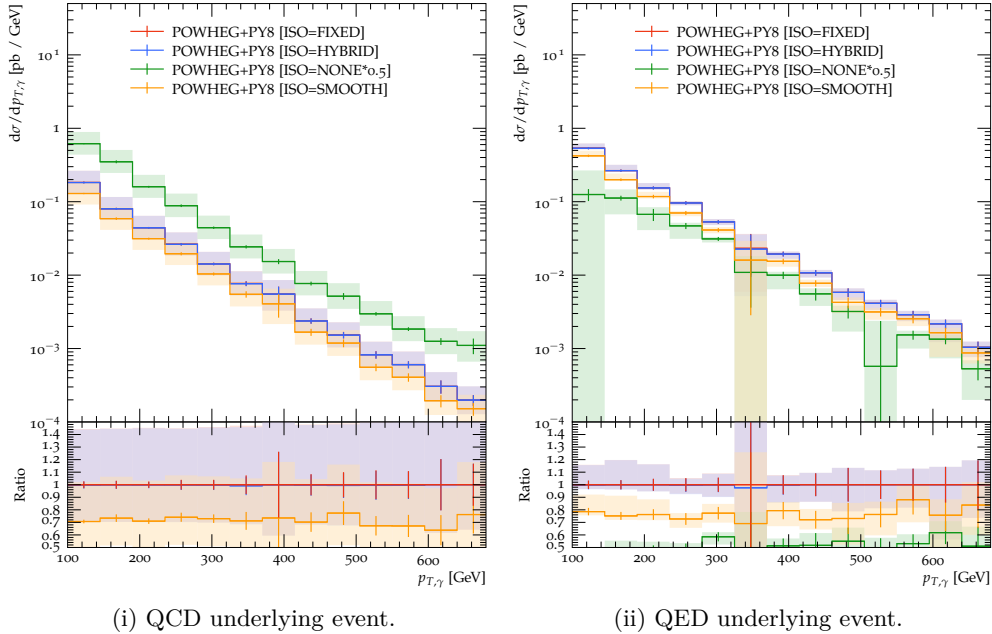


Figure 4.31: p_T distribution of the photon for different isolation schemes using PYTHIA with QCD (left) and QED (right) underlying events.

through k_T algorithm with a jet radius $R_J = 0.5$, they are sorted by transverse momentum. That is the leading jet (jet_1) is the one with the highest transverse momentum, the subleading jet (jet_2) is the one with the second most, *etc.* The same nomenclature would apply for photons, but here we are only interested in the hardest photon. The Rivet analysis ATLAS_2019_I1772071 examines several observables in different regimes, namely inclusive, direct-enriched and fragmentation-enriched contributions. In addition to the experimental data, NLO QCD predictions from **Sherpa** [340], our new calculation of direct photons in POWHEG BOX with PYTHIA 8 (PY8) and HERWIG 7 (HW7) as well as recent NLO and NNLO corrections [333] are displayed. The **Sherpa** calculation merges $\gamma + 1j$ and $\gamma + 2j$ NLO with $\gamma + 3j$ and $\gamma + 4j$ LO events and supplements it with a parton shower [Krauss:2001iv, Cascioli:2011va, Schumann:2007mg, Hoeche:2012yf] similar to the procedure in Sec. 3.3.2. The NLO and NNLO predictions do not include a fragmentation contribution, arguing that it should not exceed 5% for the inclusive and direct-enriched regime. Both the NNLO/NLO and the NLO merged calculations use a smooth-cone photon isolation at the ME level. While we will only look at the figures with photon observables, further jet distributions are available in Sec. A.5.4.

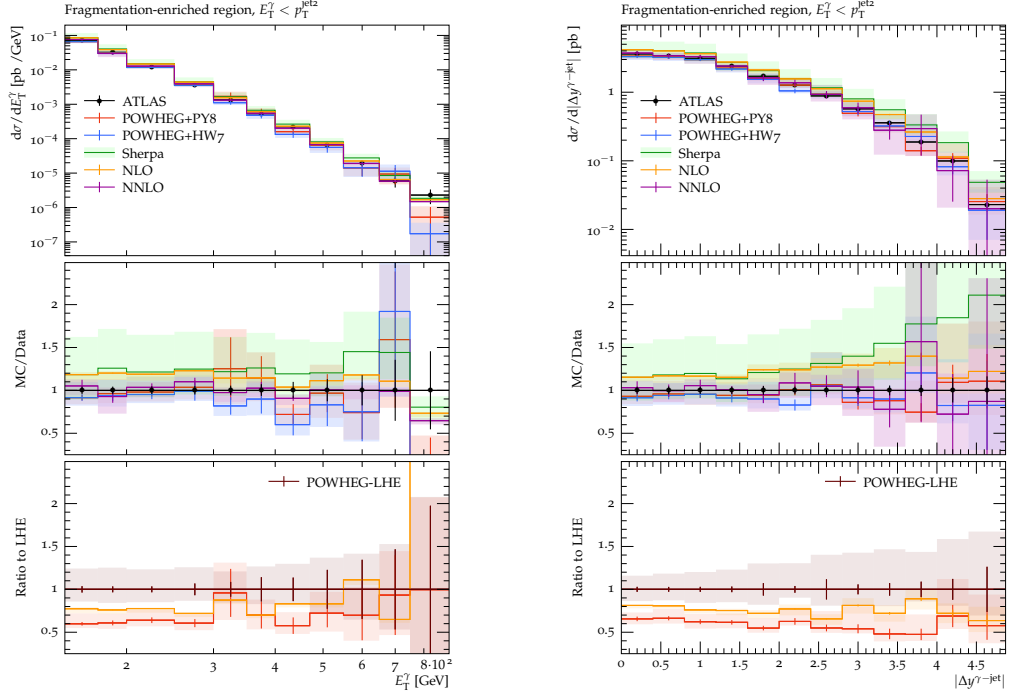
We first inspect the fragmentation-enhanced regime, which is defined by requiring both jets to be harder than the isolated prompt photon, $p_T(j_2) > E_T^\gamma$. As can be seen in Fig. 4.32i, the POWHEG BOX+PYTHIA 8 prediction describes the data well. The HERWIG 7 parton shower predicts a slightly lower rate than PY8, but still agrees reasonably well. The prediction from **Sherpa** instead predicts larger rates than the data, but still overlaps with data thanks to the large uncertainty. The NNLO prediction in the fragmentation-enriched was not shown in its publication [333] due to the omission of fragmentation

contributions, but surprisingly, it also predicts the fragmentation contribution well despite remaining large numerical and scale uncertainties. A similar picture persists in Fig. 4.32iii where Sherpa and the NLO curve are consistently 10% to 20% above the data while NNLO and POWHEG BOX are in agreement with the data and each other. Obtaining adequate statistics in the tails of the distributions of Fig. 4.32ii and Fig. 4.32iv is challenging. This results in quite some fluctuations in both the NLO+PS and the fixed order NNLO predictions. The prevailing trend also here is that the NNLO and POWHEG predictions, which overlap within uncertainties, describe the data best. We note that the shower corrections beyond NLO are quite large for all observables (10% to 20%), see the second ratio panel. The first POWHEG emission correction, already included at the LHE stage, has an appreciable phase space dependence, most notably in the photon-jet angular separation spectrum, and tends to correct in the opposite direction compared to the remaining shower emissions. Nevertheless, the total shower correction is relatively flat.

In the direct-enhanced regime the photon has a larger transverse momentum than the jets, $p_T(j_1) < E_T^\gamma$. Thus, this region has enhanced contributions from photons originating from the hard interaction. In comparison to the fragmentation regime, the direct-enhanced regime suffers less from low statistics. The NNLO calculation is in good agreement with the data in all observables, as can be seen in Fig. 4.33. While both PY8 and HW7 are mostly close to each other, the POWHEG+PY8 prediction is often slightly closer to the NNLO curve. The Sherpa calculation comes with significantly larger uncertainties than NNLO or NLO+PS calculations. Furthermore, it seems to overestimate the cross section whenever the cross sections become small. The only very distinct separation between the predictions is in Fig. 4.33iii at very low angular differences between the photon and the jet. This is most-likely due to an increased sensitivity to the activity around the photon due to the isolation criteria in this region. There the data points also carry a large uncertainty of about 10%. While NNLO and PY8 agree with them, HW7 and NLO underestimate them, and Sherpa overestimates them by more than 20%. Just as in the fragmentation-enriched region, the shower corrections are relatively large but mostly flat, except the photon-jet angular separation spectrum where its value is vanishingly small.

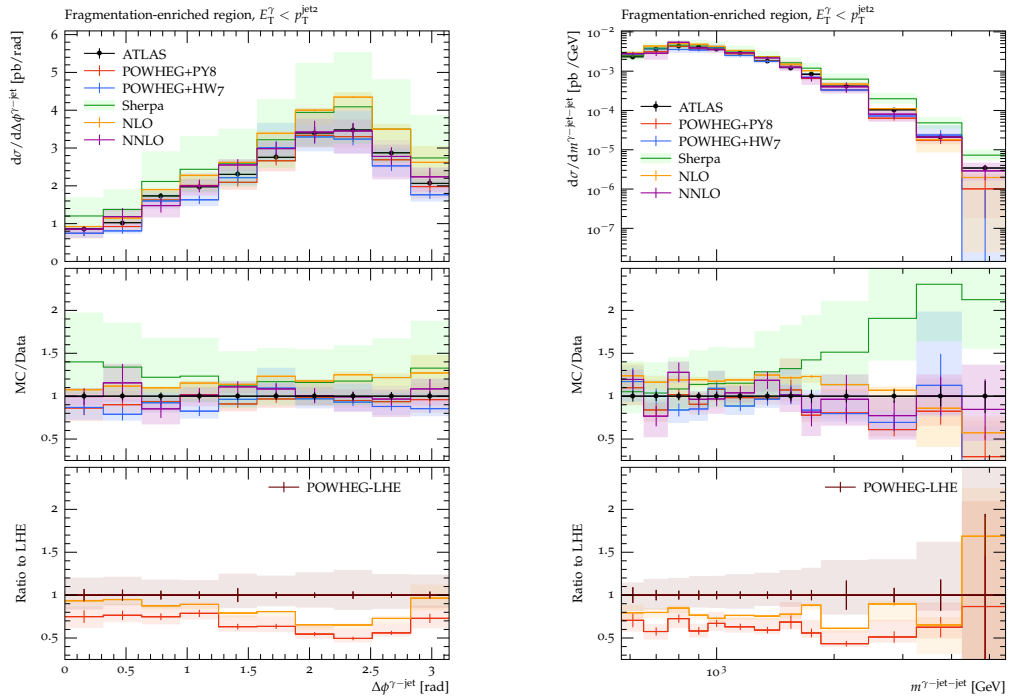
Fig. 4.34 shows the inclusive predictions which encompass both of the previous regimes, direct and fragmentation-enhanced. From comparing Figs. 4.32 and 4.33 to Fig. 4.34 it is clear that the direct regime contributes more than fragmentation regime, while the remaining contributions can stem from moderately hard photons, $p_T(j_2) < E_T^\gamma < p_T(j_1)$. Across all four observables, the NNLO calculation is in best agreement with the data. POWHEG matched either to PY8 or to HW7 also described the data well, but suffers from larger scale and numerical uncertainties than the NNLO calculation. The NLO prediction overestimates the data consistently by about 5% to 10%. This leads us to the conclusion that fixed order NLO is not sufficient to describe the data and either NNLO or NLO+PS is required.

Overall the data is described relatively well by all the tools. Both NNLO corrections and shower corrections in predictions matched using the POWHEG method, regardless of the shower details, seem to improve the description appreciably. The MC@NLO style matching with the CS dipole based shower from Sherpa instead is closer to the fixed order NLO prediction, and has been reported with surprisingly large scale uncertainties.



(i) Photon transverse momentum.

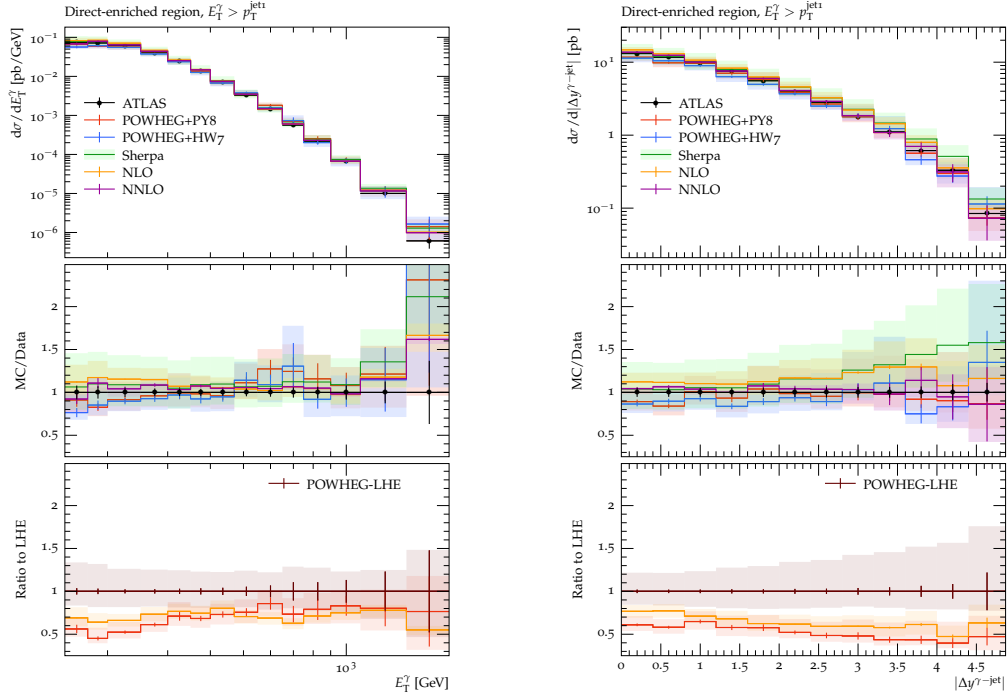
(ii) Rapidity difference between the hardest photon and each of the two hardest jets.



(iii) Azimuthal angle difference between the hardest photon and each of the two hardest jets.

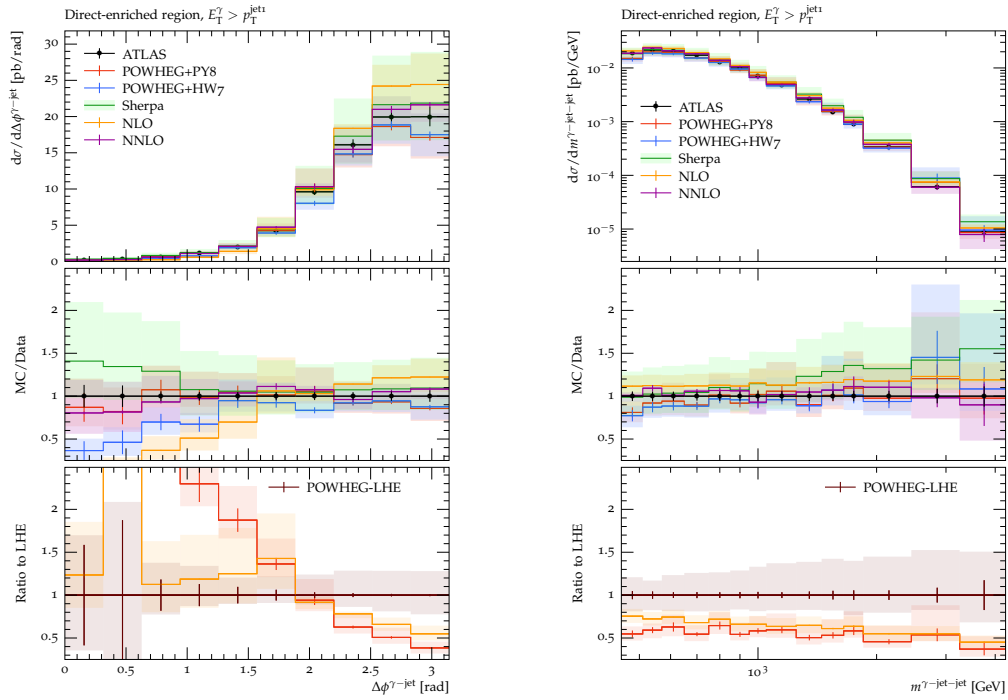
(iv) Invariant mass of the photon-jet-jet system.

Figure 4.32: Differential cross sections with respect to different observables in the fragmentation-enhanced regime as defined by ATLAS [340].



(i) Photon transverse momentum.

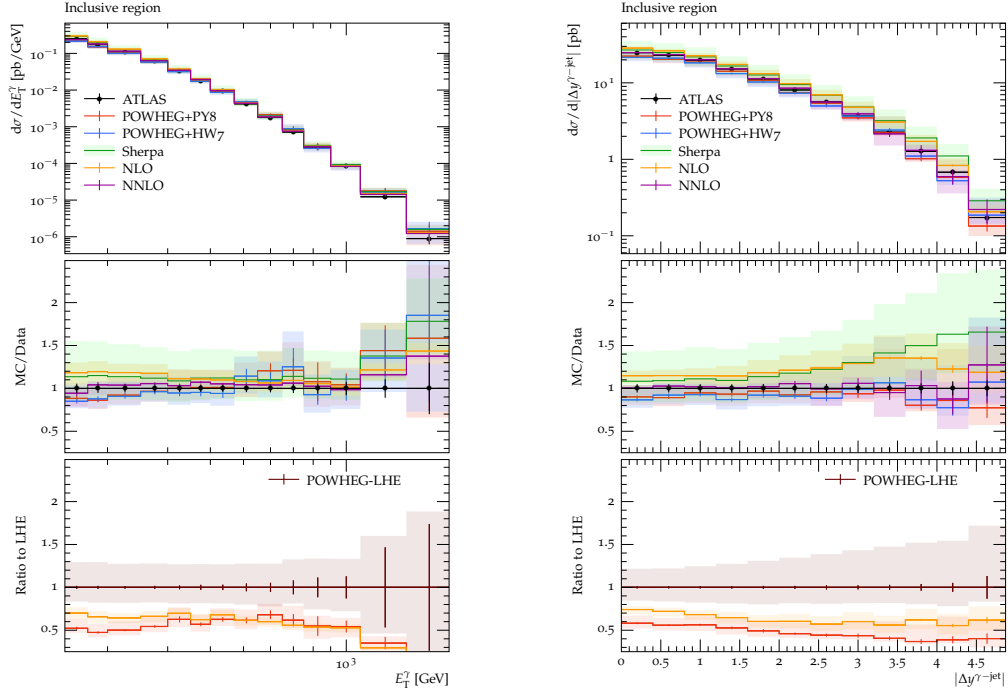
(ii) Rapidity difference between the hardest photon and each of the two hardest jets.



(iii) Azimuthal angle difference between the hardest photon and each of the two hardest jets.

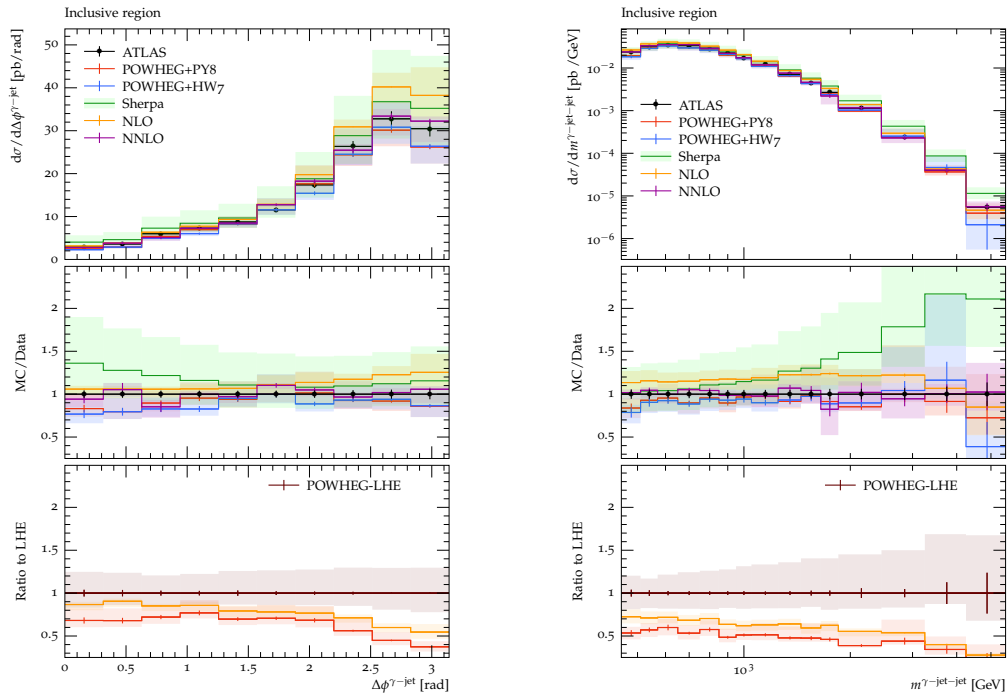
(iv) Invariant mass of the photon-jet system.

Figure 4.33: Differential cross sections with respect to different observables in the direct-enhanced regime as defined by ATLAS [340].



(i) Photon transverse momentum.

(ii) Rapidity difference between the hardest photon and each of the two hardest jets.



(iii) Azimuthal angle difference between the hardest photon and each of the two hardest jets.

(iv) Invariant mass of the photon-jet-jet system.

Figure 4.34: Differential cross sections with respect to different observables in the inclusive regime as defined by ATLAS [340].

Chapter 5

Electroweak superpartner production with Resummino

In this chapter we study SUSY phenomenology at the LHC using the `Resummino` [2, 355] program. SUSY is a symmetry between bosons and fermions, which can be studied in processes similar to previously studied photon production by replacing the final-state particles with their superpartners. Instead of producing a photon with a quark, we will produce an electroweakino with a squark, and similar to dilepton production, we will study slepton production. While we previously used a MCEG with a PS to incorporate soft effects to simulate the process, we will now use a MC integrator to calculate cross sections at fixed order combined with analytically resummed soft effects.

This chapter is organized as follows. First we introduce the MSSM in Sec. 5.1 and in Sec. 5.2 the threshold resummation formalism for soft gluons. Sec. 5.3 presents the calculation of the production of a squark and an electroweakino at NLO+NLL accuracy. Cross sections for purely electroweak SUSY production are given in Sec. 5.4. Finally, in Sec. 5.5 the cross sections are used to compare with experimental data and obtain exclusion limits.

5.1 The Minimal Supersymmetric Standard Model

In the search for Beyond the Standard Model (BSM) physics, SUSY offers a highly promising framework [356–358]. By relating bosons and fermions, SUSY stabilizes the Higgs boson mass against potentially large quantum corrections, enables the unification of gauge couplings at high energies [359–361], and provides a natural dark matter candidate [362, 363], addressing several long-standing shortcomings of the SM simultaneously.

Observations such as the rotation curves of distant stars and gravitational lensing strongly suggest that the Universe contains more than just visible matter and the neutrinos of the SM. A promising explanation for this excess mass is the introduction of a stable or long-lived weakly interacting massive particle (WIMP) within a BSM theory. One appealing approach to achieve this is by extending the theory’s symmetry group with fermionic operators, leading to SUSY QFT, which also extend the Poincaré group to its maximum limit [356, 364, 365].

To accommodate dark matter considerations, most SUSY models, particularly the

MSSM [366–369], assume the conservation of a multiplicative quantum number called R -parity [370]. In the MSSM, every degree of freedom in the SM is paired with a superpartner differing by half a unit in spin. This leads to phenomenologically viable SUSY spectra where the lightest supersymmetric particle (LSP) is electrically neutral [363], exhibiting all the characteristics of the most promising dark matter candidate the WIMP.

The scalar partners of the left- and right-handed quarks mix, as do the higgsino, bino, and wino interaction eigenstates, which after electroweak symmetry breaking form neutral and charged states known as electroweakinos (neutralinos and charginos). Since none of these particles have been observed, it is assumed that supersymmetry is broken [371, 372], causing the superpartners to be heavier than their SM counterparts.

5.1.1 Supersymmetry

Much of the success of the SM can be attributed to symmetries. In particular, external space-time symmetries and internal gauge symmetries make precise predictions possible. SUSY integrates another symmetry by relating fermionic and bosonic degrees of freedom. Only after the development of SUSY it became clear, that it provides potential solutions to remaining shortcomings of the SM. For a deeper insight into Supersymmetry, we refer the reader to our sources for this chapter and their references [130, 373–376].

The extension of the SM turns out to be not so simple, since the Coleman-Mandula theorem [364] restricts the extension of the Poincaré group. Under general assumptions about the scattering S matrix, a QFT based on the Poincaré group and internal gauge symmetries with bosonic generators can only be a direct product of the two. That is to say, the generators of the Poincaré group $M_{\mu\nu}$, rotations and boosts, and the internal gauge group must commute. Therefore internal and external symmetries can not be mixed non trivially.

To maximize the symmetry of the SM beyond trivial extensions the Haag-Lopuszanski-Sohnius theorem [365] establishes the inclusion of fermionic spinor generators Q . The transformation to a superpartner, from fermionic to bosonic states and vice versa, is carried out by the new anticommutating spinor operator Q . The anticommutation relations can be written in the Weyl representation as

$$\{Q_\alpha, Q_\beta\} = 0, \quad \{\bar{Q}^{\dot{\alpha}}, \bar{Q}^{\dot{\beta}}\} = 0, \quad (5.1.1)$$

$$\{Q_\alpha, \bar{Q}_{\dot{\beta}}\} = 2\sigma_{\alpha\dot{\beta}}^\mu P_\mu, \quad \text{and} \quad \{\bar{Q}^{\dot{\alpha}}, Q^\beta\} = 2\bar{\sigma}_{\mu}^{\dot{\alpha}\beta} P^\mu, \quad (5.1.2)$$

where P^μ generates space-time translations and σ^μ is the Pauli four-vector. For realistic theories they transform under the Lorentz group as

$$[M_{\mu\nu}, Q_\alpha] = -(\sigma_{\mu\nu})_\alpha{}^\beta Q_\beta \quad \text{and} \quad [M_{\mu\nu}, \bar{Q}^{\dot{\alpha}}] = -(\bar{\sigma}_{\mu\nu})^{\dot{\alpha}}{}_{\dot{\beta}} \bar{Q}^{\dot{\beta}}, \quad (5.1.3)$$

with $\sigma^{\mu\nu} = i(\sigma^\mu \bar{\sigma}^\nu - \sigma^\nu \bar{\sigma}^\mu)/4$. From the relation

$$[Q_\alpha, P^\mu] = [\bar{Q}^{\dot{\alpha}}, P^\mu] = 0 \quad (5.1.4)$$

we directly see that the masses of superpartners are equal, since they have the same eigenvalues P^2 . This obviously contradicts experimental observation and has the consequence that SUSY must be softly broken, which leads to higher masses.

Multiplet	Name	$S = 0$	$S = \frac{1}{2}$	$S = 1$	SM group
chiral	s-/quarks Q_L	$(\tilde{u}_L, \tilde{d}_L)$	(u_L, d_L)	-	$(\mathbf{3}, \mathbf{2}, \frac{1}{6})$
	(3 generations) U_R	\tilde{u}_R^c	u_R^\dagger	-	$(\bar{\mathbf{3}}, \mathbf{1}, -\frac{2}{3})$
	D_R	\tilde{d}_R^c	d_R^\dagger	-	$(\bar{\mathbf{3}}, \mathbf{1}, \frac{1}{3})$
	s-/leptons L_L	$(\tilde{\nu}, \tilde{e}_L)$	(ν, e_L)	-	$(\mathbf{1}, \mathbf{2}, -\frac{1}{2})$
	(3 generations) E_R	\tilde{e}_R^c	e_R^\dagger	-	$(\mathbf{1}, \mathbf{1}, 1)$
	higgs/-inos H_U	(H_u^+, H_u^0)	$(\tilde{H}_u^+, \tilde{H}_u^0)$	-	$(\mathbf{1}, \mathbf{2}, +\frac{1}{2})$
(1 generation) H_D	(H_d^0, H_d^-)	$(\tilde{H}_d^0, \tilde{H}_d^-)$	-	$(\mathbf{1}, \mathbf{2}, -\frac{1}{2})$	
gauge	gluon/-ino V_G	-	\tilde{g}	g	$(\mathbf{8}, \mathbf{1}, 0)$
	W boson/Wino V_W	-	$(\tilde{W}^\pm, \tilde{W}^0)$	(W^\pm, W^0)	$(\mathbf{1}, \mathbf{3}, 0)$
	B boson/Bino V_B	-	\tilde{B}^0	B^0	$(\mathbf{1}, \mathbf{1}, 0)$

Table 5.1: Supermultiplets in the MSSM. S denotes the spin. The transformation properties under the SM gauge group $SU(3)_C \times SU(2)_L \times U(1)_Y$ are presented in the last column.

5.1.2 Soft breaking

The MSSM is the simplest direct supersymmetrisation of the SM. It is minimal in the sense that it uses the fewest new particles to obtain a supersymmetric field theory. In Tab. 5.1 we list all the supermultiplets of the MSSM. The supersymmetric particles solely differ in spin by $\frac{1}{2}$ (before mass generation) and get marked by a tilde.

The scalar spin 0 particles do not have a helicity, the indices L (left-handed) and R (right-handed) therefore refer to the fermionic superpartner chirality. The only exception to the direct definitions of superpartners is in the definition of the Higgsinos. In the MSSM there are two Higgs supermultiplets H_D and H_U to cancel chiral anomalies and generate the masses of the up- and down-type particles. The neutral Standard Model Higgs is then obtained from the combination of H_u^0 and H_d^0 .

The procedure to describe the Lagrangian in superspace is to use a holomorphic superpotential

$$W_{\text{MSSM}}(\Phi) = U_R \mathbf{y}^u Q_L H_U - D_R \mathbf{y}^d Q_L H_D - E_R \mathbf{y}^e L_L H_D + \mu H_U H_D, \quad (5.1.5)$$

where the \mathbf{y} are 3×3 Yukawa matrices of each family and μ is a generalized Higgs mass term. Following [377] we arrive at the expanded MSSM Lagrangian that still conserves

SUSY [376]

$$\begin{aligned}
\mathcal{L}_{\text{MSSM}}^{\text{SUSY}} = & \sum_i \left[D_\mu \phi_i^\dagger D^\mu \phi^i + \frac{i}{2} (\psi^i \sigma^\mu D^\mu \bar{\psi}_i - D^\mu \psi^i \sigma^\mu \bar{\psi}_i) \right] \\
& + \sum_k \left[-\frac{1}{4} V_k^{\mu\nu} V_k^{\mu\nu} + \frac{i}{2} (\tilde{V}_k \sigma^\mu D^\mu \bar{\tilde{V}}_k - D^\mu \tilde{V}_k \sigma^\mu \bar{\tilde{V}}_k) \right] \\
& - \frac{1}{2} \sum_{i,j} \left[\frac{\partial^2 W_{\text{MSSM}}(\phi)}{\partial \phi^i \partial \phi^j} \psi^i \cdot \psi^j + \text{H.c.} \right] - \sum_i \frac{\partial W_{\text{MSSM}}(\phi)}{\partial \phi^i} \frac{W_{\text{MSSM}}^*(\phi^\dagger)}{\partial \phi_i^\dagger} \\
& - \frac{1}{2} \sum_k \left[\left(g_k \sum_j [\phi_j^\dagger T^k \phi^j] \right) \left(g_k \sum_i [\phi_i^\dagger T^k \phi^i] \right) - i2\sqrt{2} \sum_i \left(g_k \tilde{V}^k \cdot \bar{\psi}_i T_k \phi^i + \text{H.c.} \right) \right].
\end{aligned} \tag{5.1.6}$$

We write ψ or \tilde{V} for left-handed and $\bar{\psi}$ and $\bar{\tilde{V}}$ for right-handed spinors. The $\sigma_\mu = (1, \sigma^i)$ are constructed from the Pauli matrices and D_μ are covariant derivatives. The index k indicates the MSSM gauge group such that couplings g_k and generators T_k are generic. Indices i and j refer to the members of scalar ϕ or fermionic ψ supermultiplet members.

The first two lines are the typical kinetic terms for fermions and bosons in two-component Weyl fermion notation. The second derivative of the superpotential leaves us with the Yukawa interactions. From the last term in the fourth line we get interactions between gauginos, scalars and fermions. They appear by requesting supersymmetry to hold after transitioning from ordinary to gauge-covariant derivatives [373]. The remaining terms include the scalar potential.

For phenomenological studies the breaking mechanism must not be known in detail. Instead, it will get parametrized into an extra term $\mathcal{L}^{\text{soft}}$ which gets added to the $\mathcal{L}^{\text{SUSY}}$. A general approach to the soft Lagrangian is

$$\begin{aligned}
\mathcal{L}_{\text{MSSM}}^{\text{soft}} = & -\frac{1}{2} [M_1 \tilde{B} \cdot \tilde{B} + M_2 \tilde{W} \cdot \tilde{W} + M_3 \tilde{g} \cdot \tilde{g} + \text{H.c.}] \\
& - \tilde{Q}_L^\dagger \mathbf{m}_{\tilde{Q}}^2 \tilde{Q}_L - \tilde{u}_R \mathbf{m}_{\tilde{U}}^2 \tilde{u}_R^\dagger - \tilde{d}_R \mathbf{m}_{\tilde{D}}^2 \tilde{d}_R^\dagger - \tilde{L}_L \mathbf{m}_{\tilde{L}}^2 \tilde{L}_L^\dagger - \tilde{e}_R \mathbf{m}_{\tilde{E}}^2 \tilde{e}_R^\dagger \\
& - m_{H_u}^2 H_u^\dagger H_u - m_{H_d}^2 H_d^\dagger H_d \\
& - \left[\tilde{u}_R^\dagger \mathbf{T}^u \tilde{Q}_L \cdot H_u - \tilde{d}_R^\dagger \mathbf{T}^d \tilde{Q}_L \cdot H_d - \tilde{e}_R^\dagger \mathbf{T}^e \tilde{L}_L \cdot H_d + b H_u \cdot H_d + \text{H.c.} \right],
\end{aligned} \tag{5.1.7}$$

where M_k denotes the mass of the fermionic gauginos: the bino, winos and gluino. Next, there are 3×3 matrices \mathbf{m} for both squarks and sleptons and m_H masses for the two Higgs doublets. Then, the 3×3 matrices \mathbf{T} parametrize trilinear soft multiscalar interactions and the supersymmetry-breaking term of the Higgs potentials is b .

In total, the MSSM contains 124 real parameters, including 19 of the SM, but not all the parameters are completely independent. Moreover, the MSSM serves as a good proxy for other BSM theories, that are often included within its framework, making it a versatile tool for exploring a broad range of new physics. On the basis of experiments, this arbitrariness in the MSSM can be reduced by additional assumptions on the soft breaking parameters. Thus, many phenomenological Minimal Supersymmetric Standard Models (pMSSMs) include fewer parameters. Now that we have established the MSSM we can discuss some of its intriguing properties.

In the SM, the loop correction to the Higgs boson's mass exhibit quadratic divergences proportional to the masses of the particles in the loop. In its SUSY extension they are naturally cancelled by equivalent contributions from loops of superpartners with an opposite sign because of their different statistic. This is shown in the diagrammatic representation of the Higgs mass correction

$$\begin{array}{c}
 \text{---} H \text{---} \bigcirc \text{---} H \text{---} \\
 \uparrow \quad \downarrow \\
 f \quad f
 \end{array}
 +
 \begin{array}{c}
 \text{---} H \text{---} \bigcirc \text{---} H \text{---} \\
 \uparrow \quad \downarrow \\
 S
 \end{array}
 \quad (5.1.8)$$

$$\Delta m_H^2 = -\frac{\lambda^2}{8\pi^2} \Lambda_{\text{UV}}^2 + \dots + \frac{\lambda^2}{8\pi^2} \Lambda_{\text{UV}}^2 + \dots \quad (5.1.9)$$

$$= m_{\text{soft}}^2 \frac{\lambda}{16\pi^2} \log\left(\frac{\Lambda_{\text{UV}}}{m_{\text{soft}}}\right) \xrightarrow{\lambda \sim 1, \Lambda_{\text{UV}} \sim M_P} m_{\text{soft}} \sim \text{TeV}. \quad (5.1.10)$$

By assuming a cutoff Λ_{UV} at the Planck scale M_P in combination with natural couplings $\lambda \sim 1$, the smallest mass related to the soft breaking m_{soft} must be of the order of 1 TeV to reproduce the lightest observed Higgs mass without fine-tuning.

Similarly, to the new particles appearing in the Higgs loop corrections, they also appear in the running of the gauge couplings. We already explored the SM cases for QED and QCD in Sec. 2.1.1 and Sec. 2.1.4. They can be combined in one equation

$$\beta_{0,i}^{\text{SM}} = \begin{pmatrix} \beta_{0,U(1)}^{\text{SM}} \\ \beta_{0,SU(2)}^{\text{SM}} \\ \beta_{0,SU(3)}^{\text{SM}} \end{pmatrix} = \begin{pmatrix} 0 \\ \frac{22}{3} \\ 11 \end{pmatrix} - n_F \begin{pmatrix} \frac{4}{3} \\ \frac{4}{3} \\ \frac{4}{3} \end{pmatrix} - n_H \begin{pmatrix} \frac{1}{10} \\ \frac{1}{6} \\ 0 \end{pmatrix}, \quad (5.1.11)$$

where $n_F = 3$ is the number of matter multiplets and now includes the number of Higgs doublets $n_H = 1$. In the SUSY case the slopes of the RGE curves are modified

$$\beta_{0,i}^{\text{SUSY}} = \begin{pmatrix} \beta_{0,U(1)}^{\text{SUSY}} \\ \beta_{0,SU(2)}^{\text{SUSY}} \\ \beta_{0,SU(3)}^{\text{SUSY}} \end{pmatrix} = \begin{pmatrix} 0 \\ 6 \\ 9 \end{pmatrix} - n_F \begin{pmatrix} 2 \\ 2 \\ 2 \end{pmatrix} - n_H \begin{pmatrix} \frac{3}{10} \\ \frac{1}{2} \\ 0 \end{pmatrix}, \quad (5.1.12)$$

with $n_F = 3$ and $n_H = 2$, where the sign on $\beta_{0,SU(2)}$ has changed [378]. Once the scale reaches values that are close to the masses of the superpartners, the running of the couplings changes. By including them, unification of all three gauge couplings at the Grand Unified Theory (GUT) scale becomes possible for masses of the TeV order as shown in Fig. 5.1. This is observed through evolving the couplings by solving the RGEs up to the GUT scale $M_{\text{GUT}} \approx 10^{16} \text{GeV}$.

The open question on dark matter could be resolved through imposing the conserved R -Parity [380]

$$R_p = (-1)^{3(B-L)+2S}. \quad (5.1.13)$$

In the definition of the superpotential Eq. (5.1.5) we have not included any terms that violate the lepton L or baryon B number. Including such terms is heavily constrained

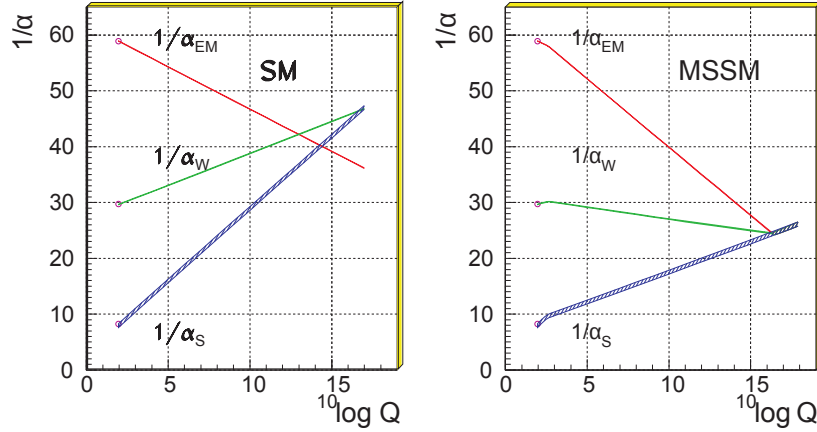


Figure 5.1: Running of the gauge couplings in the SM (left) and MSSM (right) [378, 379]. Unification is achieved only in the latter scenario. The SUSY particles are considered to contribute only at energies above the effective SUSY scale, M_{SUSY} , which is approximately 1 TeV. This contribution results in a change in the slope of the coupling constants' evolution. The thickness of the lines reflects the uncertainty in the values of these coupling constants.

from *e.g.* proton decays $p \rightarrow e^+ + \pi^0$, which have not been observed, but are possible within BSM. Only squarks and quarks have $|B| = \frac{1}{3}$ and the sleptons and leptons carry $|L| = 1$. From $\Delta S = \frac{1}{2}$ between superpartners it follows that $R_p = +1$ for SM and $R_p = -1$ for SUSY particles. Then only an even number of sparticles are allowed at each vertex, prohibiting the LSP from decaying. All remaining sparticles with a higher mass must decay into the LSP. Another consequence is that sparticles will only be produced in pairs at collider experiments.

Next, we will take a closer look at the mixing patterns of supersymmetric particles of interest for our process at leading order namely squarks and electroweakinos. At NLO electroweak production we will also encounter gluinos. While we give equations for the mixing and masses of these particles, in practice the mass spectra are generated by dedicated tools following the SUSY Les Houches Accord (SLHA) conventions [381]. We are going to use the Feynman rules from [382] in the same format as in Ref. [130] (cf. Sec. A.2).

5.1.2.1 Squarks

We will investigate the mixing of left- and right-handed squarks. The MSSM Lagrangian mass term written in the interaction basis $\tilde{q} = \begin{pmatrix} \tilde{q}_L \\ \tilde{q}_R \end{pmatrix}$ for squarks reads

$$\mathcal{L}_{\text{mass}}^{\tilde{q}} = - \sum_{\tilde{q}} \tilde{q}^\dagger \mathcal{M}_{\tilde{q}}^2 \tilde{q} \quad \text{with} \quad \mathcal{M}_{\tilde{q}}^2 = \begin{pmatrix} \mathcal{M}_{\tilde{q},LL}^2 & \mathcal{M}_{\tilde{q},LR}^2 \\ \mathcal{M}_{\tilde{q},LR}^{2*} & \mathcal{M}_{\tilde{q},RR}^2 \end{pmatrix}, \quad (5.1.14)$$

where the squark mass matrix is

$$\mathcal{M}_{\tilde{q}}^2 = \begin{pmatrix} M_{\tilde{q}}^2 + m_Z^2 \cos(2\beta)(I_3 - e_q \sin^2 \theta_W) + m_q^2 & m_q(A_q^* - \mu \tan(\beta)^{-2I_3}) \\ m_q(A_q - \mu^* \tan(\beta)^{-2I_3}) & M_{\tilde{q}'}^2 + m_Z^2 \cos(2\beta)e_q \sin^2 \theta_W + m_q^2 \end{pmatrix}. \quad (5.1.15)$$

The parameters entering are the quark mass m_q , electric charge e_q , third weak isospin I_3 , Z-boson mass m_Z and the Weinberg angle θ_W . From the MSSM we have the trilinear Higgs-squark-squark coupling A_q , higgsino mass parameter μ and mixing angle $\tan \beta = v_2/v_1$, defined by the ratio of the Higgs vacuum expectation values v_1 and v_2 . The mass terms $M_{\tilde{q}}^2$ and $M_{\tilde{q}'}^2$ parametrize the soft SUSY breaking with respect to left- and right-handed squarks.

Since we want to investigate mass eigenstates, we need to diagonalize this matrix. For the first two generations of squarks we can neglect the mixing between left- and right-handed states because the off-diagonal components are proportional to the corresponding quark mass which is negligible in high-energy computations. The mixing in the third generation of \tilde{t} will not be dropped. The diagonalization of a mass eigenstate from an interaction eigenstate is analogous to the prominent case of neutrino masses. A unitary squark mixing matrix $S^{\tilde{q}}$ should satisfy

$$S^{\tilde{q}} \mathcal{M}_{\tilde{q}}^2 S^{\tilde{q}\dagger} = \begin{pmatrix} m_{\tilde{q}_1}^2 & 0 \\ 0 & m_{\tilde{q}_2}^2 \end{pmatrix} \quad \text{and} \quad \begin{pmatrix} \tilde{q}_1 \\ \tilde{q}_2 \end{pmatrix} = S^{\tilde{q}} \begin{pmatrix} \tilde{q}_L \\ \tilde{q}_R \end{pmatrix}. \quad (5.1.16)$$

The eigenvalues of $\mathcal{M}_{\tilde{q}}^2$ are

$$m_{\tilde{q}_{1,2}}^2 = \frac{1}{2} \left[\mathcal{M}_{\tilde{q},LL}^2 + \mathcal{M}_{\tilde{q},RR}^2 \mp \sqrt{(\mathcal{M}_{\tilde{q},LL}^2 - \mathcal{M}_{\tilde{q},RR}^2)^2 + 4|\mathcal{M}_{\tilde{q},LR}|^2} \right], \quad (5.1.17)$$

with the ordering $m_{\tilde{q}_1}^2 < m_{\tilde{q}_2}^2$. The squark mixing matrix can be expressed as a rotation by a mixing angle $\theta_{\tilde{q}}$

$$\begin{pmatrix} S_{i\tilde{q}}^{\tilde{q}} & S_{i(i+3)\tilde{q}}^{\tilde{q}} \\ S_{(i+3)\tilde{q}}^{\tilde{q}} & S_{(i+3)(i+3)\tilde{q}}^{\tilde{q}} \end{pmatrix} = \begin{pmatrix} \cos \theta_{\tilde{q}} & \sin \theta_{\tilde{q}} \\ -\sin \theta_{\tilde{q}} & \cos \theta_{\tilde{q}} \end{pmatrix}, \quad \text{where} \quad \tan 2\theta_{\tilde{q}} = \frac{2\mathcal{M}_{\tilde{q},LR}^2}{\mathcal{M}_{\tilde{q},LL}^2 - \mathcal{M}_{\tilde{q},RR}^2}, \quad (5.1.18)$$

and we added an index i for each generation resulting in a 6×6 matrix. Then the coupling of a gluino to a quark I and an antisquark j is given by

$$\mathcal{R}'_{Ij} = \mathcal{L}'_{Ij} = \sqrt{2} S_{j(I+3)}^{\tilde{q}}, \quad (5.1.19)$$

$$\mathcal{L}'_{Ij} = \mathcal{R}'_{Ij} = -\sqrt{2} S_{jI}^{\tilde{q}}. \quad (5.1.20)$$

The restriction to minimal squark mixing results in

$$S_{j(I+3)}^{\tilde{q}*} S_{jJ}^{\tilde{q}} = 0 = \mathcal{L}'_{jJ}, \quad (5.1.21)$$

$$S_{jI}^{\tilde{q}*} S_{j(I+3)}^{\tilde{q}} = 0 = \mathcal{R}'_{jI}, \quad (5.1.22)$$

since one of the elements of S is an off-diagonal element which are zero.

Renormalization For studying squark-electroweakino production in Sec. 5.3 we will only need to add the squark renormalization to the already discussed quark and gluon renormalization (cf. Sec. 3.1.3). We start from a typical bare Lagrangian for scalars

$$\mathcal{L}_0 = \sum_{i=1}^2 (\partial_\mu \tilde{q}_{0,i}^\dagger \partial_\mu \tilde{q}_{0,i} - m_{0,i}^2 \tilde{q}_{0,i}^\dagger \tilde{q}_{0,i}), \quad (5.1.23)$$

but include a sum over the mass eigenstates i . Our renormalization constants are

$$\tilde{q}_{0,i} \rightarrow \sqrt{Z_{ij}} \tilde{q}_j = (\delta_{ij} + \frac{1}{2} \delta Z_{ij}) \tilde{q}_j, \quad (5.1.24)$$

$$m_{0,i}^2 \rightarrow Z_{m_i}^2 m_i^2 = (\delta_{ij} + \delta Z_{m_i}^2) m_i^2, \quad (5.1.25)$$

where the sum over j allows for the inclusion of mixing between eigenstates in loop corrections. Replacing the bare fields gives the new Lagrangian

$$\begin{aligned} \mathcal{L} = & \underbrace{\sum_{i=1}^2 (\partial_\mu \tilde{q}_i^\dagger \partial_\mu \tilde{q}_i - m_i^2 \tilde{q}_i^\dagger \tilde{q}_i)}_{\mathcal{L}_0} \\ & + \underbrace{\sum_{i=1}^2 \sum_{j=1}^2 \left(\frac{1}{2} (\delta Z_{ji}^* + \delta Z_{ij}) \partial_\mu \tilde{q}_i^\dagger \partial_\mu \tilde{q}_j - (\delta_{ij} \delta Z_{m_i}^2 + \frac{1}{2} (\delta Z_{ji} m_j^2 + \delta Z_{ij} m_i^2)) \tilde{q}_i^\dagger \tilde{q}_j \right)}_{\mathcal{L}_\times}. \end{aligned} \quad (5.1.26)$$

Repeating the same steps as for the quarks, we get a two-point function from the Lagrangian for the counterterms

$$-i\Sigma_{\times,ij} = i \left(\frac{1}{2} (\delta Z_{ij} + \delta Z_{ji}^*) p^2 - \frac{1}{2} (m_i^2 \delta Z_{ij} + m_j^2 \delta Z_{ji}^*) - m_i^2 \delta Z_{m_i}^2 \delta_{ij} \right). \quad (5.1.27)$$

Combining bare self-energy and counterterms

$$\hat{\Sigma}_{ij} = \Sigma_{ij} + \Sigma_{\times,ij} \quad (5.1.28)$$

we get the renormalized self-energy. Using the on-shell conditions again, we obtain our renormalization constants. Requiring the propagator pole to be at the physical mass in the case of $i = j$ leads to

$$\text{Re}[\hat{\Sigma}_{ii}(m_i^2)] = 0 \implies \delta Z_{m_i}^2 = -\frac{\text{Re}[\Sigma_{ii}(m_i^2)]}{m_i^2} \quad (5.1.29)$$

and the fact that the real part of the residue of the propagator must be one results in

$$\delta Z_{ii} = \text{Re}[\hat{\Sigma}_{ii}(m_i^2)]. \quad (5.1.30)$$

For $i \neq j$ the mass counterterm does not appear, since we want no transition from type i to j . Thus, we write

$$\text{Re}[\hat{\Sigma}_{12}(m_1^2)] = 0 \quad \text{and} \quad \text{Re}[\hat{\Sigma}_{12}(m_2^2)] = 0 \quad (5.1.31)$$

leading to

$$\delta Z_{12} = -2 \frac{\text{Re}[\Sigma_{12}(m_2^2)]}{m_1^2 - m_2^2} \quad \text{and} \quad \delta Z_{21} = +2 \frac{\text{Re}[\Sigma_{21}(m_1^2)]}{m_1^2 - m_2^2}. \quad (5.1.32)$$

5.1.2.2 Electroweakinos

The neutralinos and charginos are mixtures of higgsinos and electroweak gauginos. This mixing is an effect of electroweak symmetry breaking. We will occasionally refer to them loosely as gauginos, although we do not mean to include the gluino. The electroweakinos do not need any renormalization treatment, since the goal of our perturbative calculation is an improvement by $\mathcal{O}(\alpha_S)$.

Charginos As only fields with the same quantum numbers mix, the charginos will consist of charged higgsinos (\tilde{H}_u^+ and \tilde{H}_d^-) and winos (\tilde{W}^+ and \tilde{W}^-) and carry a charge of ± 1 . The relevant Lagrangian in two-component Weyl spinors is

$$\mathcal{L}_{\text{mass}}^n = -(\psi^-)^T \mathcal{M}^c \psi^+ + \text{H.c.}, \quad (5.1.33)$$

with

$$\mathcal{M}^c = \begin{pmatrix} M_2 & \sqrt{2}M_W \sin \beta \\ \sqrt{2}M_W \cos \beta & \mu \end{pmatrix}, \quad \psi^+ = \begin{pmatrix} i\tilde{W}^+ \\ \tilde{H}_u^+ \end{pmatrix} \quad \text{and} \quad \psi^- = \begin{pmatrix} i\tilde{W}^- \\ \tilde{H}_d^- \end{pmatrix}. \quad (5.1.34)$$

Mass eigenstates follow from diagonalization with two unitary matrices U and V

$$\begin{pmatrix} \tilde{\chi}_1^+ \\ \tilde{\chi}_2^+ \end{pmatrix} = V \begin{pmatrix} i\tilde{W}^+ \\ \tilde{H}_u^+ \end{pmatrix} \quad \text{and} \quad \begin{pmatrix} \tilde{\chi}_1^- \\ \tilde{\chi}_2^- \end{pmatrix} = U \begin{pmatrix} i\tilde{W}^- \\ \tilde{H}_d^- \end{pmatrix}. \quad (5.1.35)$$

The masses are again ordered $M_{\tilde{\chi}_1^\pm} < M_{\tilde{\chi}_2^\pm}$

$$M_{\tilde{\chi}_{1,2}^\pm} = \frac{1}{2} \left(|M_2|^2 + |\mu|^2 + 2m_W^2 \mp \sqrt{(|M_2|^2 + |\mu|^2 + 2m_W^2)^2 - 4|m_W^2 \sin 2\beta - \mu M_2|^2} \right). \quad (5.1.36)$$

Neutralinos The neutralino has no electric charge and is a Majorana particle. In contrast to charginos, the mixing also includes the bino \tilde{B} . The Lagrangian in the interaction basis ψ^0 is

$$\mathcal{L}_{\text{mass}}^c = -\frac{1}{2}(\psi^0)^T \mathcal{M}^n \psi^0 + \text{H.c.}, \quad (5.1.37)$$

where the mass matrix is

$$\mathcal{M}^n = \begin{pmatrix} M_1 & 0 & -M_Z c_\beta s_W & M_Z s_\beta s_W \\ 0 & M_2 & M_Z c_\beta c_W & -M_Z s_\beta c_W \\ -M_Z c_\beta s_W & M_Z c_\beta c_W & 0 & -\mu \\ M_Z s_\beta s_W & -M_Z s_\beta c_W & -\mu & 0 \end{pmatrix}, \quad \text{and} \quad (\psi^0)^T = \begin{pmatrix} i\tilde{B} \\ i\tilde{W}^0 \\ \tilde{H}_d^0 \\ \tilde{H}_u^0 \end{pmatrix}, \quad (5.1.38)$$

with abbreviated $s_W = \sin \theta_W$ and $c_W = \cos \theta_W$ for the Weinberg angle θ_W and the relation between the two Higgs vacuum expectation values β . The unitary matrix N

transforms the gauge eigenstates to a mass diagonal form via $N^* \mathcal{M}^n N^{-1}$ and the mass eigenstates are

$$\begin{pmatrix} \tilde{\chi}_1^0 \\ \tilde{\chi}_2^0 \\ \tilde{\chi}_3^0 \\ \tilde{\chi}_4^0 \end{pmatrix} = N \begin{pmatrix} i\tilde{B} \\ i\tilde{W}^0 \\ \tilde{H}_d^0 \\ \tilde{H}_u^0 \end{pmatrix}. \quad (5.1.39)$$

Assuming the usual ordering $|M_{\tilde{\chi}_1^0}| < |M_{\tilde{\chi}_2^0}| < |M_{\tilde{\chi}_3^0}| < |M_{\tilde{\chi}_4^0}|$ the lightest neutralino $\tilde{\chi}_1^0$ could emerge as the LSP and dark matter (DM) candidate.

5.1.2.3 Gluino

In the MSSM there is no other colour octet fermion that could mix with the gluino. The gluino mass enters as the parameter M_3 in the MSSM and as it is electrically neutral it is a Majorana fermion. In most scenarios the gluino is much heavier than the charginos and neutralinos. This is a consequence of requesting unification at the GUT scale and at higher-orders the gluino mass is no longer M_3 [373].

5.1.3 Collider phenomenology

The Run 3 data taking period of the LHC has started in 2022 at an unprecedented centre-of-mass energy of $\sqrt{S} = 13.6$ TeV. The two main general-purpose LHC experiments ATLAS and CMS are expected to collect an integrated luminosity of about 300 fb^{-1} , which will complement the 140 fb^{-1} already collected at 13 TeV during Run 2. This increase in luminosity and centre-of-mass energy will thus make it possible to further explore extensions of the SM of particle physics, such as the MSSM. Especially, LHC's planned extension to HL-LHC will provide access to very massive new particles [383–385]. In SUSY, the generally dominant production processes are those involving the strong interaction and thus concern the pair production of squarks and gluinos. Thus, experimental searches at the LHC have mainly focused on signatures arising from the production and decay of squarks and gluinos. For a long time, the signatures of these QCD-sensitive superparticles were consequently expected to be the first visible sign of supersymmetry in LHC data. However, with the associated mass limits being now deeply in the TeV regime and too massive for pair production at the LHC, searches for typically lighter electroweakinos and sleptons received more attention and became equally important. These processes then also have the advantage of providing insights not only on the supersymmetric masses, but also on the supersymmetric interactions [376, 386, 387]. The mass hierarchy, coupling strength, and mixing of electroweak particles are all essential factors in determining decay patterns and experimental signatures.

Subsequently, accurate theoretical calculations of signal cross sections and key kinematic distributions for all supersymmetric processes became imperative, and in particular for processes in which at least one non-strongly interacting superpartner is present in the final-state. Already by going from LO to NLO in pQCD, the theoretical uncertainty originating from the arbitrary choice of factorization and renormalization scales is reduced. However, with the possibility of light SUSY particles being excluded by direct searches at the LHC, the current mass limits imply that in any SUSY production process the kinematic configuration approaches the production threshold. This results

in large threshold logarithms ruining the convergence of the perturbative series, so that they must be resummed. This resummation procedure has been known for quite some time at the leading-logarithmic (LL) and NLL accuracy and in some cases beyond and has been found to generally further reduce the theoretical uncertainty inherent in the perturbative calculation [388–393].

The production cross section of a pair of electroweakinos at hadron colliders has been studied in numerous works, in which fixed-order predictions at LO [394, 395] and NLO [396] have been considered. Further precision was obtained by matching these fixed-order results with either parton showers [376, 397] (NLO+PS) or the threshold resummation of the NLL [398–400] (NLO+NLL). Furthermore, approximate next-to-next-to-leading-order (aNNLO) predictions have been recently matched with threshold resummation at the next-to-next-to-leading-logarithmic (NNLL) [401] giving aNNLO+NNLL accuracy. Similarly, slepton pair production total cross sections are known at LO [395, 402], NLO [396], NLO+PS [376, 403], NLO+NLL [404–406] and aNNLO+NNLL [407].

The `Resummino` program has been developed in this context and takes advantage of these developments of the last few decades. It consists of a public tool computing precision predictions including soft-gluon radiation resummation effects for the production of a pair of sleptons, electroweakinos, and for the associated production of one electroweakino and either one squark or one gluino. It combines the LO calculations for slepton-pair, electroweakino-pair, associated gluino-electroweakino and squark-electroweakino production available from [408–410] with the associated NLO SUSY-QCD corrections obtained in [1, 398, 404, 411], and with the aNNLO QCD corrections of [401, 407]. These fixed-order predictions are next matched with the threshold resummation of soft gluon radiation to all orders and at varied accuracies [1, 399, 401, 405, 407, 411], according to the standard formalism introduced in [388–393] or the collinear-improved one of [412–415]. In addition, the code can be employed to achieve NLO+NLL cross section computations in which fixed-order predictions are matched with soft gluon resummation in the small transverse momentum p_T regime [416, 417] following the formalism of [418–420], or jointly at small p_T and close to threshold [421, 422] following the formalism of [423–425].

So far, its predictions have been used by both the ATLAS and CMS collaborations in order to extract bounds on sleptons and electroweakinos. In particular, the most stringent constraints on simplified models inspired by the MSSM enforce viable slepton and electroweakino masses to be larger than about 700 GeV and 800 GeV to 1200 GeV respectively, for a not too heavy lightest SUSY particle (see *e.g.* [426–428]). The exact values of these mass limits depend on the details of the search channels, and the sensitivity of the bounds can be reduced by compressing the particle spectrum (which increases the mass of the lightest SUSY state) or by lowering the branching ratio in the final state of interest (by allowing multiple potential decay modes for a given SUSY particle). Recent experimental analyses at the LHC [429–433] pushed the lower bounds on the SUSY masses deep into the TeV regime, the exact limit depending on the scenario considered. However, in certain model scenarios such as when the SUSY spectrum is compressed, these limits may not apply, allowing for potential escape routes from the constraints imposed experimentally.

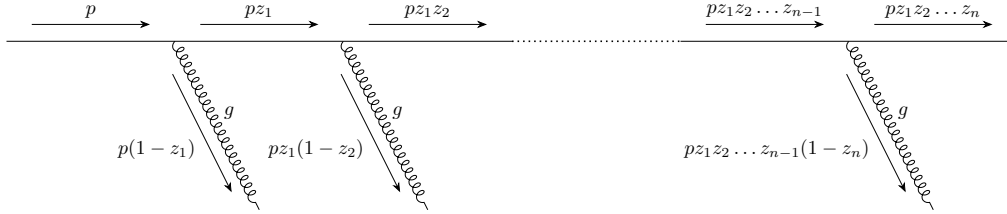


Figure 5.2: Emission of multiple soft gluons. The emitting parton can be either a quark or a gluon.

5.2 Threshold resummation of soft gluons

In Sec. 2.2.5 we have seen how parton showers can be used to simulate the soft and collinear approximated evolution of partons in the final-state. Instead of simulating their behaviour we can also resum the soft emissions to all orders in perturbation theory. This is particularly interesting when looking at the total production cross section of heavy particles, where the phase space is limited, *i.e.* they are mostly produced close to threshold [389]. To calculate the total hadronic cross section σ_{AB} for the process considered, we convolve the partonic cross section $d\sigma_{ab}$ with factorization-scale dependent PDFs $f_{i/h}(x_i, \mu_F^2)$ for a particle i of momentum fraction x_i in a hadron h ,

$$\begin{aligned} \sigma_{AB} = \int M^2 \frac{d\sigma_{AB}}{dM^2}(\tau) = \sum_{a,b} \int_0^1 dx_a dx_b dz \left[x_a f_{a/A}(x_a, \mu_F^2) \right] \left[x_b f_{b/B}(x_b, \mu_F^2) \right] \\ \times \left[z d\sigma_{ab}(z, M^2, \mu_R^2, \mu_F^2) \right] \delta(\tau - x_a x_b z), \end{aligned} \quad (5.2.1)$$

where $\tau = M^2/S$ is the ratio of the squared invariant mass M^2 over the hadronic centre-of-mass energy S [27]. The partonic fraction $z = \tau/(x_a x_b) = M^2/s$ is defined by the ratio of the squared invariant mass to the partonic centre-of-mass energy $s = x_a x_b S$ and equals one at LO.

In a NLO calculation, massless virtual loop particles (*e.g.* gluon) are integrated over the full loop momentum. This is in contrast to the particles in real emissions, since their integration is constrained. Therefore, after the cancellation of soft and collinear divergences among the real and virtual corrections, large logarithms remain near threshold [31, 126]. They take the form

$$\left(\frac{\alpha_S}{2\pi} \right)^n \left[\frac{\log^m(1-z)}{1-z} \right]_+ \quad \text{or} \quad \left(\frac{\alpha_S}{2\pi} \right)^n \log^m \left(\frac{M^2}{p_T^2} \right), \quad (5.2.2)$$

relative to the Born cross section with $m \leq 2n - 1$. The variable $1 - z = 1 - M^2/s$ describes the energy fraction of an additional emitted gluon or massless quark and thus quantifies the distance to the partonic threshold. This is depicted in Fig. 5.2 where $z_i \approx 1$ and every splitting contributes one α_S . For soft emitted particles ($z \rightarrow 1$), truncating the perturbative calculation at a fixed order does not give a reliable prediction, so that the logarithms must be resummed to all orders in α_S [130, 389].

Due to the factorization theorem we can split an IR sensitive quantity into a hard scattering \mathcal{H} and long distance \mathcal{S} behaviour, where only the latter two depend on the factorization scale μ_F

$$\sigma(M^2, m^2) = \mathcal{H}(M^2/\mu_F^2) \mathcal{S}(m^2/\mu_F^2). \quad (5.2.3)$$

Here M is the hard scale and m describing the distance to the threshold, *i.e.* similar to the evolution scale in a parton shower. Exploiting the independence of the factorization scale in σ by taking the derivative

$$0 \stackrel{!}{=} \frac{d\sigma(M^2, m^2)}{d \log \mu_F^2} = \frac{d\mathcal{H}}{d \log \mu_F^2} \mathcal{S} + \mathcal{H} \frac{d\mathcal{S}}{d \log \mu_F^2} = \mu_F^2 \frac{d\mathcal{H}}{d\mu_F^2} \mathcal{S} + \mu_F^2 \mathcal{H} \frac{d\mathcal{S}}{d\mu_F^2} \quad (5.2.4)$$

$$\implies \Gamma_S(\mu_F^2) = \mu_F^2 \frac{d\mathcal{H}}{\mathcal{H} d\mu_F^2} = -\mu_F^2 \frac{d\mathcal{S}}{\mathcal{S} d\mu_F^2}, \quad (5.2.5)$$

which is the RGE consisting of the soft anomalous dimension Γ_s for the soft function \mathcal{S} solved by an exponential ansatz

$$\mathcal{S}(m^2/\mu_F^2) = \mathcal{S}(1) \exp\left(-\int_{m^2}^{\mu_F^2} \frac{dk^2}{k^2} \Gamma_s(k^2)\right). \quad (5.2.6)$$

A natural consequence of requiring no dependence on the factorization scale is a reduced scale uncertainty in the cross section. Plugging this solution and $\mu_F = M$ into the Eq. (5.2.3) we get

$$\sigma(M^2, m^2) = \mathcal{H}(1) \mathcal{S}(1) \exp\left(-\int_{m^2}^{M^2} \frac{dk^2}{k^2} \Gamma_s(k^2)\right), \quad (5.2.7)$$

where the scale dependence is contained in the exponent. This is again the Sudakov form factor as in the parton shower Sec. 2.2.5. In the PS the integration bounds were $m^2 = \Lambda_{\text{QCD}}^2$ and $M^2 = Q^2$. Furthermore, the hard matching coefficient will be needed for matching the resummation to our NLO calculation where one must avoid double counting in the soft region.

5.2.1 Refactorization

To calculate soft gluon emission up to all orders, kinematic and dynamical factorization are necessary. One approach to kinematic factorization is by transforming into Mellin space such that the phase space factorizes

$$\int dz z^{N-1} d\phi_{2+n}(z) \approx d\phi_2 \times d\phi_n(N), \quad (5.2.8)$$

where N is our new Mellin momentum of z . Eq. (5.2.1) can be factorized by transforming its constituents into Mellin space

$$\tilde{F}(N) = \int_0^1 dy y^{N-1} F(y) \implies \left[\frac{\log^m(1-z)}{1-z} \right]_+ \xrightarrow{F} \log^{m+1} N + \dots, \quad (5.2.9)$$

with $F = \sigma_{AB}, \sigma_{ab}, f_{a/A}, f_{b/B}$ and $y = \tau, z, x_a, x_b$, respectively. We can look at the AP splitting functions (Eqs. (2.2.5) to (2.2.8)) in Mellin space

$$P_{qq}(N) = C_F \left(\frac{3}{2} + \frac{1}{N(N+1)} - 2 \sum_{k=1}^N \frac{1}{k} \right) \approx C_F \left(\frac{3}{2} - 2 \log \bar{N} \right), \quad (5.2.10)$$

$$P_{qg}(N) = C_F \left(\frac{2+N+N^2}{N(N^2-1)} \right) \approx \frac{C_F}{N}, \quad (5.2.11)$$

$$P_{gq}(N) = T_R \left(\frac{2 + N + N^2}{N(N+1)(N+2)} \right) \approx \frac{T_R}{N}, \quad (5.2.12)$$

$$P_{gg}(N) = \beta_0 + 2C_A \left(\frac{1}{N(N-1)} + \frac{1}{(N+1)(N+2)} - \sum_{k=1}^N \frac{1}{k} \right) \approx \beta_0 - 2C_A \log \bar{N}, \quad (5.2.13)$$

with $\bar{N} = Ne^{\gamma_E}$ where the logarithms arise from

$$\gamma_E = \lim_{N \rightarrow \infty} \left(\sum_{k=1}^N \frac{1}{k} - \log N \right) \approx 0.577216, \quad (5.2.14)$$

$$\lim_{N \rightarrow \infty} \log \bar{N} = \lim_{N \rightarrow \infty} (\log N + \gamma_E) = \sum_{k=1}^N \frac{1}{k}. \quad (5.2.15)$$

For $z \rightarrow 1$ the logarithms are associated to the diverging denominators while constants come from $\delta(1-z)$. From those equations we can also understand why we only resum soft gluon emissions, *i.e.* the diagonal splitting terms, that are not suppressed by $1/N$. Denoting in the following all quantities in Mellin space and therefore dropping the tilde for simplicity, we obtain from Eq. (5.2.1)

$$M^2 \frac{d\sigma_{AB}}{dM^2}(N-1) = \sum_{a,b} f_{a/A}(N, \mu_F^2) f_{b/B}(N, \mu_F^2) \sigma_{ab}(N, M^2, \mu_F^2, \mu_R^2), \quad (5.2.16)$$

such that the phase space factorizes. In this expression, the large logarithms now depend on the Mellin variable N , *e.g.* LL contributions are $\log^2 N$ and NLL contributions are $\log N$. Dynamical factorization can then be achieved by relying on eikonal Feynman rules (cf. Sec. 3.1.1.1).

The partonic cross section can be refactorized and resummed to

$$\begin{aligned} \sigma_{ab \rightarrow ij}(N, M^2, \mu_F^2, \mu_R^2) &= \sum_I \mathcal{H}_{ab \rightarrow ij, I}(M^2, \mu_F^2, \mu_R^2) \Delta_a(N, M^2, \mu_F^2, \mu_R^2) \\ &\quad \times \Delta_b(N, M^2, \mu_F^2, \mu_R^2) \Delta_{ab \rightarrow ij, I}(N, M^2, \mu_F^2, \mu_R^2), \end{aligned} \quad (5.2.17)$$

in which the hard function is given by

$$\mathcal{H}_{ab \rightarrow ij, I}(M^2, \mu_F^2, \mu_R^2) = \sum_{n=0}^{\infty} \left(\frac{\alpha_S}{2\pi} \right)^n \mathcal{H}_{ab \rightarrow ij, I}^{(n)}(M^2, \mu_F^2, \mu_R^2). \quad (5.2.18)$$

This quantity is further discussed in Sec. 5.2.2 [27, 391, 392]. The irreducible colour representation index I is dropped from now on, since electroweak production involves only a single colour tensor. Similar to Eq. (5.2.7) we have [392]

$$\sigma_{ab \rightarrow ij}^{\text{Res.}}(N, M^2, \mu_R^2, \mu_F^2) = \mathcal{H}_{ab \rightarrow ij}(M^2, \mu_R^2, \mu_F^2) \exp [G_{ab \rightarrow ij}(N, M^2, \mu_R^2, \mu_F^2)], \quad (5.2.19)$$

with the N -independent hard function $\mathcal{H}_{ab \rightarrow ij}$ and the Sudakov exponent $G_{ab \rightarrow ij}$

$$G_{ab \rightarrow ij}(N, M^2, \mu_R^2, \mu_F^2) \approx LG_{ab}^{(1)}(N) + G_{ab \rightarrow ij}^{(2)}(N, M^2, \mu_F^2, \mu_R^2) + \alpha_S G_{ab \rightarrow ij}^{(3)}(N, M^2, \mu_F^2, \mu_R^2), \quad (5.2.20)$$

with $L = \log Ne^{\gamma_E}$ and γ_E the Euler-Mascheroni constant. The soft wide-angle function $\Delta_{ab \rightarrow ij}$ and the soft collinear radiation functions $\Delta_{a,b}$ exponentiate [388–390, 393],

$$\Delta_a \Delta_b \Delta_{ab \rightarrow ij} = \exp \left[LG_{ab}^{(1)}(\lambda) + G_{ab \rightarrow ij}^{(2)}(\lambda, M^2, \mu_F^2, \mu_R^2) + G_{ab \rightarrow ij}^{(3)}(\lambda, M^2, \mu_F^2, \mu_R^2) \right], \quad (5.2.21)$$

with $\lambda = \alpha_S b_0 L$, $L = \log \bar{N}$ and $\bar{N} = Ne^{\gamma_E}$. The above expressions contain the LL $G_{ab}^{(1)}$, NLL $G_{ab \rightarrow ij}^{(2)}$ and NNLL $G_{ab \rightarrow ij}^{(3)}$ contributions. **Resumino** only provides NNLL for slepton and electroweakino pair production thus the term $G_{ab \rightarrow ij}^{(3)}$ is only required for initial quarks. We provide its expression together with that of the next two coefficients of the QCD beta function, that are relevant for the formulas given below. They were given in Eqs. (2.1.16) to (2.1.18) already and are now normalized according to $b_n = \beta_n / (2\pi)^{n+1}$ [434, 435], which gives

$$b_0 = \frac{1}{12\pi} (11C_A - 2n_f), \quad (5.2.22)$$

$$b_1 = \frac{1}{24\pi^2} (17C_A^2 - 5C_A n_f - 3C_F n_f), \quad (5.2.23)$$

$$b_2 = \frac{1}{64\pi^3} \left(\frac{2857}{54} C_A^3 - \frac{1415}{54} C_A^2 n_f + C_F^2 n_f - \frac{205}{18} C_A C_F n_f + \frac{79}{54} C_A n_f^2 + \frac{11}{9} C_F n_f^2 \right), \quad (5.2.24)$$

with $C_A = N_C = 3$, $C_F = (N^2 - 1)/(2N_C) = 4/3$ and the number of active quark flavours $n_f = 5$. They are given by [388–390, 393, 412]

$$G_{ab}^{(1)}(\lambda) = \sum_{c \in \{a,b\}} g_c^{(1)}(\lambda), \quad (5.2.25)$$

$$G_{ab \rightarrow ij}^{(2)}(\lambda, M^2, \mu_F^2, \mu_R^2) = \sum_{c \in \{a,b\}} g_c^{(2)}(\lambda, M^2, \mu_F^2, \mu_R^2) + h_{ab \rightarrow ij}^{(2)}(\lambda), \quad (5.2.26)$$

$$G_{ab \rightarrow ij}^{(3)}(\lambda, M^2, \mu_F^2, \mu_R^2) = \sum_{c \in \{a,b\}} g_c^{(3)}(\lambda, M^2, \mu_F^2, \mu_R^2) + h_{ab \rightarrow ij}^{(3)}(\lambda), \quad (5.2.27)$$

with

$$g_a^{(1)} = \frac{A_a^{(1)}}{4\pi b_0 \lambda} [2\lambda + (1 - 2\lambda) \log(1 - 2\lambda)], \quad (5.2.28)$$

$$g_a^{(2)} = \frac{A_a^{(1)} b_1}{4\pi b_0^3} \left[2\lambda + \log(1 - 2\lambda) + \frac{1}{2} \log^2(1 - 2\lambda) \right] - \frac{A_a^{(2)}}{8\pi^2 b_0^2} [2\lambda + \log(1 - 2\lambda)] \\ + \frac{A_a^{(1)}}{4\pi b_0} \left[\log(1 - 2\lambda) \log\left(\frac{M^2}{\mu_R^2}\right) + 2\lambda \log\left(\frac{\mu_F^2}{\mu_R^2}\right) \right], \quad (5.2.29)$$

whereas the third quark coefficient is given by

$$\begin{aligned}
g_q^{(3)} &= \frac{A_q^{(3)}}{\pi^3 b_0^2} \frac{\lambda^2}{1-2\lambda} + \frac{2A_q^{(1)}}{\pi} \zeta_2 \frac{\lambda}{1-2\lambda} - \frac{A_q^{(2)} b_1}{(2\pi)^2 b_0^3} \frac{2\lambda^2 + 2\lambda + \log(1-2\lambda)}{1-2\lambda} \\
&- \frac{A_q^{(2)}}{2\pi^2 b_0} \left[\frac{\lambda}{1-2\lambda} \log\left(\frac{M^2}{\mu_R^2}\right) - \lambda \log\left(\frac{\mu_F^2}{\mu_R^2}\right) \right] \\
&+ \frac{A_q^{(1)} b_1^2}{2\pi b_0^4} \frac{2\lambda^2 + 2\lambda \log(1-2\lambda) + \frac{1}{2} \log^2(1-2\lambda)}{1-2\lambda} \\
&+ \frac{A_q^{(1)} b_2}{2\pi b_0^3} \left[2\lambda + \log(1-2\lambda) + \frac{2\lambda^2}{1-2\lambda} \right] + \frac{A_q^{(1)} b_1}{2\pi b_0^2} \frac{2\lambda + \log(1-2\lambda)}{1-2\lambda} \log\left(\frac{M^2}{\mu_R^2}\right) \\
&+ \frac{A_q^{(1)}}{2\pi} \left[\frac{\lambda}{1-2\lambda} \log^2\left(\frac{M^2}{\mu_R^2}\right) - \lambda \log^2\left(\frac{\mu_F^2}{\mu_R^2}\right) \right].
\end{aligned} \tag{5.2.30}$$

The resummation coefficients entering those quantities are

$$A_a^{(1)} = 2C_a, \tag{5.2.31}$$

$$A_a^{(2)} = 2C_a \left[\left(\frac{67}{18} - \frac{\pi^2}{6} \right) C_A - \frac{5}{9} n_f \right], \tag{5.2.32}$$

and again only for quarks

$$\begin{aligned}
A_q^{(3)} &= \frac{1}{2} C_F \left[C_A^2 \left(\frac{245}{24} - \frac{67}{9} \zeta_2 + \frac{11}{6} \zeta_3 + \frac{11}{5} \zeta_2^2 \right) + C_A n_f \left(\frac{10}{9} \zeta_2 - \frac{7}{3} \zeta_3 - \frac{209}{108} \right) \right. \\
&\quad \left. - \frac{n_f^2}{27} + C_F n_f \left(2\zeta_3 - \frac{55}{24} \right) \right],
\end{aligned} \tag{5.2.33}$$

with $C_a = C_F$ for quarks and $C_a = C_A$ for gluons. The last term in Eq. (5.2.27) consists of the process-dependent contributions related to large-angle soft-gluon emissions. It can be expressed in terms of the soft anomalous dimension $\Gamma_{ab \rightarrow ij}$ associated with the partonic process $ab \rightarrow ij$, from which the DY soft anomalous dimension Γ_{ab}^{DY} has been subtracted

$$\begin{aligned}
h_{ab \rightarrow ij}^{(2)}(\lambda) &= \frac{\log(1-2\lambda)}{2\pi b_0} D_{ab \rightarrow ij}^{(1)} \\
&= \frac{\log(1-2\lambda)}{b_0 \alpha_S} \text{Re}(\Gamma_{ab \rightarrow ij} - \Gamma_{ab}^{\text{DY}}) = \frac{\log(1-2\lambda)}{b_0 \alpha_S} \text{Re}(\bar{\Gamma}_{ab \rightarrow ij}),
\end{aligned} \tag{5.2.34}$$

with

$$\Gamma_{ab}^{\text{DY}} = \frac{\alpha_S}{2\pi} \sum_{k=\{a,b\}} C_k \left[1 - \log(2) - i\pi - \log\left(\frac{(v_k \cdot n)^2}{|n|^2}\right) \right], \tag{5.2.35}$$

where n is an axial gauge vector fulfilling $|n|^2 = -n^2 + i\epsilon$.

For DY-like processes computed at the aNNLO+NNLL accuracy (namely electroweakino and slepton pair production), the coefficient $h_{ab \rightarrow ij}^{(3)}$ must be included too. It is in this case universal, and it is given by

$$h_{ab \rightarrow ij}^{(3)}(\lambda) = -\frac{2C_F}{2\pi^2 b_0} \frac{\lambda}{1-2\lambda} \left[n_f \left(\frac{14}{27} - \frac{2}{3} \zeta_2 \right) + C_A \left(-\frac{101}{27} + \frac{11}{3} \zeta_2 + \frac{7}{2} \zeta_3 \right) \right]. \quad (5.2.36)$$

To calculate the soft anomalous dimension $\bar{\Gamma}$ we use

$$\Gamma_{ab \rightarrow ij} = -\sum_{kl} C^{kl} \lim_{\epsilon \rightarrow 0} \epsilon \omega^{kl}, \quad (5.2.37)$$

where the sum goes over the eikonal lines, C^{kl} are colour factors which depend on the specific diagram. ω^{kl} are integrals on the kinematical quantities of the specific diagram

$$\omega^{kl} = g_s \int \frac{d^D q}{(2\pi)^D} \frac{-i}{q^2 + i\epsilon} \left[\frac{\Delta_k \Delta_l v_k \cdot v_l}{(\delta_k v_k \cdot q + i\epsilon)(\delta_l v_l \cdot q + i\epsilon)} - \frac{\delta_l \Delta_l \Delta_k v_k \cdot n}{\delta_k v_k \cdot q + i\epsilon} \frac{P}{(n \cdot q)} - \frac{\delta_k \Delta_k \Delta_l v_l \cdot n}{\delta_l v_l \cdot q + i\epsilon} \frac{\delta_k \Delta_k \delta_l \Delta_l P}{(n \cdot q)} + n^2 \frac{P}{(n \cdot q)^2} \right], \quad (5.2.38)$$

where P stands for principal value

$$\frac{P}{(n \cdot q)^\beta} = \frac{1}{2} \left(\frac{1}{(n \cdot q + i\epsilon)^\beta} + (-1)^\beta \frac{1}{(-n \cdot q + i\epsilon)^\beta} \right) \quad (5.2.39)$$

and the Δ and δ signs are given in Tab. 3.1.

5.2.2 Hard matching coefficient

The resummation of the logarithmic contributions as performed in Eq. (5.2.21) scales with the hard function $\mathcal{H}_{ab \rightarrow ij}(M^2, \mu_F^2, \mu_R^2)$, as shown in Eq. (5.2.17). Including higher-order contribution in the hard function hence further improves the accuracy of the predictions. The N -independent hard function \mathcal{H} can be written in terms of the LO Mellin-transformed cross section $\sigma_{ab \rightarrow ij}^{(0)}$ and the hard matching coefficient $C_{ab \rightarrow ij}$,

$$\mathcal{H}_{ab \rightarrow ij}(M^2, \mu_F^2, \mu_R^2) = \sigma_{ab \rightarrow ij}^{(0)} C_{ab \rightarrow ij}(M^2, \mu_F^2, \mu_R^2), \quad (5.2.40)$$

where the coefficient $C_{ab \rightarrow ij}$ can be computed perturbatively,

$$C_{ab \rightarrow ij}(M^2, \mu_F^2, \mu_R^2) = \sum_{n=0} \left(\frac{\alpha_S}{2\pi} \right)^n C_{ab}^{(n)}(M^2, \mu_F^2, \mu_R^2). \quad (5.2.41)$$

The hard matching coefficients $C_{ab}^{(n)}$ are then derived from fixed-order predictions in Mellin space at a given order in the strong coupling α_S . They correspond to the ratio of the finite N -independent pieces of the N^n LO correction terms over the LO cross section

$$C_{ab}^{(n)}(M^2, \mu_F^2, \mu_R^2) = \left(\frac{2\pi}{\alpha_S} \right)^n \left[\frac{\sigma_{ab \rightarrow ij}^{(n)}}{\sigma_{ab \rightarrow ij}^{(0)}} \right]_{N\text{-ind.}}. \quad (5.2.42)$$

Therefore, in addition to the LO term

$$\mathcal{H}_{ab \rightarrow ij}^{(0)}(M^2, \mu_F^2, \mu_R^2) = \sigma_{ab \rightarrow ij}^{(0)}(M^2), \quad (5.2.43)$$

we include the N -independent parts of the NLO cross section in the one-loop hard matching coefficient

$$\mathcal{H}_{ab \rightarrow ij}^{(1)}(M^2, \mu_F^2, \mu_R^2) = \sigma_{ab \rightarrow ij}^{(0)}(M^2) C_{ab \rightarrow ij}^{(1)}(M^2, \mu_F^2, \mu_R^2) \quad (5.2.44)$$

for a NLO+NLL prediction.

To compute this coefficient, we begin with the full NLO cross section of Eq. (3.1.126). We first neglect the real emission contributions due to the three-particle phase space suppression close to threshold [436, 437]. The virtual contributions $d\sigma^V$ and the integrated dipoles $\int_1 d\sigma^A$ in Eq. (3.1.126) correspond to a contribution proportional to $\delta(1-z)$, that is thus constant in N after a Mellin transform. The collinear remainder is split into two pieces related to the insertion operators \mathbf{P} and \mathbf{K} , in which only the former depends on the factorization scale μ_F [180, 191, 193]. While logarithmic, but formally suppressed $\mathcal{O}(1/N)$ contributions have been shown to exponentiate and improve the numerical scale dependence in DY like processes [412, 413, 438], we refrain from including them for our process. After discarding the $1/N$ terms that vanish in the large- N limit, only the diagonal terms survive.

With the N -independent parts of the insertion operators, the hard functions read

$$\mathcal{H}_{ab \rightarrow ij}^{(0)}(M^2, \mu^2) = \frac{\sigma^B(M^2)}{M^2}, \quad (5.2.45)$$

$$\begin{aligned} \mathcal{H}_{ab \rightarrow ij}^{(1)}(M^2, \mu^2) &= \frac{2\pi}{\alpha_S} \frac{\sigma^B(M^2)}{M^2} \left(\langle \mathbf{P} + \mathbf{K} \rangle_a + \langle \mathbf{P} + \mathbf{K} \rangle_b \right)_{N\text{-ind.}} \\ &+ \frac{2\pi}{\alpha_S} \left(\frac{\sigma^V(M^2) + \int_1 d\sigma^A(M^2)}{M^2} \right). \end{aligned} \quad (5.2.46)$$

The hard function $\mathcal{H}_{ab \rightarrow ij}^{(3)}$ is obtained similarly and the matching $C_{q\bar{q}}^{(3)}$ is the same for all DY processes. As we have ignored any $1/N$ terms in the above computation of the hard matching coefficient, we employ the standard collinear unimproved resummation formalism as opposed to the collinear improved one of Refs. [412–415]. While only the N -independent terms are necessary in practice, we included the logarithmic terms in the above expressions to be able to validate analytically the re-expansion of the resummed cross section at $\mathcal{O}(\alpha_S^2)$ in Sec. 5.2.3.

5.2.3 Matching and expansion

So far we have computed a fixed order cross section σ^{NLO} and a resummed cross section $\sigma^{\text{Res.}}$. As the latter is a good approximation near threshold and the former far from it, they should be consistently combined. Therefore, we sum up both contributions and remove the terms that are accounted for both in the resummed and the fixed-order predictions, thus avoiding any double counting. A consistent NLO matching is achieved by re-expanding $\sigma^{\text{Res.}}$ at $\mathcal{O}(\alpha_S^2)$ and subtracting this quantity $\sigma^{\text{Exp.}}$ from the sum of the resummed and fixed-order results

$$\sigma_{ab}^{\text{NLO+NLL}} = \sigma_{ab}^{\text{NLO}} + \underbrace{\sigma_{ab}^{\text{Res.}} - \sigma_{ab}^{\text{Exp.}}}_{\sigma_{ab}^{\text{NLL}}}. \quad (5.2.47)$$

The expansion is given in terms of the first- ($\mathcal{H}^{(0)}$) and second-order ($\mathcal{H}^{(1)}$) hard function coefficients of Sec. 5.2.2

$$\begin{aligned}
\sigma_{ab}^{\text{Exp.}} &= \sigma_{ab \rightarrow ij}^{(0)} C_{ab \rightarrow ij}(M^2, \mu_F^2, \mu_R^2) \exp[G_{ab \rightarrow ij}(N, M^2, \mu_F^2, \mu_R^2)] \\
&= \sigma_{ab \rightarrow ij}^{(0)} \left[1 + \left(\frac{\alpha_S}{2\pi}\right) C_{ab}^{(1)} + \left(\frac{\alpha_S}{2\pi}\right)^2 C_{ab}^{(2)} + \dots \right] \\
&\cdot \left[1 + \left(\frac{\alpha_S}{2\pi}\right) K^{(1)} + \left(\frac{\alpha_S}{2\pi}\right)^2 K^{(2)} + \dots \right] \\
&\approx \mathcal{H}_{ab \rightarrow ij}^{(0)}(M^2, \mu^2) + \frac{\alpha_S}{2\pi} \mathcal{H}_{ab \rightarrow ij}^{(1)}(M^2, \mu^2) + \frac{\alpha_S}{2\pi} \mathcal{H}_{ab \rightarrow ij}^{(0)}(M^2, \mu^2) \\
&\times \left(\left(A_a^{(1)} + A_b^{(1)} \right) \left(\log \bar{N} + \log \frac{\mu_F^2}{M^2} \right) - 2D_{ab \rightarrow ij}^{(1)} \right) \log \bar{N}.
\end{aligned} \tag{5.2.48}$$

Where the final result is already truncated for NLL accuracy. The value of $K^{(1)}$ results from the expansions in $\alpha_S \sim \lambda$

$$Lg_a^{(1)} \xrightarrow{\lambda \rightarrow 0} L \frac{\lambda}{2\pi b_0} A_a^{(1)} = L^2 \frac{\alpha_S}{2\pi} A_a^{(1)}, \tag{5.2.49}$$

$$g_a^{(2)} \xrightarrow{\lambda \rightarrow 0} \frac{\lambda}{2\pi b_0} \left(-\log \left(\frac{M^2}{\mu_R^2} \right) + \log \left(\frac{\mu_F^2}{\mu_R^2} \right) \right) = L \frac{\alpha_S}{2\pi} \log \left(\frac{\mu_F^2}{M^2} \right), \tag{5.2.50}$$

$$h_{ab \rightarrow ij}^{(2)}(\lambda) \xrightarrow{\lambda \rightarrow 0} -\frac{\lambda}{2\pi b_0} 2D_{ab \rightarrow ij}^{(1)} = -L \frac{\alpha_S}{2\pi} 2D_{ab \rightarrow ij}^{(1)}. \tag{5.2.51}$$

The $L = \log \bar{N}$ terms can be cross checked by comparing them with the \mathbf{P} and \mathbf{K} operators in Mellin space

$$\left[\frac{\sigma_{ab}^{\text{Exp.}} M^2}{\sigma^{\text{B}}} \right]_{\log \bar{N}} = \left[\langle \mathbf{P}(N) \rangle_a + \langle \mathbf{K}(N) \rangle_a + \langle \mathbf{P}(N) \rangle_b + \langle \mathbf{K}(N) \rangle_b \right]_{\log \bar{N}}. \tag{5.2.52}$$

For the DY aNNLO+NNLL expansion we refer to [2, App. A.1].

We stress the similarity to the matching procedure in POWHEG as outlined in Sec. 3.3.3.2. The POWHEG method uses a truncated shower to generate subsequent emissions. The resummation method uses only the NLL terms of the Sudakov corresponding to additional emissions on top of the NLO cross section.

Having computed the resummed and the perturbatively expanded results in Mellin space, we must multiply them with the N -moments of the PDFs according to Eq. (5.2.16). This is achieved by fitting them in x -space to the function used by the MSTW collaboration [439]

$$f(x) = A_0 x^{A_1} (1-x)^{A_2} (1 + A_3 \sqrt{x} + A_4 x + A_5 x^{\frac{3}{2}}) + A_6 x^2 + A_7 x^{\frac{5}{2}}, \tag{5.2.53}$$

with the analytical result in Mellin space

$$\begin{aligned}
F(f(x)) &= A_0 \Gamma(y) B'(A_1 + N, y) + A_3 B'(A_1 + N + \frac{1}{2}, y) + A_4 B'(A_1 + N + 1, y) \\
&+ A_5 B'(A_1 + N + \frac{3}{2}, y) + A_6 B'(A_1 + N + 2, y) + A_7 B'(A_1 + N + \frac{5}{2}, y)
\end{aligned} \tag{5.2.54}$$

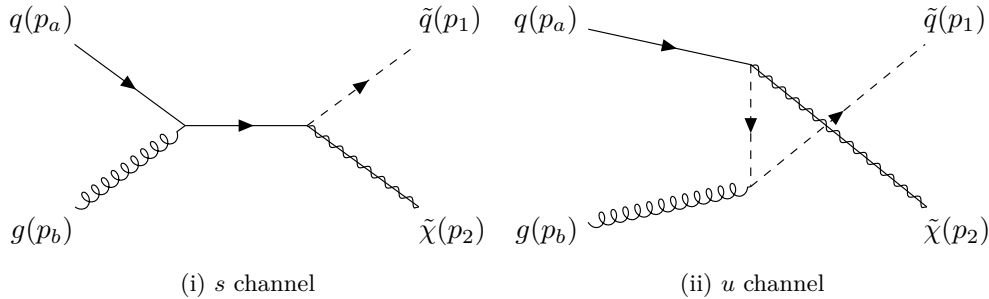


Figure 5.3: Tree-level Feynman diagrams for the associated production of a squark and an electroweakino at hadron colliders.

and

$$B'(x, y) = B'(x, A_2 + 1) = B(x, y)/\Gamma(y) = B(x, y)/\Gamma(y). \quad (5.2.55)$$

Having the cross section in Mellin space the last step is to perform an inverse Mellin transform,

$$M^2 \frac{d\sigma_{AB}}{dM^2}(\tau) = \frac{1}{2\pi i} \int_{\mathcal{C}_N} dN \tau^{-N} M^2 \frac{d\sigma_{AB}(N)}{dM^2}, \quad (5.2.56)$$

in order to obtain the hadronic cross section as a function of $\tau = M^2/S$. Special attention must be paid to the singularities in the resummed exponents $G_{ab}^{(1,2)}$, which are situated at $\lambda = 1/2$ and are related to the Landau pole of the perturbative coupling α_S . To avoid this pole as well as those in the Mellin moments of the PDFs related to the small- x (Regge) singularity $f_{a/A}(x, \mu_0^2) \propto x^\alpha (1-x)^\beta$ with $\alpha < 0$, we choose an integration contour \mathcal{C}_N according to the *principal value* procedure proposed in Ref. [440] and the *minimal prescription* proposed in Ref. [441]. We define two branches

$$\mathcal{C}_N : N = C + ze^{\pm i\phi} \quad \text{with } z \in [0, \infty[, \quad (5.2.57)$$

where the constant C is chosen such that the singularities of the N -moments of the PDFs lie to the left and the Landau pole to the right of the integration contour. Formally the angle ϕ can be chosen in the range $[\pi/2, \pi[$, but the integral converges faster if $\phi > \pi/2$.

5.3 Threshold resummation for squark electroweakino production

In this section we focus on the production of a squark and an electroweakino at hadron colliders. The corresponding Born diagrams are shown in Fig. 5.3. The similarity to prompt photon production arises from the supersymmetric Feynman rules, where an even number of fields are exchanged by their superpartner at the vertices. This results in diagrams that resemble those of the QCD Compton process, as shown in Fig. 4.20.

Since this process involves both weak $\mathcal{O}(\alpha_{\text{EM}})$ and strong $\mathcal{O}(\alpha_S)$ interactions at LO, the resulting cross section is of intermediate size. The simplest process in this category involves the production of a first- or second-generation squark together with the lightest neutralino. This process manifests itself through a hard jet originating from the squark decay and missing transverse energy from the two neutralinos leaving

the detector invisibly, one of them being a decay product of the squark and the other one being directly produced in the hard process. Such a monojet signal is particularly well-studied in the context of dark matter production at colliders [442, 443]. In recent analyses by the CMS collaboration, squark masses below 1.6 TeV were excluded in four mass-degenerate squark flavour models, assuming production with a light neutralino $\tilde{\chi}_1^0$. This limit is reduced to 1.1 TeV for a single kinematically reachable squark [444–446]. Similarly, the ATLAS collaboration gives limits of 1.4 TeV and 1.0 TeV [447, 448].

This section is based on our publication [1] with further details in Ref. [176]. We present a threshold resummation calculation for the associated production of squarks and electroweakinos at the NLO+NLL accuracy. We begin with a derivation of LO and NLO expressions for the associated production of a squark and an electroweakino at hadron colliders in Sec. 5.3.1. In Sec. 5.3.2 and Sec. 5.3.3, we compute the ingredients required for threshold resummation. The numerical validation of our NLO calculation and our new results up to NLO+NLL accuracy are given in Sec. 5.3.4 for various benchmark scenarios.

5.3.1 Leading and next-to-leading order

To calculate the total hadronic cross section σ_{AB} we use Eq. (5.2.1). The needed partonic cross section

$$\sigma_{ab}(s) = \int_2 d\sigma_{ab} = \int \frac{1}{2s} \overline{|\mathcal{M}|^2} d\text{PS}^{(2)} \quad (5.3.1)$$

is related to the squared and averaged matrix element $\overline{|\mathcal{M}|^2}$ by the usual flux factor $1/(2s)$ and the integration over the two-particle phase space $d\text{PS}^{(2)}$.

The associated production of a squark and an electroweakino with masses $m_{\tilde{q}}$ and $m_{\tilde{\chi}}$ occurs at a hadron collider at LO through the annihilation of a massless quark and a gluon. Charge conservation restricts the possible partonic processes to

$$q_{u,d}(p_a) g(p_b) \rightarrow \tilde{q}_{u,d}(p_1) \tilde{\chi}_k^0(p_2), \quad (5.3.2)$$

$$q_{u,d}(p_a) g(p_b) \rightarrow \tilde{q}_{d,u}(p_1) \tilde{\chi}_k^\pm(p_2), \quad (5.3.3)$$

where k identifies the neutralino ($\tilde{\chi}_k^0$, $k = 1, \dots, 4$) or chargino ($\tilde{\chi}_k^\pm$, $k = 1, 2$) mass eigenstate and $p_{a,b}$ and $p_{1,2}$ refer to the four-momenta of the initial- and final-state particles, respectively. The corresponding Born diagrams are shown in Fig. 5.3.

The squared matrix elements associated with the s -channel quark exchange diagram (left), the u -channel squark exchange diagram (right) and their interference can be expressed as functions of Mandelstam variables $s = (p_a + p_b)^2$, $t = (p_a - p_1)^2$ and $u = (p_a - p_2)^2$, *i.e.* as [395]

$$|\mathcal{M}_s|^2 = \frac{g_s^2 C_A C_F B}{s} 2(m_{\tilde{\chi}}^2 - t), \quad (5.3.4)$$

$$|\mathcal{M}_u|^2 = -\frac{g_s^2 C_A C_F B}{(u - m_{\tilde{q}}^2)^2} 2(m_{\tilde{\chi}}^2 - u)(m_{\tilde{q}}^2 + u), \quad (5.3.5)$$

$$2 \text{Re}[\mathcal{M}_s \mathcal{M}_u^\dagger] = 2 \frac{g_s^2 C_A C_F B}{s(u - m_{\tilde{q}}^2)} \left(2(m_{\tilde{\chi}}^4 - m_{\tilde{q}}^4) + m_{\tilde{q}}^2(2u - 3s) - 2m_{\tilde{\chi}}^2(2m_{\tilde{q}}^2 + u) - su \right). \quad (5.3.6)$$

They are all proportional to the squared electroweakino-squark-quark coupling

$$B \equiv R_{Ijk} L'_{Ijk} + L_{Ijk} R'_{Ijk} = R_{Ijk} R_{Ijk}^* + L_{Ijk} L_{Ijk}^* = |R_{Ijk}|^2 + |L_{Ijk}|^2, \quad (5.3.7)$$

where the capitalised index I labels the quark generation, the lower-case index j refers to the squark eigenstate and the index k is related as above to the electroweakino eigenstate. The definitions of the various left- and right-handed couplings $L^{(\prime)}$ and $R^{(\prime)}$ are provided in Refs. [369, 411, 449]. Using arbitrary squark mixings and mass eigenstates opens the possibility to study SUSY flavour violation [409, 450–454]. The total spin- and colour-averaged squared amplitude then reads

$$\overline{|\mathcal{M}|^2} = \frac{1}{96} (|\mathcal{M}_s|^2 + |\mathcal{M}_u|^2 + 2 \operatorname{Re}[\mathcal{M}_s \mathcal{M}_u^\dagger]) . \quad (5.3.8)$$

The NLO corrections to this cross section are well-known [376, 386, 387]. They involve one-loop self-energy, vertex and box corrections interfering with tree-level diagrams, as well as squared real gluon and quark emission diagrams, from which intermediate OS squark and gluino resonant contributions have to be subtracted to avoid spoiling the prediction power of the NLO calculation and double-counting contributions to squark-pair production and gluino-electroweakino associated production with the corresponding subsequent decays [194, 195]. We have calculated the full NLO cross section using dimensional regularization of UV and IR divergences as well as OS renormalization for all squark and gluino masses and wave functions. The strong coupling constant is renormalized in the five-flavour $\overline{\text{MS}}$ scheme after explicitly decoupling the heavier coloured particles from its running [455–457], which leaves the running determined only by the lightest coloured particles as it is usually done in global determinations of PDFs. The tHV and CDR scheme introduce a mismatch between the $(d-2)$ gluon and the 2 gluino degrees of freedom. Their regularization then breaks SUSY invariance, which we explore in chapter 5. This problem does not happen in the DRED or FHD scheme. Luckily, it is possible to include SUSY restoring counterterms for the gaugino-squark-quark \hat{g} and gluino-squark-quark \hat{g}_S vertices [458]

$$\hat{g}_S = g_S \left[1 + \frac{\alpha_S}{3\pi} \right] , \quad \hat{g} = g \left[1 - \frac{\alpha_S}{8\pi} C_F \right] . \quad (5.3.9)$$

Real and virtual contributions are combined to σ^{NLO} with the help of the CS dipole subtraction method of Sec. 3.1.4.2 to cancel infrared and collinear divergences [180, 191, 193].

5.3.2 Soft anomalous dimension

We compute the soft anomalous dimension $\Gamma_{ab \rightarrow \tilde{\chi} \tilde{q}}$ for gaugino squark production. Calculating the necessary ω^{kl} integrals in Eq. (5.2.37) is quite cumbersome. Fortunately, the results for general cases are available [459, Eqs. (7.39)-(7.42)] and we report them below for our cases of interest

$$\omega^{ab}(v_a^2 = v_b^2 = 0) = S_{ab} \frac{\alpha_S}{\epsilon\pi} \left[-\log\left(\frac{v_a \cdot v_b}{2}\right) + \frac{1}{2} \log\left(\frac{(v_a \cdot n)^2 (v_b \cdot n)^2}{|n|^2 |n|^2}\right) + i\pi - 1 \right] , \quad (5.3.10)$$

$$\omega^{ab}(v_a^2 = 0; v_b^2 \neq 0) = S_{ab} \frac{\alpha_S}{\epsilon\pi} \left[-\frac{1}{2} \log\left(\frac{(v_a \cdot v_b)^2 s}{2m_b^2}\right) + L_b + \frac{1}{2} \log\left(\frac{(v_a \cdot n)^2}{|n|^2}\right) - 1 \right] , \quad (5.3.11)$$

$$\omega^{aa}(v_a^2 \neq 0) = S_{aa} \frac{\alpha_S}{\epsilon\pi} [2L_a - 2] , \quad (5.3.12)$$

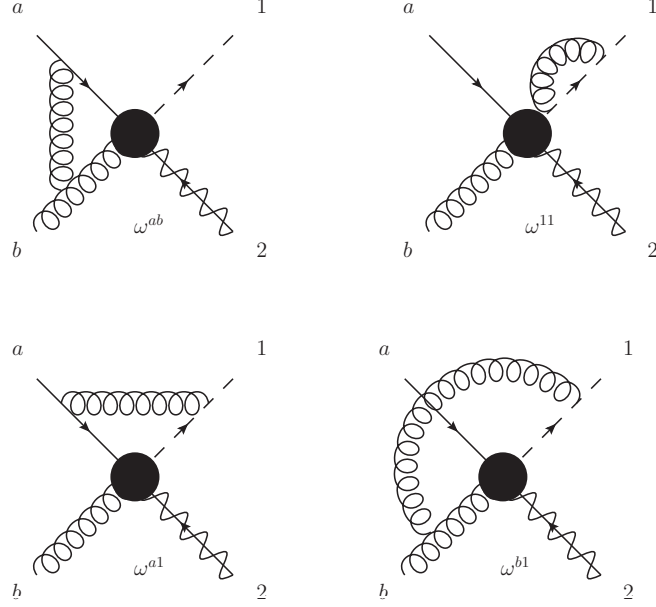


Figure 5.4: Eikonal diagrams for soft anomalous dimension in gaugino squark production. The blob in the middle represents the hard scattering process.

with

$$L_a = \frac{1}{2} [L_a(\delta_a v_a, n) + L_a(\delta_a v_a, -n)] , \quad (5.3.13)$$

and

$$L_a(\delta_a v_a, \delta_n n) = \frac{1}{2} \frac{v_a \cdot n}{\sqrt{(v_a \cdot n)^2 - 2m_a^2 n^2/s}} \left[\log \left(\frac{\delta_a \delta_n 2m_a^2/s - v_a \cdot n - \sqrt{(v_a \cdot n)^2 - 2m_a^2 n^2/s}}{\delta_a \delta_n 2m_a^2/s - v_a \cdot n + \sqrt{(v_a \cdot n)^2 - 2m_a^2 n^2/s}} \right) + \log \left(\frac{\delta_a \delta_n n^2 - v_a \cdot n - \sqrt{(v_a \cdot n)^2 - 2m_a^2 n^2/s}}{\delta_a \delta_n n^2 - v_a \cdot n + \sqrt{(v_a \cdot n)^2 - 2m_a^2 n^2/s}} \right) - \delta_a \delta_n 2i\pi \right] . \quad (5.3.14)$$

The diagrams of interest are shown in Fig. 5.4. They lead to the following result for the integrals of the kinematical quantities

$$\omega^{ab} = S_{ab} \frac{\alpha_S}{\epsilon\pi} \left[-\log \left(\frac{v_a \cdot v_b}{2} \right) + \frac{1}{2} \log \left(\frac{(v_a \cdot n)^2 (v_b \cdot n)^2}{|n|^2} \right) + i\pi - 1 \right] , \quad (5.3.15)$$

$$\omega^{a1} = S_{a1} \frac{\alpha_S}{\epsilon\pi} \left[-\frac{1}{2} \log \left(\frac{(v_a \cdot v_1)^2 s}{2m_1^2} \right) + L_1 + \frac{1}{2} \log \left(\frac{(v_a \cdot n)^2}{|n|^2} \right) - 1 \right] , \quad (5.3.16)$$

$$\omega^{b1} = S_{b1} \frac{\alpha_S}{\epsilon\pi} \left[-\frac{1}{2} \log \left(\frac{(v_b \cdot v_1)^2 s}{2m_1^2} \right) + L_1 + \frac{1}{2} \log \left(\frac{(v_b \cdot n)^2}{|n|^2} \right) - 1 \right] , \quad (5.3.17)$$

$$\omega^{11} = S_{11} \frac{\alpha_S}{\epsilon\pi} [2L_1 - 2] . \quad (5.3.18)$$

We just need to change the masses $m_1 = m_{\bar{q}}$, the signs factors $S_{ab} = \Delta_a \Delta_b \delta_a \delta_b$, the colour factors C^{kl} and the contribution from the initial-state self-energies Γ_{ab}^{DY} . Since the kinematics will be the same, we will employ the following relations

$$v_a \cdot v_b = \frac{2p_a \cdot p_b}{s} = 1, \quad (5.3.19)$$

$$v_a \cdot v_1 = \frac{2p_a \cdot p_1}{s} = \frac{m_1^2 - t}{s}, \quad (5.3.20)$$

$$v_b \cdot v_1 = \frac{2p_b \cdot p_1}{s} = \frac{m_1^2 - u}{s}, \quad (5.3.21)$$

where t and u are Mandelstam variables. Furthermore, Ref. [391] gives

$$\frac{(v_a \cdot n)^2}{|n|^2} = \frac{(v_b \cdot n)^2}{|n|^2} = \frac{1}{2}, \quad (5.3.22)$$

which is valid in the physical Coulomb $A^0 = 0$ gauge.

Finally, there is another relation that we will use. While the quantity L_1 is defined by a rather complicate expression, we can show that in the case where $\delta_1 = +1$ and in the limit where $(v_1 \cdot n)^2 \rightarrow 2m_1^2 n^2/s$ we have $L_1 \rightarrow 1$. In order to show this, we have to take the limit, since the ratio in the coefficient of $L_a(\delta_a v_a, \delta_n v_n)$ as well as the long logarithms are divergent.

We can quickly calculate the signs S_{ab} for the four diagrams

$$\begin{aligned} S_{ab} &= -1, & S_{11} &= -1, \\ S_{a1} &= +1, & S_{b1} &= +1. \end{aligned} \quad (5.3.23)$$

Note that in order to calculate those signs, one has to consider that the exchanged gluon is emitted by one particle and absorbed by the other. This changes the sign of the δ for the particle that absorbs the gluon. The colour factors C^{kl} are calculated as follows

$$\begin{aligned} C^{ab} &= \frac{\text{Tr}[T^i T^{i'} T^j] (-i) f^{i'ij}}{\text{Tr}[T^i T^i]} = -\frac{C_A}{2}, & C^{11} &= \frac{\text{Tr}[T^i T^j T^j T^i]}{\text{Tr}[T^i T^i]} = C_F, \\ C^{a1} &= \frac{\text{Tr}[T^i T^j T^i T^j]}{\text{Tr}[T^i T^i]} = C_F - \frac{C_A}{2}, & C^{b1} &= \frac{\text{Tr}[T^i T^j T^{i'}] (-i) f^{i'ij}}{\text{Tr}[T^i T^i]} = \frac{C_A}{2}, \end{aligned} \quad (5.3.24)$$

where we have used the well-known relation $T^a T^a = C_F \mathbf{1}$. With these ingredients we can calculate

$$\begin{aligned} \Gamma_{ab \rightarrow ij} &= \epsilon \left[-C_F(\omega^{a1} + \omega^{11}) + \frac{C_A}{2}(\omega^{ab} + \omega^{a1} - \omega^{b1}) \right] \\ &= \frac{\alpha_S}{2\pi} \left[C_F \left(-\log \left(\frac{(v_a \cdot n)^2}{|n|^2} \right) + \log \left(\frac{(v_a \cdot v_1)^2 s}{2m_{\bar{q}}^2} \right) + 2L_1 - 2 \right) \right. \\ &\quad + C_A \left(-\frac{1}{2} \log \left(\frac{(v_a \cdot v_1)^2 s}{2m_{\bar{q}}^2} \right) + \frac{1}{2} \log \left(\frac{(v_b \cdot v_1)^2 s}{2m_{\bar{q}}^2} \right) \right. \\ &\quad \left. \left. - \log \left(\frac{(v_b \cdot n)^2}{|n|^2} \right) + \log \left(\frac{v_a \cdot v_b}{2} \right) + 1 - i\pi \right) \right], \end{aligned} \quad (5.3.25)$$

while the contribution from the initial-state self-energies is

$$\begin{aligned} \Gamma_{ab}^{\text{DY}} = & \frac{\alpha_S}{2\pi} \left[C_F \left(1 - \log \left(\frac{(v_a \cdot n)^2}{|n|^2} \right) - \log(2) - i\pi \right) \right. \\ & \left. + C_A \left(1 - \log \left(\frac{(v_b \cdot n)^2}{|n|^2} \right) - \log(2) - i\pi \right) \right]. \end{aligned} \quad (5.3.26)$$

We observe the nice cancellation of the gauge dependent terms

$$\begin{aligned} \bar{\Gamma}_{ab \rightarrow ij} = & \frac{\alpha_S}{2\pi} \left\{ C_F \left[\log \left(\frac{(v_a \cdot v_1)^2 s}{2m_{\tilde{q}}^2} \right) + 2L_1 - 3 + \log(2) + i\pi \right] + \right. \\ & \left. + C_A \left[-\frac{1}{2} \log \left(\frac{(v_a \cdot v_1)^2 s}{2m_{\tilde{q}}^2} \right) + \frac{1}{2} \log \left(\frac{(v_b \cdot v_1)^2 s}{2m_{\tilde{q}}^2} \right) + \log \left(\frac{v_a \cdot v_b}{2} \right) + \log(2) \right] \right\} \\ = & \frac{\alpha_S}{2\pi} \left\{ C_F \left[2 \log \left(\frac{m_{\tilde{q}}^2 - t}{\sqrt{s} m_{\tilde{q}}} \right) - 1 + i\pi \right] + C_A \log \left(\frac{m_{\tilde{q}}^2 - u}{m_{\tilde{q}}^2 - t} \right) \right\}, \end{aligned} \quad (5.3.27)$$

where we have used Eqs. (5.3.19) to (5.3.21) and $L_1 \rightarrow 1$. This result is related to the one for tW production [460] and in the massless limit also to the one for the QCD Compton process [461]. It agrees in particular with [460, eq. (3.8)] after subtraction of the DY terms.

5.3.3 Hard matching coefficients

We compute the insertion operators \mathbf{P} and \mathbf{K} for squark-electroweakino production in Mellin space as required for Eq. (5.2.46). In this case we have an initial-state with a quark and a gluon. The result of gluino-electroweakino production [411] where we have two initial quarks can be widely recycled, all thou we have to consider that in this case the second parton is now a gluon, and the final-state is a squark. In total, we have two diagonal splitting of either the (anti)quark or the gluon in the initial-state, while the off-diagonal splitting, like a gluon into a quark-antiquark pair will vanish at large N . Furthermore, the various pieces have to be multiplied by the appropriate combination of PDFs. We will also need the following colour factors

$$\begin{aligned} \langle \mathbf{T}_{\tilde{q}} \cdot \mathbf{T}_{\tilde{q}} \rangle &= \mathbf{T}_{\tilde{q}}^2 = C_F, & \langle \mathbf{T}_q \cdot \mathbf{T}_q \rangle &= \mathbf{T}_q^2 = C_F, \\ \langle \mathbf{T}_g \cdot \mathbf{T}_g \rangle &= \mathbf{T}_g^2 = C_A, & \langle \mathbf{T}_{\tilde{q}} \cdot \mathbf{T}_q \rangle &= \frac{C_A}{2} - C_F, \\ \langle \mathbf{T}_g \cdot \mathbf{T}_q \rangle &= -\frac{C_A}{2}, & \langle \mathbf{T}_{\tilde{q}} \cdot \mathbf{T}_g \rangle &= -\frac{C_A}{2}, \\ \langle \mathbf{T}_q \cdot \mathbf{T}_g \rangle &= -\frac{C_A}{2}, \end{aligned} \quad (5.3.28)$$

where colour conservation $\mathbf{T}_a \mathbf{T}_b = T_R(\mathbf{T}_c^2 - \mathbf{T}_a^2 - \mathbf{T}_b^2)$ with a, b, c different coloured particles in the process q, g, \tilde{q} was used [180, App. A]. We also utilize the kinematic relations

$$xs_{ja} = m_{\tilde{q}}^2 - t, \quad xs_{jb} = m_{\tilde{q}}^2 - u, \quad xs_{ab} = s. \quad (5.3.29)$$

5.3.3.1 Mellin space \mathbf{P} operator

We can take Eq. (3.1.130) and apply the above colour factors and kinematical relations. The first diagonal diagram with the diagonal splitting of a quark in the initial-state gives ($a = q$, $a' = q$, $j = \tilde{q}$, $b = g$)

$$\langle \mathbf{P} \rangle_q(x; \mu_F^2; p_j, xp_a, p_b) = \frac{\alpha_S}{2\pi} P^{qq} \left(\frac{\mathbf{T}_{\tilde{q}} \cdot \mathbf{T}_q}{\mathbf{T}_q^2} \log \frac{\mu_F^2}{xs_{ja}} + \frac{\mathbf{T}_g \cdot \mathbf{T}_q}{\mathbf{T}_q^2} \log \frac{\mu_F^2}{xs_{ab}} \right). \quad (5.3.30)$$

Identical contribution arises from the diagram with an anti-quark in the initial-state ($a = \bar{q}$, $a' = \bar{q}$, $j = \tilde{q}$, $b = g$), which however produces an anti-squark in the final-state and also shall be multiplied by the anti-quark PDF.

The second diagonal diagrams from the splitting of a gluon in the initial-state gives ($a = g$, $a' = g$, $j = \tilde{q}$, $b = q$)

$$\langle \mathbf{P} \rangle_g(x; \mu_F^2; p_j, xp_a, p_b) = \frac{\alpha_S}{2\pi} P^{gg} \left(\frac{\mathbf{T}_{\tilde{q}} \cdot \mathbf{T}_g}{\mathbf{T}_g^2} \log \frac{\mu_F^2}{xs_{ja}} + \frac{\mathbf{T}_q \cdot \mathbf{T}_g}{\mathbf{T}_g^2} \log \frac{\mu_F^2}{xs_{ab}} \right). \quad (5.3.31)$$

Also in this case, the same contribution arises from the diagram with an anti-quark as particle b ($a = g$, $a' = g$, $j = \tilde{q}$, $b = \bar{q}$), and also in this case this is associated to the production of an anti-squark in the final-state and shall be multiplied by the anti-quark PDF.

Finally, we have to remember that we have to sum also all the contributions where initial-states particles are exchanged (meaning that the particle splitting is the particle b). This is obtained by simply replacing $s_{ja} \rightarrow s_{jb}$. In Mellin space, only the diagonal terms survive and writing explicitly their colour factors, we obtain

$$\langle \mathbf{P} \rangle_q(N) = \frac{\alpha_S}{2\pi} \left(\log \bar{N} - \frac{3}{4} \right) \left(2C_F \log \frac{\mu_F^2}{m_{\tilde{q}}^2 - t} - C_A \log \frac{s}{m_{\tilde{q}}^2 - t} \right), \quad (5.3.32)$$

$$\langle \mathbf{P} \rangle_g(N) = \frac{\alpha_S}{2\pi} \left(C_A \log \bar{N} - \frac{\beta_0}{2} \right) \log \frac{\mu_F^4}{s(m_{\tilde{q}}^2 - t)}. \quad (5.3.33)$$

To those we have to add identical terms with $t \rightarrow u$ which represents the diagrams with initial-states particles exchanged.

5.3.3.2 Mellin space \mathbf{K} operator

For the K operator we apply the same procedure to Eq. (3.1.131) with constants listed in Sec. A.3.4. Also in this case we only care about the plus distributions and the delta functions as other terms do not contribute in the large N limit. We suppress the arguments for several functions given that they follow from Eq. (3.1.131).

The first diagonal diagram with the diagonal splitting of a quark in the initial-state

gives ($a = q$, $a' = q$, $j = \tilde{q}$, $b = g$)

$$\begin{aligned}
 \langle \mathbf{K} \rangle_q(x; \mu_F^2; p_j, p_a, p_b) &= \frac{\alpha_S}{2\pi} \left\{ \bar{K}^{qq} - \mathbf{T}_{\tilde{q}} \cdot \mathbf{T}_q \mathcal{K}_{\tilde{q}}^{q,q} \right. \\
 &- \frac{\mathbf{T}_{\tilde{q}} \cdot \mathbf{T}_q}{\mathbf{T}_q^2} \left[P_{\text{reg}}^{qq} \log \frac{(1-x)s_{ja}}{(1-x)s_{ja} + m_j^2} \right. \\
 &\quad \left. \left. + \gamma_q \delta(1-x) \left(\log \frac{s_{ja} - 2m_j \sqrt{s_{ja} + m_j^2} + 2m_j^2}{s_{ja}} + \frac{2m_j}{\sqrt{s_{ja} + m_j^2} + m_j} \right) \right] \right. \\
 &\left. - \mathbf{T}_g \cdot \mathbf{T}_q \left[\frac{1}{\mathbf{T}_q^2} P_{\text{reg}}^{qq} \log(1-x) + \left(2 \left(\frac{\log(1-x)}{1-x} \right)_+ - \frac{\pi^2}{3} \delta(1-x) \right) \right] \right\}.
 \end{aligned} \tag{5.3.34}$$

Identical contribution arises from the diagram with an anti-quark in the initial-state ($a = \bar{q}$, $a' = \bar{q}$, $j = \tilde{q}$, $b = g$), which however produces an anti-squark in the final-state and shall be multiplied by the anti-quark PDF.

The second diagonal diagrams from the splitting of a gluon in the initial-state gives ($a = g$, $a' = g$, $j = \tilde{q}$, $b = q$)

$$\begin{aligned}
 \langle \mathbf{K} \rangle_g(x; \mu_F^2; p_j, p_a, p_b) &= \frac{\alpha_S}{2\pi} \left\{ \bar{K}^{gg} - \mathbf{T}_{\tilde{q}} \cdot \mathbf{T}_g \mathcal{K}_{\tilde{q}}^{g,g} \right. \\
 &- \frac{\mathbf{T}_{\tilde{q}} \cdot \mathbf{T}_g}{\mathbf{T}_g^2} \left[P_{\text{reg}}^{gg} \log \frac{(1-x)s_{ja}}{(1-x)s_{ja} + m_j^2} \right. \\
 &\quad \left. \left. + \gamma_g \delta(1-x) \left(\log \frac{s_{ja} - 2m_j \sqrt{s_{ja} + m_j^2} + 2m_j^2}{s_{ja}} + \frac{2m_j}{\sqrt{s_{ja} + m_j^2} + m_j} \right) \right] \right. \\
 &\left. - \mathbf{T}_q \cdot \mathbf{T}_g \left[\frac{1}{\mathbf{T}_g^2} P_{\text{reg}}^{gg} \log(1-x) + \left(2 \left(\frac{\log(1-x)}{1-x} \right)_+ - \frac{\pi^2}{3} \delta(1-x) \right) \right] \right\}.
 \end{aligned} \tag{5.3.35}$$

Also in this case, the same contribution arises from the diagram with an anti-quark as particle b ($a = g$, $a' = g$, $j = \tilde{q}$, $b = \bar{q}$), and it is associated to the production of an anti-squark in the final-state and shall be multiplied by the anti-quark PDF.

Finally, we have to remember that we have to sum also all the contributions where initial-states particles are exchanged (meaning that the particle splitting is the particle b). This is again obtained by simply replacing $s_{ja} \rightarrow s_{jb}$.

Since the \mathbf{K} operator is a bit more complicated, we will give the Mellin transforms $F[\dots]$ of the various operators separately. The Mellin transform of the diagonal \bar{K}^{aa} is

$$\begin{aligned}
 \bar{K}^{aa}(N) &= \mathbf{T}_a^2 F \left[\left(\frac{2}{1-x} \log \frac{1-x}{x} \right)_+ \right] - F \left[\delta(1-x) \left(\gamma_a + K_a - \frac{5}{6} \pi^2 \mathbf{T}_a^2 \right) \right] \\
 &= \mathbf{T}_a^2 \left(\log^2 \bar{N} - \frac{\pi^2}{6} \right) - \left(\gamma_a + K_a - \frac{5}{6} \pi^2 \mathbf{T}_a^2 \right) \\
 &= \mathbf{T}_a^2 \log^2 \bar{N} + \mathbf{T}_a^2 \frac{2}{3} \pi^2 - \gamma_a - K_a.
 \end{aligned} \tag{5.3.36}$$

The second term involves $\mathcal{K}_g^{q,q}$. We start with its function $\left[J_{gQ}^q(x, \mu_s)\right]_+$

$$\begin{aligned}
 \left[J_{gQ}^q(N, \mu_s)\right]_+ &= F \left[\left(\frac{1-x}{2(1+\mu_s^2-x)^2} \right)_+ \right] - F \left[\left(\frac{2}{1-x} \right)_+ \right] \\
 &\quad - F \left[\left(\frac{2}{1-x} \log(1+\mu_s^2-x) \right)_+ \right] + F \left[\left(\frac{2}{1-x} \right)_+ \log(2+\mu_s^2-x) \right] \\
 &= \frac{1}{2} \left(\frac{1}{1+\mu_s^2} + \log \left(\frac{\mu_s^2}{1+\mu_s^2} \right) \right) + 2 \log \bar{N} + \\
 &\quad + \left[2 \log \bar{N} \log(\mu_s^2) - \frac{\pi^2}{3} + 2 \log(\mu_s^2) \log \left(\frac{\mu_s^2}{1+\mu_s^2} \right) + 2 \text{Li}_2 \left(\frac{1+\mu_s^2}{\mu_s^2} \right) \right] \\
 &\quad - 2 \log \bar{N} \log(1+\mu_s^2) = \\
 &= 2 \log \bar{N} \left(1 + \log \frac{\mu_s^2}{1+\mu_s^2} \right) + \frac{1}{2} \frac{1}{1+\mu_s^2} + \frac{1}{2} \log \frac{\mu_s^2}{1+\mu_s^2} \\
 &\quad + 2 \log(\mu_s^2) \log \left(\frac{\mu_s^2}{1+\mu_s^2} \right) + 2 \text{Li}_2 \left(\frac{1+\mu_s^2}{\mu_s^2} \right) - \frac{\pi^2}{3},
 \end{aligned} \tag{5.3.37}$$

where $\mu_s = m_{\bar{q}}/s_{\bar{q}q}$. Then we write directly the Mellin transform of the operator $\mathcal{K}_{\bar{q}}^{q,q}$

$$\begin{aligned}
 \mathcal{K}_{\bar{q}}^{q,q}(N; s_{ja}, m_j) &= F \left[2 \left(\frac{\log(1-x)}{1-x} \right)_+ \right] + F \left[J_{gQ}^q \left(x, \frac{m_j}{\sqrt{s_{ja}}} \right) \right]_+ - F \left[\delta(1-x) \frac{\gamma_{\bar{q}}}{C_F} \right] \\
 &\quad + F \left[\left(\frac{2}{1-x} \right)_+ \log \frac{(2-x)s_{ja}}{(2-x)s_{ja} + m_j^2} \right] - F \left[\left(\frac{(1-x)s_{ja}^2}{2[(1-x)s_{ja} + m_j^2]^2} \right)_+ \right] \\
 &= \left(\log^2 \bar{N} + \frac{\pi^2}{6} \right) + \left[J_{gQ}^q \left(N, \frac{m_j}{\sqrt{s_{ja}}} \right) \right]_+ - \frac{\gamma_{\bar{q}}}{C_F} \\
 &\quad + \left[-2 \log \bar{N} \log(s_{ja}) + 2 \log \bar{N} \log(s_{ja} + m_j^2) \right] + \left(\frac{1}{2} \frac{s_{ja}}{s_{ja} + m_j^2} + \frac{1}{2} \log \frac{m_j^2}{s_{ja} + m_j^2} \right) \\
 &= \log^2 \bar{N} + 2 \log \bar{N} \left(1 + \log \frac{m_j^2}{s_{ja}} \right) + 2 \text{Li}_2 \left(\frac{s_{ja} + m_j^2}{m_j^2} \right) \\
 &\quad + \log \frac{m_j^2}{s_{ja} + m_j^2} \left(1 + 2 \log \frac{m_j^2}{s_{ja}} \right) + \frac{s_{ja}}{s_{ja} + m_j^2} - \frac{\gamma_{\bar{q}}}{C_F} - \frac{\pi^2}{6}.
 \end{aligned} \tag{5.3.38}$$

So the full Mellin transform of the \mathbf{K} operator is

$$\begin{aligned}
 \langle \mathbf{K} \rangle_q(N) &= \frac{\alpha_S}{2\pi} \left\{ F[\bar{K}^{qq}] - \mathbf{T}_{\bar{q}} \cdot \mathbf{T}_q F[\mathcal{K}_{\bar{q}}^{q,q}] \right. \\
 &\quad \left. - \frac{\mathbf{T}_{\bar{q}} \cdot \mathbf{T}_q}{\mathbf{T}_q^2} F \left[\gamma_q \delta(1-x) \left(\log \frac{s_{ja} - 2m_j \sqrt{s_{ja} + m_j^2} + 2m_j^2}{s_{ja}} + \frac{2m_j}{\sqrt{s_{ja} + m_j^2} + m_j} \right) \right] \right. \\
 &\quad \left. - \mathbf{T}_g \cdot \mathbf{T}_q F \left[2 \left(\frac{\log(1-x)}{1-x} \right)_+ \right] - \mathbf{T}_g \cdot \mathbf{T}_q F \left[\delta(1-x) \frac{\pi^2}{3} \right] \right\} \\
 &= \frac{\alpha_S}{2\pi} \left\{ C_F \log^2 \bar{N} - \gamma_q - K_q + \frac{2}{3} \pi^2 C_F \right. \\
 &\quad - \left(\frac{C_A}{2} - C_F \right) \left[\log^2 \bar{N} + 2 \log \bar{N} \left(1 + \log \frac{m_j^2}{s_{ja}} \right) + 2 \text{Li}_2 \left(\frac{s_{ja} + m_j^2}{m_j^2} \right) \right. \\
 &\quad \left. + \log \frac{m_j^2}{s_{ja} + m_j^2} \left(1 + 2 \log \frac{m_j^2}{s_{ja}} \right) + \frac{s_{ja}}{s_{ja} + m_j^2} - \frac{\gamma_{\bar{q}}}{C_F} - \frac{\pi^2}{6} \right] \\
 &\quad - \left(\frac{C_A - 2C_F}{2C_F} \right) \frac{3}{2} C_F \left(\log \frac{s_{ja} - 2m_j \sqrt{s_{ja} + m_j^2} + 2m_j^2}{s_{ja}} + \frac{2m_j}{\sqrt{s_{ja} + m_j^2} + m_j} \right) \\
 &\quad \left. + \frac{C_A}{2} \left(\log^2 \bar{N} + \frac{\pi^2}{6} \right) - \frac{C_A}{2} \frac{\pi^2}{3} \right\}
 \end{aligned} \tag{5.3.39}$$

and finally we can write it as

$$\begin{aligned}
 \langle \mathbf{K} \rangle_q(N) &= \frac{\alpha_S}{2\pi} \left\{ C_F \left(2 \log^2 \bar{N} + \frac{\pi^2}{2} - \frac{\gamma_q}{C_F} - \frac{K_q}{C_F} \right) \right. \\
 &\quad \left. + \left(C_F - \frac{C_A}{2} \right) \left[2 \log \bar{N} \left(1 + \log \frac{m_j^2}{s_{ja}} \right) + \mathcal{Q} \right] \right\},
 \end{aligned} \tag{5.3.40}$$

with

$$\begin{aligned}
 \mathcal{Q} &= \frac{s_{ja}}{s_{ja} + m_j^2} + \frac{3m_j}{m_j + \sqrt{s_{ja} + m_j^2}} + \log \frac{m_j^2}{s_{ja} + m_j^2} \left(1 + 2 \log \frac{m_j^2}{s_{ja}} \right) \\
 &\quad - \frac{3}{2} \log \frac{s_{ja} + 2m_j^2 - 2m_j \sqrt{s_{ja} + m_j^2}}{s_{ja}} + 2 \text{Li}_2 \left(\frac{s_{ja} + m_j^2}{m_j^2} \right) - \frac{\gamma_{\bar{q}}}{C_F}.
 \end{aligned} \tag{5.3.41}$$

Note that we will need also the same expression for the diagrams where the initial-state particles are exchanged. We can obtain it by means of the simple replacement $s_{ja} \rightarrow s_{jb}$.

For the \mathbf{K} operator from the gluon initial particle we need first the Mellin transform of \bar{K}^{gg} and of $\mathcal{K}_{\bar{q}}^{g,g}$. Both are similar to expressions we have already encountered

$$F[\bar{K}^{gg}] = \mathbf{T}_g^2 \log^2 \bar{N} - \gamma_g - K_g + \frac{2}{3} \pi^2 \mathbf{T}_g^2. \tag{5.3.42}$$

While for the second we obtain an analogous expression as in the previous case of $\mathcal{K}_{\bar{q}}^{q,q}$.

$$\begin{aligned} \mathcal{K}_{\bar{q}}^{g,g}(N; s_{ja}, m_j) &= \log^2 \bar{N} + 2 \log \bar{N} \left(1 + \log \frac{m_j^2}{s_{ja}} \right) + 2 \text{Li}_2 \left(\frac{s_{ja} + m_j^2}{m_j^2} \right) \\ &\quad + \log \frac{m_j^2}{s_{ja} + m_j^2} \left(1 + 2 \log \frac{m_j^2}{s_{ja}} \right) + \frac{s_{ja}}{s_{ja} + m_j^2} - \frac{\gamma_{\bar{q}}}{C_F} - \frac{\pi^2}{6} \end{aligned} \quad (5.3.43)$$

Transforming the whole operator

$$\begin{aligned} \langle \mathbf{K} \rangle_g(N) &= \frac{\alpha_S}{2\pi} \left\{ F [\bar{K}^{gg}] - \mathbf{T}_{\bar{q}} \cdot \mathbf{T}_g F [\mathcal{K}_{\bar{q}}^{gg}] \right. \\ &\quad \left. - \frac{\mathbf{T}_{\bar{q}} \cdot \mathbf{T}_g}{\mathbf{T}_g^2} F \left[\gamma_g \delta(1-x) \left(\log \frac{s_{ja} - 2m_j \sqrt{s_{ja} + m_j^2} + 2m_j^2}{s_{ja}} + \frac{2m_j}{\sqrt{s_{ja} + m_j^2} + m_j} \right) \right] \right. \\ &\quad \left. - \mathbf{T}_q \cdot \mathbf{T}_g F \left[2 \left(\frac{\log(1-x)}{1-x} \right)_+ \right] + \mathbf{T}_q \cdot \mathbf{T}_g F \left[\delta(1-x) \frac{\pi^2}{3} \right] \right\} \end{aligned} \quad (5.3.44)$$

$$\begin{aligned} &= \frac{\alpha_S}{2\pi} \left\{ C_A \log^2 \bar{N} - \gamma_g - K_g + \frac{2}{3} \pi^2 C_A \right. \\ &\quad + \frac{C_A}{2} \left[\log^2 \bar{N} + 2 \log \bar{N} \left(1 + \log \frac{m_j^2}{s_{ja}} \right) + 2 \text{Li}_2 \left(\frac{s_{ja} + m_j^2}{m_j^2} \right) \right. \\ &\quad \left. + \left(1 + 2 \log \frac{m_j^2}{s_{ja}} \right) \log \frac{m_j^2}{s_{ja} + m_j^2} + \frac{s_{ja}}{s_{ja} + m_j^2} - \frac{\gamma_{\bar{q}}}{C_F} - \frac{\pi^2}{6} \right] \\ &\quad + \frac{C_A}{2C_A} \beta_0 \left(\log \frac{s_{ja} - 2m_j \sqrt{s_{ja} + m_j^2} + 2m_j^2}{s_{ja}} + \frac{2m_j}{\sqrt{s_{ja} + m_j^2} + m_j} \right) \\ &\quad \left. + \frac{C_A}{2} \left(\log^2 \bar{N} + \frac{\pi^2}{6} \right) - \frac{C_A}{2} \frac{\pi^2}{3} \right\}, \end{aligned} \quad (5.3.45)$$

we can finally write it as

$$\langle \mathbf{K} \rangle_g(N) = \frac{\alpha_S}{2\pi} \frac{C_A}{2} \left[4 \log^2 \bar{N} + 2 \log \bar{N} \left(1 + \log \frac{m_j^2}{s_{ja}} \right) + \pi^2 - \frac{2\gamma_g}{C_A} - \frac{2K_g}{C_A} + \mathcal{G} \right], \quad (5.3.46)$$

with

$$\begin{aligned} \mathcal{G} &= \frac{s_{ja}}{s_{ja} + m_j^2} + \log \frac{m_j^2}{s_{ja} + m_j^2} \left(1 + 2 \log \frac{m_j^2}{s_{ja}} \right) + 2 \text{Li}_2 \left(\frac{s_{ja} + m_j^2}{m_j^2} \right) - \frac{\gamma_{\bar{q}}}{C_F} \\ &\quad + \frac{\beta_0}{C_A} \left(\log \frac{s_{ja} - 2m_j \sqrt{s_{ja} + m_j^2} + 2m_j^2}{s_{ja}} + \frac{2m_j}{\sqrt{s_{ja} + m_j^2} + m_j} \right). \end{aligned} \quad (5.3.47)$$

Note that also in this case we will need the same expression for the diagrams where the initial-state particles are exchanged. Again, we can obtain it by means of the simple replacement $s_{ja} \rightarrow s_{jb}$.

pMSSM-11 scenario A			pMSSM-11 scenario B		
M_1	M_2	M_3	M_1	M_2	M_3
0.25	0.25	-3.86	0.51	0.48	3.00
$M_{(U,D,Q)1,2}$	$M_{(U,D,Q)3}$	μ	$M_{(U,D,Q)1,2}$	$M_{(U,D,Q)3}$	μ
4.0	1.7	1.33	0.9	2.0	-9.4
$M_{(L,E)1,2}$	$M_{(L,E)3}$	$\tan\beta$	$M_{(L,E)1,2}$	$M_{(L,E)3}$	$\tan\beta$
0.35	0.47	36	1.85	1.33	33
M_A	A_0		M_A	A_0	
4.0	2.8		3.0	-3.4	
$m_{\tilde{\chi}_1^0}$	$m_{\tilde{u}}$	$m_{\tilde{g}}$	$m_{\tilde{\chi}_1^0}$	$m_{\tilde{u}}$	$m_{\tilde{g}}$
0.249	4.07	3.90	0.505	0.96	2.94

Table 5.2: Higgs and soft SUSY breaking parameters in our pMSSM-11 benchmark models, together with the relevant resulting physical particle masses. All values, except for $\tan\beta$, are given in TeV.

5.3.4 Numerical results

For our numerical predictions, we identify the Standard Model parameters with those determined by the PDG [26]. The running of the strong coupling with five active quark flavours is chosen in agreement with the selected PDF set as provided by the LHAPDF 6 library. As our default choice of PDFs, we employ the sets of MSHT20 unless stated otherwise. To be specific, we use at LO the set MSHT20lo_as130 [44] with $\alpha_S(M_Z) = 0.130$, and at NLO and NLO+NLL the set MSHT20nlo_as118 [44] with $\alpha_S(M_Z) = 0.118$. Again unless stated otherwise, we consider the dominant squark-electroweakino production channel at the LHC, *i.e.* the production of a left-handed or a right-handed up-type squark in association with the lightest neutralino.

5.3.4.1 Total cross sections and their scale uncertainty

In the following, we present results for two specific phenomenological MSSM scenarios with eleven parameters (pMSSM-11). The input parameters and the relevant resulting physical masses obtained with SPheno 3 [462] are listed in Tab. 5.2. First, we focus on a scenario featuring large squark masses of 4 TeV, referred to as scenario A. Second, scenario B explores squark and gaugino masses expected to be within the reach of Run 3 of the LHC. Both scenarios are based on the global fits of Ref. [463]. Scenario A is derived from a fit that includes data from the anomalous magnetic moment of the muon [464], while scenario B does not include it. In addition, we have lowered the parameters M_1 and M_2 in scenario B and have increased the parameter M_3 to bring the squark and gluino masses in agreement with the current SUSY limits from the LHC [445, 447, 448].

In Fig. 5.5, We present predictions for the total cross section related to the process $pp \rightarrow \tilde{u}_L \tilde{\chi}_1^0$ in scenarios A and B with squark masses of 4 TeV and 1 TeV, respectively, together with the associated scale uncertainties. The results are shown at LO, NLO and NLO+NLL for a centre-of-mass energy of $\sqrt{S} = 13$ TeV. Our predictions show a

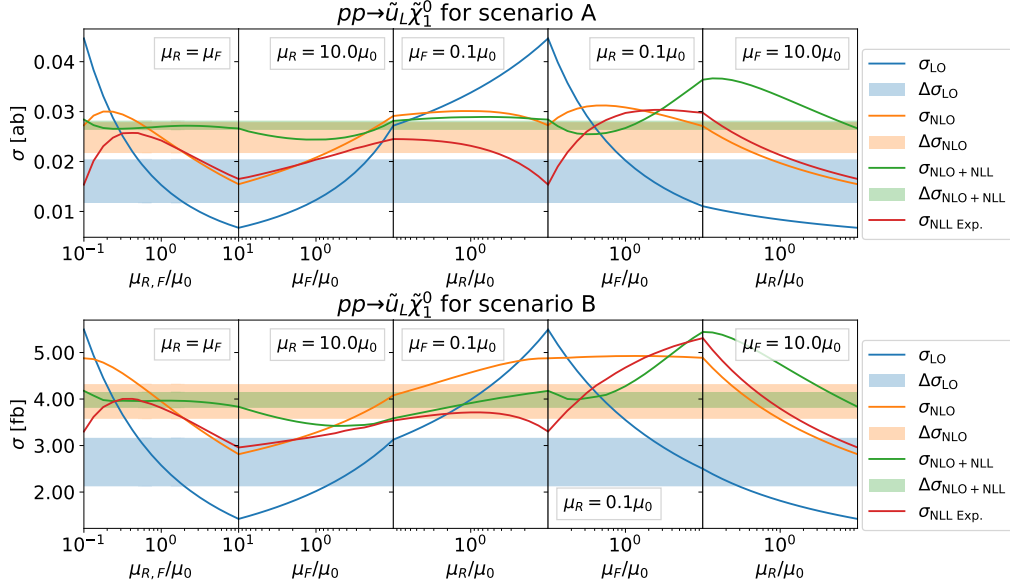


Figure 5.5: Profiles of the renormalization and factorization scale dependence of the total cross section corresponding to the process $pp \rightarrow \tilde{u}_L \tilde{\chi}_1^0$ in scenarios A and B. The plots cover $\mu_{F,R} \in (0.1 - 10)\mu_0$ (reversely in panels 2 and 3) with a central scale $\mu_0 = (m_{\tilde{q}} + m_{\tilde{\chi}})/2$. The bands correspond to scale uncertainties evaluated with the seven-point method, and we use $\sqrt{S} = 13$ TeV and MSHT20 PDFs. We present predictions at LO, NLO and NLO+NLL, as well as for the $\mathcal{O}(\alpha_S^2)$ expansion of the NLL result. Note that the axis changes directions between some panels.

significant increase of the total cross section in scenario A when including NLO+NLL corrections as well as a reduction of the scale uncertainties in both scenarios. The uncertainty bands are again determined by the seven-point method, where the factorization and renormalization scales are both varied independently by factors of two up and down around the central scale $\mu_0 = (m_{\tilde{q}} + m_{\tilde{\chi}})/2$, excluding the cases where $\mu_F/\mu_R = 4$ or $1/4$. For both examined scenarios, we observe that the relative scale uncertainties are reduced from about $\pm 20\%$ at LO to $\pm 10\%$ at NLO, and finally fall below $\pm 5\%$ at NLO+NLL. The kink in the NLO cross section at $\mu_F = \mu_R = 0.1\mu_0$ between panels three and four is more prominent in scenario A than in scenario B. It originates from the subtraction of on-shell squark and gluino resonant contributions from the real emission component of the cross section. We also include predictions for the expansion of the NLL predictions at $\mathcal{O}(\alpha_S^2)$, following Eq. (5.2.48) (solid red curve). As expected for large scales the logarithmic terms become dominant, and the expansion consequently approximates well the NLO result. Full control over the scale dependence at NNLO and beyond can of course only be obtained with an explicit calculation.

5.3.4.2 Parton density uncertainties of the total cross section

So far we have only studied scale uncertainties associated with the total rates for squark-electroweakino production at the LHC. There is, however, a second important source of theoretical uncertainties, *i.e.* those coming from the PDF. The computation of the PDF

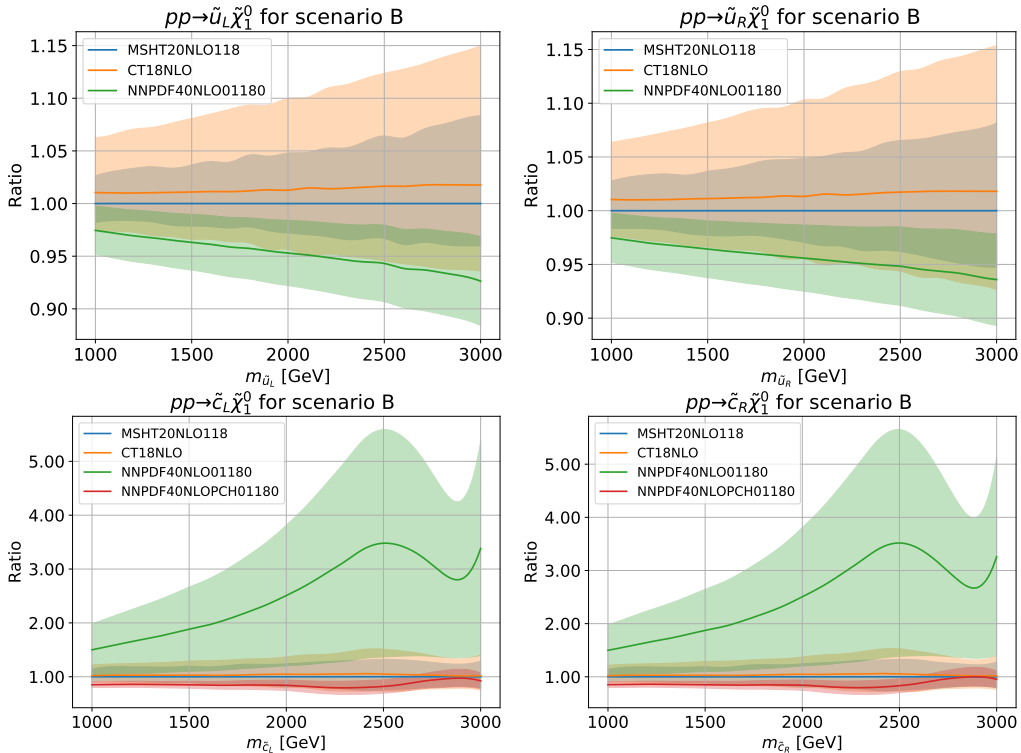


Figure 5.6: Relative PDF uncertainties of the total cross sections for the processes $pp \rightarrow \tilde{q}_{L,R} \tilde{\chi}_1^0$ at the LHC with a centre-of-mass energy of $\sqrt{S} = 13$ TeV and at NLO+NLL. The uncertainties are shown as a function of the squark mass $m_{\tilde{q}_{L,R}}$ and for four different choices of PDFs, namely MSHT20nlo_as118 (blue), CT18NLO [47] (orange), NNPDF40_nlo_as_01180 [42] (green) and NNPDF40_nlo_pch_as_01180 [42] (red).

uncertainties goes as already described in Sec. 2.2.2.

For our predictions at NLO and NLO+NLL, we calculated the PDF uncertainties at 90% confidence level following the convention of Ref. [47]. The resummation of large logarithms does not significantly alter the size of the relative PDF uncertainties, as the same set of PDFs is used in both calculations. For scenario B we show in Fig. 5.6 the PDF uncertainties associated with NLO+NLL total cross sections for the different choices of parton densities mentioned above, *i.e.* for MSHT20, CT18 and NNPDF40 [42]. We consider the process $pp \rightarrow \tilde{u}_{L,R} \tilde{\chi}_1^0$ in the top row of the figure and present predictions as a function of the squark mass. While the uncertainty is of about 5% for 1 TeV up-squarks, it increases up to 10% to 15% for squark masses of 3 TeV. This increase is related to the large partonic momentum fractions x relevant for such a large mass, where the PDFs are less constrained in their fitting procedure. The central cross section values obtained with the MSHT20 and CT18 sets agree consistently at the percent level in the explored mass range, the MSHT20 errors being slightly smaller as a consequence of this set being more recent than the CT18 one. On the other hand, the NNPDF40 predictions are a few percent lower, although they are still in reasonable agreement within their uncertainty intervals with the predictions achieved with other PDFs.

In the lower two plots of Fig. 5.6 we show results for the production of a charm squark in association with the lightest neutralino. We observe that the results obtained with the central NNPDF40_lo_as_01180 [42] set with $\alpha_S(M_Z) = 0.118$ give cross sections that are larger by a factor of three to four with respect to those obtained with the CT18NLO [47] set and with the MSHT20nlo_as118 set, both also with $\alpha_S(M_Z) = 0.118$. In addition, the uncertainties associated with the NNPDF40 predictions are of about 30% to 50%, in contrast with predictions obtained with CT18 and MSHT20, that have much smaller uncertainties. This discrepancy can be traced back to the treatment of the charm quark in the NNPDF40 fit [465] and is expected to be even more significant in processes with two charm quarks or antiquarks in the initial-state. The cross sections estimated with the alternative NNPDF40_nlo_pch_as_01180 [42] PDF fit (red) with $\alpha_S(M_Z) = 0.118$, in which the treatment of the charm quark is kept purely perturbative, are, in contrast, in good agreement with CT18 and MSHT20 both for the central values and the uncertainties.

5.3.4.3 Squark and gaugino mass dependence of the total cross section

The dependence of the total cross section for associated squark-electroweakino production on the masses of the produced particles is important to estimate the sensitivity of Run 3 at the LHC to this process. A precise quantitative statement of course requires a detailed signal and background analysis, which follows in Sec. 5.5. Therefore, we show in Fig. 5.7 the total cross sections and resulting relative scale uncertainties for scenario B as a function of the SUSY particle masses, both for $\tilde{u}_L\tilde{\chi}_1^0$ (left) and $\tilde{u}_R\tilde{\chi}_1^0$ (right) production. As expected, the cross sections fall steeply with either mass. Our predictions indicate that an integrated luminosity of 350 fb^{-1} at $\sqrt{S} = 13\text{ TeV}$ from the LHC Run 3 [383] will lead to the production of hundreds of squark-electroweakino events for a neutralino mass of 0.5 TeV and squark masses ranging up to 2 TeV.

In the lower panels of the plots, we observe an improvement in the precision of the predictions over the whole mass range. Resummation effects reduce the scale dependence from $\pm 10\%$ at NLO to below $\pm 5\%$ at NLO+NLL. The black curves in the lower insets of the figures represent the ratio of the NLO+NLL predictions to the NLO ones and demonstrate the increasing impact of resummation with rising mass values. As in the previous sections, this demonstrates once more that resummation effects are larger near the hadronic threshold. While the central cross section values are enlarged by 50% when adding NLO corrections to the LO rates, the additional increase from NLL resummation reaches only about 6% for the mass ranges observable at the LHC in the near future.

5.4 Precision predictions for electroweak SUSY processes in simplified models at 13.6 TeV

We make use of `Resummino` to compute the total production rates at aNNLO+NNLL obtained for the LHC Run 3, operating at a centre-of-mass energy of 13.6 TeV. We consider simplified model scenarios in which all superparticles are decoupled, excepted for those produced in the final-state. Our results highlight how theoretical uncertainties are reduced relative to the perturbative order of the fixed-order and resummed component of the matched predictions and how they compare with predictions at a centre-of-mass energy of 13 TeV. Moreover, we explore next-to-minimal scenarios, and discuss the impact of internal squark masses on the predictions for configurations in which squarks are not decoupled but only slightly heavier than the lighter electroweakinos.

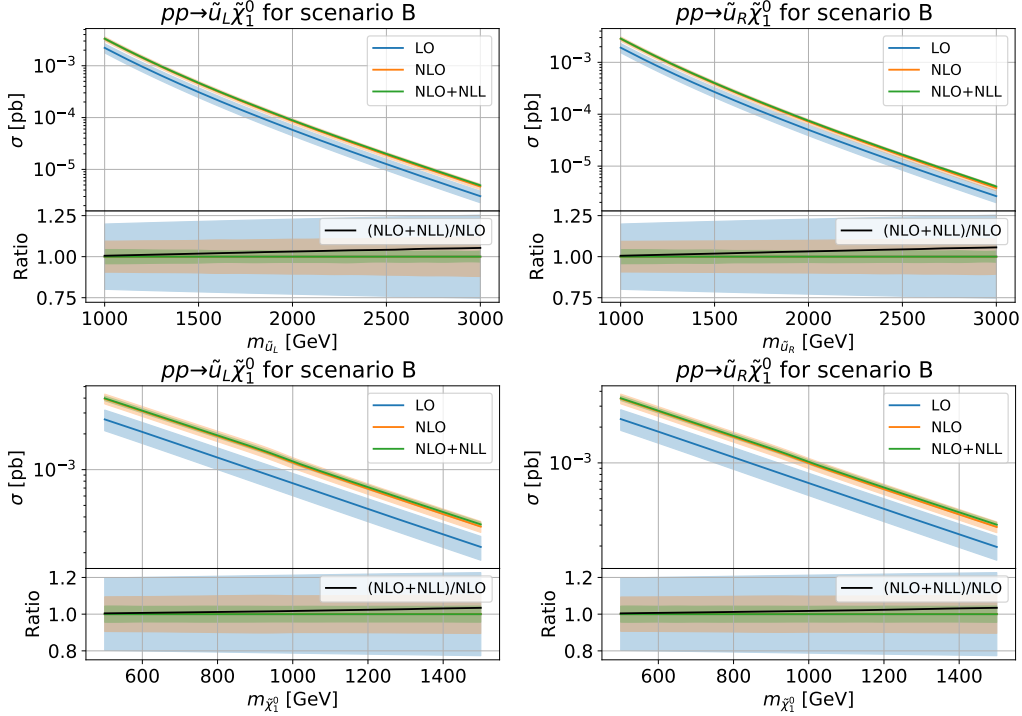


Figure 5.7: Total cross sections for the processes $pp \rightarrow \tilde{u}_{L,R} \tilde{\chi}_1^0$ and their relative scale uncertainties (top panels) as well as $(\text{NLO+NLL})/\text{NLO}$ K -factors (bottom panels) in scenario B. In the first row, we vary the squark mass $m_{\tilde{u}_{L,R}}$, keeping a fixed distance between the left- and right-handed squark masses $m_{\tilde{u}_L} - m_{\tilde{u}_R} = 100$ GeV. In the second row, we vary the electroweakino mass $m_{\tilde{\chi}}$. The other parameters defining scenario B are not modified. The LHC energy is $\sqrt{S} = 13$ TeV, and we use MSHT20 PDFs.

We employ the PDF4LHC21_40 [466] set of parton distribution functions, and we provide results together with the associated PDF and scale uncertainties (the latter being obtained with the seven-point method) added in quadrature. As this section is based on our publication [2], complementary to the figures shown in this section, the complete collection of numerical predictions are shown in its appendix tables.

We consider simplified SUSY models inspired by the MSSM, and we explore several typical scenarios. In the context of slepton pair production, we focus on a configuration in which all SUSY particles are decoupled by setting their masses to 100 TeV, except a single slepton species that is taken either left-handed \tilde{e}_L , right-handed \tilde{e}_R or maximally mixed $\tilde{\tau}_1 = 1/\sqrt{2}[\tilde{\tau}_L + \tilde{\tau}_R]$. This last scenario is representative of models featuring light tau sleptons, as originating from many SUSY scenarios [405].

Electroweakino pair production rates are estimated in similar scenarios, in which all SUSY particles are decoupled except the lightest electroweakinos [399]. We begin our study with scenarios in which the three lightest electroweakinos are all higgsinos. In the first setup, all higgsinos are taken mass-degenerate and the lightest states are defined

by the mixing matrices

$$N = \begin{pmatrix} 0 & 0 & 2^{-\frac{1}{2}} & 2^{-\frac{1}{2}} \\ 0 & 0 & 2^{-\frac{1}{2}} & -2^{-\frac{1}{2}} \\ 0 & 0 & 0 & 0 \\ 0 & 0 & 0 & 0 \end{pmatrix}, \quad V = U = \begin{pmatrix} 0 & 1 \\ 0 & 0 \end{pmatrix}, \quad (5.4.1)$$

and equivalently

$$\tilde{\chi}_{1,2}^0 \sim \frac{1}{\sqrt{2}} (\tilde{H}_u^0 \pm \tilde{H}_d^0), \quad \tilde{\chi}_1^\pm \sim \tilde{H}_{u,d}^\pm. \quad (5.4.2)$$

Whereas this choice of a real neutralino mixing matrix implies a negative $m(\chi_1^0)$ eigenvalue, it can always be transformed back to positive a mass eigenvalue through a chiral rotation [467]. In a second setup, we introduce some mass splitting between the three electroweakinos, such a splitting being typical of next-to-minimal electroweakino simplified models studied at the LHC, and that turn out to be more realistic in the light of concrete MSSM scenarios [468]. We define the three lightest electroweakinos by

$$N = \begin{pmatrix} 0 & 0 & 2^{-\frac{1}{2}} & -2^{-\frac{1}{2}} \\ 0 & 0 & -2^{-\frac{1}{2}} & -2^{-\frac{1}{2}} \\ 1 & 0 & 0 & 0 \\ 0 & 0 & -1 & 0 \end{pmatrix}, \quad V = U = \begin{pmatrix} 0 & 1 \\ 1 & 0 \end{pmatrix}, \quad (5.4.3)$$

$$\Rightarrow \tilde{\chi}_{1,2}^0 \sim -\frac{1}{\sqrt{2}} (\mp \tilde{H}_u^0 + \tilde{H}_d^0), \quad \tilde{\chi}_1^\pm \sim \tilde{H}_{u,d}^\pm. \quad (5.4.4)$$

Finally, we consider a scenario in which all lightest electroweakinos are mass-degenerate gauginos, that is mixing matrices

$$N = \begin{pmatrix} 1 & 0 & 0 & 0 \\ 0 & 1 & 0 & 0 \\ 0 & 0 & 0 & 0 \\ 0 & 0 & 0 & 0 \end{pmatrix}, \quad V = U = \begin{pmatrix} 1 & 0 \\ 0 & 0 \end{pmatrix}, \quad (5.4.5)$$

resulting in the following eigenstates

$$\tilde{\chi}_1^0 \sim i\tilde{B}, \quad \tilde{\chi}_2^0 \sim i\tilde{W}^3, \quad \tilde{\chi}_1^\pm \sim \tilde{W}^\pm. \quad (5.4.6)$$

In this last SUSY configuration, we additionally investigate squark mass effects on gaugino pair production. Here, we consider an eight-fold degeneracy of all first-generation and second-generation squarks, the spectrum featuring thus many states reachable at the LHC.

Before going into the detailed results we show a summary of the total cross sections for the different scenarios considered in Tab. 5.3. As a rule of thumb valid for all investigated processes, QCD threshold resummation reduces the typical scale dependence

Final-state particle mass	1 TeV	1.5 TeV	2 TeV
$\sigma_{13.6 \text{ TeV}}/\sigma_{13 \text{ TeV}}$	~ 1.2	~ 1.3	~ 1.6
PDF4LHC21 unc.	13% to 20%	35% to 40%	>100%
Scale unc.	<0.3%	<0.2%	<0.1%

Table 5.3: Behaviour of aNNLO+NNLL total cross sections for slepton and electroweakino pair production at the LHC, for a centre-of-mass energy of $\sqrt{S} = 13.6 \text{ TeV}$. The results are given as a function of the average mass of the final-state particles, and we provide the typical increase in cross section related to predictions at $\sqrt{S} = 13 \text{ TeV}$, and information about the size of the theoretical PDF and scale uncertainties inherent to the calculations achieved.

to less than 1% at aNNLO+NNLL. These contributions to the combined theory error hence become generally negligible, or at least subleading. For the production of low-mass SUSY states, PDF and scale uncertainties are of the same order of magnitude, so that theory systematics are under good control. In our predictions, we have employed the PDF4LHC21 [466] set of parton densities that originates from a combination of variants of the CT18, MSHT20 and NNPDF3.1 [469] global PDF fits. Such a set generally leads to larger PDF uncertainties compared to the individual global sets, particularly at large Bjorken $x \gtrsim 0.4$ [466]. In this region, yet poorly constrained by experimental data, discrepancies between predictions relying on the different global sets can be significant as the parton density behaviour is mainly driven by the theoretical assumptions made. For instance, recent studies have shown how the recent NNPDF4.0 set predicts (anti)quark distributions falling much faster (slower) with respect to the other sets [470]. Moreover, the sea over valence quark ratio is a determining factor for DY-like processes [471], and in turn it also has a strong impact on the determination of the gluon density at high x values and large scale [472]. Predictions for (differential) cross section can therefore vary substantially with the choice of the PDF set, especially in scenarios featuring heavy SUSY particles. This issue will however be naturally fixed with time, as more data gets collected at high scale by the LHC collaborations.

5.4.1 Slepton pair production

In Fig. 5.8 we display aNNLO+NNLL cross section predictions for slepton pair production at the LHC as a function of the slepton mass $m_{\tilde{\ell}}$. We consider two centre-of-mass energies fixed to $\sqrt{S} = 13.6 \text{ TeV}$ (orange) and 13 TeV (blue), and we focus in the upper, central and lower panel of the figure on the respective processes

$$pp \rightarrow \tilde{e}_L^+ \tilde{e}_L^-, \quad \tilde{e}_R^+ \tilde{e}_R^-, \quad \tilde{\tau}_1^+ \tilde{\tau}_1^-. \quad (5.4.7)$$

In the figures, we restrict the mass range shown to $m_{\tilde{\ell}} \lesssim 1 \text{ TeV}$. This corresponds to cross section values larger than 0.01 fb , to which the LHC Run 3 is in principle sensitive as dozens signal events could populate the signal regions of the relevant ATLAS and CMS analyses.¹

¹The actual numbers of events populating these signal regions depend on the details of the different relevant LHC analyses. However, their precise estimation lies beyond the scope of this article that is solely dedicated to precision predictions for total slepton and electroweakino production rates at the LHC Run 3.

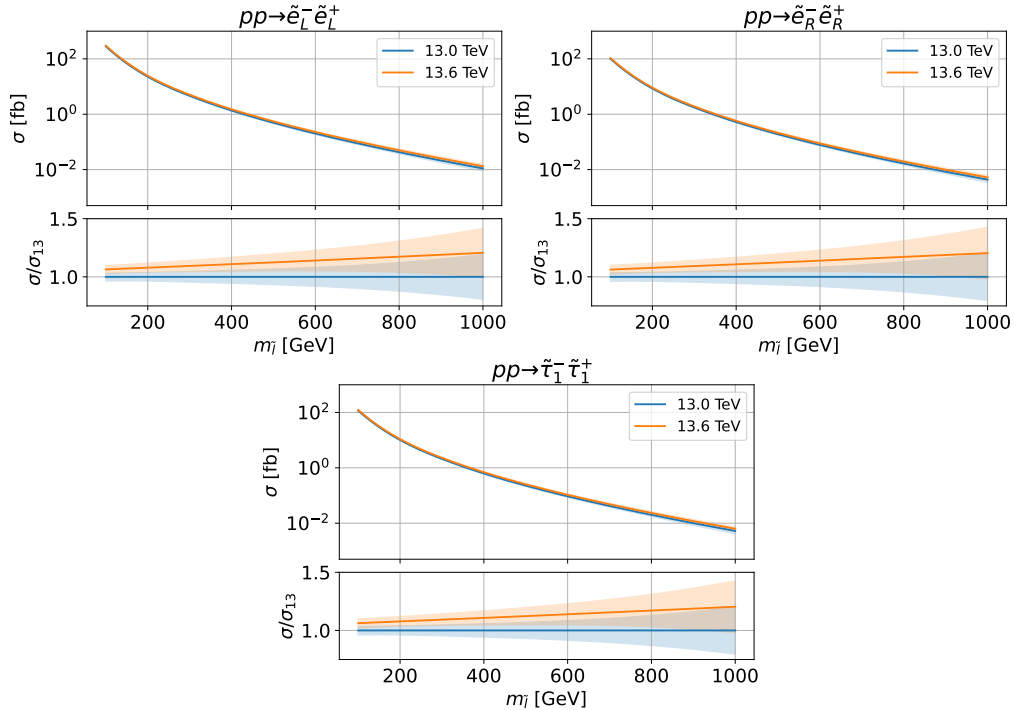


Figure 5.8: Total cross sections for slepton pair production at the LHC, operating at centre-of-mass energies $\sqrt{S} = 13.6$ TeV and 13 TeV (upper insets), shown together with their ratios to the 13 TeV total rates (lower insets) in which combined scale and PDF uncertainties are included. We consider the production of a pair of left-handed sleptons (left), right-handed sleptons (right) and maximally-mixed sleptons (bottom), and predictions are presented as a function of the slepton mass $m_{\tilde{\ell}}$.

Whereas cross sections for $\sqrt{S} = 13$ TeV and 13.6 TeV are both shown in the upper insets of the three subfigures, the gain in rate at Run 3 is more visible from the ratio plots presented in their lower insets. This indeed illustrates better how cross section increases ranging up to 20% can be obtained in the three classes of scenarios considered, especially for large slepton masses. As expected from the structure of the slepton couplings to the Z -boson (see *e.g.* in Ref. [408]), left-handed sleptons are more easily produced in high-energy hadronic collisions than their right-handed counterparts that only couple through their hypercharge. Consequently, cross sections corresponding to mixed scenarios lie between the two extreme non-mixing cases for a given slepton mass $m_{\tilde{\ell}}$.

The different ratio plots of the lower insets of the subfigures also show the dependence of the theoretical systematic uncertainty bands on the slepton mass. The collider energy upgrade achieved at Run 3 naturally leads to a reduction of the PDF uncertainties as the gain in centre-of-mass energy yields a smaller relevant Bjorken- x regime in which parton distribution functions are better fitted. Scale uncertainties contribute to at most 2% of the combined theoretical uncertainty in the entire mass range probed, regardless of the centre-of-mass energies considered. In contrast, PDF errors vary from 3% to 18% at 13.6 TeV, which must be compared to a variation ranging from 3% to 20% at 13 TeV. For a phenomenological study on the reduction of PDF uncertainties in slepton

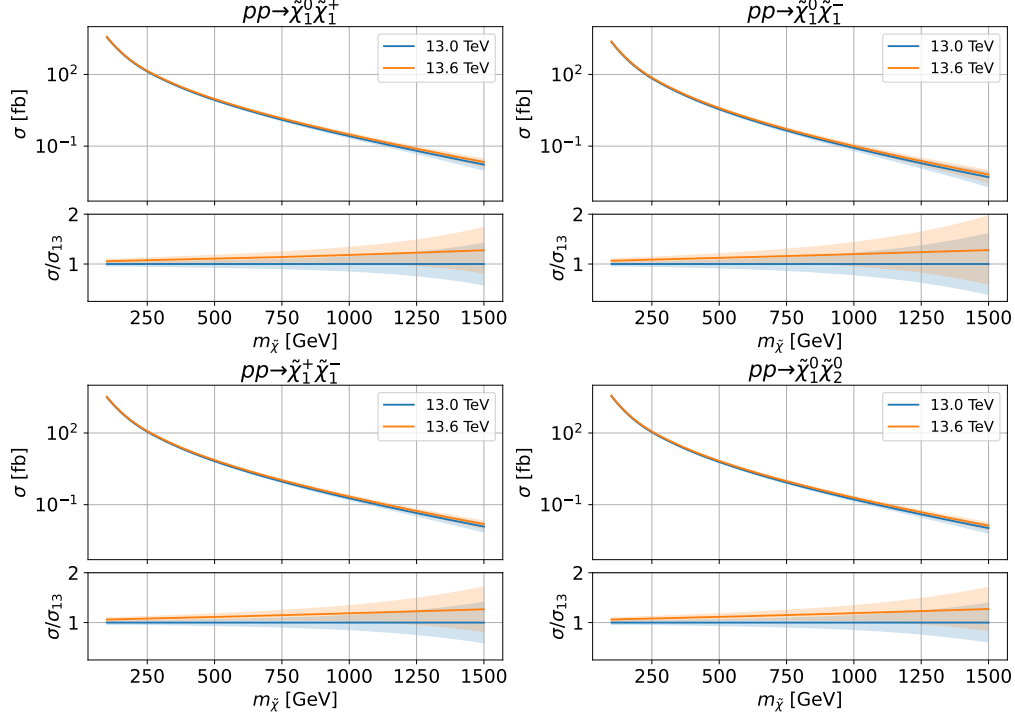


Figure 5.9: Total cross sections for mass-degenerate higgsino pair production at the LHC, operating at centre-of-mass energies $\sqrt{S} = 13.6$ TeV and 13 TeV (top panels), shown together with their ratios to the 13 TeV total rates (bottom panels) in which combined scale and PDF uncertainties are included. We consider the production of associated $\tilde{\chi}_1^0 \tilde{\chi}_1^+$ (upper left) and $\tilde{\chi}_1^0 \tilde{\chi}_1^-$ (upper right) pairs, as well as that of a pair of charginos $\tilde{\chi}_1^+ \tilde{\chi}_1^-$ (lower left) and neutralinos $\tilde{\chi}_2^0 \tilde{\chi}_1^0$ (lower right). Predictions are presented as a function of the electroweakino mass $m_{\tilde{\chi}}$.

pair production see [406].

5.4.2 Higgsino pair production

We now turn to scenarios in which all SUSY particles are decoupled by setting their masses at 100 TeV, except all higgsino states. We begin with a calculation of aNNLO+NNLL predictions relevant for higgsino pair production in a scenario in which all higgsinos, defined as in Eq. (5.4.2), are mass-degenerate, *i.e.* in which

$$m(\tilde{\chi}_1^0) = m(\tilde{\chi}_2^0) = m(\tilde{\chi}_1^\pm) \equiv m(\tilde{\chi}). \quad (5.4.8)$$

Our results are shown in Fig. 5.9 for the four processes

$$pp \rightarrow \tilde{\chi}_1^0 \tilde{\chi}_1^+, \quad \tilde{\chi}_1^0 \tilde{\chi}_1^-, \quad \tilde{\chi}_1^+ \tilde{\chi}_1^-, \quad \tilde{\chi}_2^0 \tilde{\chi}_1^0, \quad (5.4.9)$$

since in the case of a degenerate spectrum $\sigma(\tilde{\chi}_1^0 \tilde{\chi}_1^\pm) = \sigma(\tilde{\chi}_2^0 \tilde{\chi}_1^\pm)$. In the results displayed, we restrict the mass range considered to $m_{\tilde{\chi}} \lesssim 1.5$ TeV, which corresponds to production rates at the LHC larger than 0.01 fb and therefore potentially reachable at Run 3. The

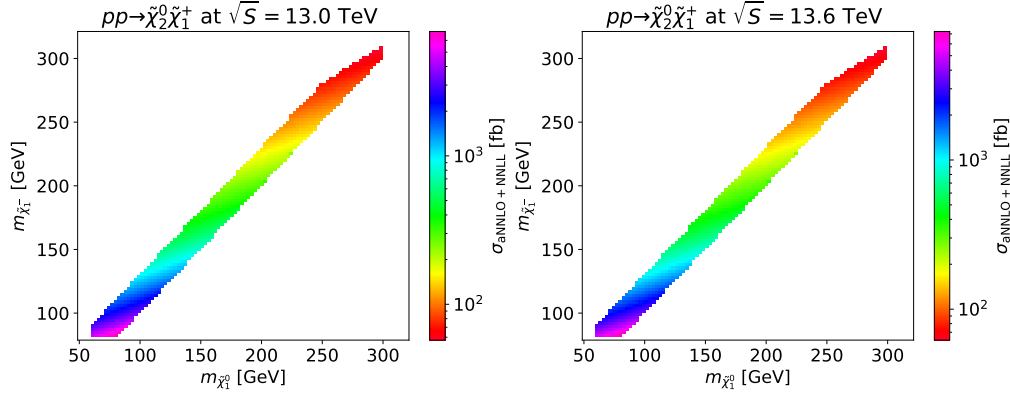


Figure 5.10: Total cross sections for $\tilde{\chi}_2^0\tilde{\chi}_1^+$ production at the LHC, operating at centre-of-mass energies $\sqrt{S} = 13$ TeV (left) and 13.6 TeV (right), in a scenario where all SUSY particles are decoupled with the exception of the non-degenerate produced states.

largest cross sections are obtained for the charged-current process $pp \rightarrow \tilde{\chi}_1^0\tilde{\chi}_1^+$, such an effect originates from a PDF enhancement related to the ratio of valence and sea quarks in the proton and from the structure of the higgsino gauge couplings. This additionally leads to similar neutral-current higgsino production rates ($pp \rightarrow \tilde{\chi}_1^+\tilde{\chi}_1^-$ and $pp \rightarrow \tilde{\chi}_2^0\tilde{\chi}_1^0$), and the cross section of the negative charged-current process $pp \rightarrow \tilde{\chi}_1^0\tilde{\chi}_1^-$ is then smaller.

As in the slepton case explored in Sec. 5.4.1, we find an enhancement of total production cross sections at 13.6 TeV relative to those at 13 TeV thanks to the modest gain in phase space. Rates are indeed found to be 10% to 30% larger at $\sqrt{S} = 13.6$ TeV than at $\sqrt{S} = 13$ TeV, for low and high electroweakino masses respectively.

Still similarly to the slepton case, theoretical uncertainties get reduced with the increase in centre-of-mass energy. Scale uncertainties contribute negligibly to the total theory errors for both centre-of-mass energies, scale variations indeed leading to errors of about 1% to 2% for low higgsino masses and lying in the permille range for $m_{\tilde{\chi}} \gtrsim 300$ GeV. In contrast, total rates at 13 TeV are plagued with PDF uncertainties varying from a few percent at low masses to more than 20% to 40% for higgsino masses larger than about 1.2 TeV. The reduction of the average Bjorken- x value inherent to the larger centre-of-mass energy of 13.6 TeV subsequently leads to smaller PDF errors that are found reduced by about a few permille at low masses, up to 5% to 7% at large masses. For a phenomenological study on the reduction of PDF uncertainties in higgsino pair production see [400].

We now move on with a second higgsino scenario in which the three lightest higgsino states are defined as in Eq. (5.4.4). Moreover, their spectrum is enforced to feature a significant level of compression, so that all three higgsino states exhibit a mass splitting of a few percent². In the following, we impose that

$$m(\chi_1^\pm) = \frac{m(\chi_2^0) - m(\chi_1^0)}{2}, \quad (5.4.10)$$

with all masses being taken positive.

Given these mass relations, we present in Fig. 5.10 aNNLO+NNLL total cross sections for the process $pp \rightarrow \tilde{\chi}_1^0\tilde{\chi}_1^+$ at the LHC, for centre-of-mass energies of $\sqrt{S} =$

²The masses of the decoupled squarks are set to 4.5 TeV in order to avoid numerical complications.

13 TeV (left) and 13.6 TeV (right). We consider the mass range in which all higgsinos are lighter than 300 GeV, as this consists of the relevant mass configurations in terms of LHC sensitivity to compressed SUSY higgsino scenarios [473–475].

In the figures, associated rates are shown logarithmically through a colour code. In this scheme, other higgsino production modes yield almost identical figures, that we therefore omit for brevity. For the considered mass range, theoretical systematics are found in very good control, the combined uncertainties being of about 5% for all mass configurations explored. Whereas scale uncertainties decrease from 2% to 3% in the lightest configurations considered to a few permille for higgsinos of about 200 GeV to 300 GeV, PDF errors increase from 2% to 3% in the lightest scenarios to 4% to 5% in the heavier cases. The combined theory errors are thus similar in size for all scenarios studied.

As for the previous calculations achieved, a cross section increase at 13.6 TeV results from the phase space enhancement inherent to the increased centre-of-mass energy relative to the 13 TeV case. Moreover, a rate hierarchy similar to that observed in the mass-degenerate case is obtained, phase space effects being minimal for compressed scenarios with a non-degenerate spectrum compared to mass-degenerate scenarios in which all higgsinos have exactly the same mass. The process $pp \rightarrow \tilde{\chi}_1^0 \tilde{\chi}_1^+$ hence dominates, followed by the neutral current modes ($pp \rightarrow \tilde{\chi}_1^0 \tilde{\chi}_2^0$ and $pp \rightarrow \tilde{\chi}_1^+ \tilde{\chi}_1^-$) and finally the charged-current channel $pp \rightarrow \tilde{\chi}_1^0 \tilde{\chi}_1^-$. We remind that such a hierarchy is dictated by the structure of the higgsino gauge couplings to the W and Z bosons, and by the PDF ratio of valence and sea quarks in the proton.

5.4.3 Gaugino pair production

We now turn to the analysis of the gaugino scenarios introduced in Eq. (5.4.6), in which the lightest electroweakinos consist of bino and wino eigenstates. In our analysis, we consider that the two wino eigenstates are mass-degenerate, with respective masses satisfying

$$m(\tilde{\chi}_2^0) = m(\tilde{\chi}_1^\pm) \equiv m(\tilde{\chi}). \quad (5.4.11)$$

In the following, we then focus on the processes

$$pp \rightarrow \tilde{\chi}_2^0 \tilde{\chi}_1^+, \quad \tilde{\chi}_2^0 \tilde{\chi}_1^-, \quad \tilde{\chi}_1^+ \tilde{\chi}_1^- \quad (5.4.12)$$

and we present aNNLO+NNLL predictions for the associated total rates in Fig. 5.11. Other processes are irrelevant as the corresponding cross sections vanish due to the structure of the bino and wino gauge couplings. As in the previous subsections, we consider results at centre-of-mass energies of 13 TeV (blue) and 13.6 TeV (orange) in the upper insets of the figures. This time, however, we display predictions for wino masses ranging up to 2 TeV, the cross sections being much larger than in the higgsino case by virtue of the weak triplet nature of the winos. Consequently, we can expect a better LHC sensitivity to signatures of wino production and decays, due to the machine being capable to naturally probe a larger mass regime.

In accord with parton density effects, the charged-current process $pp \rightarrow \tilde{\chi}_2^0 \tilde{\chi}_1^+$ dominates for a given wino mass, its rate being a factor of 1.5 to 3 larger than that of the other charged-current process $pp \rightarrow \tilde{\chi}_2^0 \tilde{\chi}_1^-$ in the case of lighter and heavier mass setups respectively. Furthermore, total cross sections for the neutral current process $pp \rightarrow \tilde{\chi}_1^+ \tilde{\chi}_1^-$, mediated by virtual photon and Z -boson exchanges, are usually 1.25 – 1.5 smaller than rates corresponding to the charged-current mode $pp \rightarrow \tilde{\chi}_2^0 \tilde{\chi}_1^+$, in which

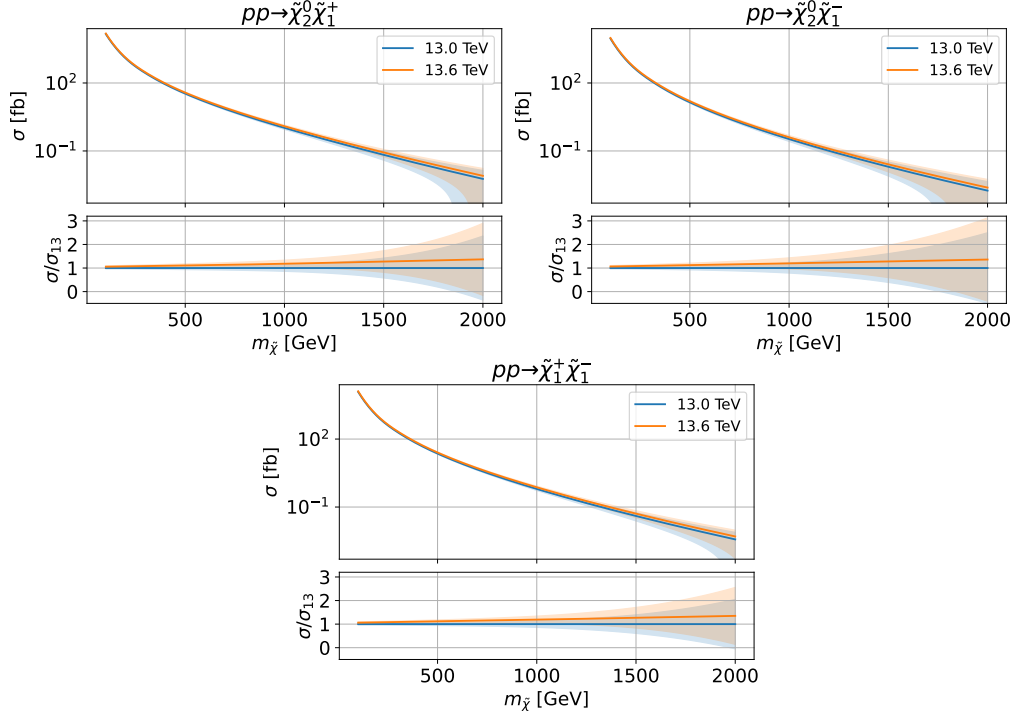


Figure 5.11: Total cross sections for wino pair production at the LHC, operating at centre-of-mass energies $\sqrt{S} = 13.6$ TeV and 13 TeV (upper insets), shown together with their ratios to the 13 TeV total rates (lower insets) in which combined scale and PDF uncertainties are included. We consider the charged-current production of a $\tilde{\chi}_2^0 \tilde{\chi}_1^+$ (left) and $\tilde{\chi}_1^0 \tilde{\chi}_1^-$ (right) wino pair, as well as the neutral-current production of a $\tilde{\chi}_1^+ \tilde{\chi}_1^-$ pair (bottom). Predictions are presented as a function of the wino mass $m_{\tilde{\chi}}$.

the final-state is produced from virtual W -boson exchanges. On the other hand, the increase in cross section observed when the hadronic centre-of-mass energy is modified from 13 TeV to 13.6 TeV can be quite substantial in such mass-degenerate wino scenarios. While for light produced particles the increase is only modest and lies in the 5 % to 10 % range for all three processes, it increases with the wino mass $m_{\tilde{\chi}}$ and reaches 35 % to 40 % for wino masses of about 2 TeV.

In the lower insets of the three subfigures, we display the ratio of the total production rates at 13 TeV and 13.6 TeV to that at 13 TeV, including the combined theory systematic error. For the entire mass range considered, scale uncertainties are under good control. They are about 1 % to 2 % at low masses, and then decrease to a few permille for wino masses larger than 300 GeV. In contrast, PDF errors are smaller than 10 % for wino masses smaller than about 1 TeV, but quickly increase for heavier mass configurations. In this case, typical Bjorken- x values are large and correspond to phase space regimes in which parton densities are poorly constrained, as already pointed out in Ref. [376]. This issue will nevertheless be automatically cured with time. Time will indeed allow the LHC collaborations to collect better-quality SM data at large scales, which will consequently help in reducing the PDF errors. For a corresponding theoretical study

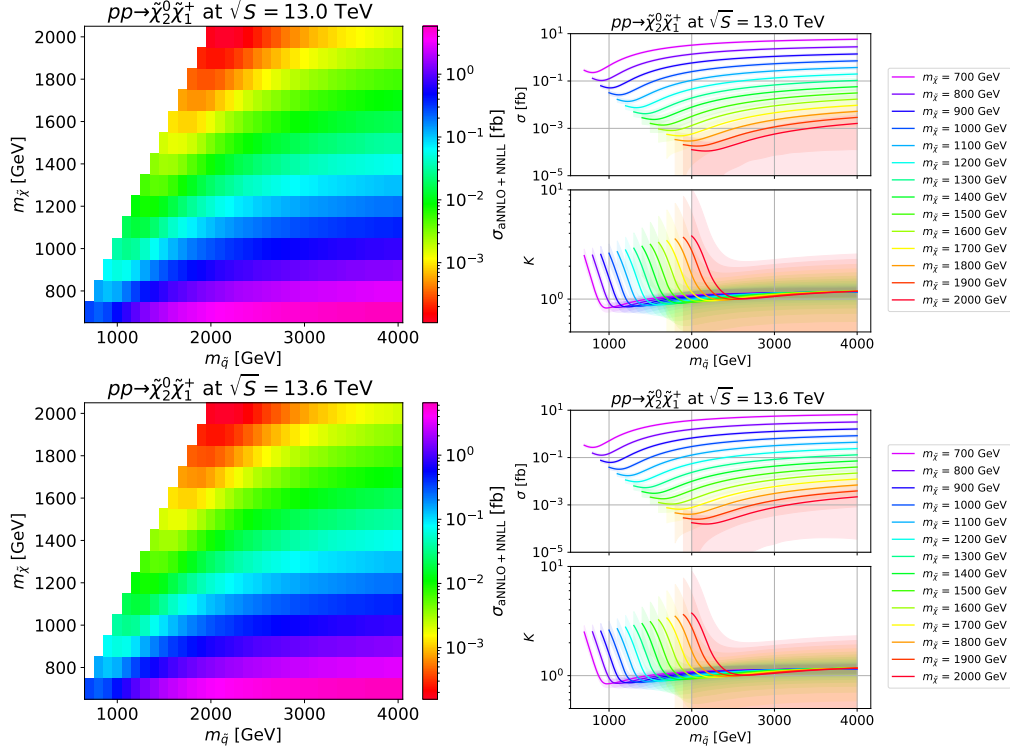


Figure 5.12: Total cross sections for wino pair production at the LHC, operating at centre-of-mass energies $\sqrt{S} = 13$ TeV (upper) and 13.6 TeV (lower). We consider the charged-current production of a $\tilde{\chi}_2^0 \tilde{\chi}_1^+$ wino pair, and present predictions as a function of the wino mass $m_{\tilde{\chi}}$ and the common first-generation and second-generation squark mass $m_{\tilde{q}}$.

see [400].

In order to explore the phenomenological consequences of next-to-minimality, we now consider scenarios in which first-generation and second-generation squarks are mass-degenerate, but not decoupled. We introduce the squark mass parameter $m_{\tilde{q}}$ defined by

$$m(\tilde{u}_{L,R}) = m(\tilde{d}_{L,R}) = m(\tilde{s}_{L,R}) = m(\tilde{c}_{L,R}) \equiv m_{\tilde{q}}, \quad (5.4.13)$$

that we then vary between 800 GeV and 4 TeV. For illustrative purposes, we focus on the charged-current process

$$pp \rightarrow \tilde{\chi}_2^0 \tilde{\chi}_1^+, \quad (5.4.14)$$

that gives rise to the largest wino production cross sections for a specific mass spectrum. The discussion and the results below are however applicable to other wino production modes as well. The latter indeed includes a complete set of numerical predictions for all wino pair production processes in the presence of not too heavy squarks, once again together with separate information on the total rate values, and the associated scale and PDF uncertainties presented separately.

In Fig. 5.12 we present aNNLO+NNLO total cross sections for the process of

Eq. (5.4.14) as a function of the wino and squark masses $m_{\tilde{\chi}}$ and $m_{\tilde{q}}$ ³. Results are presented for collider energies of $\sqrt{S} = 13$ TeV and 13.6 TeV in the top and bottom row of the figure respectively. In the left subfigures, the rates are represented through a logarithmic colour code, which shows that they exhibit a non-trivial dependence on the squark mass. Due to the destructive interference of s -channel gauge boson exchange diagrams with t/u -channel squark exchange diagrams, the cross section starts by decreasing when the SUSY spectrum is varied from a configuration in which $m_{\tilde{\chi}} = m_{\tilde{q}}$ to one with a larger squark mass value still in the vicinity of the same wino mass $m_{\tilde{\chi}}$. The rate then gets larger and larger with increasing squark masses (the wino mass being constant), and it finally saturates when squarks decouple.

This feature is further illustrated in the two upper insets of the right subfigures, that display aNNLO+NNLL production cross sections for $\tilde{\chi}_2^0 \tilde{\chi}_1^+$ production at the LHC as a function of the squark mass for several choices of wino masses. For a given wino mass $m_{\tilde{\chi}}$, we observe that the cross section always begins by decreasing before quickly reaching a minimum, and then increases for larger and larger squark masses. In the limit of very heavy squarks, the latter decouple and the rates become independent of the squark properties. They hence solely depend on the wino mass.

In the lower inset of these two right subfigures, we present K -factors defined as the ratio of the most precise aNNLO+NNLL rates to the LO ones for a given mass configuration,

$$K = \frac{\sigma_{\text{aNNLO+NNLL}}}{\sigma_{\text{LO}}}. \quad (5.4.15)$$

This further illustrates the squark decoupling at large $m_{\tilde{q}}$ values, the K -factor becoming constant. Moreover, the dependence of the K -factors on the squark mass additionally shows how the minimum of the cross section, for a given wino mass, is shifted by tens of GeV by virtue of the higher-order corrections.

In all the insets included in the right subfigures, we additionally include combined theory uncertainties. In general, those uncertainties are under good control, except in the heaviest scenarios in which the PDF errors get very large, as already above-mentioned. On the contrary, scale uncertainties always lie in the percent or permille level for all scenarios considered, the error bars being in fact drastically impacted (and reduced) by QCD resummation.

5.5 LHC SUSY search

To further profit from the already collected LHC data and from all searches for multiple jets and missing energy, it is necessary to also add pure weak production channels in which a pair of electroweakinos is produced. Such weak processes could indeed be relevant in specific regions of the SUSY parameter space. The mutual impact of squark pair and associated squark-neutralino production on SUSY exclusions computed from the signal region (SR) of a specific LHC analysis providing the best expectation has been recently examined [476]. Furthermore, the new physics search programme at the LHC includes a variety of searches for jets and missing transverse energy, each leveraging slightly different handles on the signal. It is therefore crucial to combine SRs of a specific analysis as well as different analyses, although this must be achieved in a statistically

³Similarly to the non-fully-degenerate higgsino scenario, here the mass of the decoupled gluino is set between 5 TeV and 100 TeV.

sound approach without double counting any effect. Experimental collaborations have recently made efforts to provide information on the statistical models used for limit setting, including correlations between SRs, either exactly [477] or approximately [478]. However, comprehensive information is only available for a limited number of LHC analyses. On the other hand, the code TACO [479] tackles the problem of combining SRs from different channels by approximating the existing correlation between SRs of possibly different LHC analyses for a specific set of signal events. This information then provides a way to compute exclusion limits from the best possible and meaningful combination of a given set of SRs, that is in practice obtained by means of a graph-based algorithm. While this approach offers a first insight into the gain in sensitivity achieved by combining SRs from various analyses, it ignores correlated systematic uncertainties like those originating from parton densities, luminosity measurements or limitations arising from overlapping signal regions of a particular analysis and control regions from other analyses.

This section is based on our publication [4] with further details in Ref. [480]. We calculate the best estimation to date of limits on non-minimal SUSY models with squarks and electroweakinos, complementing earlier work assessing the gain in sensitivity obtained from the combination of various ATLAS and CMS searches for electroweakinos [481] and third-generation squarks [482]. These bounds are obtained not only from simulations of the full corresponding SUSY signal, but also from the combination of several searches for SUSY relying on jets and missing transverse energy. To this aim, we consider a simplified SUSY scenario in which the set of relevant superpartners is restricted to one neutralino and one squark, as described in Sec. 5.5.1. In this section, we also discuss the different processes contributing to the signal. Limits are determined from the toolchain setup introduced in Sec. 5.5.2, that allows for event generation, detector simulation, cross section calculation, LHC recasting and SR combination. The results displayed in Sec. 5.5.3 then showcase the resulting gain in exclusion power.

5.5.1 Theoretical setup and hard-scattering signal simulation

We consider a simplified model inspired by the MSSM, in which the SM is extended by one squark flavour $\tilde{q} \equiv \tilde{u}_R$ and one neutralino state $\tilde{\chi}_1^0$, all other superpartners having masses of 30 TeV and being thus decoupled. Furthermore, the neutralino mixing matrix is taken to be diagonal, so that the lightest $\tilde{\chi}_1^0$ state is effectively bino-like. In this new physics parametrisation, the mass of the squark $m_{\tilde{q}}$ and that of the neutralino $m_{\tilde{\chi}_1^0}$ are free parameters, and their values are imposed to satisfy the condition $m_{\tilde{q}} > m_{\tilde{\chi}_1^0}$. This ensures that the $\tilde{\chi}_1^0$ state is the LSP, and therefore a good candidate for dark matter (thanks to R -parity conservation). The associated collider signal therefore includes three processes: the strong production of a pair of squarks ($pp \rightarrow \tilde{q}\tilde{q}^*$), the associated production of a neutralino and a squark ($pp \rightarrow \tilde{q}\tilde{\chi}_1^0 + \text{H.c.}$), and the weak production of a pair of neutralinos ($pp \rightarrow \tilde{\chi}_1^0\tilde{\chi}_1^0$). All superpartners different from the \tilde{q} and $\tilde{\chi}_1^0$ states being decoupled, the squark \tilde{q} is unstable and always decays promptly via the process $\tilde{q} \rightarrow \tilde{\chi}_1^0 q$. The global signature of the signal, once squark decays are accounted for, is therefore made of multiple jets and missing transverse energy carried away by the stable neutralino states.

In this way, signal simulation is achieved by means of `MadGraph5_aMC@NLO 3.5.1`. Making use of the `UFO` [483] implementation of the MSSM [484] obtained with `FeynRules` [485, 486], we independently generate hard-scattering events for the three

considered sub-processes. To this aim, we convolute LO matrix elements featuring up to two additional jets (from either initial-state or final-state radiation) with the MSHT201o_as130 LO set of PDF provided by LHAPDF 6.5.4, *i.e.* we compute the following processes

$$pp \rightarrow \tilde{q}\tilde{q}^* + \tilde{q}\tilde{q}^*j + \tilde{q}\tilde{q}^*jj, \quad (5.5.1)$$

$$pp \rightarrow \tilde{q}\tilde{\chi}_1^0 + \tilde{q}\tilde{\chi}_1^0j + \tilde{q}\tilde{\chi}_1^0jj + \text{H.c.}, \quad (5.5.2)$$

$$pp \rightarrow \tilde{\chi}_1^0\tilde{\chi}_1^0 + \tilde{\chi}_1^0\tilde{\chi}_1^0j + \tilde{\chi}_1^0\tilde{\chi}_1^0jj. \quad (5.5.3)$$

To maintain consistency in the analysis, it is imperative to avoid double counting any contribution across the three production modes. Thus, we manually prohibit intermediate squarks from being on-shell in any $2 \rightarrow 3$ or $2 \rightarrow 4$ diagram (*i.e.* with one or two QCD emissions). The produced events are next re-weighted according to K -factors defined by the ratio of total rates including state-of-the-art higher-order corrections obtained with **Resummino** 3.1.2 and **NNLL-fast** 2.0 [487] to LO predictions computed with these two codes.

Neutralino pair production cross sections are calculated with **Resummino** through the **Python** interface **HEPi** [6]. The code combines, following the standard threshold resummation formalism [388, 389, 393], matrix elements including aNNLO corrections in QCD [396, 401] with the resummation of soft-gluon radiation at the NNLL accuracy [398–401]. We additionally use **Resummino** to compute associated neutralino-squark production rates by matching NLO matrix elements [387] with threshold resummation at the NLL accuracy [1]. Finally, total cross sections for squark pair production are calculated with **NNLL-fast**. The latter combines aNNLO matrix elements [488, 489], soft-gluon resummation at NNLL in the absolute threshold limit, and the resummation of Coulomb gluons with an NLO Coulomb potential and bound-state contributions [436, 437, 490–493].⁴

As an illustration of the impact of the K -factors for the three processes considered, we focus on a scenario in which the mass of the lightest neutralino is fixed to $m_{\tilde{\chi}_1^0} = 400$ GeV, and we then show in Fig. 5.13 the dependence of the three production cross sections on the squark mass $m_{\tilde{q}}$. We present, in the upper panel of the figure, predictions at LO (dashed lines) and after including state-of-the-art higher-order corrections in QCD (solid lines). As expected, the relative uncertainties stemming from scale variation, that are also shown on the figure, decrease significantly when adding resummation contributions to the LO cross sections. We remind that a thorough error handling including PDF uncertainties for resummed cross sections can be found in Refs. [1, 2] for the weak and associated production channels. In the following analysis, the experimental errors nevertheless dominate such that the theoretical uncertainties are only shown to present an overview. In the lower inset of the figure, we additionally display the ratio between the two. For light squarks, the cross section corresponding to strong squark pair production ($\sigma \propto \alpha_S^2$) is the highest, while the semi-weak/semi-strong associated neutralino-squark production cross section ($\sigma \propto \alpha_S\alpha$) and the weak neutralino pair production cross section ($\sigma \propto \alpha^2$) are suppressed by about one and three orders of magnitude, respectively. As the squark gets heavier, the strong cross section

⁴While **NNLL-fast** assumes a tenfold-degenerate squark spectrum, the dependence of the cross section on the nature of the squarks factorizes when the gluino is decoupled. Moreover, **NNLL-fast** is unable to calculate rates at precision below NLO. We therefore utilize its predecessor **NLL-fast** [494] and its predictions at NLO and LO to calculate a global K factor defined by $K = (\sigma_{\text{NLO}}/\sigma_{\text{LO}})_{\text{NLL-fast}} \times (\sigma_{\text{aNNLO+NNLL}}/\sigma_{\text{NLO}})_{\text{NNLL-fast}}$.

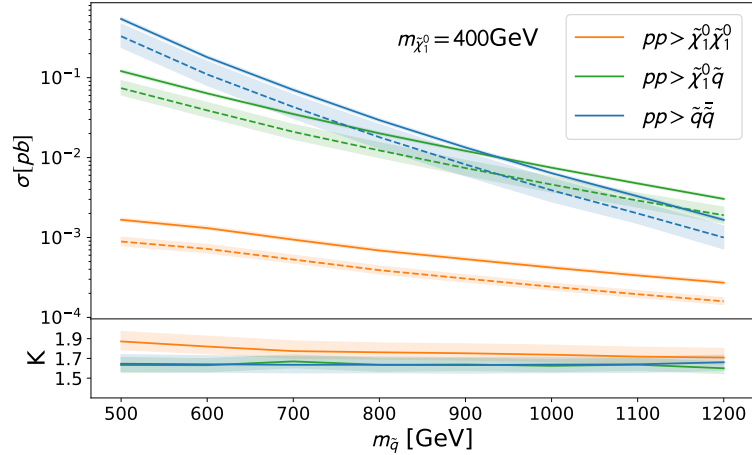


Figure 5.13: LO (dashed) and higher-order resummed (solid) cross section predictions in pp collisions at the LHC with a centre-of-mass energy of 13 TeV for the three considered processes (upper panel) and associated K -factors (lower panel) including scale uncertainties, for a scenario featuring a fixed neutralino mass of $m_{\tilde{\chi}_1^0} = 400$ GeV and a varying squark mass $m_{\tilde{q}}$.

decreases quickly due to phase space suppression, and is eventually overcome by the semi-weak process rates. The turnover occurs, in our example with $m_{\tilde{\chi}_1^0} = 400$ GeV, at around $m_{\tilde{q}} \approx 920$ GeV. By virtue of the same effect, at even higher squark masses the purely weak process become increasingly relevant. K -factors are generally large and exhibit little dependence on the squark mass. Such large K -factors (especially for small squark masses in the weak $pp \rightarrow \tilde{\chi}_1^0 \tilde{\chi}_1^0$ channel) have been cross-checked with Prospino [495], and are also outlined in [496].

Taking into account current exclusions that slowly reach the TeV regime, all three processes could have comparable cross sections in any given realistic scenario. Their contribution in the modelling of the SUSY signal should therefore be correctly incorporated, which further motivates the necessity of their unified analysis as demonstrated in the following sections.

5.5.2 Analysis setup

The computation of the exclusion associated with each point in the model parameter space carried out according to the toolchain outlined in Fig. 5.14. For each combination of squark and neutralino masses, we generate 150k events with MadGraph5_aMC@NLO 3.5.1 which is then interfaced with PYTHIA 8.306 for parton showering and hadronisation. Additionally, we employ PYTHIA to merge event samples featuring a different final-state partonic multiplicity following the CKKW-L algorithm as outlined in Sec. 3.3.2.1. The merging scale is set to one quarter of the SUSY hard scale defined by the average mass of the produced heavy particles. For the three

considered sub-processes, this scale is thus equal to

$$Q_{\text{MS}} = \begin{cases} \frac{1}{4}m_{\tilde{\chi}_1^0} & \text{for } pp \rightarrow \tilde{\chi}_1^0\tilde{\chi}_1^0 \\ \frac{1}{8}(m_{\tilde{q}} + m_{\tilde{\chi}_1^0}) & \text{for } pp \rightarrow \tilde{\chi}_1^0\tilde{q} + \tilde{\chi}_1^0\tilde{q}^* \\ \frac{1}{4}m_{\tilde{q}} & \text{for } pp \rightarrow \tilde{q}\tilde{q} \end{cases} . \quad (5.5.4)$$

The merging procedure is validated using DJR distributions as already outlined in Sec. 3.3.2.2. A smooth transition between the different jet multiplicities is desired, as this indicates that the merging scale Q_{MS} has been appropriately chosen. However, default settings in `MadGraph5` often result in bumps indicative of resonances for the considered signal. These bumps stem from certain diagrams exhibiting the exchange of intermediate s -channel off-shell squarks that see their off-shell nature modified by QCD radiation. To address this issue, the `bwcutoff` parameter introduced in Sec. 3.1.5.2 was increased from the default 15 to 35. This adjustment broadens the region around the squark pole mass where they are treated as on-shell, which also affects the exclusion of their contributions in processes with neutralinos in the final-state (see Sec. 5.5.1). We validated the merging prescription for a variety of different mass combinations, that we illustrate for the case $m_{\tilde{\chi}_1^0} = 200$ GeV and $m_{\tilde{q}} = 600$ GeV in Fig. 5.15. We present, for neutralino-pair (top row), squark-neutralino (middle row) and squark-pair (bottom row) production, total DJR spectra (green), together with the individual contributions emerging from matrix elements featuring no extra jet (blue), one extra jet (orange) and two extra jets (purple).

After the merging, the event weights are then re-scaled so that total rates encompass higher-order resummed corrections, as outlined in the previous sections of this chapter. All generated events, along with their associated resummed cross sections, are processed using `MadAnalysis` [497–499] to reinterpret the results of four Run 2 ATLAS and CMS analyses at a centre-of-mass energy of $\sqrt{s} = 13$ TeV. These analyses account for integrated luminosities of 139 fb^{-1} and 137 fb^{-1} of data, respectively.

We simulate the response of the LHC detectors using `MadAnalysis5` 1.10.2, which relies either on `Delphes3` [500, 501] or its built-in `SFS` [502] simulator. Specifically, we investigate four searches that target jets and missing transverse momentum and that include SRs focusing not only on a monojet signature but also on a topology allowing for multiple hard jets. These searches are identified as ATLAS-EXOT-2018-06 [503], ATLAS-CONF-2019-040 [447], CMS-SUS-19-006 [445], and CMS-EXO-20-004 [504], and they have demonstrated the highest sensitivity to the considered simplified scenario. For each LHC analysis considered, we employ a tuned detector parametrization and the validated analysis implementation within `MadAnalysis`. Details regarding their integration into `MadAnalysis`, along with corresponding validation notes, can be found on the `MadAnalysis` dataverse [505–508], on the `MadAnalysis` PAD [509], as well as in the works [504, 510–513].

This allows us to assess the selection efficiency for our signal across all SRs of all analyses examined, and to construct an acceptance matrix where each event corresponds to a row and each SR to a column. We next utilize the software `TACO` to convert the acceptance matrix into a correlation matrix. This conversion enables the determination of which combination of uncorrelated SRs yields the highest exclusion power. To achieve this, we employ a generalized version of the `PathFinder` software, initially implemented within `TACO`.⁵ The gathered information is next passed to the statistical tool `SPEY` [514],

⁵This generalized version of the `PathFinder` software can be found at <https://github.com/J-Yellen/>

which applies a variety of likelihood-based methods for hypothesis testing and calculating the confidence level of exclusion (CL) of a single SR, or of a combination of multiple SRs. Since the number of events surviving the cuts varies from SR to SR, if the number of events populating the SR with the highest exclusion power is too low, we regenerate events with increased statistics.

By iterating this procedure across the relevant mass points in the model parameter space, we derive the 95% CL exclusion contour for each individual process as well as for their combined analysis. The exclusion limits are first calculated for the individual processes within each analysis, where the most sensitive SR is identified as the one yielding the highest exclusion value. This approach is then extended to determine the combined exclusion limits for all three sub-processes together.

PathFinder. A performance improved version <https://github.com/APN-Pucky/PathFinder> even allows to check all combinations within reasonable compute times.

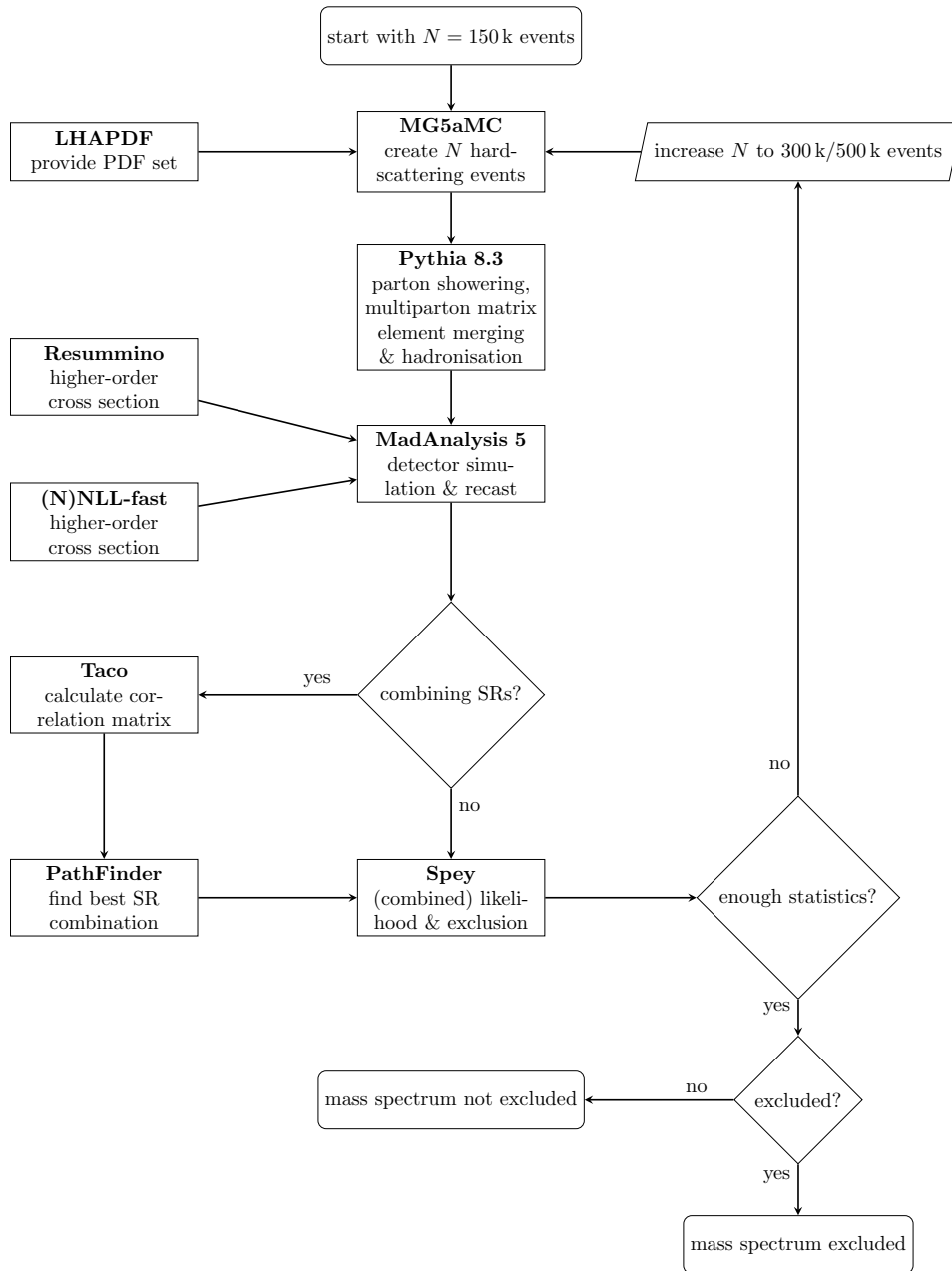


Figure 5.14: Flowchart diagram of the used toolchain.

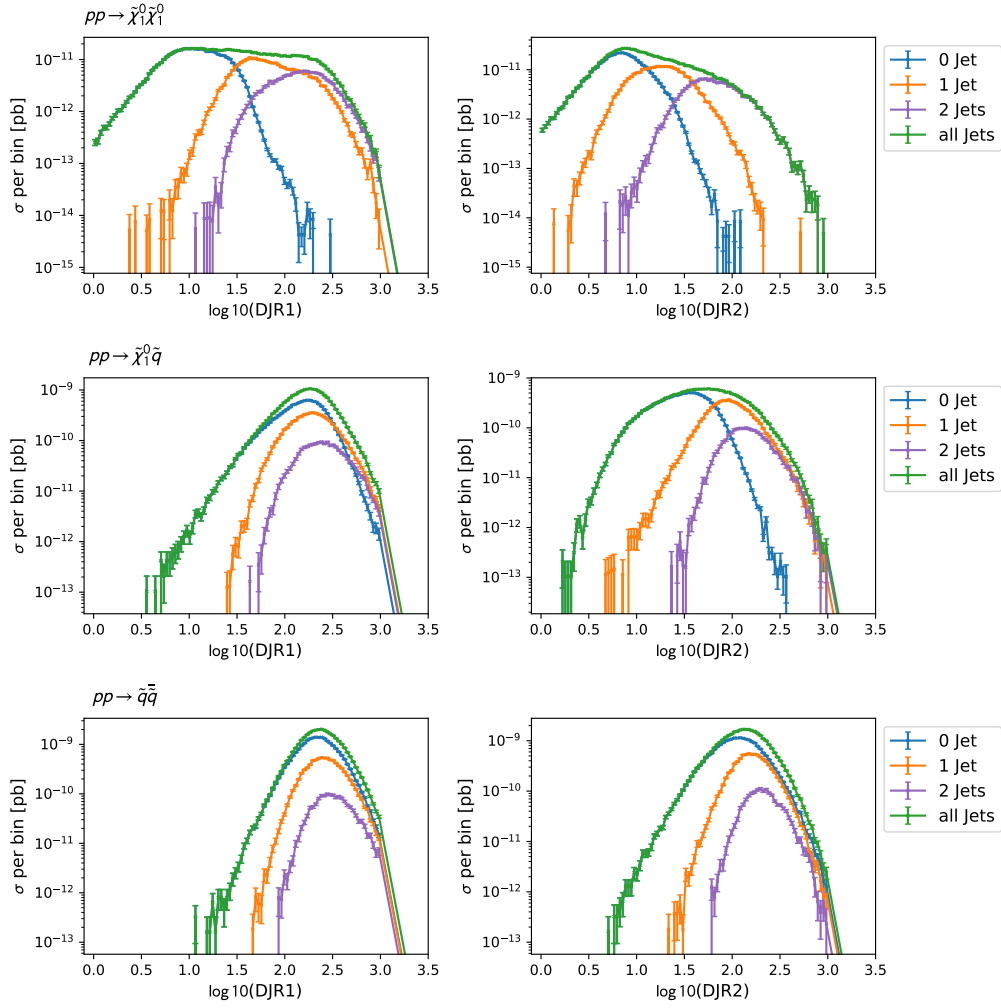


Figure 5.15: DJR distributions for the three different processes considered, and a scenario defined by $m_{\tilde{\chi}_1^0} = 200$ GeV and $m_{\tilde{q}} = 600$ GeV. DJR1(2) describes the transition between 0(1) and 1(2) jets.

5.5.3 Results

In Fig. 5.16, we focus on the bounds obtained from each of the four considered analyses individually. Expected (solid lines) and observed (dashed lines) 95% CL exclusion limits are presented in the $(m_{\bar{q}}, m_{\tilde{\chi}_1^0})$ mass plane, and we compute them based on signal predictions determined as outlined in Sec. 5.5.2. The exclusion contours are computed by interpolating between the considered mass points. Their smoothness and regularity is therefore a result of both the parameter space coverage regarding our simplified model of the considered analysis and the quality of the interpolation. Each figure showcases sensitivity contours distinguished by their colour coding. We compare bounds that are determined from a signal involving only strong production of a pair of squarks, each decaying into a neutralino and jets (blue). Such a signal definition matches how SUSY signals are simulated in experimental analyses up to now. Next, we examine the variation of the bounds when contributions from associated neutralino-squark production (orange) and neutralino-pair production (red) are included. We recall that these limits are derived by considering solely the most sensitive among all SRs within each analysis.

The ‘full’ bounds, incorporating all three sub-processes (red contours), largely coincide with the bounds derived from the combination of squark-pair and associated neutralino-squark production only (orange contours). This suggests that neutralino pair production has a marginal impact on the exclusions computed for a given mass spectrum. While the strong channel contributes dominantly, associated production has a non-negligible impact and therefore allows for a strengthening of the limits. This is particularly evident in the parameter space regions where the squark mass is large, and where, as already discussed in Sec. 5.5.1 regarding cross sections, squark-pair production begins to be phase space suppressed. For example, at $m_{\tilde{\chi}_1^0} = 250$ GeV, both observed and expected exclusion limits exhibit gains in squark mass of approximately 10 GeV for the CMS-EXO-20-004 analysis, and up to about 100 GeV for the other three analyses. These results reinforce the need for better and more accurate signal modelling in all existing LHC searches for SUSY, whenever it is computationally achievable.

Moreover, the four analyses demonstrate sensitivity to different regions in the parameter space, hinting at the potential to enhance overall sensitivity through their combination. Notably, the ATLAS-EXOT-2018-06 and CMS-SUS-19-006 analyses show increased sensitivity in the vicinity of the diagonal of the mass plane, where the squark-neutralino spectrum is compressed. In such scenarios, neutralinos emerging from squark decays carry almost all the squark energy so that the associated jets have low energy. Consequently, the overall jet multiplicity in the signal events is lower than in split mass configurations where highly-energetic jets could originate from squark decays. Furthermore, the CMS-SUS-19-006 analysis yields the strongest exclusion limits among all four analyses considered. Unlike the others, there is no requirement on the presence of a specific very highly energetic jet. Instead, it imposes constraints on global hadronic activity that has to surpass a certain threshold. Consequently, this analysis allows for several jets with smaller transverse momentum to collectively fulfil the hadronic activity requirements, rather than relying on a single jet embedding the bulk of it. Thus, at this point, we conclude that analyses that are more inclusive in terms of jet energy and multiplicity are preferable to probe the considered MSSM-inspired simplified model.

The exclusion limits obtained by combining uncorrelated SRs from the four different analyses are depicted in Fig. 5.17. Bounds are computed from the most sensitive combination of SRs determined by the `PathFinder` package. We analyse signal scenarios involving squark-pair production only (blue), and assess the impact of adding

contributions from associated neutralino-squark production (orange) and neutralino-pair production (red). As above, neutralino-pair production has no discernible effect, as evidenced by the superposition of the red and orange contours. The comparison of the bounds computed from a signal comprising only squark-pair production, as currently modelled in experimental LHC analyses, to those derived from the full squark and neutralino signal, underscores once again the significant potential improvement achievable through better signal modelling including all contributing sub-processes, especially when the spectrum is not too compressed.

We compare these findings with limits derived from a signal including all three sub-processes, and utilizing the most sensitive SR of the CMS-SUS-19-006 analysis (dashed contour). This comparison is motivated by the fact that the CMS-SUS-19-006 analysis has consistently emerged as the most constraining analysis (see Fig. 5.16). Combining multiple uncorrelated SRs of different analyses results in an additional gain in sensitivity compared to using the best SR from individual analyses to derive bounds, the gain being more pronounced when the spectrum is more split. Bounds on squark masses typically increase by approximately 100 GeV for both expected and observed limits, reaching up to 200 GeV in certain regions of the parameter space. Notably, employing a conservative modelling of the SUSY signal including only squark-pair production together with the best combination of uncorrelated regions (blue contours) yields increased sensitivity compared to relying on the best signal modelling possible but without combining any SR. Thus, while improving signal modelling is important, correlating findings from different analyses or sub-analyses is equally, and possibly more, essential.

While other analyses are generally less constraining than the CMS-SUS-19-006 analysis, they still make substantially contributions to the combined results. This is especially true for the ATLAS-EXOT-2018-06 and ATLAS-CONF-2019-040 analyses, as ATLAS and CMS searches are naturally considered uncorrelated. Additionally, despite the expected lower impact of the monojet CMS-EXO-20-004 analysis, due to its smaller relevance (as displayed in Fig. 5.16) and a potential stronger correlation with the CMS-SUS-19-006 analysis, its effects cannot be neglected. Therefore, we advocate for combining analyses whenever possible to ensure the best possible coverage of the parameter space with available data.

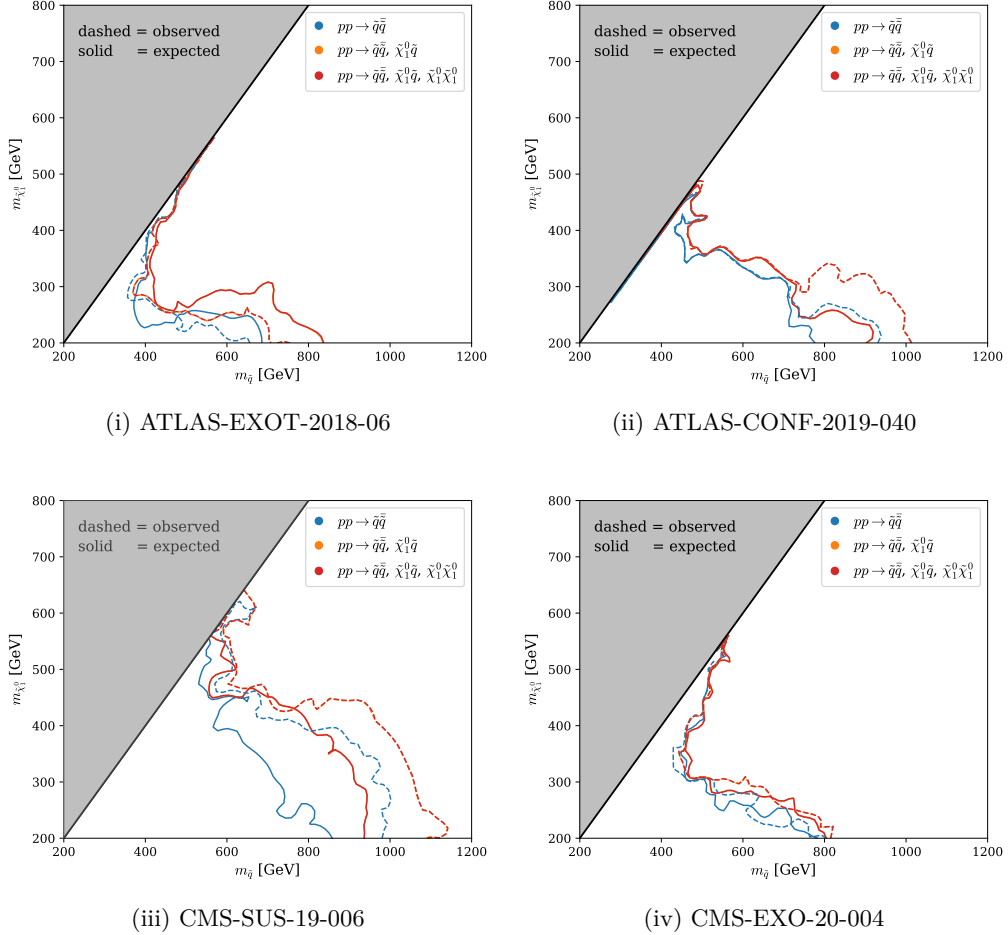


Figure 5.16: Exclusion contours at 95 % CL on the considered simplified model, presented in the squark and neutralino mass plane. Bounds have been obtained by the reinterpretation of the results of the ATLAS-EXOT-2018-06 (top left), ATLAS-CONF-2019-040 (top right), CMS-SUS-19-006 (bottom left) and CMS-EXO-20-004 (bottom right) analyses. We consider three scenarios for signal modelling: a signal involving only squark-pair production (blue), both squark-pair and associated neutralino-squark production (orange), and all three production sub-processes (red). Expected (solid) and observed (dashed) bounds are derived from the most constraining SR in each specific analysis.

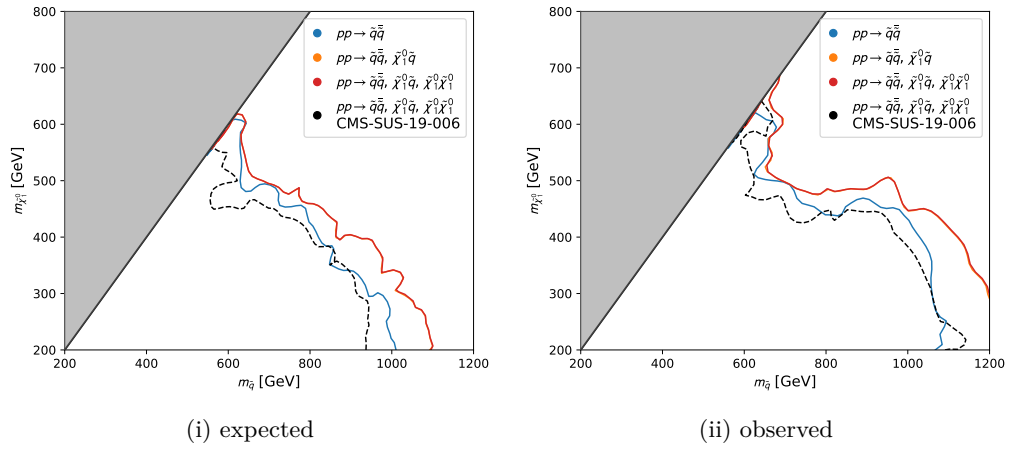


Figure 5.17: Expected (left) and observed (right) exclusion contours at 95% CL on the considered simplified model, presented in the squark and neutralino mass plane. Bounds have been derived from the most sensitive combination of uncorrelated SRs of the ATLAS-EXOT-2018-06, ATLAS-CONF-2019-040, CMS-SUS-19-006 and CMS-EXO-20-004 analyses. We consider three scenarios for signal modelling: a signal involving only squark-pair production (blue), both squark-pair and associated neutralino-squark production (orange), and all three production sub-processes (red). For comparison, the exclusion contour determined from the most sensitive SR of the CMS-SUS-19-006 analysis is also shown (dashed, black).

Chapter 6

Conclusion and outlook

6.1 Conclusion

In conclusion, this thesis explored several interconnected aspects of collider physics, particularly focusing on resummation methods, parton showers, and MC event simulations, which play an important role in modern particle physics research.

First we presented a calculation of virtual photon production in pp and pPb collisions, compared to ALICE measurements. We used the POWHEG BOX V2 framework for calculating the DY-process in association with at least one jet, matched to PYTHIA 8, and recalculated predictions for dileptons coming from semileptonic decays of heavy quarks. By fitting their predictions to experimental data, effectively normalizing the scale uncertainty to a shape uncertainty, the large uncertainties of open charm production were reduced, but large uncertainties remain in the heavy quark contributions. Including the virtual photon contribution resulted in a reduction of the normalizations of other contributions, but did not have a significant impact.

Next, we presented a new NLO QCD calculation for prompt photon production including up to three jets using the POWHEG method for parton shower matching. By comparing direct photon production with two jets to ATLAS data and NNLO calculations, we showed that adding parton showers (POWHEG BOX+PYTHIA, POWHEG BOX+HERWIG) improves prediction accuracy. Our results align well with experimental data and support the use of parton showers instead of fragmentation functions.

Switching to supersymmetry and resummation, we present a threshold resummation calculation at NLO+NLL accuracy for squark and electroweakino production at the LHC in the MSSM. This process, alongside gluino and electroweakino production, is gaining more importance as new experimental limits increase the expected masses of squarks and gluinos. The NLL contributions increase the total NLO cross section by 2% to 6%, for squark masses of 1 TeV to 3 TeV, and significantly reduce the dependence on renormalization and factorization scales from $\pm 10\%$ to below $\pm 5\%$.

Then, we explored several simplified MSSM-inspired models where most superpartners are decoupled, except for a few states whose production at the LHC has been studied. We provided predictions combining fixed-order aNNLO QCD calculations with soft gluon resummation at NNLL. We highlighted the impact of increasing the centre-of-mass energy from 13 TeV to 13.6 TeV, resulting in a 20% to 40% rate increase for

SUSY processes depending on the mass spectrum. Additionally, we examined the effects of non-degenerate compressed higgsino pair production and squark decoupling on wino pair production, both of which showed significant impacts on future search interpretations.

In the final topic we combined MCEGs with resummed calculations. We analysed four LHC searches targeting jets and missing transverse energy, considering squark pair, squark-neutralino, and neutralino pair production, each merged with up to two hard jet at LO. Our results showed that adding squark-neutralino production significantly boosts exclusion power, especially for split SUSY spectra and neutralino masses below 400 GeV. While neutralino pair production has minimal impact with current data, its role may grow with future constraints. Combining uncorrelated SRs extends search reach, increasing mass bounds by 100 GeV to 200 GeV, highlighting the value of combining results from different analyses, as done using the TACO method in this thesis.

6.2 Outlook

Towards the end of my PhD, I am still part of two small projects that I plan to continue developing in the future. The first project involves sneutralino production and `MadAnalysis` recasting utilizing TACO. This project extends the combination of analysis to sneutralino production, utilizing `MadAnalysis` for recasting to refine our understanding and predictions related to sneutralino events in high-energy physics experiments. The second project focuses on improving `POWHEG BOX`'s performance and efficiency through the application of machine learning, particularly in challenging processes and regimes.

A possible approach for future work involves MiNLO prompt photon production in `POWHEG BOX`. Since NLO $\gamma + j$ and $\gamma + j + j$ production are now available in `POWHEG BOX`, the next step is to combine them with MiNLO to better handle scale uncertainties and extend the predictions. This extension is challenging due to the complex Born contributions of pure QCD and mixed QED to both processes. However, successfully combining these elements will provide more accurate and reliable predictions.

In our virtual photon study, we were unable to explore invariant dilepton masses below 1 GeV. Revisiting the Kroll-Wada approximation and adding a dilepton production mode to `POWHEG BOX`'s `directphoton` production would be interesting. This new mode can then be compared to `PYTHIA`'s method of splitting the on-shell photon into a dilepton pair, as well as similar analytic calculations. This comparison would refine our understanding of low-mass dilepton production and improve the accuracy of theoretical predictions.

Further, the purely electroweak processes in `Resummino` are currently available at aNNLO+NNLL and NLO+NLL. However, the associated productions of $\tilde{g} + \tilde{\chi}$ and $\tilde{q} + \tilde{\chi}$ have only been computed at NLO+NLL thus far. The natural next step would be to extend the resummation to aNNLO+NNLL for these associated processes, which comes with an increased difficulty due to the no longer trivial colour structure. Before making further improvements in prediction accuracy, it would be motivating if the LHC collaborations investigate these associated processes in simplified models more.

These projects and ideas represent a continuation of my PhD work, aimed at enhancing theoretical predictions and optimizing computational efficiency in high-energy physics. I look forward to starting my Postdoc position at the University of Milano-Bicocca with Simone Alioli and continuing my research in the area of MCEGs.

Chapter A

Appendix

A.1 Notations

In this section we summarize the notations used in this thesis.

A.1.1 Natural units

We use the common high-energy physics (HEP) units with $c = \hbar = 1$, since it simplifies the notation and the calculations.

A.1.2 Einstein summation convention

The Einstein summation convention is a notation used to simplify mathematical expressions that involve sums over indices, commonly seen in tensor calculus. In this convention, whenever an index appears more than once in a single term it is assumed that you sum over all possible values of that index. For example, without the Einstein summation convention, you might write:

$$C_i = \sum_{j=1}^n A_{ij} B_j = A_{ij} B_j \quad (\text{A.1.1})$$

We will however sometimes explicitly write out the summation symbol to make it clear that we are summing over an index.

A.1.3 Lorentz indices

We do not separate covariant vectors with lower indices from contravariant vectors with upper indices, since we are working in a flat space-time. Instead, we implicitly assume contraction with the right Minkowski metric $g_{\mu\nu} = \eta_{\mu\nu}$

$$A^\mu B_\mu = A_\mu B^\mu = A^\mu B^\mu = A_\mu B_\mu. \quad (\text{A.1.2})$$

A.1.4 Subtraction methods

The following notations define a very convenient way to express the unintegrated and integrated dipoles. Using them we write the colour-correlated squared amplitude as

$${}_2\langle \dots, j; k, \dots | \mathbf{T}_j \mathbf{T}_k | \dots, j; k, \dots \rangle_2 = \mathcal{M}_{\text{LO}}^{\dots, b_j, b_k, \dots *} \mathcal{T}_{b_j a_j}^n \mathcal{T}_{b_k a_k}^n \mathcal{M}_{\text{LO}}^{\dots, a_j, a_k, \dots}. \quad (\text{A.1.3})$$

A.1.4.1 Matrix elements

A basis for colour c and helicity s space is introduced such that an amplitude of m particles is written as

$$\mathcal{M}_m^{c_1, \dots, c_m; s_1, \dots, s_m}(p_1, \dots, p_m) := (\langle c_1, \dots, c_m | \otimes \langle s_1, \dots, s_m | | 1, \dots, m \rangle_m \quad (\text{A.1.4})$$

and the squared matrix element is

$$|\mathcal{M}_m|^2 = {}_m\langle 1, \dots, m | 1, \dots, m \rangle_m. \quad (\text{A.1.5})$$

A.1.4.2 Colour structure

We use \mathbf{T}_i to represent the emission of a gluon from parton i

$$\langle c_1, \dots, c_m | \mathbf{T}_i | c'_1, \dots, c'_m \rangle_m = \delta_{c_1 c'_1} \dots \mathcal{T}_{c_i c'_i} \dots \delta_{c_m c'_m}, \quad (\text{A.1.6})$$

where

$$\mathcal{T}_{cb}^a := \begin{cases} if_{cab} & \text{adjoint representation (} i \text{ gluon or gluino),} \\ \pm T_{cb}^a & \text{fundamental representation (} i \text{ quark or squark).} \end{cases} \quad (\text{A.1.7})$$

The $(-)$ case is for antiparticles. Since $|1, \dots, m\rangle_m$ is a colour-singlet state, colour conservation can be written as

$$\sum_i^m \mathbf{T}_i |1, \dots, m\rangle_m = 0. \quad (\text{A.1.8})$$

Lastly, the colour charge algebra commutes unless it is a quadratic Casimir operator

$$[\mathbf{T}_i, \mathbf{T}_j] = 0 \quad \mathbf{T}_i^2 = C_i = \begin{cases} C_F = \frac{4}{3} & i \text{ fundamental,} \\ C_A = 3 & i \text{ adjoint.} \end{cases} \quad (\text{A.1.9})$$

A.1.5 Feynman Rules

We adopt the generalised couplings and conventions from [130]:

- First Greek letters (α, β, \dots) denote fundamental colour indices.
- Middle Greek letters ($\kappa, \lambda, \mu, \nu, \dots$) denote Lorentz indices.
- Lowercase beginning Latin letters (a, b, \dots) refer adjoint colour indices.
- Uppercase middle Latin letters (I, J, \dots) are generation indices.
- Lowercase middle Latin letters (i, j, \dots) label sfermions.
- Lowercase middle Latin letters (k, \dots) indicate different neutralinos or charginos.

A.2 Feynman rules

All momenta go into the vertex.

A.2.1 Standard model

We refer to [10, 39, 127] for a detailed introduction to the Feynman rules of the SM.

A.2.1.1 Propagators

Quark propagator:

$$q_{I,\beta} \longrightarrow \bar{q}_{J,\alpha} = \frac{i(\not{p} + m)}{p^2 - m^2} \delta_{\beta\alpha} \delta_{IJ} = \frac{i}{\not{p} - m} \delta_{\beta\alpha} \delta_{IJ} \quad (\text{A.2.1})$$

Gluon propagator:

$$g_\mu \text{-----} g_\nu = \begin{cases} \frac{-i}{p^2} \delta_{ab} g_{\mu\nu} & \text{Feynman gauge} \\ \frac{-i}{p^2} \delta_{ab} \left(g_{\mu\nu} - \frac{n^\mu p^\nu + n^\nu p^\mu}{p \cdot n} + \frac{n^\mu p^\nu p^\nu}{(p \cdot n)^2} \right) & \text{axial gauge, } n \cdot p \neq 0 \end{cases} \quad (\text{A.2.2})$$

Ghost propagator:

$$\bar{c}_a \text{.....} c_b = \frac{i}{p^2} \delta_{ba} \quad (\text{A.2.3})$$

A.2.1.2 Vertices

Quark-photon vertex:

$$q_{I,\beta} \begin{array}{c} \nearrow \gamma^\mu \\ \searrow \bar{q}_{J,\alpha} \end{array} = -i g_e e_q \gamma^\mu \delta_{\alpha\beta} \delta_{IJ} \quad (\text{A.2.4})$$

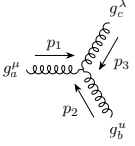
Quark-gluon vertex:

$$q_{I,\beta} \begin{array}{c} \nearrow g_a^\mu \\ \searrow \bar{q}_{J,\alpha} \end{array} = -i g_s \gamma^\mu T_{\alpha\beta}^a \delta_{IJ} \quad (\text{A.2.5})$$

Ghost-gluon vertex:

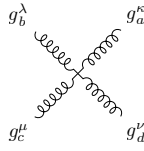
$$\bar{c}^c \begin{array}{c} \nearrow p \\ \searrow c^b \end{array} g_a^\mu = g_s p^\mu f^{abc} \quad (\text{A.2.6})$$

Three-gluon vertex:



$$= -g_s f_{abc} (g^{\mu\nu} (p_1 - p_2)^\lambda + g^{\nu\lambda} (p_2 - p_3)^\mu + g^{\mu\lambda} (p_3 - p_1)^\nu) \quad (\text{A.2.7})$$

Four-gluon vertex:



$$= -ig_s^2 (f^{abc} f^{cde} (g^{\kappa\mu} g^{\lambda\nu} - g^{\kappa\nu} g^{\lambda\mu})$$

$$+ f^{ade} f^{bce} (g^{\kappa\lambda} g^{\mu\nu} - g^{\kappa\mu} g^{\nu\lambda})$$

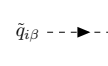
$$+ f^{ace} f^{bde} (g^{\kappa\lambda} g^{\nu\mu} - g^{\kappa\nu} g^{\mu\lambda})) \quad (\text{A.2.8})$$

A.2.2 Minimal Supersymmetric Standard Model

The displayed rules are a subset taken from the complete set [382].

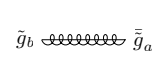
A.2.2.1 Propagators

Squark propagator:



$$= \frac{i}{p^2 - m^2} \delta_{\alpha\beta} \delta_{ij} \quad (\text{A.2.9})$$

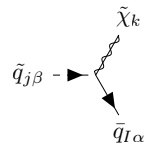
Glino propagator:



$$= \frac{i(\not{p} + m)}{p^2 - m^2} \delta_{ab} = \frac{i}{\not{p} - m} \delta_{ab} \quad (\text{A.2.10})$$

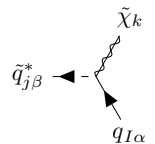
A.2.2.2 Vertices

Electroweakino-squark vertex:



$$= i(L_{Ijk} P_L + R_{Ijk} P_R) \delta_{\alpha\beta} \quad (\text{A.2.11})$$

Electroweakino-antisquark vertex:



$$= i(L'_{Ijk} P_L + R'_{Ijk} P_R) \delta_{\alpha\beta} \quad (\text{A.2.12})$$

Glino-gluon vertex:

$$\begin{array}{c}
 g_c^\mu \\
 \diagup \\
 \tilde{g}_b \text{---} \text{---} \text{---} \\
 \diagdown \\
 \tilde{g}_a
 \end{array}
 = -ig_s \gamma^\mu f_{abc}
 \quad (\text{A.2.13})$$

Three-squark-gluon vertex:

$$\begin{array}{c}
 g_a^\mu \\
 \diagup \\
 \tilde{q}_{i\beta} \text{---} \text{---} \text{---} p_1 \\
 \diagdown \\
 p_2 \text{---} \text{---} \text{---} \tilde{q}_{j\alpha}^*
 \end{array}
 = ig_s (p_2 - p_1)^\mu T_{\alpha\beta}^a \delta_{ij}
 \quad (\text{A.2.14})$$

Glino-(s)quark vertex:

$$\begin{array}{c}
 \tilde{g}_a \\
 \diagup \\
 \tilde{q}_{j\beta} \text{---} \text{---} \text{---} \\
 \diagdown \\
 \tilde{q}_{I\alpha}
 \end{array}
 = i(\mathcal{L}_{Ij} P_L + \mathcal{R}_{Ij} P_R) T_{\alpha\beta}^a
 \quad (\text{A.2.15})$$

Glino-anti(s)quark vertex:

$$\begin{array}{c}
 \tilde{g}_a \\
 \diagup \\
 \tilde{q}_{j\beta}^* \text{---} \text{---} \text{---} \\
 \diagdown \\
 q_{I\alpha}
 \end{array}
 = i(\mathcal{L}'_{Ij} P_L + \mathcal{R}'_{Ij} P_R) T_{\alpha\beta}^a
 \quad (\text{A.2.16})$$

Four-squark-gluon vertex:

$$\begin{array}{c}
 \tilde{q}_{i\alpha}^* \text{---} \text{---} \text{---} \tilde{q}_{j\beta} \\
 \diagdown \quad \diagup \\
 g_a^\mu \text{---} \text{---} \text{---} g_b^\nu
 \end{array}
 = ig_s^2 g^{\mu\nu} \delta_{ij} (T^a T^b + T^b T^a)_{\alpha\beta}
 \quad (\text{A.2.17})$$

Four-squark vertex:

$$\begin{array}{c}
 \tilde{q}_{j\beta}^* \text{---} \text{---} \text{---} \tilde{q}_{i\alpha} \\
 \diagdown \quad \diagup \\
 \tilde{q}_{k\gamma} \text{---} \text{---} \text{---} \tilde{q}_{l\delta}^*
 \end{array}
 = -i(X_{ijkl} \delta_{\alpha\beta} \delta_{\gamma\delta} + Y_{ijkl} \delta_{\alpha\delta} \delta_{\gamma\beta} + Z_{ijkl} \delta_{\alpha\gamma} \delta_{\beta\delta})
 \quad (\text{A.2.18})$$

A.3 Relations

A list of useful equations.

A.3.1 Colour

These relations are available in most standard text books on quantum field theory and the standard model (*e.g.* [10]).

A.3.1.1 Definitions

The colour constants are defined as

$$T_F = T_R = \frac{1}{2}, \quad (\text{A.3.1})$$

$$C_A = T_a = N_c = N = 3, \quad (\text{A.3.2})$$

$$C_F = \frac{N^2 - 1}{2N} = \frac{4}{3}. \quad (\text{A.3.3})$$

$$\text{Tr}[T^a T^b] = T_R \delta_{ab} \quad (\text{A.3.4})$$

A.3.1.2 Fierz identity

The Fierz identity is

$$T_{\alpha\beta}^a T_{\gamma\delta}^a = \frac{1}{2}(\delta_{\alpha\delta}\delta_{\gamma\beta} - \frac{1}{N}\delta_{\alpha\beta}\delta_{\gamma\delta}), \quad (\text{A.3.5})$$

and consequently

$$T_{\alpha\gamma}^a T_{\beta\delta}^a = C_F \delta_{\alpha\beta} \quad (\text{A.3.6})$$

follows. One can also solve

$$f^{abc} T_{\beta\alpha}^c T_{\gamma\beta}^b = i C_A T_R T_{\gamma\alpha}^a \quad (\text{A.3.7})$$

$$T_{\beta\delta}^b T_{\gamma\alpha}^b T_{\delta\gamma}^a = -\frac{T_R}{C_A} T_{\alpha\beta}^a. \quad (\text{A.3.8})$$

A.3.2 Gamma Matrix

Again, the relations are available in most standard text books on quantum field theory and the standard model (*e.g.* [10]).

A.3.2.1 Gamma trace relations

$$\text{Tr}[\gamma_\mu \gamma_\nu] = 4g_{\mu\nu} \quad (\text{A.3.9})$$

$$\text{Tr}[\gamma_\mu \gamma_\nu \gamma_\delta] = 0 \quad (\text{A.3.10})$$

$$\text{Tr}[\gamma_\mu \gamma_\nu \gamma_\delta \gamma_\rho] = 4(g_{\mu\nu}g_{\delta\rho} - g_{\mu\delta}g_{\nu\rho} + g_{\mu\rho}g_{\nu\delta}) \quad (\text{A.3.11})$$

A.3.2.2 D-dimensional Gamma Matrix

$$\gamma^\mu \gamma^\nu \gamma^\mu = (2 - D)\gamma^\nu \quad (\text{A.3.12})$$

$$\gamma^\mu \gamma^\nu \gamma^\sigma \gamma^\mu = (D - 4)\gamma^\nu \gamma^\sigma + 4g^{\nu\sigma} \quad (\text{A.3.13})$$

$$\gamma^\mu \gamma^\nu \gamma^\sigma \gamma^\rho \gamma^\mu = -2\gamma^\rho \gamma^\sigma \gamma^\nu - (D - 4)\gamma^\nu \gamma^\sigma \gamma^\rho \quad (\text{A.3.14})$$

A.3.3 P-operators

We repeat the splitting functions' complete form Eqs. (2.2.5) to (2.2.8)

$$P_{qq}(z) = C_F \left(\frac{1+z^2}{[1-z]_+} + \frac{3}{2} \delta(1-z) \right), \quad (\text{A.3.15})$$

$$P_{qg}(z) = C_F \frac{1+(1-z)^2}{z}, \quad (\text{A.3.16})$$

$$P_{gq}(z) = T_R (z^2 + (1-z)^2), \quad (\text{A.3.17})$$

$$P_{gg}(z) = 2C_A \left(\frac{z}{[1-z]_+} + \frac{1-z}{z} + z(1-z) \right) + \delta(1-z)\beta_0, \quad (\text{A.3.18})$$

give them next in their regularized version [191, Eq. (5.89)]

$$P_{\text{reg}}^{qq}(x) = -C_F(1+x), \quad (\text{A.3.19})$$

$$P_{\text{reg}}^{gq}(x) = T_R [x^2 + (1-x)^2], \quad (\text{A.3.20})$$

$$P_{\text{reg}}^{qg}(x) = C_F \frac{1+(1-x)^2}{x}, \quad (\text{A.3.21})$$

$$P_{\text{reg}}^{gg}(x) = 2C_A \left[\frac{1-x}{x} - 1 + x(1-x) \right], \quad (\text{A.3.22})$$

and residue form [191, Eq. (5.93)]

$$\hat{P}'^{qq}(x) = C_F(1-x), \quad (\text{A.3.23})$$

$$\hat{P}'^{gq}(x) = 2T_R x(1-x), \quad (\text{A.3.24})$$

$$\hat{P}'^{qg}(x) = C_F x, \quad (\text{A.3.25})$$

$$\hat{P}'^{gg}(x) = 0. \quad (\text{A.3.26})$$

The complete splitting functions can be reconstructed [191, Eq. (5.94)]

$$P^{ab}(x) = P_{\text{reg}}^{ab}(x) + \delta^{ab} \left[2\mathbf{T}_a^2 \left(\frac{1}{1-x} \right)_+ + \gamma_a \delta(1-x) \right]. \quad (\text{A.3.27})$$

A.3.4 K-operator

Using the following identities

$$\begin{aligned} x s_{ja} &= 2p_j \cdot p_a = m_j^2 - t, \\ x s_{jb} &= 2p_j \cdot p_b = m_j^2 - u, \\ x s_{ab} &= 2p_a \cdot p_b = s, \end{aligned} \quad (\text{A.3.28})$$

and constants

$$\begin{aligned}
\gamma_q &= \frac{3}{2}C_F & K_q &= \left(\frac{7}{2} - \frac{\pi^2}{6}\right)C_F \\
\gamma_g = \beta_0 &= \frac{11}{6}C_A - \frac{2}{3}T_R N_f & K_g &= \left(\frac{67}{18} - \frac{\pi^2}{6}\right)C_A - \frac{10}{9}T_R N_f \\
\gamma_{\bar{q}} &= 2C_F & K_{\bar{q}} &= \left(4 - \frac{\pi^2}{6}\right)C_F \\
\gamma_{\bar{g}} &= \frac{3}{2}C_A & K_{\bar{g}} &= \left(\frac{7}{2} - \frac{\pi^2}{6}\right)C_A
\end{aligned} \tag{A.3.29}$$

the K operators read:

$$\begin{aligned}
\bar{K}^{aa'}(x) &= P_{\text{reg}}^{aa'}(x) \log \frac{1-x}{x} + \hat{P}'^{aa'}(x) \\
&+ \delta^{aa'} \left[\mathbf{T}_a^2 \left(\frac{2}{1-x} \log \frac{1-x}{x} \right)_+ - \delta(1-x) \left(\gamma_a + K_a - \frac{5}{6}\pi^2 \mathbf{T}_a^2 \right) \right]
\end{aligned} \tag{A.3.30}$$

$$K_{\text{F.S.}}^{aa'}(x) = 0 \quad \text{in the } \overline{\text{MS}} \text{ scheme} \tag{A.3.31}$$

$$\begin{aligned}
\mathcal{K}_{\bar{g}}^{q,q}(x; s_{ja}, m_j) &= \mathcal{K}_{q \rightarrow \bar{g}}^{q,q}(x; s_{ja}, m_j) = 2 \left[\left(\frac{\log(1-x)}{1-x} \right)_+ - \frac{\log(2-x)}{1-x} \right] \\
&+ \left[J_{gQ}^a \left(x, \frac{m_j}{\sqrt{s_{ja}}} \right) \right]_+ + 2 \left(\frac{1}{1-x} \right)_+ \log \frac{(2-x)s_{ja}}{(2-x)s_{ja} + m_j^2} \\
&+ \delta(1-x) \left(\frac{m_j^2}{s_{ja}} \log \frac{m_j^2}{s_{ja} + m_j^2} + \frac{1}{2} \frac{m_j^2}{s_{ja} + m_j^2} - \frac{\gamma_{\bar{g}}}{C_A} \right)
\end{aligned} \tag{A.3.32}$$

$$\mathcal{K}_{\bar{g}}^{q,g}(x; s_{ja}, m_j) = \mathcal{K}_q^{q,g}(x; s_{ja}, m_j) = 2 \frac{C_F}{C_A} \frac{m_j^2}{x s_{ja}} \log \frac{m_j^2}{(1-x)s_{ja} + m_j^2} \tag{A.3.33}$$

$$\begin{aligned}
\mathcal{K}_{\bar{q}}^{q,q}(x; s_{ja}, m_j) &= \mathcal{K}_q^{q,q}(x; s_{ja}, m_j) - \left(\frac{(1-x)s_{ja}^2}{2[(1-x)s_{ja} + m_j^2]^2} \right)_+ \\
&+ \delta(1-x) \left(-\frac{m_j^2}{s_{ja}} \log \frac{m_j^2}{Q_{ja}^2} - \frac{1}{2} \frac{m_j^2}{Q_{ja}^2} + \frac{\gamma_q - \gamma_{\bar{q}}}{C_F} \right) \\
&= 2 \left[\left(\frac{\log(1-x)}{1-x} \right)_+ - \frac{\log(2-x)}{1-x} \right] + \left[J_{gQ}^a \left(x, \frac{m_j}{\sqrt{s_{ja}}} \right) \right]_+ \\
&+ 2 \left(\frac{1}{1-x} \right)_+ \log \frac{(2-x)s_{ja}}{(2-x)s_{ja} + m_j^2} - \left(\frac{(1-x)s_{ja}^2}{2[(1-x)s_{ja} + m_j^2]^2} \right)_+
\end{aligned} \tag{A.3.34}$$

$$-\delta(1-x)\frac{\gamma_{\bar{q}}}{C_F} \quad (\text{A.3.35})$$

$$\mathcal{K}_{\bar{q}}^{q,g}(x; s_{ja}, m_j) = \mathcal{K}_q^{q,g}(x; s_{ja}, m_j) = 2\frac{C_F}{C_A} \frac{m_j^2}{xs_{ja}} \log \frac{m_j^2}{(1-x)s_{ja} + m_j^2} \quad (\text{A.3.36})$$

$$\mathcal{K}_{\bar{q}}^{g,q}(x; s_{ja}, m_j) = \mathcal{K}_q^{g,q}(x; s_{ja}, m_j) = 0 \quad (\text{A.3.37})$$

$$\begin{aligned} \mathcal{K}_{\bar{q}}^{g,g}(x; s_{ja}, m_j) &= \mathcal{K}_q^{g,g}(x; s_{ja}, m_j) - \left(\frac{(1-x)s_{ja}^2}{2[(1-x)s_{ja} + m_j^2]^2} \right)_+ \\ &\quad + \delta(1-x) \left(-\frac{m_j^2}{s_{ja}} \log \frac{m_j^2}{Q_{ja}^2} - \frac{m_j^2}{2Q_{ja}^2} + \frac{\gamma_q - \gamma_{\bar{q}}}{C_F} \right) \\ &= \mathcal{K}_q^{g,q}(x; s_{ja}, m_j) + \frac{C_A}{C_F} \mathcal{K}_q^{q,g}(x; s_{ja}, m_j) \\ &\quad - \left(\frac{(1-x)s_{ja}^2}{2[(1-x)s_{ja} + m_j^2]^2} \right)_+ + \delta(1-x) \left(-\frac{m_j^2}{s_{ja}} \log \frac{m_j^2}{Q_{ja}^2} - \frac{m_j^2}{2Q_{ja}^2} + \frac{\gamma_q - \gamma_{\bar{q}}}{C_F} \right) \end{aligned} \quad (\text{A.3.38})$$

$$\begin{aligned} &= 2 \left[\left(\frac{\log(1-x)}{1-x} \right)_+ - \frac{\log(2-x)}{1-x} \right] + \left[J_{gQ}^a \left(x, \frac{m_j}{\sqrt{s_{ja}}} \right) \right]_+ \\ &\quad + 2 \left(\frac{1}{1-x} \right)_+ \log \frac{(2-x)s_{ja}}{(2-x)s_{ja} + m_j^2} - \left(\frac{(1-x)s_{ja}^2}{2[(1-x)s_{ja} + m_j^2]^2} \right)_+ \\ &\quad + 2 \frac{m_j^2}{xs_{ja}} \log \frac{m_j^2}{(1-x)s_{ja} + m_j^2} - \delta(1-x) \frac{\gamma_{\bar{q}}}{C_F} \end{aligned} \quad (\text{A.3.39})$$

where we have used that $Q_{ja}^2 = s_{ja} + m_j^2$, and

$$\begin{aligned} \left[J_{gQ}^a \left(x, \frac{m_j}{\sqrt{s_{ja}}} \right) \right]_+ &= \left(\frac{1-x}{2 \left(1-x + \frac{m_j^2}{s_{ja}} \right)^2} - \frac{2}{1-x} \left[1 + \log \left(1-x + \frac{m_j^2}{s_{ja}} \right) \right] \right)_+ \\ &\quad + \left(\frac{2}{1-x} \right)_+ \log \left(2-x + \frac{m_j^2}{s_{ja}} \right). \end{aligned}$$

A.4 Distributions

A distribution, also known as a generalized function, extends the concept of functions and instead of producing values directly, defines how to obtain a number by integrating against a test function.

A.4.1 Dirac delta distribution

The delta distribution, often denoted as $\delta(x)$, is a mathematical construct that is not a function in the traditional sense but rather a distribution or a generalized function. The delta distribution is defined by the integral for any sufficiently smooth function $f(x)$,

$$\int_{-\infty}^{\infty} f(x)\delta(x-a) dx = f(a). \quad (\text{A.4.1})$$

This property means that the delta distribution effectively “picks out” the value of $f(x)$ at $x = a$.

A.4.2 Heaviside step function

The Heaviside step function, $\theta(x)$, is a discontinuous function that jumps from 0 to 1 at $x = 0$. It is defined as

$$\theta(x) = \begin{cases} 0 & \text{if } x < 0, \\ 1 & \text{if } x \geq 0. \end{cases} \quad (\text{A.4.2})$$

While $\theta(x)$ is a simple and intuitive function, it can also be understood as a distribution. As a distribution, the Heaviside step function is defined by its action on a test function $\phi(x)$. This means that instead of focusing on its pointwise values, we consider how it integrates against a smooth test function. Specifically, the Heaviside function $\theta(x)$ acts on a test function $\phi(x)$ as follows:

$$\int_{-\infty}^{\infty} \theta(x)\phi(x) dx = \int_0^{\infty} \phi(x) dx \quad (\text{A.4.3})$$

This integral highlights that $H(x)$ effectively “turns on” the test function $\phi(x)$ at $x = 0$ and integrates it from 0 to ∞ . Furthermore, the Heaviside step function is closely related to the Dirac delta distribution. The derivative of $\theta(x)$ in the distributional sense is the Dirac delta function $\delta(x)$

$$\frac{d\theta(x)}{dx} = \delta(x). \quad (\text{A.4.4})$$

This relationship can be understood through the integral property of the delta function as

$$\theta(x) = \int_{-\infty}^x \delta(y)dy \quad (\text{A.4.5})$$

reproduces the step function.

A.4.3 Plus distribution

The idea behind plus distributions is to modify the integration process in such a way that singularities are properly managed. The notation for a plus distribution is typically written as $(f(x))_+$, where $f(x)$ is a function that may have a singularity at some point, often at $x = 0$. The plus distribution is defined in such a way that it behaves like $f(x)$ almost everywhere but ensures that the integral of $f(x)$ against any test function $\phi(x)$ remains finite. Formally, the plus distribution is defined by the subtraction of the

singular part of the function in such a way that the resulting integral is well-defined. For instance, if $f(x)$ has a singularity at $x = 0$, its plus distribution is given by

$$\int_{-\infty}^{\infty} (f(x))_+ \phi(x) dx = \int_{-\infty}^{\infty} f(x) (\phi(x) - \phi(0)) dx. \quad (\text{A.4.6})$$

Here, $\phi(x)$ is a test function that is smooth and vanishes at infinity. The subtraction of $\phi(0)$ inside the integral ensures that the singularity at $x = 0$ does not lead to an infinite result, thereby regularizing the integral. Similarly, when the divergence does not occur at $x = 0$

$$\int_{-1}^1 dx \left(\frac{1}{1-x} \right)_+ g(x) = \int_{-1}^1 dx \left(\frac{1}{1-x} \right) (g(x) - g(1)). \quad (\text{A.4.7})$$

A.5 Bonus Material

In this section, we provide additional related materials that did not fit into the main text.

A.5.1 SISCone jet algorithm

The SISCone algorithm [515] is a sequential recombination algorithm that improves the Snowmass Cone algorithm to be IRC safe. The algorithm does not need a seed and instead loops over all particles i to find a list of protojets. It considers cones over all particles j within $2R$ of particle i such that i and j are on the circumference of the circle. Considering all permutations of including or excluding particles i and j results in four cones that are checked for being unstable, that is if the inclusion and exclusion of i and j is not consistent. After going over every particle the remaining non-unstable cones are explicitly checked for stability and considered as protojets if they are stable. Finally, in a split merging procedure the protojets are clustered into jets.

A.5.2 MLM jet merging

We start with describing the MLM algorithm for merging [516, 517].

1. Generate events and calculate the cross section up to a cutoff defined by the jet algorithm.
2. Randomly select a parton multiplicity with a probability proportional to its integrated cross section at fixed strong coupling α_S .
3. Using the k_T jet algorithm (Sec. 3.3.1.5) to cluster the matrix element partons and reweight the event, using the clustering scales as input for α_S .
4. Start the parton shower with the scale set to a reasonable value (E_{CM} for e^+e^- , $\sqrt{m_W^2 + p_{T,W}^2}$ for W-production, ...).
5. Finally, the event will only be accepted if running the jet algorithm on the showered event yields the same number of jets as used the matrix element.

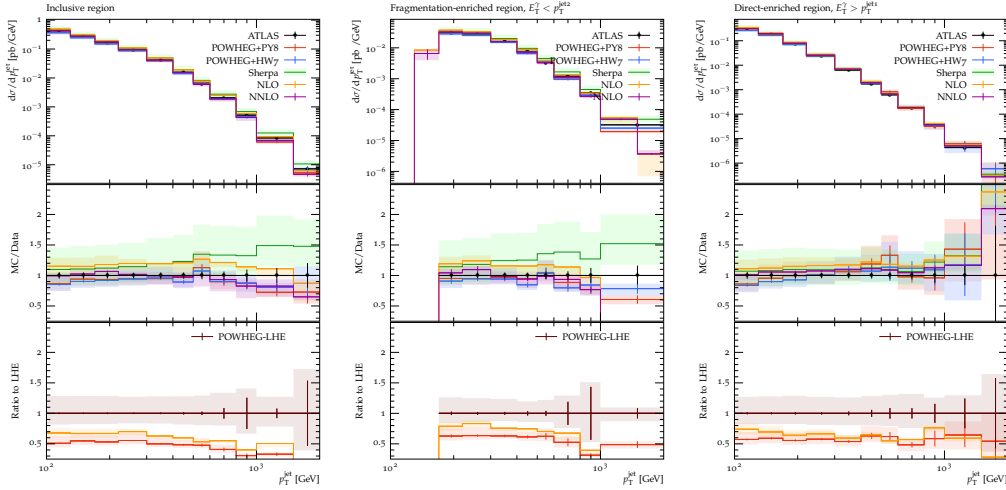


Figure A.1: Jet transverse momentum as defined by ATLAS [340].

A.5.3 FxFx jet merging

We have seen two merging algorithms that are based on leading order matrix elements. The FxFx merging algorithm [518] and matrix element + parton shower matching (MEPS)@NLO algorithm [519] are based on NLO MEs. While FxFx is closely linked to the MiNLO approach [297], MEPS@NLO instead uses shower kernels to prevent issues with mismatches in shower ordering values. Going to NLO, another potential source of double counting arises from an overlap between virtual corrections and the Sudakov suppression in the zero-emission probability. While in principle similar to the CKKW-L algorithm it also uses aspects from the MLM algorithm. A tree-level matrix element now also is the real correction to the parton sample with its multiplicity reduced by one. This is resolved by introducing a function $D(\rho)$ that splits the soft, intermediate and hard regions, based on the transition scale ρ between a j and $j - 1$ -jet through the Durham k_T algorithm. Then the proper pieces (Born, Virtuals, Reals, parton shower counterterms) of each of the multiple NLO samples are enabled and disabled scale-dependently preventing double counting. While proceeding as in the CKKW-L prescription two improvements are included. First, instead of computing the leading-logarithm Sudakov form factor to reweight, the actual Monte Carlo Sudakovs from the real-emission matrix elements are used. Secondly, instead of reweighting by α_S the MiNLO procedure [297] is adopted to obtain a scale, *i.e.* the geometric mean of intermediate scales. Finally, there is a MLM-like check if the resulting jets match to the hard subprocesses. For more technical details on the implementation of the FxFx algorithm within MadGraph MC@NLO, we refer to the original publication [518].

A.5.4 Jet observables

In this section we show some observables from our ATLAS [340] analysis that did not include a photon (except for the selection of events).

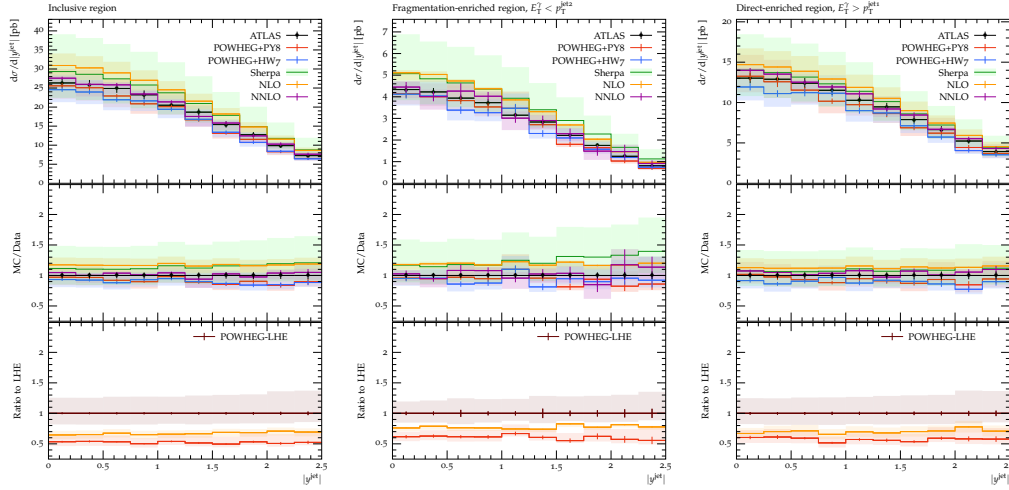


Figure A.2: Jet rapidity as defined by ATLAS [340].

A.6 Files

A.6.1 POWHEG-BOX-V2

The complete set of POWHEG BOX, PYTHIA and HERWIG input files used are available under <https://gitlab.com/APN-Pucky/powheg-slurm-runs>.

File A.1: POWHEG input file

```

vdecaymode 1

numevts 10000
ih1 1
ih2 1
ebeam1 2510d0
ebeam2 2510d0

bornktmin 0.25
#bornsuppfact 10d0

! To be set only if using LHA pdfs
lhans1 27100
lhans2 27100

! Parameters to allow or not the use of stored data
use-old-grid 1
use-old-ubound 1

ncall1 500000
itmx1 5
ncall2 80000
itmx2 3
foldcsi 5
foldy 10
foldphi 5
nubound 2000000

! OPTIONAL PARAMETERS
bornonly 1
mass_low 0.1
mass_high 10.0

```

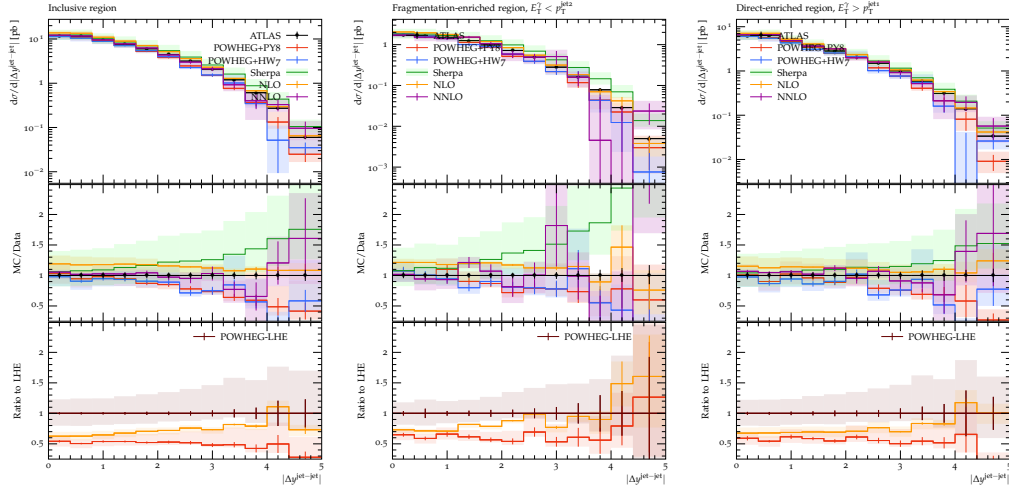


Figure A.3: Jet rapidity difference as defined by ATLAS [340].

```

storemintupb 1
QEDShower 1
rivetAnalysis "ALICE_2020_I1797621"
iseed 10103
manyseeds 1

```

A.6.2 Resummino

All the SLHA and Resummino input files are available under <https://github.com/APN-Pucky/HEPi/tree/master/distribute>.

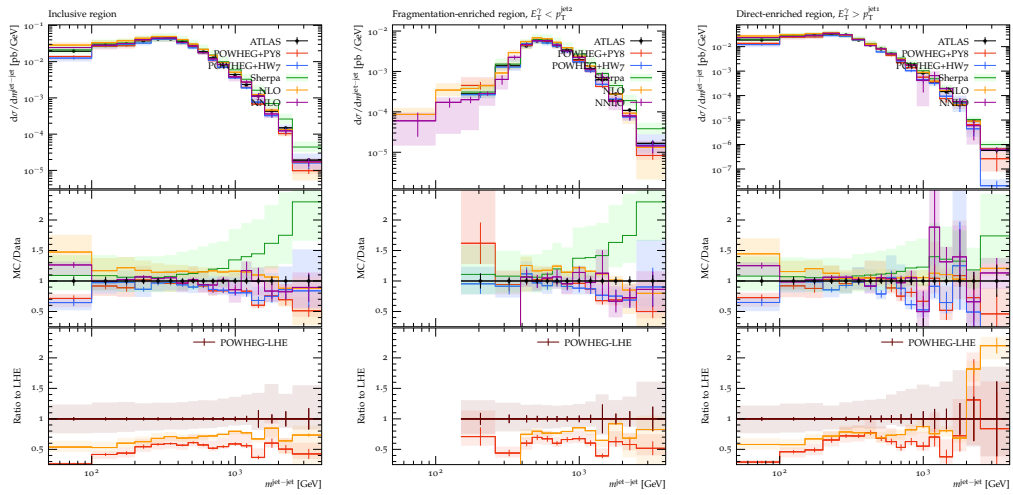


Figure A.4: Jet system mass as defined by ATLAS [340].

List of Programs

- NNPDF4.0** A PDF set [42]. 13, 14, 161
- LHAPDF** Les Houches Accord (LHA) PDF unified library [45]. 13, 14, 89, 115, 155, 170
- MSHT20nlo_as118** A PDF set [44]. 14, 155, 157, 158
- CT18** A PDF set [47]. 14, 157, 158, 161
- MSHT20** A PDF set [44]. 14, 155, 156, 157, 158, 159, 161
- BFG I** A FF parametrization [69]. 23
- JetPhox** A program for the calculation of prompt photon production in hadronic collisions [70–72]. 23, 104
- PYTHIA** Lund Monte Carlo high-energy physics event generator [61, 81–83]. 25, 57, 89, 90, 91, 92, 95, 96, 97, 103, 109, 110, 115, 116, 117, 118, 119, 171, 181, 182, 195
- HERWIG** Multipurpose Event Generator (MPEG) [85–89]. 25, 57, 115, 116, 117, 118, 119, 181, 195
- Sherpa** Simulation of High-Energy Reactions of PArticles [90, 91]. 25, 57, 104, 119, 120
- EPPS16** A nPDF set [106]. 26
- nCTEQ15** A nPDF set [107]. 27
- nCTEQ15HQ** A nPDF set [108]. 28, 89, 93, 94, 95, 96, 97, 103, 104
- HELAS** HELicity Amplitude Subroutines [139]. 41, 43
- MadGraph** framework that aims at providing all the elements necessary for SM and BSM phenomenology [140]. 41, 43, 55, 56, 57, 73, 74, 114, 169, 171, 172, 194
- Whizard** MPEG [141, 142]. 41
- FormCalc** can be used for automatic Feynman diagram computation [143]. 41, 113, 114
- HELAC-NLO** HELicity Amplitude at NLO [144]. 41
- LoopTools** loop library [143]. 43, 46
- FF** loop library [166]. 46

-
- Collier** loop library [167]. 46
- OneLoop** loop library [168]. 46
- CutTools** loop library [169]. 46
- QCDloop** loop library [170]. 46
- MadLoop** loop library [171]. 46
- Golem** loop library [172]. 46
- Ninja** loop library [173]. 46
- Samurai** loop library [174]. 46
- POWHEG BOX** NLO and higher-order calculations in SMC programs according to the POWHEG method [63, 188, 189]. 51, 57, 63, 82, 83, 84, 85, 86, 87, 88, 89, 90, 91, 92, 95, 96, 97, 103, 104, 109, 110, 111, 112, 113, 114, 115, 117, 119, 120, 181, 182, 195
- VEGAS** Adaptive multidimensional Monte Carlo integration [199, 200]. 56
- CUBA** library for multidimensional numerical integration [201, 202]. 56
- FOAM** MC integrator [203]. 56
- i-flow** MC integrator [204]. 57
- SPRING-BASES** MC integrator [205]. 57
- MINT** MC integrator [206]. 57, 84
- FastJet** A software package for jet finding in pp and e+e- collision [238]. 70
- Z** $pp \rightarrow Z, \gamma \rightarrow \bar{l}l$ NLO process in POWHEG BOX [295]. 83, 85
- Zj** $pp \rightarrow Zj, \gamma j \rightarrow \bar{l}lj$ NLO process in POWHEG BOX [296]. 87, 88, 91
- h_{vq}** HQ production at NLO in POWHEG BOX [305]. 88, 91
- HEPdata** HEP data repository [307]. 89, 92
- MSHT20n1o** A PDF set [44]. 89, 93, 94, 95, 96, 97, 115
- Rivet** Robust Independent Validation of Experiment and Theory [309–311]. 89, 90, 92, 114, 115, 116
- HepMC** Event Record for Monte Carlo Generator [315, 316]. 92, 115
- EXODUS** MCEG [267]. 92
- CTEQ6.6** A PDF set [317]. 92
- iminuit** numerical function minimization in Python [319, 320]. 101
- MCFM** MC for FeMtobarn processes [328–331]. 104, 114

- NNLOJET** MC integrator for NNLO calculations [78, 332]. 104
- trijet** $pp \rightarrow jjj$ NLO process in POWHEG BOX [187]. 111, 112, 114
- dijet** $pp \rightarrow jj$ NLO process in POWHEG BOX [345]. 111, 112
- directphoton** $pp \rightarrow \gamma j$ NLO process in POWHEG BOX [300]. 111, 112, 182
- FORM** Symbolic manipulation system [348–350]. 114
- SymPy** Python library for symbolic mathematics [351]. 114
- OpenLoops 2** Evaluation of tree and one-loop matrix elements for any SM [352]. 114
- Recola 2** Recursive Computation of 1-Loop Amplitudes [353]. 114
- YODA** Yet more Objects for (HEP) Data Analysis [309–311]. 114
- POWHEG-RIVET-PYTHIA** Interface for combining POWHEG BOX with Pythia and Rivet [3, 5]. 115
- Resummino** Resummation for electroweak BSM particles [2, 355]. 125, 135, 139, 158, 170, 182, 196
- MSHT201o_as130** A PDF set [44]. 155, 170
- SPheno** SPheno stands for S(upersymmetric) Pheno(menology [462]. 155
- CT18NLO** A PDF set [47]. 157, 158
- NNPDF40_nlo_as_01180** A PDF set [42]. 157
- NNPDF40_nlo_pch_as_01180** A PDF set [42]. 157, 158
- NNPDF40** A PDF set [42]. 157, 158
- NNPDF40_lo_as_01180** A PDF set [42]. 158
- PDF4LHC21_40** A PDF set [466]. 159
- PDF4LHC21** A PDF set [466]. 161
- NNPDF3.1** A PDF set [469]. 161
- TACO** Code for the Testing Analyses' COrrrelations [479]. 169, 172, 182
- UFO** Universal FeynRules Output [483]. 169
- FeynRules** allows the calculation of Feynman rules in momentum space for any QFT physics model [485, 486]. 169
- NNLL-fast** Resummation for squarks and gluino [487]. 170
- HEPi** Python interface for gluing together several HEP programs [6]. 170
- LL-fast** Resummation for squarks and gluino [494]. 170

- MadAnalysis** A package for event file analysis and recasting of LHC results [497–499]. 172, 182
- Delphes** performs a fast multipurpose detector response simulation [500, 501]. 172
- SFS** Simplified Fast detector Simulation [502]. 172
- dataverse** Open source research data repository software [505–508]. 172
- PAD** Public Analysis Database [509]. 172
- SPEY** Smooth inference for reinterpretation studies [514]. 172

KI Disclaimer

In dieser wissenschaftlichen Arbeit wurden Künstliche-Intelligenz und Maschinelles Lernen Technologien zur Unterstützung verschiedener Aspekte der Forschung eingesetzt. Die Nutzung umfasste unter anderem die Analyse und Auswertung von Literatur und die Unterstützung bei der Datenauswertung. Es wird ausdrücklich darauf hingewiesen, dass die endgültige Verantwortung für die inhaltliche Richtigkeit, die kritische Reflexion und die Interpretation der Ergebnisse beim Autor dieser Arbeit liegt. Die KI diene lediglich als Werkzeug und nicht als Ersatz für das kritische und analytische Denken des Forschenden. Die verschiedenen Tools im Einsatz waren:

ChatGPT¹: Lösungsvorschläge für technische Probleme, Debugging, Brainstorming und Korrekturlesen.

Skype Copilot², Google search engine³: Internetsuchmaschine.

GitHub Copilot⁴: Programmiervervollständigung und Codedokumentation.

metamorph⁵, Google Translate⁶, Deep L⁷: Umformulierung von Texten und Synonymfindung.

LanguageTool⁸: Rechtschreibprüfung und Grammatikprüfung.

equation_database_grabber⁹, pix2tex¹⁰: Bild zu LaTeX Formel Konvertierung.

¹⁰<https://chatgpt.com/>

¹⁰<https://copilot.microsoft.com/>

¹⁰<https://google.com/>

¹⁰<https://github.com/features/copilot>

¹⁰<https://github.com/APN-Pucky/metamorph>

¹⁰<https://translate.google.com/>

¹⁰<https://www.deepl.com>

¹⁰<https://languagetool.org/>

¹⁰<https://github.com/APN-Pucky/equation-database-grabber>

¹⁰<https://github.com/lukas-blecher/LaTeX-OCR>

Acronyms

AA nucleus-nucleus. 26

ALICE A Large Ion Collider Experiment. 28, 82, 89, 90, 92, 93, 95, 98, 99, 100, 101, 102, 105, 110, 181

aNNLO approximate next-to-next-to-leading-order. 135, 141, 143, 158, 161, 163, 164, 165, 167, 168, 170, 181, 182

AP Altarelli-Parisi. 11, 17, 22, 53, 64, 76, 137

ATLAS A Toroidal LHC ApparatuS. 105, 118, 121, 122, 123, 134, 135, 145, 161, 169, 172, 177, 181, 194, 195, 196, 197

AuAu gold-gold. 106

BFKL Balitsky-Fadin-Kuraev-Lipatov. 28, 29

BK Balitsky-Kovchegov. 28, 29

BRST Becchi-Rouet-Stora-Tyutin. 7

BSM Beyond the Standard Model. 125, 128, 130, 199, 201

BW Breit-Wigner. 16, 55, 56, 60

CDR Conventional Dimensional Regularization. 42, 50, 53, 146

CGC Color Glass Condensate. 28

CKKW-L Catani-Krauss-Kuhn-Webber-Lönnblad. 71, 77, 171, 194

CL confidence level of exclusion. 173, 176, 178, 179

CMS Compact Muon Solenoid. 105, 134, 135, 145, 161, 169, 172, 177

CPU central processing unit. 63, 115

CS Catani-Seymour. 33, 49, 51, 55, 76, 120, 146

DCA distance of closest approach. 82, 83

DESY Deutsches Elektronen-Synchrotron. 68

-
- DGLAP** Dokshitzer-Gribov-Lipatov-Altarelli-Parisi. 12, 17, 22, 28, 29
- DIS** deep inelastic scattering. 9, 10, 13, 26, 30
- DJR** differential jet rate. 72, 73, 172, 175
- DM** dark matter. 134
- DR** Diagram Removal. 55
- DRED** Dimensional Reduction. 42, 43, 146
- DS** Diagram Subtraction. 55
- DY** Drell-Yan. 9, 10, 13, 82, 87, 88, 90, 99, 140, 141, 142, 143, 149, 161, 181
- EIC** Electron Ion Collider. 30
- EM** electromagnetic. 22, 30
- EMC** European Muon Collaboration. 27
- EW** electroweak. 6
- FF** fragmentation function. 1, 21, 22, 23, 90, 106, 107, 113, 118, 199
- FHD** Four Helicity Dimension. 43, 146
- FKS** Frixione-Kunst-Signer. 33, 49, 50, 73, 75, 76, 114
- FoCal** Forward Calorimeter. 28, 30, 110, 111, 112
- FSR** final-state radiation. 17, 49, 111
- FxFx** Frederix-Frixione. 71, 194
- GPEG** General-Purpose Event Generator. 72
- GUT** Grand Unified Theory. 129, 134
- HEP** high-energy physics. 183, 200, 201
- HF** heavy-flavour. 92, 93, 95, 98
- HL-LHC** High Luminosity LHC. 73, 134
- HQ** heavy quark. 88, 89, 91, 101, 200
- IC** iterative cone. 68
- IC-SM** IC split-merge. 68
- IC-PR** IC progressive removal. 68
- IMR** intermediate-mass region. 81, 91, 92, 93, 98, 99

- IR** infrared. 17, 22, 33, 42, 49, 50, 51, 52, 73, 106, 114, 136, 146
- IRC** infrared-collinear. 24, 67, 68, 81, 193
- ISR** initial-state radiation. 17, 49, 110, 111
- JIMWLK** Jalilian-Marian-Iancu-McLerran-Weigert-Leonidov-Kovner. 28, 29
- KLN** Kinoshita-Lee-Nauenberg. 10, 33, 51
- LF** light-flavour. 92, 98, 101
- LHA** Les Houches Accord. 199
- LHC** Large Hadron Collider. 1, 2, 10, 24, 25, 28, 29, 30, 57, 75, 81, 89, 92, 104, 110, 125, 134, 135, 155, 156, 157, 158, 159, 160, 161, 162, 163, 164, 165, 166, 167, 168, 169, 171, 172, 176, 177, 181, 182, 202
- LHCb** LHC beauty. 30
- LHE** Les Houches Event. 89, 93, 94, 107, 108, 109, 115, 116, 118, 120
- LL** leading-logarithmic. 135, 138, 139
- LMR** low-mass region. 81, 92, 95, 98, 101
- LO** leading-order. 1, 10, 11, 22, 23, 47, 72, 73, 86, 87, 88, 110, 119, 134, 135, 136, 141, 142, 144, 145, 155, 156, 158, 168, 170, 171, 182
- LSP** lightest supersymmetric particle. 126, 130, 134, 169
- MC** Monte Carlo. 1, 13, 14, 55, 56, 57, 59, 74, 75, 76, 82, 84, 94, 104, 120, 125, 181, 194, 200, 201
- MCEG** Monte Carlo Event Generator. 92, 125, 182, 200
- MCMC** Monte Carlo Markov Chain. 57
- ME** matrix element. 15, 21, 55, 119, 194
- MEPS** matrix element + parton shower matching. 194
- MiNLO** multi scale improved NLO. 87, 182, 194
- MiNNLO** multi scale improved NNLO. 87
- MLM** Michelangelo-L.-Mangano. 71, 73, 193, 194
- MPEG** Multipurpose Event Generator. 199
- MPI** multiple parton interactions. 90
- MSSM** Minimal Supersymmetric Standard Model. 1, 2, 56, 125, 126, 127, 128, 130, 131, 134, 135, 155, 159, 160, 169, 176, 181

- NLL** next-to-leading-logarithmic. 104, 125, 135, 138, 139, 142, 143, 145, 155, 156, 157, 158, 159, 170, 181, 182
- NLO** next-to-leading-order. 1, 10, 11, 12, 15, 21, 22, 33, 41, 48, 73, 74, 75, 76, 82, 83, 84, 85, 87, 88, 93, 94, 95, 104, 105, 106, 107, 109, 110, 111, 113, 114, 119, 120, 125, 130, 134, 135, 136, 137, 142, 143, 145, 146, 155, 156, 157, 158, 159, 170, 181, 182, 194, 199, 200, 201
- NNLL** next-to-next-to-leading-logarithmic. 135, 139, 141, 143, 158, 161, 163, 164, 165, 168, 170, 181, 182
- NNLO** next-to-next-to-leading-order. 11, 15, 87, 104, 119, 120, 156, 167, 181, 201
- nPDF** nuclear parton distribution function. 1, 26, 28, 82, 89, 95, 104, 199
- ODE** ordinary differential equation. 18
- OS** on-shell. 12, 16, 33, 47, 48, 49, 54, 55, 56, 88, 146
- pA** proton-nucleus. 28
- PbPb** lead-lead. 82, 89, 93, 102
- PDF** parton distribution function. 9, 10, 12, 13, 14, 17, 21, 22, 26, 27, 28, 29, 49, 71, 76, 82, 89, 92, 93, 94, 95, 96, 97, 98, 102, 103, 104, 106, 115, 117, 118, 136, 143, 144, 146, 149, 150, 151, 155, 156, 157, 158, 159, 161, 162, 163, 164, 165, 166, 167, 168, 170, 199, 200, 201
- PDG** Particle Data Group. 9, 16, 155
- PHENIX** Pioneering High Energy Nuclear Interaction eXperiment. 105
- pMSSM** phenomenological Minimal Supersymmetric Standard Model. 128, 155
- POWHEG** Positive Weight Hardest Emission Generator. 1, 75, 76, 77, 81, 88, 90, 105, 107, 110, 111, 113, 118, 120, 143, 181, 200
- pp** proton-proton. 10, 26, 29, 81, 89, 92, 93, 94, 95, 98, 99, 100, 101, 102, 105, 109, 118, 171, 181, 200
- pPb** proton-lead. 89, 92, 93, 94, 95, 98, 99, 100, 101, 102, 181
- pQCD** perturbative quantum-chromodynamics. 9, 14, 25, 82, 134
- PS** parton shower. 1, 19, 74, 89, 93, 94, 95, 104, 107, 108, 109, 110, 113, 116, 117, 120, 125, 135, 137
- PV** Passarino-Veltman. 43, 46
- QCD** quantum chromodynamics. 1, 7, 8, 9, 10, 15, 17, 25, 29, 31, 36, 57, 64, 65, 67, 71, 80, 82, 87, 88, 89, 104, 107, 110, 114, 115, 118, 119, 129, 134, 135, 139, 144, 149, 160, 168, 170, 172, 181, 182
- QED** quantum electrodynamics. 4, 7, 64, 89, 90, 107, 115, 118, 119, 129, 182

-
- QFT** quantum field theory. 3, 15, 34, 125, 126, 201
- QGP** quark-gluon plasma. 1, 25, 26, 28, 29, 30, 31, 79, 80, 81, 106, 110
- RGE** renormalization group equation. 5, 8, 129, 137
- RHIC** Relativistic Heavy Ion Collider. 1, 25, 29, 30, 81, 104, 106
- SISCone** Seedless Infrared-Safe Cone. 68, 70, 193
- SLHA** SUSY Les Houches Accord. 130, 196
- SM** Standard Model. 1, 2, 3, 4, 5, 6, 7, 33, 125, 126, 127, 128, 129, 130, 134, 166, 169, 185, 199, 201
- SMC** Shower Monte Carlo. 21, 107, 200
- SppS** Super Proton-antiproton Synchrotron. 104
- SpS** Super Proton Synchrotron. 81
- SR** signal region. 168, 169, 172, 173, 176, 177, 178, 179, 182
- SUSY** supersymmetry. 2, 125, 126, 128, 129, 130, 131, 134, 135, 146, 155, 158, 159, 160, 161, 163, 164, 165, 168, 169, 171, 176, 177, 182
- tHV** 't Hooft Veltman. 42, 53, 146
- UPC** ultra-peripheral collision. 26, 30
- UV** ultraviolet. 5, 33, 42, 46, 47, 49, 114, 146
- WIMP** weakly interacting massive particle. 125, 126

Bibliography

- [1] Juri Fiaschi et al. “Soft gluon resummation for associated squark-electroweakino production at the LHC”. In: *JHEP* 06 (2022), p. 130. DOI: 10.1007/JHEP06(2022)130. arXiv: 2202.13416 [hep-ph].
- [2] Juri Fiaschi et al. “Electroweak superpartner production at 13.6 TeV with Resummino”. In: *Eur. Phys. J. C* 83.8 (2023), p. 707. DOI: 10.1140/epjc/s10052-023-11888-y. arXiv: 2304.11915 [hep-ph].
- [3] Anton Andronic et al. “Di-electron production at the LHC: unravelling virtual-photon and heavy-flavour contributions”. In: *JHEP* 05 (2024), p. 222. DOI: 10.1007/JHEP05(2024)222. arXiv: 2401.12875 [hep-ph].
- [4] Alexander Feike et al. “Combination and reinterpretation of LHC SUSY searches”. In: *JHEP* 07 (2024), p. 122. DOI: 10.1007/JHEP07(2024)122. arXiv: 2403.11715 [hep-ph].
- [5] Tomáš Ježo, Michael Klasen, and Alexander Neuwirth. “Prompt photon production with two jets in POWHEG”. In: (Sept. 2024). arXiv: 2409.01424 [hep-ph].
- [6] Alexander Puck Neuwirth. *APN-Pucky/HEPi: v0.2.18*. Version 0.2.18. Feb. 2024. DOI: 10.5281/zenodo.10671795. URL: <https://doi.org/10.5281/zenodo.10671795>.
- [7] Alexander Puck Neuwirth and Kevin Pedro. *APN-Pucky/pyfeyn2: 2.3.10*. Version 2.3.10. Nov. 2023. DOI: 10.5281/zenodo.10067115. URL: <https://doi.org/10.5281/zenodo.10067115>.
- [8] Alexander Puck Neuwirth. *APN-Pucky/feynml: Zenodo Release*. Version 0.2.19. Oct. 2023. DOI: 10.5281/zenodo.8430845. URL: <https://doi.org/10.5281/zenodo.8430845>.
- [9] Alexander Puck Neuwirth. *APN-Pucky/feynamp: Zenodo release*. Version 0.0.10. Apr. 2024. DOI: 10.5281/zenodo.11091562. URL: <https://doi.org/10.5281/zenodo.11091562>.
- [10] Matthew D. Schwartz. *Quantum Field Theory and the Standard Model*. Cambridge University Press, Mar. 2014. ISBN: 978-1-107-03473-0, 978-1-107-03473-0.
- [11] Oskar Klein. “Quantum Theory and Five-Dimensional Theory of Relativity. (In German and English)”. In: *Z. Phys.* 37 (1926). Ed. by J. C. Taylor, pp. 895–906. DOI: 10.1007/BF01397481.
- [12] W. Gordon. “Der Comptoneffekt nach der Schrödingerschen Theorie”. In: *Z. Phys.* 40.1 (1926), pp. 117–133. DOI: 10.1007/BF01390840.
- [13] Paul A. M. Dirac. “The quantum theory of the electron”. In: *Proc. Roy. Soc. Lond. A* 117 (1928), pp. 610–624. DOI: 10.1098/rspa.1928.0023.
- [14] G. Abbiendi et al. “Tests of the standard model and constraints on new physics from measurements of fermion pair production at 183-GeV at LEP”. In: *Eur. Phys. J. C* 6 (1999), pp. 1–18. DOI: 10.1007/s100529801027. arXiv: hep-ex/9808023.

- [15] S. Navas et al. “Review of particle physics”. In: *Phys. Rev. D* 110.3 (2024), p. 030001. DOI: 10.1103/PhysRevD.110.030001.
- [16] Carlo Michel Carloni Calame et al. “Precision Measurement of the W-Boson Mass: Theoretical Contributions and Uncertainties”. In: *Phys. Rev. D* 96.9 (2017), p. 093005. DOI: 10.1103/PhysRevD.96.093005. arXiv: 1612.02841 [hep-ph].
- [17] Ashutosh Vijay Kotwal. “The precision measurement of the W boson mass and its impact on physics”. In: *Nature Rev. Phys.* 6.3 (2024), pp. 180–193. DOI: 10.1038/s42254-023-00682-0. arXiv: 2409.08244 [hep-ex].
- [18] Chen-Ning Yang and Robert L. Mills. “Conservation of Isotopic Spin and Isotopic Gauge Invariance”. In: *Phys. Rev.* 96 (1954). Ed. by Jong-Ping Hsu and D. Fine, pp. 191–195. DOI: 10.1103/PhysRev.96.191.
- [19] John C. Collins and Davison E. Soper. “The Theorems of Perturbative QCD”. In: *Ann. Rev. Nucl. Part. Sci.* 37 (1987), pp. 383–409. DOI: 10.1146/annurev.ns.37.120187.002123.
- [20] C. Becchi, A. Rouet, and R. Stora. “Renormalization of Gauge Theories”. In: *Annals Phys.* 98 (1976), pp. 287–321. DOI: 10.1016/0003-4916(76)90156-1.
- [21] David J. Gross and Frank Wilczek. “Ultraviolet Behavior of Nonabelian Gauge Theories”. In: *Phys. Rev. Lett.* 30 (1973). Ed. by J. C. Taylor, pp. 1343–1346. DOI: 10.1103/PhysRevLett.30.1343.
- [22] H. David Politzer. “Reliable Perturbative Results for Strong Interactions?” In: *Phys. Rev. Lett.* 30 (1973). Ed. by J. C. Taylor, pp. 1346–1349. DOI: 10.1103/PhysRevLett.30.1346.
- [23] Alexandre Deur, Stanley J. Brodsky, and Guy F. de Teramond. “The QCD Running Coupling”. In: *Nucl. Phys.* 90 (2016), p. 1. DOI: 10.1016/j.pnpnp.2016.04.003. arXiv: 1604.08082 [hep-ph].
- [24] Konstantin Chetyrkin, Pavel Baikov, and Johann Kühn. “The β -function of Quantum Chromodynamics and the effective Higgs-gluon-gluon coupling in five-loop order”. In: *PoS LL2016* (2016), p. 010. DOI: 10.22323/1.260.0010.
- [25] F. Herzog et al. “The five-loop beta function of Yang-Mills theory with fermions”. In: *JHEP* 02 (2017), p. 090. DOI: 10.1007/JHEP02(2017)090. arXiv: 1701.01404 [hep-ph].
- [26] P. A. Zyla et al. “Review of Particle Physics”. In: *PTEP* 2020.8 (2020), p. 083C01. DOI: 10.1093/ptep/ptaa104.
- [27] John C. Collins, Davison E. Soper, and George F. Sterman. “Factorization of Hard Processes in QCD”. In: *Adv. Ser. Direct. High Energy Phys.* 5 (1989), pp. 1–91. DOI: 10.1142/9789814503266_0001. arXiv: hep-ph/0409313.
- [28] C. Patrignani et al. “Review of Particle Physics”. In: *Chin. Phys. C* 40.10 (2016), p. 100001. DOI: 10.1088/1674-1137/40/10/100001.
- [29] John Campbell, Joey Huston, and Frank Krauss. *The Black Book of Quantum Chromodynamics : a Primer for the LHC Era*. Oxford University Press, 2018. ISBN: 978-0-19-965274-7. DOI: 10.1093/oso/9780199652747.001.0001.
- [30] Huey-Wen Lin et al. “Parton distributions and lattice QCD calculations: a community white paper”. In: *Prog. Part. Nucl. Phys.* 100 (2018), pp. 107–160. DOI: 10.1016/j.pnpnp.2018.01.007. arXiv: 1711.07916 [hep-ph].
- [31] T. Kinoshita. “Mass singularities of Feynman amplitudes”. In: *J. Math. Phys.* 3 (1962), pp. 650–677. DOI: 10.1063/1.1724268.
- [32] M. Bohm, Ansgar Denner, and H. Joos. *Gauge theories of the strong and electroweak interaction*. 2001. ISBN: 978-3-519-23045-8, 978-3-322-80162-3, 978-3-322-80160-9. DOI: 10.1007/978-3-322-80160-9.

- [33] Tilman Plehn. “Lectures on LHC Physics”. In: *Lect. Notes Phys.* 844 (2012), pp. 1–193. DOI: 10.1007/978-3-642-24040-9. arXiv: 0910.4182 [hep-ph].
- [34] Guido Altarelli and G. Parisi. “Asymptotic Freedom in Parton Language”. In: *Nucl. Phys. B* 126 (1977), pp. 298–318. DOI: 10.1016/0550-3213(77)90384-4.
- [35] G. Curci, W. Furmanski, and R. Petronzio. “Evolution of Parton Densities Beyond Leading Order: The Nonsinglet Case”. In: *Nucl. Phys. B* 175 (1980), pp. 27–92. DOI: 10.1016/0550-3213(80)90003-6.
- [36] Yuri L. Dokshitzer. “Calculation of the Structure Functions for Deep Inelastic Scattering and e^+e^- Annihilation by Perturbation Theory in Quantum Chromodynamics.” In: *Sov. Phys. JETP* 46 (1977), pp. 641–653.
- [37] S. Moch, J. A. M. Vermaseren, and A. Vogt. “The Three loop splitting functions in QCD: The Nonsinglet case”. In: *Nucl. Phys. B* 688 (2004), pp. 101–134. DOI: 10.1016/j.nuclphysb.2004.03.030. arXiv: hep-ph/0403192.
- [38] A. Vogt, S. Moch, and J. A. M. Vermaseren. “The Three-loop splitting functions in QCD: The Singlet case”. In: *Nucl. Phys. B* 691 (2004), pp. 129–181. DOI: 10.1016/j.nuclphysb.2004.04.024. arXiv: hep-ph/0404111.
- [39] John Collins. *Foundations of Perturbative QCD*. Vol. 32. Cambridge Monographs on Particle Physics, Nuclear Physics and Cosmology. Cambridge University Press, July 2023. ISBN: 978-1-009-40184-5, 978-1-009-40183-8, 978-1-009-40182-1. DOI: 10.1017/9781009401845.
- [40] V. N. Gribov and L. N. Lipatov. “Deep inelastic electron scattering in perturbation theory”. In: *Phys. Lett. B* 37 (1971), pp. 78–80. DOI: 10.1016/0370-2693(71)90576-4.
- [41] L. N. Lipatov. “The parton model and perturbation theory”. In: *Yad. Fiz.* 20 (1974), pp. 181–198.
- [42] Richard D. Ball et al. “The path to proton structure at 1% accuracy”. In: *Eur. Phys. J. C* 82.5 (2022), p. 428. DOI: 10.1140/epjc/s10052-022-10328-7. arXiv: 2109.02653 [hep-ph].
- [43] Roy Stegeman. “The negligible impact of experimental inconsistencies in the NNPDF4.0 global dataset”. In: *PoS ICHEP2022* (2022), p. 787. DOI: 10.22323/1.414.0787. arXiv: 2212.07703 [hep-ph].
- [44] S. Bailey et al. “Parton distributions from LHC, HERA, Tevatron and fixed target data: MSHT20 PDFs”. In: *Eur. Phys. J. C* 81.4 (2021), p. 341. DOI: 10.1140/epjc/s10052-021-09057-0. arXiv: 2012.04684 [hep-ph].
- [45] Andy Buckley et al. “LHAPDF6: parton density access in the LHC precision era”. In: *Eur. Phys. J. C* 75 (2015), p. 132. DOI: 10.1140/epjc/s10052-015-3318-8. arXiv: 1412.7420 [hep-ph].
- [46] Jon Butterworth et al. “PDF4LHC recommendations for LHC Run II”. In: *J. Phys. G* 43 (2016), p. 023001. DOI: 10.1088/0954-3899/43/2/023001. arXiv: 1510.03865 [hep-ph].
- [47] Tie-Jiun Hou et al. “New CTEQ global analysis of quantum chromodynamics with high-precision data from the LHC”. In: *Phys. Rev. D* 103.1 (2021), p. 014013. DOI: 10.1103/PhysRevD.103.014013. arXiv: 1912.10053 [hep-ph].
- [48] Frank Wilczek. “Asymptotic freedom: From paradox to paradigm”. In: *Proc. Nat. Acad. Sci.* 102 (2005), pp. 8403–8413. DOI: 10.1103/RevModPhys.77.857. arXiv: hep-ph/0502113.
- [49] R. Keith Ellis, W. James Stirling, and B. R. Webber. *QCD and collider physics*. Vol. 8. Cambridge University Press, Feb. 2011. ISBN: 978-0-511-82328-2, 978-0-521-54589-1. DOI: 10.1017/CB09780511628788.

- [50] S. Mandelstam. “Determination of the pion - nucleon scattering amplitude from dispersion relations and unitarity. General theory”. In: *Phys. Rev.* 112 (1958), pp. 1344–1360. DOI: 10.1103/PhysRev.112.1344.
- [51] Steven Weinberg. *The Quantum theory of fields. Vol. 1: Foundations*. Cambridge University Press, June 2005. ISBN: 978-0-521-67053-1, 978-0-511-25204-4. DOI: 10.1017/CB09781139644167.
- [52] F. Halzen and Alan D. Martin. *QUARKS AND LEPTONS: AN INTRODUCTORY COURSE IN MODERN PARTICLE PHYSICS*. 1984. ISBN: 978-0-471-88741-6.
- [53] Jonathan M. Butterworth et al. “Jet substructure as a new Higgs search channel at the LHC”. In: *Phys. Rev. Lett.* 100 (2008), p. 242001. DOI: 10.1103/PhysRevLett.100.242001. arXiv: 0802.2470 [hep-ph].
- [54] S. Ceci, M. Vukšić, and B. Zauner. “Breit-Wigner phase is a fundamental property of a resonance”. In: (Aug. 2014). arXiv: 1408.2437 [hep-ph].
- [55] S. Schael et al. “Precision electroweak measurements on the Z resonance”. In: *Phys. Rept.* 427 (2006), pp. 257–454. DOI: 10.1016/j.physrep.2005.12.006. arXiv: hep-ex/0509008.
- [56] Gregory Soyez. “Jet substructure for parton showers and resummation”. Parton Showers and Resummations (PSR), 6-8 June 2023. 2023. URL: <https://indico.cern.ch/event/1202436/contributions/5288130/attachments/2660262/4608836/lund.pdf>.
- [57] T. Sjostrand and Peter Z. Skands. “Transverse-momentum-ordered showers and interleaved multiple interactions”. In: *Eur. Phys. J. C* 39 (2005), pp. 129–154. DOI: 10.1140/epjc/s2004-02084-y. arXiv: hep-ph/0408302.
- [58] Paolo Nason and Bryan Webber. “Next-to-Leading-Order Event Generators”. In: *Ann. Rev. Nucl. Part. Sci.* 62 (2012), pp. 187–213. DOI: 10.1146/annurev-nucl-102711-094928. arXiv: 1202.1251 [hep-ph].
- [59] Stefan Höche. “Introduction to parton-shower event generators”. In: *Theoretical Advanced Study Institute in Elementary Particle Physics: Journeys Through the Precision Frontier: Amplitudes for Colliders*. 2015, pp. 235–295. DOI: 10.1142/9789814678766_0005. arXiv: 1411.4085 [hep-ph].
- [60] Stefan Höche, Daniel Reichelt, and Frank Siegert. “Momentum conservation and unitarity in parton showers and NLL resummation”. In: *JHEP* 01 (2018), p. 118. DOI: 10.1007/JHEP01(2018)118. arXiv: 1711.03497 [hep-ph].
- [61] Christian Bierlich et al. “A comprehensive guide to the physics and usage of PYTHIA 8.3”. In: *SciPost Phys. Codeb.* 2022 (2022), p. 8. DOI: 10.21468/SciPostPhysCodeb.8. arXiv: 2203.11601 [hep-ph].
- [62] Michael H. Seymour. “Matrix element corrections to parton shower algorithms”. In: *Comput. Phys. Commun.* 90 (1995), pp. 95–101. DOI: 10.1016/0010-4655(95)00064-M. arXiv: hep-ph/9410414.
- [63] Paolo Nason. “A New method for combining NLO QCD with shower Monte Carlo algorithms”. In: *JHEP* 11 (2004), p. 040. DOI: 10.1088/1126-6708/2004/11/040. arXiv: hep-ph/0409146.
- [64] E. G. Floratos, C. Kounnas, and R. Lacaze. “Higher Order QCD Effects in Inclusive Annihilation and Deep Inelastic Scattering”. In: *Nucl. Phys. B* 192 (1981), pp. 417–462. DOI: 10.1016/0550-3213(81)90434-X.
- [65] Michael Klasen. “Theory of hard photoproduction”. In: *Rev. Mod. Phys.* 74 (2002), pp. 1221–1282. DOI: 10.1103/RevModPhys.74.1221. arXiv: hep-ph/0206169.

- [66] Paolo Nason and Carlo Oleari. “On the fragmentation function for heavy quarks in $e^+ e^-$ collisions”. In: *Phys. Lett. B* 418 (1998), pp. 199–208. DOI: 10.1016/S0370-2693(97)01414-7. arXiv: hep-ph/9709358.
- [67] A. Adare et al. “Direct photon production in $d+Au$ collisions at $\sqrt{s_{NN}} = 200$ GeV”. In: *Phys. Rev. C* 87 (2013), p. 054907. DOI: 10.1103/PhysRevC.87.054907. arXiv: 1208.1234 [nucl-ex].
- [68] Michael Klasen and F. König. “New information on photon fragmentation functions”. In: *Eur. Phys. J. C* 74.8 (2014), p. 3009. DOI: 10.1140/epjc/s10052-014-3009-x. arXiv: 1403.2290 [hep-ph].
- [69] L. Bourhis, M. Fontannaz, and J. P. Guillet. “Quark and gluon fragmentation functions into photons”. In: *Eur. Phys. J.* 2.3 (1998), pp. 529–537. DOI: 10.1007/s100529800708. arXiv: hep-ph/9704447.
- [70] S. Catani et al. “Cross-section of isolated prompt photons in hadron hadron collisions”. In: *JHEP* 05 (2002), p. 028. DOI: 10.1088/1126-6708/2002/05/028. arXiv: hep-ph/0204023.
- [71] Patrick Aurenche et al. “A New critical study of photon production in hadronic collisions”. In: *Phys. Rev. D* 73 (2006), p. 094007. DOI: 10.1103/PhysRevD.73.094007. arXiv: hep-ph/0602133.
- [72] Z. Belghobsi et al. “Photon - Jet Correlations and Constraints on Fragmentation Functions”. In: *Phys. Rev. D* 79 (2009), p. 114024. DOI: 10.1103/PhysRevD.79.114024. arXiv: 0903.4834 [hep-ph].
- [73] David d’Enterria and Juan Rojo. “Quantitative constraints on the gluon distribution function in the proton from collider isolated-photon data”. In: *Nucl. Phys. B* 860 (2012), pp. 311–338. DOI: 10.1016/j.nuclphysb.2012.03.003. arXiv: 1202.1762 [hep-ph].
- [74] S. Amoroso et al. “Les Houches 2019: Physics at TeV Colliders: Standard Model Working Group Report”. In: *11th Les Houches Workshop on Physics at TeV Colliders: PhysTeV Les Houches*. Mar. 2020. arXiv: 2003.01700 [hep-ph].
- [75] S. Frixione. “Isolated photons without fragmentation contribution”. In: *29th International Conference on High-Energy Physics*. July 1998, pp. 790–794. arXiv: hep-ph/9809397.
- [76] Ryan Atkin. “Review of jet reconstruction algorithms”. In: *J. Phys. Conf. Ser.* 645.1 (2015). Ed. by Alan S. Cornell and Bruce Mellado, p. 012008. DOI: 10.1088/1742-6596/645/1/012008.
- [77] Frank Siegert. “A practical guide to event generation for prompt photon production with Sherpa”. In: *J. Phys. G* 44.4 (2017), p. 044007. DOI: 10.1088/1361-6471/aa5f29. arXiv: 1611.07226 [hep-ph].
- [78] Xuan Chen et al. “Isolated photon and photon+jet production at NNLO QCD accuracy”. In: *JHEP* 04 (2020), p. 166. DOI: 10.1007/JHEP04(2020)166. arXiv: 1904.01044 [hep-ph].
- [79] Bo Andersson et al. “Parton Fragmentation and String Dynamics”. In: *Phys. Rept.* 97 (1983), pp. 31–145. DOI: 10.1016/0370-1573(83)90080-7.
- [80] Torbjorn Sjostrand. “Jet Fragmentation of Nearby Partons”. In: *Nucl. Phys. B* 248 (1984), pp. 469–502. DOI: 10.1016/0550-3213(84)90607-2.
- [81] Torbjorn Sjostrand, Stephen Mrenna, and Peter Z. Skands. “PYTHIA 6.4 Physics and Manual”. In: *JHEP* 05 (2006), p. 026. DOI: 10.1088/1126-6708/2006/05/026. arXiv: hep-ph/0603175.

- [82] Torbjorn Sjostrand, Stephen Mrenna, and Peter Z. Skands. “A Brief Introduction to PYTHIA 8.1”. In: *Comput. Phys. Commun.* 178 (2008), pp. 852–867. DOI: 10.1016/j.cpc.2008.01.036. arXiv: 0710.3820 [hep-ph].
- [83] Torbjörn Sjöstrand et al. “An introduction to PYTHIA 8.2”. In: *Comput. Phys. Commun.* 191 (2015), pp. 159–177. DOI: 10.1016/j.cpc.2015.01.024. arXiv: 1410.3012 [hep-ph].
- [84] G. Marchesini and B. R. Webber. “Simulation of QCD Jets Including Soft Gluon Interference”. In: *Nucl. Phys. B* 238 (1984), pp. 1–29. DOI: 10.1016/0550-3213(84)90463-2.
- [85] G. Corcella et al. “HERWIG 6: An Event generator for hadron emission reactions with interfering gluons (including supersymmetric processes)”. In: *JHEP* 01 (2001), p. 010. DOI: 10.1088/1126-6708/2001/01/010. arXiv: hep-ph/0011363.
- [86] M. Bahr et al. “Herwig++ Physics and Manual”. In: *Eur. Phys. J. C* 58 (2008), pp. 639–707. DOI: 10.1140/epjc/s10052-008-0798-9. arXiv: 0803.0883 [hep-ph].
- [87] Johannes Bellm et al. “Herwig 7.0/Herwig++ 3.0 release note”. In: *Eur. Phys. J. C* 76.4 (2016), p. 196. DOI: 10.1140/epjc/s10052-016-4018-8. arXiv: 1512.01178 [hep-ph].
- [88] Johannes Bellm et al. “Herwig 7.2 release note”. In: *Eur. Phys. J. C* 80.5 (2020), p. 452. DOI: 10.1140/epjc/s10052-020-8011-x. arXiv: 1912.06509 [hep-ph].
- [89] Gavin Bewick et al. “Herwig 7.3 Release Note”. In: (Dec. 2023). arXiv: 2312.05175 [hep-ph].
- [90] T. Gleisberg et al. “Event generation with SHERPA 1.1”. In: *JHEP* 02 (2009), p. 007. DOI: 10.1088/1126-6708/2009/02/007. arXiv: 0811.4622 [hep-ph].
- [91] Enrico Bothmann et al. “Event Generation with Sherpa 2.2”. In: *SciPost Phys.* 7.3 (2019), p. 034. DOI: 10.21468/SciPostPhys.7.3.034. arXiv: 1905.09127 [hep-ph].
- [92] D. Amati and G. Veneziano. “Preconfinement as a Property of Perturbative QCD”. In: *Phys. Lett. B* 83 (1979), pp. 87–92. DOI: 10.1016/0370-2693(79)90896-7.
- [93] Phil Ilten et al. “Modeling hadronization using machine learning”. In: *SciPost Phys.* 14.3 (2023), p. 027. DOI: 10.21468/SciPostPhys.14.3.027. arXiv: 2203.04983 [hep-ph].
- [94] Aishik Ghosh et al. “Towards a deep learning model for hadronization”. In: *Phys. Rev. D* 106.9 (2022), p. 096020. DOI: 10.1103/PhysRevD.106.096020. arXiv: 2203.12660 [hep-ph].
- [95] Jay Chan et al. “Fitting a deep generative hadronization model”. In: *JHEP* 09 (2023), p. 084. DOI: 10.1007/JHEP09(2023)084. arXiv: 2305.17169 [hep-ph].
- [96] E. Rutherford. “The scattering of alpha and beta particles by matter and the structure of the atom”. In: *Phil. Mag. Ser. 6* 21 (1911), pp. 669–688. DOI: 10.1080/14786440508637080.
- [97] Wit Busza, Krishna Rajagopal, and Wilke van der Schee. “Heavy Ion Collisions: The Big Picture, and the Big Questions”. In: *Ann. Rev. Nucl. Part. Sci.* 68 (2018), pp. 339–376. DOI: 10.1146/annurev-nucl-101917-020852. arXiv: 1802.04801 [hep-ph].
- [98] Javier L. Albacete, Adrian Dumitru, and Cyrille Marquet. “The initial state of heavy-ion collisions”. In: *Int. J. Mod. Phys. A* 28 (2013), p. 1340010. DOI: 10.1142/S0217751X13400101. arXiv: 1302.6433 [hep-ph].
- [99] Michael L. Miller et al. “Glauber modeling in high energy nuclear collisions”. In: *Ann. Rev. Nucl. Part. Sci.* 57 (2007), pp. 205–243. DOI: 10.1146/annurev.nucl.57.090506.123020. arXiv: nucl-ex/0701025.
- [100] Betty Abelev et al. “Centrality determination of Pb-Pb collisions at $\sqrt{s_{NN}} = 2.76$ TeV with ALICE”. In: *Phys. Rev. C* 88.4 (2013), p. 044909. DOI: 10.1103/PhysRevC.88.044909. arXiv: 1301.4361 [nucl-ex].

- [101] R. J. Glauber. “Cross-sections in deuterium at high-energies”. In: *Phys. Rev.* 100 (1955), pp. 242–248. DOI: 10.1103/PhysRev.100.242.
- [102] B. Alver et al. “The PHOBOS Glauber Monte Carlo”. In: (May 2008). arXiv: 0805.4411 [nucl-ex].
- [103] David d’Enterria and Constantin Loizides. “Progress in the Glauber Model at Collider Energies”. In: *Ann. Rev. Nucl. Part. Sci.* 71 (2021), pp. 315–344. DOI: 10.1146/annurev-nucl-102419-060007. arXiv: 2011.14909 [hep-ph].
- [104] Christian Klein-Bösing. “Study of the Quark-Gluon Plasma with Hard and Electromagnetic Probes”. Munster U., 2013. URL: <https://cds.cern.ch/record/2729069>.
- [105] Michele Arneodo. “Nuclear effects in structure functions”. In: *Phys. Rept.* 240 (1994), pp. 301–393. DOI: 10.1016/0370-1573(94)90048-5.
- [106] Kari J. Eskola et al. “EPPS16: Nuclear parton distributions with LHC data”. In: *Eur. Phys. J. C* 77.3 (2017), p. 163. DOI: 10.1140/epjc/s10052-017-4725-9. arXiv: 1612.05741 [hep-ph].
- [107] K. Kovarik et al. “nCTEQ15 - Global analysis of nuclear parton distributions with uncertainties in the CTEQ framework”. In: *Phys. Rev. D* 93.8 (2016), p. 085037. DOI: 10.1103/PhysRevD.93.085037. arXiv: 1509.00792 [hep-ph].
- [108] P. Duwentäster et al. “Impact of heavy quark and quarkonium data on nuclear gluon PDFs”. In: *Phys. Rev. D* 105.11 (2022), p. 114043. DOI: 10.1103/PhysRevD.105.114043. arXiv: 2204.09982 [hep-ph].
- [109] Tomáš Ježo. “Nuclear PDF updates from nCTEQ”. In: *Forward Physics and QCD at the LHC and EIC*. Presented on 23-27 October 2023. Oct. 2023. URL: https://indico.cern.ch/event/1339885/contributions/5640544/attachments/2740178/4767061/slides_public.pdf.
- [110] J. J. Aubert et al. “The ratio of the nucleon structure functions F_2^n for iron and deuterium”. In: *Phys. Lett. B* 123 (1983), pp. 275–278. DOI: 10.1016/0370-2693(83)90437-9.
- [111] P. R. Norton. “The EMC effect”. In: *Rept. Prog. Phys.* 66 (2003), pp. 1253–1297. DOI: 10.1088/0034-4885/66/8/201.
- [112] Gavin P. Salam. “An Introduction to leading and next-to-leading BFKL”. In: *Acta Phys. Polon. B* 30 (1999). Ed. by A. Bialas and M. Praszalowicz, pp. 3679–3705. arXiv: hep-ph/9910492.
- [113] T. Lappi and H. Mäntysaari. “Next-to-leading order Balitsky-Kovchegov equation with resummation”. In: *Phys. Rev. D* 93.9 (2016), p. 094004. DOI: 10.1103/PhysRevD.93.094004. arXiv: 1601.06598 [hep-ph].
- [114] Alfred H. Mueller. “A Simple derivation of the JIMWLK equation”. In: *Phys. Lett. B* 523 (2001), pp. 243–248. DOI: 10.1016/S0370-2693(01)01343-0. arXiv: hep-ph/0110169.
- [115] Florian Jonas. “Probing the initial state of heavy-ion collisions with isolated prompt photons”. PhD thesis. LBL, Berkeley, May 2023.
- [116] *Letter of Intent: A Forward Calorimeter (FoCal) in the ALICE experiment*. Tech. rep. Geneva: CERN, 2020. URL: <http://cds.cern.ch/record/2719928>.
- [117] R. Rapp, J. Wambach, and H. van Hees. “The Chiral Restoration Transition of QCD and Low Mass Dileptons”. In: *Landolt-Bornstein* 23 (2010). Ed. by R. Stock, p. 134. DOI: 10.1007/978-3-642-01539-7_6. arXiv: 0901.3289 [hep-ph].
- [118] Frithjof Karsch and Martin Lutgemeier. “Deconfinement and chiral symmetry restoration in an SU(3) gauge theory with adjoint fermions”. In: *Nucl. Phys. B* 550 (1999), pp. 449–464. DOI: 10.1016/S0550-3213(99)00129-7. arXiv: hep-lat/9812023.

- [119] Owe Philipsen. “Constraining the phase diagram of QCD at finite temperature and density”. In: *PoS LATTICE2019* (2019), p. 273. DOI: 10.22323/1.363.0273. arXiv: 1912.04827 [hep-lat].
- [120] Anton Andronic et al. “Decoding the phase structure of QCD via particle production at high energy”. In: *Nature* 561.7723 (2018), pp. 321–330. DOI: 10.1038/s41586-018-0491-6. arXiv: 1710.09425 [nucl-th].
- [121] L. Adamczyk et al. “Bulk Properties of the Medium Produced in Relativistic Heavy-Ion Collisions from the Beam Energy Scan Program”. In: *Phys. Rev. C* 96.4 (2017), p. 044904. DOI: 10.1103/PhysRevC.96.044904. arXiv: 1701.07065 [nucl-ex].
- [122] T. Niida and Y. Miake. “Signatures of QGP at RHIC and the LHC”. In: *AAPPS Bull.* 31.1 (2021), p. 12. DOI: 10.1007/s43673-021-00014-3. arXiv: 2104.11406 [nucl-ex].
- [123] Patrick Steinbrecher. “The QCD crossover at zero and non-zero baryon densities from Lattice QCD”. In: *Nucl. Phys. A* 982 (2019). Ed. by Federico Antinori et al., pp. 847–850. DOI: 10.1016/j.nuclphysa.2018.08.025. arXiv: 1807.05607 [hep-lat].
- [124] Y. Aoki et al. “The Order of the quantum chromodynamics transition predicted by the standard model of particle physics”. In: *Nature* 443 (2006), pp. 675–678. DOI: 10.1038/nature05120. arXiv: hep-lat/0611014.
- [125] A. Bazavov et al. “Chiral crossover in QCD at zero and non-zero chemical potentials”. In: *Phys. Lett. B* 795 (2019), pp. 15–21. DOI: 10.1016/j.physletb.2019.05.013. arXiv: 1812.08235 [hep-lat].
- [126] T. D. Lee and M. Nauenberg. “Degenerate Systems and Mass Singularities”. In: *Phys. Rev.* 133 (1964). Ed. by G. Feinberg, B1549–B1562. DOI: 10.1103/PhysRev.133.B1549.
- [127] Michael E. Peskin and Daniel V. Schroeder. *An Introduction to quantum field theory*. Reading, USA: Addison-Wesley, 1995. ISBN: 9780201503975, 0201503972. URL: <http://www.slac.stanford.edu/~mpeskin/QFT.html>.
- [128] John Clive Ward. “An Identity in Quantum Electrodynamics”. In: *Phys. Rev.* 78 (1950), p. 182. DOI: 10.1103/PhysRev.78.182.
- [129] Y. Takahashi. “On the generalized Ward identity”. In: *Nuovo Cim.* 6 (1957), p. 371. DOI: 10.1007/BF02832514.
- [130] Marcel Rothering. “Precise predictions for supersymmetric particle production at the LHC”. dissertation. Westfälischen Wilhelms-Universität Münster, 2016. URL: https://www.uni-muenster.de/imperia/md/content/physik_tp/theses/klasen/rothering_phd.pdf.
- [131] W. Kilian et al. “QCD in the Color-Flow Representation”. In: *JHEP* 10 (2012), p. 022. DOI: 10.1007/JHEP10(2012)022. arXiv: 1206.3700 [hep-ph].
- [132] F. Maltoni et al. “Color Flow Decomposition of QCD Amplitudes”. In: *Phys. Rev. D* 67 (2003), p. 014026. DOI: 10.1103/PhysRevD.67.014026. arXiv: hep-ph/0209271.
- [133] Gerard 't Hooft. “A Planar Diagram Theory for Strong Interactions”. In: *Nucl. Phys. B* 72 (1974). Ed. by J. C. Taylor, p. 461. DOI: 10.1016/0550-3213(74)90154-0.
- [134] H. U. Bengtsson. “The Lund Monte Carlo for High p_T Physics”. In: *Comput. Phys. Commun.* 31 (1984), p. 323. DOI: 10.1016/0010-4655(84)90018-3.
- [135] R. Keith Ellis, G. Marchesini, and B. R. Webber. “Soft Radiation in Parton Parton Scattering”. In: *Nucl. Phys. B* 286 (1987). [Erratum: Nucl.Phys.B 294, 1180 (1987)], p. 643. DOI: 10.1016/0550-3213(87)90456-1.
- [136] G. Marchesini and B. R. Webber. “Monte Carlo Simulation of General Hard Processes with Coherent QCD Radiation”. In: *Nucl. Phys. B* 310 (1988), pp. 461–526. DOI: 10.1016/0550-3213(88)90089-2.

- [137] Michelangelo L. Mangano, Stephen J. Parke, and Zhan Xu. “Duality and Multi - Gluon Scattering”. In: *Nucl. Phys. B* 298 (1988), pp. 653–672. DOI: 10.1016/0550-3213(88)90001-6.
- [138] Leif Gellersen. *MC Tutorial Background: Parton Showers, Matching, Merging*. <https://indico.cern.ch/event/1131319/contributions/4895915/attachments/2477520/4252738/gellersenPSMM.pdf>. Presented at the 2022 CTEQ Summer School, July 8th, 2022. 2022.
- [139] H. Murayama, I. Watanabe, and Kaoru Hagiwara. “HELAS: HELicity amplitude sub-routines for Feynman diagram evaluations”. In: (Jan. 1992).
- [140] J. Alwall et al. “The automated computation of tree-level and next-to-leading order differential cross sections, and their matching to parton shower simulations”. In: *JHEP* 07 (2014), p. 079. DOI: 10.1007/JHEP07(2014)079. arXiv: 1405.0301 [hep-ph].
- [141] Wolfgang Kilian, Thorsten Ohl, and Jurgen Reuter. “WHIZARD: Simulating Multi-Particle Processes at LHC and ILC”. In: *Eur. Phys. J. C* 71 (2011), p. 1742. DOI: 10.1140/epjc/s10052-011-1742-y. arXiv: 0708.4233 [hep-ph].
- [142] Mauro Moretti, Thorsten Ohl, and Jurgen Reuter. “O’Mega: An Optimizing matrix element generator”. In: (Feb. 2001). Ed. by Ties Behnke et al., pp. 1981–2009. arXiv: hep-ph/0102195.
- [143] T. Hahn and M. Perez-Victoria. “Automatized one loop calculations in four-dimensions and D-dimensions”. In: *Comput. Phys. Commun.* 118 (1999), pp. 153–165. DOI: 10.1016/S0010-4655(98)00173-8. arXiv: hep-ph/9807565.
- [144] G. Bevilacqua et al. “HELAC-NLO”. In: *Comput. Phys. Commun.* 184 (2013), pp. 986–997. DOI: 10.1016/j.cpc.2012.10.033. arXiv: 1110.1499 [hep-ph].
- [145] Gerard ’t Hooft and M. J. G. Veltman. “Regularization and Renormalization of Gauge Fields”. In: *Nucl. Phys. B* 44 (1972), pp. 189–213. DOI: 10.1016/0550-3213(72)90279-9.
- [146] Adrian Signer and Dominik Stockinger. “Using Dimensional Reduction for Hadronic Collisions”. In: *Nucl. Phys. B* 808 (2009), pp. 88–120. DOI: 10.1016/j.nuclphysb.2008.09.016. arXiv: 0807.4424 [hep-ph].
- [147] Celine Degrande. “Automatic evaluation of UV and R2 terms for beyond the Standard Model Lagrangians: a proof-of-principle”. In: *Comput. Phys. Commun.* 197 (2015), pp. 239–262. DOI: 10.1016/j.cpc.2015.08.015. arXiv: 1406.3030 [hep-ph].
- [148] S. Catani, M. H. Seymour, and Z. Trocsanyi. “Regularization scheme independence and unitarity in QCD cross-sections”. In: *Phys. Rev. D* 55 (1997), pp. 6819–6829. DOI: 10.1103/PhysRevD.55.6819. arXiv: hep-ph/9610553.
- [149] William B. Kilgore. “Regularization Schemes and Higher Order Corrections”. In: *Phys. Rev. D* 83 (2011), p. 114005. DOI: 10.1103/PhysRevD.83.114005. arXiv: 1102.5353 [hep-ph].
- [150] C. Gnendiger et al. “To d , or not to d : recent developments and comparisons of regularization schemes”. In: *Eur. Phys. J. C* 77.7 (2017), p. 471. DOI: 10.1140/epjc/s10052-017-5023-2. arXiv: 1705.01827 [hep-ph].
- [151] Zoltan Kunszt, Adrian Signer, and Zoltan Trocsanyi. “One loop helicity amplitudes for all $2 \rightarrow 2$ processes in QCD and N=1 supersymmetric Yang-Mills theory”. In: *Nucl. Phys. B* 411 (1994), pp. 397–442. DOI: 10.1016/0550-3213(94)90456-1. arXiv: hep-ph/9305239.
- [152] William B. Kilgore. “The Four Dimensional Helicity Scheme Beyond One Loop”. In: *Phys. Rev. D* 86 (2012), p. 014019. DOI: 10.1103/PhysRevD.86.014019. arXiv: 1205.4015 [hep-ph].

- [153] F. Jegerlehner. “Facts of life with $\gamma(5)$ ”. In: *Eur. Phys. J. C* 18 (2001), pp. 673–679. DOI: 10.1007/s100520100573. arXiv: hep-th/0005255.
- [154] G. ’t Hooft and M. Veltman. “Scalar one-loop integrals”. In: *Nuclear Physics B* 153 (Jan. 1979), pp. 365–401. DOI: 10.1016/0550-3213(79)90605-9. URL: [https://doi.org/10.1016/0550-3213\(79\)90605-9](https://doi.org/10.1016/0550-3213(79)90605-9).
- [155] G. Passarino and M. Veltman. “One-loop corrections for e^+e^- annihilation into $\mu^+\mu^-$ in the Weinberg model”. In: *Nuclear Physics B* 160.1 (Nov. 1979), pp. 151–207. DOI: 10.1016/0550-3213(79)90234-7. URL: [https://doi.org/10.1016/0550-3213\(79\)90234-7](https://doi.org/10.1016/0550-3213(79)90234-7).
- [156] Ansgar Denner. “Techniques for calculation of electroweak radiative corrections at the one loop level and results for W physics at LEP-200”. In: *Fortsch. Phys.* 41 (1993), pp. 307–420. DOI: 10.1002/prop.2190410402. arXiv: 0709.1075 [hep-ph].
- [157] G. Passarino and M. J. G. Veltman. “One Loop Corrections for e^+e^- Annihilation Into $\mu^+\mu^-$ in the Weinberg Model”. In: *Nucl. Phys. B* 160 (1979), pp. 151–207. DOI: 10.1016/0550-3213(79)90234-7.
- [158] M. Consoli. “One Loop Corrections to $e^+e^- \rightarrow e^+e^-$ in the Weinberg Model”. In: *Nucl. Phys. B* 160 (1979), pp. 208–252. DOI: 10.1016/0550-3213(79)90235-9.
- [159] Martin Green and M. J. G. Veltman. “Weak and Electromagnetic Radiative Corrections to Low-Energy Processes”. In: *Nucl. Phys. B* 169 (1980). [Erratum: Nucl.Phys.B 175, 547 (1980)], pp. 137–164. DOI: 10.1016/0550-3213(80)90257-6.
- [160] K. Kovarik. “Hitchhiker’s guide to renormalization”. unpublished manuscript.
- [161] D. B. Melrose. “Reduction of Feynman diagrams”. In: *Nuovo Cim.* 40 (1965), pp. 181–213. DOI: 10.1007/BF02832919.
- [162] Robin G. Stuart. “Algebraic Reduction of One Loop Feynman Diagrams to Scalar Integrals”. In: *Comput. Phys. Commun.* 48 (1988), pp. 367–389. DOI: 10.1016/0010-4655(88)90202-0.
- [163] Robin G. Stuart and A. Gongora. “Algebraic Reduction of One Loop Feynman Diagrams to Scalar Integrals. 2.” In: *Comput. Phys. Commun.* 56 (1990), pp. 337–350. DOI: 10.1016/0010-4655(90)90019-w.
- [164] Dominik Bendle et al. “Integration-by-parts reductions of Feynman integrals using Singular and GPI-Space”. In: *JHEP* 02 (2020), p. 079. DOI: 10.1007/JHEP02(2020)079. arXiv: 1908.04301 [hep-th].
- [165] S. Laporta. “High-precision calculation of multiloop Feynman integrals by difference equations”. In: *Int. J. Mod. Phys. A* 15 (2000), pp. 5087–5159. DOI: 10.1142/S0217751X00002159. arXiv: hep-ph/0102033.
- [166] G. J. van Oldenborgh and J. A. M. Vermaseren. “New Algorithms for One Loop Integrals”. In: *Z. Phys. C* 46 (1990), pp. 425–438. DOI: 10.1007/BF01621031.
- [167] Ansgar Denner, Stefan Dittmaier, and Lars Hofer. “Collier: a fortran-based Complex One-Loop Library in Extended Regularizations”. In: *Comput. Phys. Commun.* 212 (2017), pp. 220–238. DOI: 10.1016/j.cpc.2016.10.013. arXiv: 1604.06792 [hep-ph].
- [168] A. van Hameren. “OneLoop: For the evaluation of one-loop scalar functions”. In: *Comput. Phys. Commun.* 182 (2011), pp. 2427–2438. DOI: 10.1016/j.cpc.2011.06.011. arXiv: 1007.4716 [hep-ph].
- [169] Giovanni Ossola, Costas G. Papadopoulos, and Roberto Pittau. “CutTools: A Program implementing the OPP reduction method to compute one-loop amplitudes”. In: *JHEP* 03 (2008), p. 042. DOI: 10.1088/1126-6708/2008/03/042. arXiv: 0711.3596 [hep-ph].

- [170] Stefano Carrazza, R. Keith Ellis, and Giulia Zanderighi. “QCDLoop: a comprehensive framework for one-loop scalar integrals”. In: *Comput. Phys. Commun.* 209 (2016), pp. 134–143. DOI: 10.1016/j.cpc.2016.07.033. arXiv: 1605.03181 [hep-ph].
- [171] Valentin Hirschi et al. “Automation of one-loop QCD corrections”. In: *JHEP* 05 (2011), p. 044. DOI: 10.1007/JHEP05(2011)044. arXiv: 1103.0621 [hep-ph].
- [172] T. Binoth et al. “Golem95: A Numerical program to calculate one-loop tensor integrals with up to six external legs”. In: *Comput. Phys. Commun.* 180 (2009), pp. 2317–2330. DOI: 10.1016/j.cpc.2009.06.024. arXiv: 0810.0992 [hep-ph].
- [173] Tiziano Peraro. “Ninja: Automated Integrand Reduction via Laurent Expansion for One-Loop Amplitudes”. In: *Comput. Phys. Commun.* 185 (2014), pp. 2771–2797. DOI: 10.1016/j.cpc.2014.06.017. arXiv: 1403.1229 [hep-ph].
- [174] P. Mastrolia et al. “Scattering AMplitudes from Unitarity-based Reduction Algorithm at the Integrand-level”. In: *JHEP* 08 (2010), p. 080. DOI: 10.1007/JHEP08(2010)080. arXiv: 1006.0710 [hep-ph].
- [175] S. Heinemeyer, H. Rzehak, and C. Schappacher. “Proposals for Bottom Quark/Squark Renormalization in the Complex MSSM”. In: *Phys. Rev. D* 82 (2010), p. 075010. DOI: 10.1103/PhysRevD.82.075010. arXiv: 1007.0689 [hep-ph].
- [176] Alexander Puck Neuwirth. “Resummation predictions for associated production of squarks and electroweakinos at the LHC”. Master’s Thesis. Universität Münster, 2021. URL: https://www.uni-muenster.de/imperia/md/content/physik_tp/theses/klasen/neuwirth_msc.pdf.
- [177] S. Frixione, Z. Kunszt, and A. Signer. “Three jet cross-sections to next-to-leading order”. In: *Nucl. Phys. B* 467 (1996), pp. 399–442. DOI: 10.1016/0550-3213(96)00110-1. arXiv: hep-ph/9512328.
- [178] S. Frixione. “A General approach to jet cross-sections in QCD”. In: *Nucl. Phys. B* 507 (1997), pp. 295–314. DOI: 10.1016/S0550-3213(97)00574-9. arXiv: hep-ph/9706545.
- [179] Rikkert Frederix et al. “Automation of next-to-leading order computations in QCD: The FKS subtraction”. In: *JHEP* 10 (2009), p. 003. DOI: 10.1088/1126-6708/2009/10/003. arXiv: 0908.4272 [hep-ph].
- [180] S. Catani and M. H. Seymour. “A General algorithm for calculating jet cross-sections in NLO QCD”. In: *Nucl. Phys. B* 485 (1997). [Erratum: *Nucl.Phys.B* 510, 503–504 (1998)], pp. 291–419. DOI: 10.1016/S0550-3213(96)00589-5. arXiv: hep-ph/9605323.
- [181] S. Catani and M. H. Seymour. “The Dipole formalism for the calculation of QCD jet cross-sections at next-to-leading order”. In: *Phys. Lett. B* 378 (1996), pp. 287–301. DOI: 10.1016/0370-2693(96)00425-X. arXiv: hep-ph/9602277.
- [182] Lewis J. Bergmann. “NEXT-TO-LEADING LOG QCD CALCULATION OF SYMMETRIC DIHADRON PRODUCTION”. Other thesis. 1989.
- [183] F. Gutbrod, G. Kramer, and G. Schierholz. “Higher Order QCD Corrections to the Three Jet Cross-Sections: Bare Versus Dressed Jets”. In: *Z. Phys. C* 21 (1984), p. 235. DOI: 10.1007/BF01577037.
- [184] H. Baer, J. Ohnemus, and J. F. Owens. “A Next-To-Leading Logarithm Calculation of Jet Photoproduction”. In: *Phys. Rev. D* 40 (1989), p. 2844. DOI: 10.1103/PhysRevD.40.2844.
- [185] B. W. Harris and J. F. Owens. “The Two cutoff phase space slicing method”. In: *Phys. Rev. D* 65 (2002), p. 094032. DOI: 10.1103/PhysRevD.65.094032. arXiv: hep-ph/0102128.

- [186] Qing-Hong Cao. “Demonstration of One Cutoff Phase Space Slicing Method: Next-to-Leading Order QCD Corrections to the tW Associated Production in Hadron Collision”. In: (Jan. 2008). arXiv: 0801.1539 [hep-ph].
- [187] Adam Kardos, Paolo Nason, and Carlo Oleari. “Three-jet production in POWHEG”. In: *JHEP* 04 (2014), p. 043. DOI: 10.1007/JHEP04(2014)043. arXiv: 1402.4001 [hep-ph].
- [188] Stefano Frixione, Paolo Nason, and Carlo Oleari. “Matching NLO QCD computations with Parton Shower simulations: the POWHEG method”. In: *JHEP* 11 (2007), p. 070. DOI: 10.1088/1126-6708/2007/11/070. arXiv: 0709.2092 [hep-ph].
- [189] Simone Alioli et al. “A general framework for implementing NLO calculations in shower Monte Carlo programs: the POWHEG BOX”. In: *JHEP* 06 (2010), p. 043. DOI: 10.1007/JHEP06(2010)043. arXiv: 1002.2581 [hep-ph].
- [190] Stefan Dittmaier. “A General approach to photon radiation off fermions”. In: *Nucl. Phys. B* 565 (2000), pp. 69–122. DOI: 10.1016/S0550-3213(99)00563-5. arXiv: hep-ph/9904440.
- [191] Stefano Catani et al. “The Dipole formalism for next-to-leading order QCD calculations with massive partons”. In: *Nucl. Phys. B* 627 (2002), pp. 189–265. DOI: 10.1016/S0550-3213(02)00098-6. arXiv: hep-ph/0201036.
- [192] Julia Harz et al. “Dipole formalism for massive initial-state particles and its application to dark matter calculations”. In: *Phys. Rev. D* 107.5 (2023), p. 056020. DOI: 10.1103/PhysRevD.107.056020. arXiv: 2210.03409 [hep-ph].
- [193] Stefano Catani, Stefan Dittmaier, and Zoltan Trocsanyi. “One loop singular behavior of QCD and SUSY QCD amplitudes with massive partons”. In: *Phys. Lett. B* 500 (2001), pp. 149–160. DOI: 10.1016/S0370-2693(01)00065-X. arXiv: hep-ph/0011222.
- [194] Wolfgang Hollik, Jonas M. Lindert, and Davide Pagani. “NLO corrections to squark-squark production and decay at the LHC”. In: *JHEP* 03 (2013), p. 139. DOI: 10.1007/JHEP03(2013)139. arXiv: 1207.1071 [hep-ph].
- [195] Ryan Gavin et al. “Matching Squark Pair Production at NLO with Parton Showers”. In: *JHEP* 10 (2013), p. 187. DOI: 10.1007/JHEP10(2013)187. arXiv: 1305.4061 [hep-ph].
- [196] Robin G. Stuart. “Gauge invariance, analyticity and physical observables at the Z_0 resonance”. In: *Phys. Lett. B* 262 (1991), pp. 113–119. DOI: 10.1016/0370-2693(91)90653-8.
- [197] M. Beneke et al. “Effective theory approach to unstable particle production”. In: *Phys. Rev. Lett.* 93 (2004), p. 011602. DOI: 10.1103/PhysRevLett.93.011602. arXiv: hep-ph/0312331.
- [198] R. Keith Ellis, W. T. Giele, and Z. Kunszt. “A Numerical Unitarity Formalism for Evaluating One-Loop Amplitudes”. In: *JHEP* 03 (2008), p. 003. DOI: 10.1088/1126-6708/2008/03/003. arXiv: 0708.2398 [hep-ph].
- [199] G. Peter Lepage. “A New Algorithm for Adaptive Multidimensional Integration”. In: *J. Comput. Phys.* 27 (1978), p. 192. DOI: 10.1016/0021-9991(78)90004-9.
- [200] G. Peter Lepage. “VEGAS: AN ADAPTIVE MULTIDIMENSIONAL INTEGRATION PROGRAM”. In: (Mar. 1980).
- [201] T. Hahn. “CUBA: A Library for multidimensional numerical integration”. In: *Comput. Phys. Commun.* 168 (2005), pp. 78–95. DOI: 10.1016/j.cpc.2005.01.010. arXiv: hep-ph/0404043.
- [202] T. Hahn. “The CUBA library”. In: *Nucl. Instrum. Meth. A* 559 (2006). Ed. by J. Blumlein et al., pp. 273–277. DOI: 10.1016/j.nima.2005.11.150. arXiv: hep-ph/0509016.

- [203] S. Jadach. “Foam: A General purpose cellular Monte Carlo event generator”. In: *Comput. Phys. Commun.* 152 (2003), pp. 55–100. DOI: 10.1016/S0010-4655(02)00755-5. arXiv: physics/0203033.
- [204] Christina Gao, Joshua Isaacson, and Claudius Krause. “i-flow: High-dimensional Integration and Sampling with Normalizing Flows”. In: *Mach. Learn. Sci. Tech.* 1.4 (2020), p. 045023. DOI: 10.1088/2632-2153/abab62. arXiv: 2001.05486 [physics.comp-ph].
- [205] Setsuya Kawabata. “A New version of the multidimensional integration and event generation package BASES/SPRING”. In: *Comput. Phys. Commun.* 88 (1995), pp. 309–326. DOI: 10.1016/0010-4655(95)00028-E.
- [206] Paolo Nason. “MINT: A Computer program for adaptive Monte Carlo integration and generation of unweighted distributions”. In: (Sept. 2007). arXiv: 0709.2085 [hep-ph].
- [207] Barry A. Cipra. “The Best of the 20th Century: Editors Name Top 10 Algorithms”. In: *SIAM News* 33 (2000), pp. 1–2.
- [208] Andreas Papaefstathiou. “How-to: write a parton-level Monte Carlo particle physics event generator”. In: *Eur. Phys. J. Plus* 135.6 (2020), p. 497. DOI: 10.1140/epjp/s13360-020-00499-1. arXiv: 1412.4677 [hep-ph].
- [209] Andreas Papaefstathiou. “Phenomenological aspects of new physics at high energy hadron colliders”. Other thesis. Aug. 2011. DOI: 10.17863/CAM.16577. arXiv: 1108.5599 [hep-ph].
- [210] F. James. “Monte-Carlo phase space”. In: (May 1968).
- [211] Wikimedia Commons. *Monte Carlo Integration Circle*. 2014. URL: <https://en.m.wikipedia.org/wiki/File:MonteCarloIntegrationCircle.svg>.
- [212] Wikimedia Commons. *Relative error of a Monte Carlo integration to calculate pi*. 2012. URL: https://en.m.wikipedia.org/wiki/File:Relative_error_of_a_Monte_Carlo_integration_to_calculate_pi.svg.
- [213] Manuel Aguilar Rios et al. “True Random Numbers from Pairs of SRAM Devices”. In: *Intelligent Computing*. Ed. by Kohei Arai. Cham: Springer Nature Switzerland, 2024, pp. 630–650. ISBN: 978-3-031-62269-4.
- [214] Fatemeh Tehranipoor, Wei Yan, and John A. Chandy. “Robust hardware true random number generators using DRAM remanence effects”. In: *2016 IEEE International Symposium on Hardware Oriented Security and Trust (HOST)*. 2016, pp. 79–84. DOI: 10.1109/HST.2016.7495561.
- [215] Seongmo Park et al. “Efficient hardware implementation and analysis of true random-number generator based on beta source”. In: *ETRI Journal* 42.4 (2020), pp. 518–526. DOI: <https://doi.org/10.4218/etrij.2020-0083>. eprint: <https://onlinelibrary.wiley.com/doi/pdf/10.4218/etrij.2020-0083>. URL: <https://onlinelibrary.wiley.com/doi/abs/10.4218/etrij.2020-0083>.
- [216] Hannah Belle Neuwirth. “Durch kosmische Strahlung zur Zufallszahl: Langzeitmessung von Myonenzerfällen als Basis für einen nichtdeterministischen Zufallszahlengenerator”. de. In: *Junge Wissenschaft*. Paper 11/2021 (Feb. 3, 2022). Ed. by ISNI: 0000 0001 2186 1887 Physikalisch-Technische Bundesanstalt (PTB), p. 16. DOI: 10.7795/320.202111. URL: <https://doi.org/10.7795/320.202111>.
- [217] Edmund Hlawka. “Funktionen von beschränkter Variatiou in der Theorie der Gleichverteilung”. In: *Annali di Matematica Pura ed Applicata* 54.1 (Dec. 1961), pp. 325–333. ISSN: 1618-1891. DOI: 10.1007/bf02415361. URL: <http://dx.doi.org/10.1007/BF02415361>.

- [218] I.M Sobol'. "On the distribution of points in a cube and the approximate evaluation of integrals". In: *USSR Computational Mathematics and Mathematical Physics* 7.4 (1967), pp. 86–112. ISSN: 0041-5553. DOI: [https://doi.org/10.1016/0041-5553\(67\)90144-9](https://doi.org/10.1016/0041-5553(67)90144-9). URL: <https://www.sciencedirect.com/science/article/pii/0041555367901449>.
- [219] Viveca Lindahl. *Detection Prospects of Doubly Charged Higgs Bosons from the Higgs Triplet Model at the LHC*. 2011.
- [220] Stefano Frixione and Bryan R. Webber. "Matching NLO QCD computations and parton shower simulations". In: *JHEP* 06 (2002), p. 029. DOI: 10.1088/1126-6708/2002/06/029. arXiv: [hep-ph/0204244](https://arxiv.org/abs/hep-ph/0204244).
- [221] R. Frederix et al. "On the reduction of negative weights in MC@NLO-type matching procedures". In: *JHEP* 07 (2020), p. 238. DOI: 10.1007/JHEP07(2020)238. arXiv: 2002.12716 [[hep-ph](https://arxiv.org/abs/hep-ph)].
- [222] Rikkert Frederix and Paolo Torrielli. "A new way of reducing negative weights in MC@NLO". In: *Eur. Phys. J. C* 83.11 (2023), p. 1051. DOI: 10.1140/epjc/s10052-023-12243-x. arXiv: 2310.04160 [[hep-ph](https://arxiv.org/abs/hep-ph)].
- [223] Paolo Nason and Giovanni Ridolfi. "A Positive-weight next-to-leading-order Monte Carlo for Z pair hadroproduction". In: *JHEP* 08 (2006), p. 077. DOI: 10.1088/1126-6708/2006/08/077. arXiv: [hep-ph/0606275](https://arxiv.org/abs/hep-ph/0606275).
- [224] George F. Sterman and Steven Weinberg. "Jets from Quantum Chromodynamics". In: *Phys. Rev. Lett.* 39 (1977), p. 1436. DOI: 10.1103/PhysRevLett.39.1436.
- [225] G. Arnison et al. "Hadronic Jet Production at the CERN Proton - anti-Proton Collider". In: *Phys. Lett. B* 132 (1983), p. 214. DOI: 10.1016/0370-2693(83)90254-X.
- [226] Gerald C. Blazey et al. "Run II jet physics". In: *Physics at Run II: QCD and Weak Boson Physics Workshop: Final General Meeting*. May 2000, pp. 47–77. arXiv: [hep-ex/0005012](https://arxiv.org/abs/hep-ex/0005012).
- [227] John E. Huth et al. "Toward a standardization of jet definitions". In: *1990 DPF Summer Study on High-energy Physics: Research Directions for the Decade (Snowmass 90)*. Dec. 1990, pp. 0134–136.
- [228] Gavin P. Salam. "A Practical seedless infrared safe cone algorithm". In: *42nd Rencontres de Moriond on QCD and High Energy Hadronic Interactions*. May 2007, pp. 139–142. arXiv: 0705.2696 [[hep-ph](https://arxiv.org/abs/hep-ph)].
- [229] R. Brandelik et al. "Evidence for Planar Events in e+ e- Annihilation at High-Energies". In: *Phys. Lett. B* 86 (1979), pp. 243–249. DOI: 10.1016/0370-2693(79)90830-X.
- [230] P. Duinker. "Review of Electron - Positron Physics at PETRA". In: *Rev. Mod. Phys.* 54 (1982), p. 325. DOI: 10.1103/RevModPhys.54.325.
- [231] W. Bartel et al. "Experimental Studies on Multi-Jet Production in e+ e- Annihilation at PETRA Energies". In: *Z. Phys. C* 33 (1986). Ed. by J. Tran Thanh Van, p. 23. DOI: 10.1007/BF01410449.
- [232] S. Bethke and A. Wagner. "The JADE Experiment at the PETRA e+e- collider – history, achievements and revival". In: *Eur. Phys. J. H* 47 (2022), p. 16. DOI: 10.1140/epjh/s13129-022-00047-8. arXiv: 2208.11076 [[hep-ex](https://arxiv.org/abs/hep-ex)].
- [233] Yuri L. Dokshitzer et al. "Better jet clustering algorithms". In: *JHEP* 08 (1997), p. 001. DOI: 10.1088/1126-6708/1997/08/001. arXiv: [hep-ph/9707323](https://arxiv.org/abs/hep-ph/9707323).
- [234] S. Catani et al. "New clustering algorithm for multi - jet cross-sections in e+ e- annihilation". In: *Phys. Lett. B* 269 (1991), pp. 432–438. DOI: 10.1016/0370-2693(91)90196-W.
- [235] Stephen D. Ellis and Davison E. Soper. "Successive combination jet algorithm for hadron collisions". In: *Phys. Rev. D* 48 (1993), pp. 3160–3166. DOI: 10.1103/PhysRevD.48.3160. arXiv: [hep-ph/9305266](https://arxiv.org/abs/hep-ph/9305266).

- [236] M. Wobisch and T. Wengler. “Hadronization corrections to jet cross-sections in deep inelastic scattering”. In: *Workshop on Monte Carlo Generators for HERA Physics (Plenary Starting Meeting)*. Apr. 1998, pp. 270–279. arXiv: [hep-ph/9907280](#).
- [237] Matteo Cacciari, Gavin P. Salam, and Gregory Soyez. “The anti- k_t jet clustering algorithm”. In: *JHEP* 04 (2008), p. 063. DOI: [10.1088/1126-6708/2008/04/063](#). arXiv: [0802.1189 \[hep-ph\]](#).
- [238] Matteo Cacciari, Gavin P. Salam, and Gregory Soyez. “FastJet User Manual”. In: *Eur. Phys. J. C* 72 (2012), p. 1896. DOI: [10.1140/epjc/s10052-012-1896-2](#). arXiv: [1111.6097 \[hep-ph\]](#).
- [239] Nils Lavesson and Leif Lonnblad. “Merging parton showers and matrix elements: Back to basics”. In: *JHEP* 04 (2008), p. 085. DOI: [10.1088/1126-6708/2008/04/085](#). arXiv: [0712.2966 \[hep-ph\]](#).
- [240] S. Catani et al. “QCD matrix elements + parton showers”. In: *JHEP* 11 (2001), p. 063. DOI: [10.1088/1126-6708/2001/11/063](#). arXiv: [hep-ph/0109231](#).
- [241] Leif Lonnblad. “Correcting the color dipole cascade model with fixed order matrix elements”. In: *JHEP* 05 (2002), p. 046. DOI: [10.1088/1126-6708/2002/05/046](#). arXiv: [hep-ph/0112284](#).
- [242] Leif Lonnblad and Stefan Prestel. “Matching Tree-Level Matrix Elements with Interleaved Showers”. In: *JHEP* 03 (2012), p. 019. DOI: [10.1007/JHEP03\(2012\)019](#). arXiv: [1109.4829 \[hep-ph\]](#).
- [243] Jung Chang et al. “Higgs-boson-pair production $H(\rightarrow bb^-)H(\rightarrow \gamma\gamma)$ from gluon fusion at the HL-LHC and HL-100 TeV hadron collider”. In: *Phys. Rev. D* 100.9 (2019), p. 096001. DOI: [10.1103/PhysRevD.100.096001](#). arXiv: [1804.07130 \[hep-ph\]](#).
- [244] John Campbell. “Overview of Monte Carlo Generators”. URL: <https://indico.fnal.gov/event/9650/attachments/74470/89343/MCGenerators.pdf>.
- [245] Leif Gellersen. “MC Tutorial Background: Parton Showers, Matching, Merging”. CTEQ Summer School 2022. 2022. URL: <https://indico.cern.ch/event/1131319/contributions/4895915/attachments/2477520/4252738/gellersenPSMM.pdf>.
- [246] Stefano Frixione, Paolo Nason, and Bryan R. Webber. “Matching NLO QCD and parton showers in heavy flavor production”. In: *JHEP* 08 (2003), p. 007. DOI: [10.1088/1126-6708/2003/08/007](#). arXiv: [hep-ph/0305252](#).
- [247] Klaus Reygers. *Direct photon measurements*. <https://indico.cern.ch/event/1174824/contributions/5066277/>. Accessed: 2023-03-17. 2022.
- [248] Meike Charlotte Danisch. “Measurement of neutral mesons and direct photons in Pb-Pb collisions at $\sqrt{s_{NN}} = 5.02$ TeV with ALICE at the LHC”. Presented 12 Jan 2022. Heidelberg U., 2021. URL: <https://cds.cern.ch/record/2800150>.
- [249] Florian König. “Prompt Photon Production Predictions at NLO and in POWHEG”. dissertation. Westfälischen Wilhelms-Universität Münster, 2016. URL: https://www.uni-muenster.de/imperia/md/content/physik_tp/theses/klasen/koenig_phd.pdf.
- [250] Itzhak Tserruya. “Electromagnetic Probes”. In: *Landolt-Bornstein* 23 (2010). Ed. by R. Stock, p. 176. DOI: [10.1007/978-3-642-01539-7_7](#). arXiv: [0903.0415 \[nucl-ex\]](#).
- [251] Joseph I. Kapusta, P. Lichard, and D. Seibert. “High-energy photons from quark - gluon plasma versus hot hadronic gas”. In: *Phys. Rev. D* 44 (1991). [Erratum: *Phys.Rev.D* 47, 4171 (1993)], pp. 2774–2788. DOI: [10.1103/PhysRevD.47.4171](#).
- [252] R. Baier et al. “Production rate of hard thermal photons and screening of quark mass singularity”. In: *Z. Phys. C* 53 (1992), pp. 433–438. DOI: [10.1007/BF01625902](#).

- [253] Peter Brockway Arnold, Guy D. Moore, and Laurence G. Yaffe. “Photon emission from quark gluon plasma: Complete leading order results”. In: *JHEP* 12 (2001), p. 009. DOI: 10.1088/1126-6708/2001/12/009. arXiv: hep-ph/0111107.
- [254] Simon Turbide, Ralf Rapp, and Charles Gale. “Hadronic production of thermal photons”. In: *Phys. Rev. C* 69 (2004), p. 014903. DOI: 10.1103/PhysRevC.69.014903. arXiv: hep-ph/0308085.
- [255] W. Liu and R. Rapp. “Low-energy thermal photons from meson-meson bremsstrahlung”. In: *Nucl. Phys. A* 796 (2007), pp. 101–121. DOI: 10.1016/j.nuclphysa.2007.08.014. arXiv: nucl-th/0604031.
- [256] O. Linnyk et al. “Hadronic and partonic sources of direct photons in relativistic heavy-ion collisions”. In: *Phys. Rev. C* 92.5 (2015), p. 054914. DOI: 10.1103/PhysRevC.92.054914. arXiv: 1504.05699 [nucl-th].
- [257] Nathan P. M. Holt and Ralf Rapp. “Baryonic Sources of Thermal Photons”. In: *Eur. Phys. J. A* 56.11 (2020), p. 292. DOI: 10.1140/epja/s10050-020-00301-x. arXiv: 2008.00116 [hep-ph].
- [258] T. Lappi and L. McLerran. “Some features of the glasma”. In: *Nucl. Phys. A* 772 (2006), pp. 200–212. DOI: 10.1016/j.nuclphysa.2006.04.001. arXiv: hep-ph/0602189.
- [259] Scott McDonald, Sangyong Jeon, and Charles Gale. “Exploring Longitudinal Observables with 3+1D IP-Glasma”. In: *Nucl. Phys. A* 1005 (2021). Ed. by Feng Liu et al., p. 121771. DOI: 10.1016/j.nuclphysa.2020.121771. arXiv: 2001.08636 [nucl-th].
- [260] Jurgen Berges et al. “Parametric estimate of the relative photon yields from the glasma and the quark-gluon plasma in heavy-ion collisions”. In: *Phys. Rev. C* 95.5 (2017), p. 054904. DOI: 10.1103/PhysRevC.95.054904. arXiv: 1701.05064 [nucl-th].
- [261] K. Koller, T. F. Walsh, and P. M. Zerwas. “Testing QCD: Direct Photons in e^+e^- Collisions”. In: *Z. Phys. C* 2 (1979), p. 197. DOI: 10.1007/BF01474661.
- [262] E. Laermann et al. “Direct Photons in e^+e^- Annihilation”. In: *Nucl. Phys. B* 207 (1982), pp. 205–232. DOI: 10.1016/0550-3213(82)90162-6.
- [263] Stefano Frixione. “Isolated photons in perturbative QCD”. In: *Phys. Lett. B* 429 (1998), pp. 369–374. DOI: 10.1016/S0370-2693(98)00454-7. arXiv: hep-ph/9801442.
- [264] R. Rapp and J. Wambach. “Chiral symmetry restoration and dileptons in relativistic heavy ion collisions”. In: *Adv. Nucl. Phys.* 25 (2000), p. 1. DOI: 10.1007/0-306-47101-9_1. arXiv: hep-ph/9909229.
- [265] Maurice Coquet et al. “Intermediate mass dileptons as pre-equilibrium probes in heavy ion collisions”. In: *Phys. Lett. B* 821 (2021), p. 136626. DOI: 10.1016/j.physletb.2021.136626. arXiv: 2104.07622 [nucl-th].
- [266] A. Adare et al. “Dilepton mass spectra in p+p collisions at $s^{*(1/2)} = 200$ -GeV and the contribution from open charm”. In: *Phys. Lett. B* 670 (2009), pp. 313–320. DOI: 10.1016/j.physletb.2008.10.064. arXiv: 0802.0050 [hep-ex].
- [267] A. Adare et al. “Detailed measurement of the e^+e^- pair continuum in $p+p$ and Au+Au collisions at $\sqrt{s_{NN}} = 200$ GeV and implications for direct photon production”. In: *Phys. Rev. C* 81 (2010), p. 034911. DOI: 10.1103/PhysRevC.81.034911. arXiv: 0912.0244 [nucl-ex].
- [268] L. Adamczyk et al. “Di-electron spectrum at mid-rapidity in $p+p$ collisions at $\sqrt{s} = 200$ GeV”. In: *Phys. Rev. C* 86 (2012), p. 024906. DOI: 10.1103/PhysRevC.86.024906. arXiv: 1204.1890 [nucl-ex].
- [269] Shreyasi Acharya et al. “Dielectron production in proton-proton collisions at $\sqrt{s} = 7$ TeV”. In: *JHEP* 09 (2018), p. 064. DOI: 10.1007/JHEP09(2018)064. arXiv: 1805.04391 [hep-ex].

- [270] Shreyasi Acharya et al. “Dielectron and heavy-quark production in inelastic and high-multiplicity proton–proton collisions at $\sqrt{s_{NN}} = 13\text{TeV}$ ”. In: *Phys. Lett. B* 788 (2019), pp. 505–518. DOI: 10.1016/j.physletb.2018.11.009. arXiv: 1805.04407 [hep-ex].
- [271] G. Agakichiev et al. “Enhanced production of low mass electron pairs in 200-GeV/u S - Au collisions at the CERN SPS”. In: *Phys. Rev. Lett.* 75 (1995), pp. 1272–1275. DOI: 10.1103/PhysRevLett.75.1272.
- [272] G. Agakichiev et al. “Low mass e+ e- pair production in 158/A-GeV Pb - Au collisions at the CERN SPS, its dependence on multiplicity and transverse momentum”. In: *Phys. Lett. B* 422 (1998), pp. 405–412. DOI: 10.1016/S0370-2693(98)00083-5. arXiv: nucl-ex/9712008.
- [273] D. Adamova et al. “Modification of the rho-meson detected by low-mass electron-positron pairs in central Pb-Au collisions at 158-A-GeV/c”. In: *Phys. Lett. B* 666 (2008), pp. 425–429. DOI: 10.1016/j.physletb.2008.07.104. arXiv: nucl-ex/0611022.
- [274] D. Adamova et al. “Enhanced production of low mass electron pairs in 40-AGeV Pb - Au collisions at the CERN SPS”. In: *Phys. Rev. Lett.* 91 (2003), p. 042301. DOI: 10.1103/PhysRevLett.91.042301. arXiv: nucl-ex/0209024.
- [275] R. Arnaldi et al. “First measurement of the rho spectral function in high-energy nuclear collisions”. In: *Phys. Rev. Lett.* 96 (2006), p. 162302. DOI: 10.1103/PhysRevLett.96.162302. arXiv: nucl-ex/0605007.
- [276] R. Arnaldi et al. “NA60 results on thermal dimuons”. In: *Eur. Phys. J. C* 61 (2009), pp. 711–720. DOI: 10.1140/epjc/s10052-009-0878-5. arXiv: 0812.3053 [nucl-ex].
- [277] A. Adare et al. “Enhanced production of direct photons in Au+Au collisions at $\sqrt{s_{NN}} = 200\text{ GeV}$ and implications for the initial temperature”. In: *Phys. Rev. Lett.* 104 (2010), p. 132301. DOI: 10.1103/PhysRevLett.104.132301. arXiv: 0804.4168 [nucl-ex].
- [278] L. Adamczyk et al. “Dielectron Mass Spectra from Au+Au Collisions at $\sqrt{s_{NN}} = 200\text{ GeV}$ ”. In: *Phys. Rev. Lett.* 113.2 (2014). [Addendum: *Phys.Rev.Lett.* 113, 049903 (2014)], p. 022301. DOI: 10.1103/PhysRevLett.113.022301. arXiv: 1312.7397 [hep-ex].
- [279] L. Adamczyk et al. “Measurements of Dielectron Production in Au+Au Collisions at $\sqrt{s_{NN}} = 200\text{ GeV}$ from the STAR Experiment”. In: *Phys. Rev. C* 92.2 (2015), p. 024912. DOI: 10.1103/PhysRevC.92.024912. arXiv: 1504.01317 [hep-ex].
- [280] A. Adare et al. “Centrality dependence of low-momentum direct-photon production in Au+Au collisions at $\sqrt{s_{NN}} = 200\text{ GeV}$ ”. In: *Phys. Rev. C* 91.6 (2015), p. 064904. DOI: 10.1103/PhysRevC.91.064904. arXiv: 1405.3940 [nucl-ex].
- [281] Jaroslav Adam et al. “Direct photon production in Pb-Pb collisions at $\sqrt{s_{NN}} = 2.76\text{ TeV}$ ”. In: *Phys. Lett. B* 754 (2016), pp. 235–248. DOI: 10.1016/j.physletb.2016.01.020. arXiv: 1509.07324 [nucl-ex].
- [282] R. Arnaldi et al. “Evidence for the production of thermal-like muon pairs with masses above 1-GeV/c**2 in 158-A-GeV Indium-Indium Collisions”. In: *Eur. Phys. J. C* 59 (2009), pp. 607–623. DOI: 10.1140/epjc/s10052-008-0857-2. arXiv: 0810.3204 [nucl-ex].
- [283] R. Arnaldi et al. “Evidence for radial flow of thermal dileptons in high-energy nuclear collisions”. In: *Phys. Rev. Lett.* 100 (2008), p. 022302. DOI: 10.1103/PhysRevLett.100.022302. arXiv: 0711.1816 [nucl-ex].
- [284] Shreyasi Acharya et al. “Measurement of dielectron production in central Pb-Pb collisions at $\sqrt{s_{NN}} = 2.76\text{ TeV}$ ”. In: *Phys. Rev. C* 99.2 (2019), p. 024002. DOI: 10.1103/PhysRevC.99.024002. arXiv: 1807.00923 [nucl-ex].

- [285] Norman M. Kroll and Walter Wada. “Internal pair production associated with the emission of high-energy gamma rays”. In: *Phys. Rev.* 98 (1955), pp. 1355–1359. DOI: 10.1103/PhysRev.98.1355.
- [286] M. Klasen et al. “How robust is a thermal photon interpretation of the ALICE low- p_T data?” In: *JHEP* 10 (2013), p. 119. DOI: 10.1007/JHEP10(2013)119. arXiv: 1307.7034 [hep-ph].
- [287] V. Greco, C. M. Ko, and R. Rapp. “Quark coalescence for charmed mesons in ultrarelativistic heavy ion collisions”. In: *Phys. Lett. B* 595 (2004), pp. 202–208. DOI: 10.1016/j.physletb.2004.06.064. arXiv: nucl-th/0312100.
- [288] A. Andronic et al. “Statistical hadronization of charm in heavy ion collisions at SPS, RHIC and LHC”. In: *Phys. Lett. B* 571 (2003), pp. 36–44. DOI: 10.1016/j.physletb.2003.07.066. arXiv: nucl-th/0303036.
- [289] R. Baier et al. “Radiative energy loss and p(T) broadening of high-energy partons in nuclei”. In: *Nucl. Phys. B* 484 (1997), pp. 265–282. DOI: 10.1016/S0550-3213(96)00581-0. arXiv: hep-ph/9608322.
- [290] Eric Braaten and Markus H. Thoma. “Energy loss of a heavy quark in the quark - gluon plasma”. In: *Phys. Rev. D* 44.9 (1991), R2625. DOI: 10.1103/PhysRevD.44.R2625.
- [291] Roel Aaij et al. “Measurements of prompt charm production cross-sections in pp collisions at $\sqrt{s} = 13$ TeV”. In: *JHEP* 03 (2016). [Erratum: *JHEP* 09, 013 (2016), Erratum: *JHEP* 05, 074 (2017)], p. 159. DOI: 10.1007/JHEP03(2016)159. arXiv: 1510.01707 [hep-ex].
- [292] Armen Tumasyan et al. “Measurement of prompt open-charm production cross sections in proton-proton collisions at $\sqrt{s} = 13$ TeV”. In: *JHEP* 11 (2021), p. 225. DOI: 10.1007/JHEP11(2021)225. arXiv: 2107.01476 [hep-ex].
- [293] Shreyasi Acharya et al. “Measurement of beauty and charm production in pp collisions at $\sqrt{s} = 5.02$ TeV via non-prompt and prompt D mesons”. In: *JHEP* 05 (2021), p. 220. DOI: 10.1007/JHEP05(2021)220. arXiv: 2102.13601 [nucl-ex].
- [294] Daiki Sekihata for the ALICE Collaboration. “Electromagnetic radiation in pp and Pb-Pb collisions with dielectrons in ALICE”. In: *Quark Matter 2023*. Center for Nuclear Study, the University of Tokyo. 03-09 September 2023, Sept. 2023. URL: https://indico.cern.ch/event/1139644/contributions/5540095/attachments/2707601/4704115/20230905_qm2023_sekihata_v9.pdf.
- [295] Simone Alioli et al. “NLO vector-boson production matched with shower in POWHEG”. In: *JHEP* 07 (2008), p. 060. DOI: 10.1088/1126-6708/2008/07/060. arXiv: 0805.4802 [hep-ph].
- [296] Simone Alioli et al. “Vector boson plus one jet production in POWHEG”. In: *JHEP* 01 (2011), p. 095. DOI: 10.1007/JHEP01(2011)095. arXiv: 1009.5594 [hep-ph].
- [297] Keith Hamilton, Paolo Nason, and Giulia Zanderighi. “MINLO: Multi-Scale Improved NLO”. In: *JHEP* 10 (2012), p. 155. DOI: 10.1007/JHEP10(2012)155. arXiv: 1206.3572 [hep-ph].
- [298] Pier Francesco Monni et al. “MiNNLO_{PS}: a new method to match NNLO QCD to parton showers”. In: *JHEP* 05 (2020). [Erratum: *JHEP* 02, 031 (2022)], p. 143. DOI: 10.1007/JHEP05(2020)143. arXiv: 1908.06987 [hep-ph].
- [299] Pier Francesco Monni, Emanuele Re, and Marius Wiesemann. “MiNNLO_{PS}: optimizing $2 \rightarrow 1$ hadronic processes”. In: *Eur. Phys. J. C* 80.11 (2020), p. 1075. DOI: 10.1140/epjc/s10052-020-08658-5. arXiv: 2006.04133 [hep-ph].

- [300] Tomas Jezo, Michael Klasen, and Florian König. “Prompt photon production and photon-hadron jet correlations with POWHEG”. In: *JHEP* 11 (2016), p. 033. DOI: 10.1007/JHEP11(2016)033. arXiv: 1610.02275 [hep-ph].
- [301] M. Klasen, G. Kramer, and B. Potter. “Inclusive jet production with virtual photons in next-to-leading order QCD”. In: *Eur. Phys. J. C* 1 (1998), pp. 261–270. DOI: 10.1007/BF01245816. arXiv: hep-ph/9703302.
- [302] Payal Mohanty, Sabyasachi Ghosh, and Sukanya Mitra. “Electromagnetic Radiations from Heavy Ion Collision”. In: *Adv. High Energy Phys.* 2013 (2013), p. 176578. DOI: 10.1155/2013/176578.
- [303] Roberto Bonciani et al. “Electroweak top-quark pair production at the LHC with Z' bosons to NLO QCD in POWHEG”. In: *JHEP* 02 (2016), p. 141. DOI: 10.1007/JHEP02(2016)141. arXiv: 1511.08185 [hep-ph].
- [304] Davide Pagani, Ioannis Tsinikos, and Marco Zaro. “The impact of the photon PDF and electroweak corrections on $t\bar{t}$ distributions”. In: *Eur. Phys. J. C* 76.9 (2016), p. 479. DOI: 10.1140/epjc/s10052-016-4318-z. arXiv: 1606.01915 [hep-ph].
- [305] Stefano Frixione, Paolo Nason, and Giovanni Ridolfi. “A Positive-weight next-to-leading-order Monte Carlo for heavy flavour hadroproduction”. In: *JHEP* 09 (2007), p. 126. DOI: 10.1088/1126-6708/2007/09/126. arXiv: 0707.3088 [hep-ph].
- [306] Shreyasi Acharya et al. “Dielectron production in proton-proton and proton-lead collisions at $\sqrt{s_{NN}} = 5.02$ TeV”. In: *Phys. Rev. C* 102.5 (2020), p. 055204. DOI: 10.1103/PhysRevC.102.055204. arXiv: 2005.11995 [nucl-ex].
- [307] Eamonn Maguire, Lukas Heinrich, and Graeme Watt. “HEPData: a repository for high energy physics data”. In: *J. Phys. Conf. Ser.* 898.10 (2017). Ed. by Richard Mount and Craig Tull, p. 102006. DOI: 10.1088/1742-6596/898/10/102006. arXiv: 1704.05473 [hep-ex].
- [308] Shreyasi Acharya et al. “Dielectron production in central Pb–Pb collisions at $\sqrt{s_{NN}} = 5.02$ TeV”. In: (Aug. 2023). arXiv: 2308.16704 [nucl-ex].
- [309] Andy Buckley et al. “Rivet user manual”. In: *Comput. Phys. Commun.* 184 (2013), pp. 2803–2819. DOI: 10.1016/j.cpc.2013.05.021. arXiv: 1003.0694 [hep-ph].
- [310] Christian Bierlich et al. “Robust Independent Validation of Experiment and Theory: Rivet version 3”. In: *SciPost Phys.* 8 (2020), p. 026. DOI: 10.21468/SciPostPhys.8.2.026. arXiv: 1912.05451 [hep-ph].
- [311] Andy Buckley et al. “Consistent, multidimensional differential histogramming and summary statistics with YODA 2”. In: (Dec. 2023). arXiv: 2312.15070 [hep-ph].
- [312] Tomáš Jezo et al. “New NLOPS predictions for $t\bar{t} + b$ -jet production at the LHC”. In: *Eur. Phys. J. C* 78.6 (2018), p. 502. DOI: 10.1140/epjc/s10052-018-5956-0. arXiv: 1802.00426 [hep-ph].
- [313] Silvia Ferrario Ravasio and Carlo Oleari. “NLO + parton-shower generator for W production in the POWHEG BOX RES”. In: *Eur. Phys. J. C* 83.7 (2023), p. 684. DOI: 10.1140/epjc/s10052-023-11853-9. arXiv: 2304.13791 [hep-ph].
- [314] R. L. Workman et al. “Review of Particle Physics”. In: *PTEP* 2022 (2022), p. 083C01. DOI: 10.1093/ptep/ptac097.
- [315] Matt Dobbs and Jorgen Beck Hansen. “The HepMC C++ Monte Carlo event record for High Energy Physics”. In: *Comput. Phys. Commun.* 134 (2001), pp. 41–46. DOI: 10.1016/S0010-4655(00)00189-2.
- [316] Andrii Verbitskyi et al. “HepMC3 Event Record Library for Monte Carlo Event Generators”. In: *J. Phys. Conf. Ser.* 1525.1 (2020), p. 012017. DOI: 10.1088/1742-6596/1525/1/012017.

- [317] Pavel M. Nadolsky et al. “Implications of CTEQ global analysis for collider observables”. In: *Phys. Rev. D* 78 (2008), p. 013004. DOI: 10.1103/PhysRevD.78.013004. arXiv: 0802.0007 [hep-ph].
- [318] R. Averbeck et al. “Reference Heavy Flavour Cross Sections in pp Collisions at $\sqrt{s} = 2.76$ TeV, using a pQCD-Driven \sqrt{s} -Scaling of ALICE Measurements at $\sqrt{s} = 7$ TeV”. In: (July 2011). arXiv: 1107.3243 [hep-ph].
- [319] F. James and M. Roos. “Minuit - a system for function minimization and analysis of the parameter errors and correlations”. In: *Computer Physics Communications* 10.6 (Dec. 1975), pp. 343–367. DOI: 10.1016/0010-4655(75)90039-9. URL: [https://doi.org/10.1016/0010-4655\(75\)90039-9](https://doi.org/10.1016/0010-4655(75)90039-9).
- [320] Hans Dembinski et al. *scikit-hep/iminuit*. 2023. DOI: 10.5281/ZENODO.3949207. URL: <https://zenodo.org/record/3949207>.
- [321] Shreyasi Acharya et al. “Measurement of electrons from semileptonic heavy-flavour hadron decays at midrapidity in pp and Pb-Pb collisions at $\sqrt{s_{NN}} = 5.02$ TeV”. In: *Phys. Lett. B* 804 (2020), p. 135377. DOI: 10.1016/j.physletb.2020.135377. arXiv: 1910.09110 [nucl-ex].
- [322] Taesoo Song et al. “Open charm and dileptons from relativistic heavy-ion collisions”. In: *Phys. Rev. C* 97.6 (2018), p. 064907. DOI: 10.1103/PhysRevC.97.064907. arXiv: 1803.02698 [nucl-th].
- [323] M. Klasen et al. “QCD analysis and effective temperature of direct photons in lead-lead collisions at the LHC”. In: *Nucl. Part. Phys. Proc.* 273-275 (2016). Ed. by M Aguilar-Benítez et al., pp. 1509–1512. DOI: 10.1016/j.nuclphysbps.2015.09.244. arXiv: 1409.3363 [hep-ph].
- [324] Jamal Jalilian-Marian et al. “The Intrinsic glue distribution at very small x”. In: *Phys. Rev. D* 55 (1997), pp. 5414–5428. DOI: 10.1103/PhysRevD.55.5414. arXiv: hep-ph/9606337.
- [325] Nestor Armesto et al. “Signatures of gluon saturation from structure-function measurements”. In: *Phys. Rev. D* 105.11 (2022), p. 114017. DOI: 10.1103/PhysRevD.105.114017. arXiv: 2203.05846 [hep-ph].
- [326] H. Baer, J. Ohnemus, and J. F. Owens. “A Next-to-leading Logarithm Calculation of Direct Photon Production”. In: *Phys. Rev. D* 42 (1990), pp. 61–71. DOI: 10.1103/PhysRevD.42.61.
- [327] L. E. Gordon and W. Vogelsang. “Polarized and unpolarized isolated prompt photon production beyond the leading order”. In: *Phys. Rev. D* 50 (1994), pp. 1901–1916. DOI: 10.1103/PhysRevD.50.1901.
- [328] John M. Campbell, R. Keith Ellis, and Ciaran Williams. “Direct Photon Production at Next-to-Next-to-Leading Order”. In: *Phys. Rev. Lett.* 118.22 (2017). [Erratum: *Phys.Rev.Lett.* 124, 259901 (2020)], p. 222001. DOI: 10.1103/PhysRevLett.118.222001. arXiv: 1612.04333 [hep-ph].
- [329] John M. Campbell, R. Keith Ellis, and Ciaran Williams. “Driving missing data at the LHC: NNLO predictions for the ratio of $\gamma + j$ and $Z + j$ ”. In: *Phys. Rev. D* 96.1 (2017), p. 014037. DOI: 10.1103/PhysRevD.96.014037. arXiv: 1703.10109 [hep-ph].
- [330] John M. Campbell et al. “Direct photon production and PDF fits reloaded”. In: *Eur. Phys. J. C* 78.6 (2018), p. 470. DOI: 10.1140/epjc/s10052-018-5944-4. arXiv: 1802.03021 [hep-ph].
- [331] John Campbell and Tobias Neumann. “Precision Phenomenology with MCFM”. In: *JHEP* 12 (2019), p. 034. DOI: 10.1007/JHEP12(2019)034. arXiv: 1909.09117 [hep-ph].

- [332] Robin Schuermann et al. “NNLO Photon Production with Realistic Photon Isolation”. In: *PoS LL2022* (2022), p. 034. DOI: 10.22323/1.416.0034. arXiv: 2208.02669 [hep-ph].
- [333] Simon Badger et al. “Isolated photon production in association with a jet pair through next-to-next-to-leading order in QCD”. In: (Apr. 2023). arXiv: 2304.06682 [hep-ph].
- [334] L. Adamczyk et al. “Direct virtual photon production in Au+Au collisions at $\sqrt{s_{NN}} = 200$ GeV”. In: *Phys. Lett. B* 770 (2017), pp. 451–458. DOI: 10.1016/j.physletb.2017.04.050. arXiv: 1607.01447 [nucl-ex].
- [335] Charles Gale et al. “Multimessenger heavy-ion collision physics”. In: *Phys. Rev. C* 105.1 (2022), p. 014909. DOI: 10.1103/PhysRevC.105.014909. arXiv: 2106.11216 [nucl-th].
- [336] S. S. Adler et al. “Measurement of direct photon production in p + p collisions at $s^{*(1/2)} = 200$ -GeV”. In: *Phys. Rev. Lett.* 98 (2007), p. 012002. DOI: 10.1103/PhysRevLett.98.012002. arXiv: hep-ex/0609031.
- [337] Shreyasi Acharya et al. “Measurement of the inclusive isolated photon production cross section in pp collisions at $\sqrt{s} = 7$ TeV”. In: *Eur. Phys. J. C* 79.11 (2019), p. 896. DOI: 10.1140/epjc/s10052-019-7389-9. arXiv: 1906.01371 [nucl-ex].
- [338] Georges Aad et al. “Measurement of the inclusive isolated-photon cross section in pp collisions at $\sqrt{s} = 13$ TeV using 36 fb^{-1} of ATLAS data”. In: *JHEP* 10 (2019), p. 203. DOI: 10.1007/JHEP10(2019)203. arXiv: 1908.02746 [hep-ex].
- [339] Albert M Sirunyan et al. “Measurement of differential cross sections for inclusive isolated-photon and photon+jets production in proton-proton collisions at $\sqrt{s} = 13$ TeV”. In: *Eur. Phys. J. C* 79.1 (2019), p. 20. DOI: 10.1140/epjc/s10052-018-6482-9. arXiv: 1807.00782 [hep-ex].
- [340] Georges Aad et al. “Measurement of isolated-photon plus two-jet production in pp collisions at $\sqrt{s} = 13$ TeV with the ATLAS detector”. In: *JHEP* 03 (2020), p. 179. DOI: 10.1007/JHEP03(2020)179. arXiv: 1912.09866 [hep-ex].
- [341] Johan Alwall et al. “A Standard format for Les Houches event files”. In: *Comput. Phys. Commun.* 176 (2007), pp. 300–304. DOI: 10.1016/j.cpc.2006.11.010. arXiv: hep-ph/0609017.
- [342] Stefan Hoeche, Steffen Schumann, and Frank Siegert. “Hard photon production and matrix-element parton-shower merging”. In: *Phys. Rev. D* 81 (2010), p. 034026. DOI: 10.1103/PhysRevD.81.034026. arXiv: 0912.3501 [hep-ph].
- [343] Leif Lönnblad. “Fooling Around with the Sudakov Veto Algorithm”. In: *Eur. Phys. J. C* 73.3 (2013), p. 2350. DOI: 10.1140/epjc/s10052-013-2350-9. arXiv: 1211.7204 [hep-ph].
- [344] Albert M Sirunyan et al. “Measurements of the differential cross sections of the production of Z + jets and γ + jets and of Z boson emission collinear with a jet in pp collisions at $\sqrt{s} = 13$ TeV”. In: *JHEP* 05 (2021), p. 285. DOI: 10.1007/JHEP05(2021)285. arXiv: 2102.02238 [hep-ex].
- [345] Simone Alioli et al. “Jet pair production in POWHEG”. In: *JHEP* 04 (2011), p. 081. DOI: 10.1007/JHEP04(2011)081. arXiv: 1012.3380 [hep-ph].
- [346] F. del Aguila et al. “Techniques for one loop calculations in constrained differential renormalization”. In: *Nucl. Phys. B* 537 (1999), pp. 561–585. DOI: 10.1016/S0550-3213(98)00645-2. arXiv: hep-ph/9806451.
- [347] Lance J. Dixon. “A brief introduction to modern amplitude methods”. In: *Theoretical Advanced Study Institute in Elementary Particle Physics: Particle Physics: The Higgs Boson and Beyond*. 2014, pp. 31–67. DOI: 10.5170/CERN-2014-008.31. arXiv: 1310.5353 [hep-ph].

- [348] J. A. M. Vermaseren. “New features of FORM”. In: (Oct. 2000). arXiv: [math-ph/0010025](https://arxiv.org/abs/math-ph/0010025).
- [349] J. Kuipers et al. “FORM version 4.0”. In: *Comput. Phys. Commun.* 184 (2013), pp. 1453–1467. DOI: [10.1016/j.cpc.2012.12.028](https://doi.org/10.1016/j.cpc.2012.12.028). arXiv: [1203.6543](https://arxiv.org/abs/1203.6543) [[cs.SC](https://arxiv.org/abs/cs.SC)].
- [350] T. Ueda et al. “Further developments of FORM”. In: *J. Phys. Conf. Ser.* 1525 (2020), p. 012013. DOI: [10.1088/1742-6596/1525/1/012013](https://doi.org/10.1088/1742-6596/1525/1/012013).
- [351] Aaron Meurer et al. “SymPy: symbolic computing in Python”. In: *PeerJ Computer Science* 3 (Jan. 2017), e103. ISSN: 2376-5992. DOI: [10.7717/peerj-cs.103](https://doi.org/10.7717/peerj-cs.103). URL: <https://doi.org/10.7717/peerj-cs.103>.
- [352] Federico Buccioni et al. “OpenLoops 2”. In: *Eur. Phys. J. C* 79.10 (2019), p. 866. DOI: [10.1140/epjc/s10052-019-7306-2](https://doi.org/10.1140/epjc/s10052-019-7306-2). arXiv: [1907.13071](https://arxiv.org/abs/1907.13071) [[hep-ph](https://arxiv.org/abs/hep-ph)].
- [353] Ansgar Denner, Jean-Nicolas Lang, and Sandro Uccirati. “Recola2: REcursive Computation of One-Loop Amplitudes 2”. In: *Comput. Phys. Commun.* 224 (2018), pp. 346–361. DOI: [10.1016/j.cpc.2017.11.013](https://doi.org/10.1016/j.cpc.2017.11.013). arXiv: [1711.07388](https://arxiv.org/abs/1711.07388) [[hep-ph](https://arxiv.org/abs/hep-ph)].
- [354] Silvia Ferrario Ravasio and Carlo Oleari. “NLO + parton-shower generator for Wc production in the POWHEG BOX RES”. In: *Eur. Phys. J. C* 83.7 (2023), p. 684. DOI: [10.1140/epjc/s10052-023-11853-9](https://doi.org/10.1140/epjc/s10052-023-11853-9). arXiv: [2304.13791](https://arxiv.org/abs/2304.13791) [[hep-ph](https://arxiv.org/abs/hep-ph)].
- [355] Benjamin Fuks et al. “Precision predictions for electroweak superpartner production at hadron colliders with Resummino”. In: *Eur. Phys. J. C* 73 (2013), p. 2480. DOI: [10.1140/epjc/s10052-013-2480-0](https://doi.org/10.1140/epjc/s10052-013-2480-0). arXiv: [1304.0790](https://arxiv.org/abs/1304.0790) [[hep-ph](https://arxiv.org/abs/hep-ph)].
- [356] J. Wess and B. Zumino. “Supergauge Transformations in Four-Dimensions”. In: *Nucl. Phys. B* 70 (1974). Ed. by A. Salam and E. Sezgin, pp. 39–50. DOI: [10.1016/0550-3213\(74\)90355-1](https://doi.org/10.1016/0550-3213(74)90355-1).
- [357] Abdus Salam and J. A. Strathdee. “Supergauge Transformations”. In: *Nucl. Phys. B* 76 (1974), pp. 477–482. DOI: [10.1016/0550-3213\(74\)90537-9](https://doi.org/10.1016/0550-3213(74)90537-9).
- [358] S. Ferrara and B. Zumino. “Supergauge Invariant Yang-Mills Theories”. In: *Nucl. Phys. B* 79 (1974), p. 413. DOI: [10.1016/0550-3213\(74\)90559-8](https://doi.org/10.1016/0550-3213(74)90559-8).
- [359] N. Sakai. “Naturalness in Supersymmetric Guts”. In: *Z. Phys. C* 11 (1981), p. 153. DOI: [10.1007/BF01573998](https://doi.org/10.1007/BF01573998).
- [360] Ali H. Chamseddine, Richard L. Arnowitt, and Pran Nath. “Locally Supersymmetric Grand Unification”. In: *Phys. Rev. Lett.* 49 (1982), p. 970. DOI: [10.1103/PhysRevLett.49.970](https://doi.org/10.1103/PhysRevLett.49.970).
- [361] John R. Ellis, S. Kelley, and Dimitri V. Nanopoulos. “Probing the desert using gauge coupling unification”. In: *Phys. Lett. B* 260 (1991), pp. 131–137. DOI: [10.1016/0370-2693\(91\)90980-5](https://doi.org/10.1016/0370-2693(91)90980-5).
- [362] John R. Ellis et al. “Supersymmetric Relics from the Big Bang”. In: *Nucl. Phys. B* 238 (1984). Ed. by M. A. Srednicki, pp. 453–476. DOI: [10.1016/0550-3213\(84\)90461-9](https://doi.org/10.1016/0550-3213(84)90461-9).
- [363] Gerard Jungman, Marc Kamionkowski, and Kim Griest. “Supersymmetric dark matter”. In: *Phys. Rept.* 267 (1996), pp. 195–373. DOI: [10.1016/0370-1573\(95\)00058-5](https://doi.org/10.1016/0370-1573(95)00058-5). arXiv: [hep-ph/9506380](https://arxiv.org/abs/hep-ph/9506380).
- [364] Sidney R. Coleman and J. Mandula. “All Possible Symmetries of the S Matrix”. In: *Phys. Rev.* 159 (1967). Ed. by A. Zichichi, pp. 1251–1256. DOI: [10.1103/PhysRev.159.1251](https://doi.org/10.1103/PhysRev.159.1251).
- [365] Rudolf Haag, Jan T. Lopuszanski, and Martin Sohnius. “All Possible Generators of Supersymmetries of the s Matrix”. In: *Nucl. Phys. B* 88 (1975), p. 257. DOI: [10.1016/0550-3213\(75\)90279-5](https://doi.org/10.1016/0550-3213(75)90279-5).
- [366] Pierre Fayet and S. Ferrara. “Supersymmetry”. In: *Phys. Rept.* 32 (1977), pp. 249–334. DOI: [10.1016/0370-1573\(77\)90066-7](https://doi.org/10.1016/0370-1573(77)90066-7).

- [367] Kenzo Inoue et al. “Aspects of Grand Unified Models with Softly Broken Supersymmetry”. In: *Prog. Theor. Phys.* 68 (1982). [Erratum: *Prog.Theor.Phys.* 70, 330 (1983)], p. 927. DOI: 10.1143/PTP.68.927.
- [368] Hans Peter Nilles. “Supersymmetry, Supergravity and Particle Physics”. In: *Phys. Rept.* 110 (1984), pp. 1–162. DOI: 10.1016/0370-1573(84)90008-5.
- [369] Howard E. Haber and Gordon L. Kane. “The Search for Supersymmetry: Probing Physics Beyond the Standard Model”. In: *Phys. Rept.* 117 (1985), pp. 75–263. DOI: 10.1016/0370-1573(85)90051-1.
- [370] Glennys R. Farrar and Pierre Fayet. “Phenomenology of the Production, Decay, and Detection of New Hadronic States Associated with Supersymmetry”. In: *Phys. Lett. B* 76 (1978), pp. 575–579. DOI: 10.1016/0370-2693(78)90858-4.
- [371] Edward Witten. “Dynamical Breaking of Supersymmetry”. In: *Nucl. Phys. B* 188 (1981), p. 513. DOI: 10.1016/0550-3213(81)90006-7.
- [372] L. Girardello and Marcus T. Grisaru. “Soft Breaking of Supersymmetry”. In: *Nucl. Phys. B* 194 (1982), p. 65. DOI: 10.1016/0550-3213(82)90512-0.
- [373] Stephen P. Martin. “A Supersymmetry Primer”. In: (1997). DOI: 10.1142/9789812839657_0001. eprint: arXiv:hep-ph/9709356.
- [374] Moritz Meinecke. “SUSY-QCD Corrections to the (Co)Annihilation of Neutralino Dark Matter within the MSSM”. dissertation. Westfälischen Wilhelms-Universität Münster, 2015. URL: https://www.uni-muenster.de/imperia/md/content/physik_tp/theses/klasen/meinecke_phd.pdf.
- [375] David Regalado Lamprea. “Precision computations for gaugino and scalar dark matter”. dissertation. Westfälischen Wilhelms-Universität Münster, 2018. URL: https://www.uni-muenster.de/imperia/md/content/physik_tp/theses/klasen/rothering_phd.pdf.
- [376] Stefano Frixione et al. “Automated simulations beyond the Standard Model: supersymmetry”. In: *JHEP* 12 (2019), p. 008. DOI: 10.1007/JHEP12(2019)008. arXiv: 1907.04898 [hep-ph].
- [377] Benjamin Fuks. “Supersymmetry - When Theory Inspires Experimental Searches”. PhD thesis. U. Strasbourg, 2013. arXiv: 1401.6277 [hep-ph].
- [378] D. I. Kazakov. “Beyond the standard model: In search of supersymmetry”. In: *2000 European School of High-Energy Physics*. Aug. 2000, pp. 125–199. arXiv: hep-ph/0012288.
- [379] Ugo Amaldi, Wim de Boer, and Hermann Furstenau. “Comparison of grand unified theories with electroweak and strong coupling constants measured at LEP”. In: *Phys. Lett. B* 260 (1991), pp. 447–455. DOI: 10.1016/0370-2693(91)91641-8.
- [380] M. Drees, R. Godbole, and P. Roy. *Theory and phenomenology of sparticles: An account of four-dimensional N=1 supersymmetry in high energy physics*. 2004.
- [381] B. C. Allanach et al. “SUSY Les Houches Accord 2”. In: *Comput. Phys. Commun.* 180 (2009), pp. 8–25. DOI: 10.1016/j.cpc.2008.08.004. arXiv: 0801.0045 [hep-ph].
- [382] Janusz Rosiek. “Complete Set of Feynman Rules for the Minimal Supersymmetric Extension of the Standard Model”. In: *Phys. Rev. D* 41 (1990), p. 3464. DOI: 10.1103/PhysRevD.41.3464. arXiv: hep-ph/9511250.
- [383] I. Zurbano Fernandez et al. “High-Luminosity Large Hadron Collider (HL-LHC): Technical design report”. In: 10/2020 (Dec. 2020). Ed. by I. Béjar Alonso et al. DOI: 10.23731/CYRM-2020-0010.

- [384] Xabier Cid Vidal et al. “Report from Working Group 3: Beyond the Standard Model physics at the HL-LHC and HE-LHC”. In: *CERN Yellow Rep. Monogr.* 7 (2019). Ed. by Andrea Dainese et al., pp. 585–865. DOI: 10.23731/CYRM-2019-007.585. arXiv: 1812.07831 [hep-ph].
- [385] F. Gianotti et al. “Physics potential and experimental challenges of the LHC luminosity upgrade”. In: *Eur. Phys. J. C* 39 (2005), pp. 293–333. DOI: 10.1140/epjc/s2004-02061-6. arXiv: hep-ph/0204087.
- [386] Thomas Binoth et al. “Automized Squark-Neutralino Production to Next-to-Leading Order”. In: *Phys. Rev. D* 84 (2011), p. 075005. DOI: 10.1103/PhysRevD.84.075005. arXiv: 1108.1250 [hep-ph].
- [387] Julien Baglio et al. “Next-to-leading-order QCD corrections and parton-shower effects for weakino+squark production at the LHC”. In: *JHEP* 12 (2021), p. 020. DOI: 10.1007/JHEP12(2021)020. arXiv: 2110.04211 [hep-ph].
- [388] George F. Sterman. “Summation of Large Corrections to Short Distance Hadronic Cross-Sections”. In: *Nucl. Phys. B* 281 (1987), pp. 310–364. DOI: 10.1016/0550-3213(87)90258-6.
- [389] S. Catani and L. Trentadue. “Resummation of the QCD Perturbative Series for Hard Processes”. In: *Nucl. Phys. B* 327 (1989), pp. 323–352. DOI: 10.1016/0550-3213(89)90273-3.
- [390] S. Catani and L. Trentadue. “Comment on QCD exponentiation at large x ”. In: *Nucl. Phys. B* 353 (1991), pp. 183–186. DOI: 10.1016/0550-3213(91)90506-S.
- [391] Nikolaos Kidonakis and George F. Sterman. “Resummation for QCD hard scattering”. In: *Nucl. Phys. B* 505 (1997), pp. 321–348. DOI: 10.1016/S0550-3213(97)00506-3. arXiv: hep-ph/9705234.
- [392] Nikolaos Kidonakis, Gianluca Oderda, and George F. Sterman. “Threshold resummation for dijet cross-sections”. In: *Nucl. Phys. B* 525 (1998), pp. 299–332. DOI: 10.1016/S0550-3213(98)00243-0. arXiv: hep-ph/9801268.
- [393] A. Vogt. “Next-to-next-to-leading logarithmic threshold resummation for deep inelastic scattering and the Drell-Yan process”. In: *Phys. Lett. B* 497 (2001), pp. 228–234. DOI: 10.1016/S0370-2693(00)01344-7. arXiv: hep-ph/0010146.
- [394] Vernon D. Barger et al. “Production of Gauge Fermions at Colliders”. In: *Phys. Lett. B* 131 (1983), p. 372. DOI: 10.1016/0370-2693(83)90519-1.
- [395] Sally Dawson, E. Eichten, and C. Quigg. “Search for Supersymmetric Particles in Hadron - Hadron Collisions”. In: *Phys. Rev. D* 31 (1985), p. 1581. DOI: 10.1103/PhysRevD.31.1581.
- [396] W. Beenakker et al. “The Production of charginos / neutralinos and sleptons at hadron colliders”. In: *Phys. Rev. Lett.* 83 (1999). [Erratum: *Phys.Rev.Lett.* 100, 029901 (2008)], pp. 3780–3783. DOI: 10.1103/PhysRevLett.100.029901. arXiv: hep-ph/9906298.
- [397] Julien Baglio, Barbara Jäger, and Matthias Kesenheimer. “Electroweakino pair production at the LHC: NLO SUSY-QCD corrections and parton-shower effects”. In: *JHEP* 07 (2016), p. 083. DOI: 10.1007/JHEP07(2016)083. arXiv: 1605.06509 [hep-ph].
- [398] Jonathan Debove, Benjamin Fuks, and Michael Klasen. “Threshold resummation for gaugino pair production at hadron colliders”. In: *Nucl. Phys. B* 842 (2011), pp. 51–85. DOI: 10.1016/j.nuclphysb.2010.08.016. arXiv: 1005.2909 [hep-ph].
- [399] Benjamin Fuks et al. “Gaugino production in proton-proton collisions at a center-of-mass energy of 8 TeV”. In: *JHEP* 10 (2012), p. 081. DOI: 10.1007/JHEP10(2012)081. arXiv: 1207.2159 [hep-ph].

- [400] Juri Fiaschi and Michael Klasen. “Neutralino-chargino pair production at NLO+NLL with resummation-improved parton density functions for LHC Run II”. In: *Phys. Rev. D* 98.5 (2018), p. 055014. DOI: 10.1103/PhysRevD.98.055014. arXiv: 1805.11322 [hep-ph].
- [401] Juri Fiaschi and Michael Klasen. “Higgsino and gaugino pair production at the LHC with aNNLO+NNLL precision”. In: *Phys. Rev. D* 102.9 (2020), p. 095021. DOI: 10.1103/PhysRevD.102.095021. arXiv: 2006.02294 [hep-ph].
- [402] Howard Baer et al. “Detecting Sleptons at Hadron Colliders and Supercolliders”. In: *Phys. Rev. D* 49 (1994), pp. 3283–3290. DOI: 10.1103/PhysRevD.49.3283. arXiv: hep-ph/9311248.
- [403] Barbara Jager, Andreas von Manteuffel, and Stephan Thier. “Slepton pair production in the POWHEG BOX”. In: *JHEP* 10 (2012), p. 130. DOI: 10.1007/JHEP10(2012)130. arXiv: 1208.2953 [hep-ph].
- [404] Giuseppe Bozzi, Benjamin Fuks, and Michael Klasen. “Threshold Resummation for Slepton-Pair Production at Hadron Colliders”. In: *Nucl. Phys. B* 777 (2007), pp. 157–181. DOI: 10.1016/j.nuclphysb.2007.03.052. arXiv: hep-ph/0701202.
- [405] Benjamin Fuks et al. “Revisiting slepton pair production at the Large Hadron Collider”. In: *JHEP* 01 (2014), p. 168. DOI: 10.1007/JHEP01(2014)168. arXiv: 1310.2621 [hep-ph].
- [406] Juri Fiaschi and Michael Klasen. “Slepton pair production at the LHC in NLO+NLL with resummation-improved parton densities”. In: *JHEP* 03 (2018), p. 094. DOI: 10.1007/JHEP03(2018)094. arXiv: 1801.10357 [hep-ph].
- [407] Juri Fiaschi, Michael Klasen, and Marthijn Sunder. “Slepton pair production with aNNLO+NNLL precision”. In: *JHEP* 04 (2020), p. 049. DOI: 10.1007/JHEP04(2020)049. arXiv: 1911.02419 [hep-ph].
- [408] G. Bozzi, B. Fuks, and M. Klasen. “Slepton production in polarized hadron collisions”. In: *Phys. Lett. B* 609 (2005), pp. 339–350. DOI: 10.1016/j.physletb.2005.01.060. arXiv: hep-ph/0411318.
- [409] Giuseppe Bozzi et al. “Squark and gaugino hadroproduction and decays in non-minimal flavour violating supersymmetry”. In: *Nucl. Phys. B* 787 (2007), pp. 1–54. DOI: 10.1016/j.nuclphysb.2007.05.031. arXiv: 0704.1826 [hep-ph].
- [410] Jonathan Dabove, Benjamin Fuks, and Michael Klasen. “Model-independent analysis of gaugino-pair production in polarized and unpolarized hadron collisions”. In: *Phys. Rev. D* 78 (2008), p. 074020. DOI: 10.1103/PhysRevD.78.074020. arXiv: 0804.0423 [hep-ph].
- [411] B. Fuks, M. Klasen, and M. Rothering. “Soft gluon resummation for associated gluino-gaugino production at the LHC”. In: *JHEP* 07 (2016), p. 053. DOI: 10.1007/JHEP07(2016)053. arXiv: 1604.01023 [hep-ph].
- [412] Michael Kramer, Eric Laenen, and Michael Spira. “Soft gluon radiation in Higgs boson production at the LHC”. In: *Nucl. Phys. B* 511 (1998), pp. 523–549. DOI: 10.1016/S0550-3213(97)00679-2. arXiv: hep-ph/9611272.
- [413] Stefano Catani, Daniel de Florian, and Massimiliano Grazzini. “Higgs production in hadron collisions: Soft and virtual QCD corrections at NNLO”. In: *JHEP* 05 (2001), p. 025. DOI: 10.1088/1126-6708/2001/05/025. arXiv: hep-ph/0102227.
- [414] Anna Kulesza, George F. Sterman, and Werner Vogelsang. “Joint resummation in electroweak boson production”. In: *Phys. Rev. D* 66 (2002), p. 014011. DOI: 10.1103/PhysRevD.66.014011. arXiv: hep-ph/0202251.

- [415] Leandro G. Almeida, George F. Sterman, and Werner Vogelsang. “Threshold Resummation for Di-hadron Production in Hadronic Collisions”. In: *Phys. Rev. D* 80 (2009), p. 074016. DOI: 10.1103/PhysRevD.80.074016. arXiv: 0907.1234 [hep-ph].
- [416] Jonathan Debove, Benjamin Fuks, and Michael Klasen. “Transverse-momentum resummation for gaugino-pair production at hadron colliders”. In: *Phys. Lett. B* 688 (2010), pp. 208–211. DOI: 10.1016/j.physletb.2010.04.013. arXiv: 0907.1105 [hep-ph].
- [417] G. Bozzi, B. Fuks, and M. Klasen. “Transverse-momentum resummation for slepton-pair production at the CERN LHC”. In: *Phys. Rev. D* 74 (2006), p. 015001. DOI: 10.1103/PhysRevD.74.015001. arXiv: hep-ph/0603074.
- [418] John C. Collins and Davison E. Soper. “Back-To-Back Jets: Fourier Transform from B to K-Transverse”. In: *Nucl. Phys. B* 197 (1982), pp. 446–476. DOI: 10.1016/0550-3213(82)90453-9.
- [419] John C. Collins and Davison E. Soper. “Back-To-Back Jets in QCD”. In: *Nucl. Phys. B* 193 (1981). [Erratum: Nucl.Phys.B 213, 545 (1983)], p. 381. DOI: 10.1016/0550-3213(81)90339-4.
- [420] John C. Collins, Davison E. Soper, and George F. Sterman. “Transverse Momentum Distribution in Drell-Yan Pair and W and Z Boson Production”. In: *Nucl. Phys. B* 250 (1985), pp. 199–224. DOI: 10.1016/0550-3213(85)90479-1.
- [421] Jonathan Debove, Benjamin Fuks, and Michael Klasen. “Joint Resummation for Gaugino Pair Production at Hadron Colliders”. In: *Nucl. Phys. B* 849 (2011), pp. 64–79. DOI: 10.1016/j.nuclphysb.2011.03.015. arXiv: 1102.4422 [hep-ph].
- [422] Giuseppe Bozzi, Benjamin Fuks, and Michael Klasen. “Joint resummation for slepton pair production at hadron colliders”. In: *Nucl. Phys. B* 794 (2008), pp. 46–60. DOI: 10.1016/j.nuclphysb.2007.10.021. arXiv: 0709.3057 [hep-ph].
- [423] Hsiang-nan Li. “Unification of the k(T) and threshold resummations”. In: *Phys. Lett. B* 454 (1999), pp. 328–334. DOI: 10.1016/S0370-2693(99)00350-0. arXiv: hep-ph/9812363.
- [424] Eric Laenen, George F. Sterman, and Werner Vogelsang. “Higher order QCD corrections in prompt photon production”. In: *Phys. Rev. Lett.* 84 (2000), pp. 4296–4299. DOI: 10.1103/PhysRevLett.84.4296. arXiv: hep-ph/0002078.
- [425] Eric Laenen, George F. Sterman, and Werner Vogelsang. “Recoil and threshold corrections in short distance cross-sections”. In: *Phys. Rev. D* 63 (2001), p. 114018. DOI: 10.1103/PhysRevD.63.114018. arXiv: hep-ph/0010080.
- [426] Georges Aad et al. “Search for electroweak production of charginos and sleptons decaying into final states with two leptons and missing transverse momentum in $\sqrt{s} = 13$ TeV pp collisions using the ATLAS detector”. In: *Eur. Phys. J. C* 80.2 (2020), p. 123. DOI: 10.1140/epjc/s10052-019-7594-6. arXiv: 1908.08215 [hep-ex].
- [427] Georges Aad et al. “Search for charginos and neutralinos in final states with two boosted hadronically decaying bosons and missing transverse momentum in pp collisions at $\sqrt{s} = 13$ TeV with the ATLAS detector”. In: *Phys. Rev. D* 104.11 (2021), p. 112010. DOI: 10.1103/PhysRevD.104.112010. arXiv: 2108.07586 [hep-ex].
- [428] “Combined search for electroweak production of winos, binos, higgsinos, and sleptons in proton-proton collisions at $\sqrt{s} = 13$ TeV”. In: (2023).
- [429] Georges Aad et al. “Search for R-parity-violating supersymmetry in a final state containing leptons and many jets with the ATLAS experiment using $\sqrt{s} = 13$ TeV proton-proton collision data”. In: *Eur. Phys. J. C* 81.11 (2021), p. 1023. DOI: 10.1140/epjc/s10052-021-09761-x. arXiv: 2106.09609 [hep-ex].

- [430] Georges Aad et al. “Search for pair production of squarks or gluinos decaying via sleptons or weak bosons in final states with two same-sign or three leptons with the ATLAS detector”. In: *JHEP* 02 (2024), p. 107. DOI: 10.1007/JHEP02(2024)107. arXiv: 2307.01094 [hep-ex].
- [431] Georges Aad et al. “ATLAS Run 2 searches for electroweak production of supersymmetric particles interpreted within the pMSSM”. In: (Feb. 2024). arXiv: 2402.01392 [hep-ex].
- [432] Aram Hayrapetyan et al. “Search for new physics in multijet events with at least one photon and large missing transverse momentum in proton-proton collisions at 13 TeV”. In: *JHEP* 10 (2023), p. 046. DOI: 10.1007/JHEP10(2023)046. arXiv: 2307.16216 [hep-ex].
- [433] Armen Tumasyan et al. “Search for top squark pair production in a final state with at least one hadronically decaying tau lepton in proton-proton collisions at $\sqrt{s} = 13$ TeV”. In: *JHEP* 07 (2023), p. 110. DOI: 10.1007/JHEP07(2023)110. arXiv: 2304.07174 [hep-ex].
- [434] O. V. Tarasov, A. A. Vladimirov, and A. Yu. Zharkov. “The Gell-Mann-Low Function of QCD in the Three Loop Approximation”. In: *Phys. Lett. B* 93 (1980), pp. 429–432. DOI: 10.1016/0370-2693(80)90358-5.
- [435] S. A. Larin and J. A. M. Vermaseren. “The Three loop QCD Beta function and anomalous dimensions”. In: *Phys. Lett. B* 303 (1993), pp. 334–336. DOI: 10.1016/0370-2693(93)91441-0. arXiv: hep-ph/9302208.
- [436] Wim Beenakker et al. “Towards NNLL resummation: hard matching coefficients for squark and gluino hadroproduction”. In: *JHEP* 10 (2013), p. 120. DOI: 10.1007/JHEP10(2013)120. arXiv: 1304.6354 [hep-ph].
- [437] Wim Beenakker et al. “NNLL resummation for squark-antisquark pair production at the LHC”. In: *JHEP* 01 (2012), p. 076. DOI: 10.1007/JHEP01(2012)076. arXiv: 1110.2446 [hep-ph].
- [438] Robert V. Harlander and William B. Kilgore. “Soft and virtual corrections to proton proton \rightarrow H + x at NNLO”. In: *Phys. Rev. D* 64 (2001), p. 013015. DOI: 10.1103/PhysRevD.64.013015. arXiv: hep-ph/0102241.
- [439] A. D. Martin et al. “Parton distributions for the LHC”. In: *Eur. Phys. J. C* 63 (2009), pp. 189–285. DOI: 10.1140/epjc/s10052-009-1072-5. arXiv: 0901.0002 [hep-ph].
- [440] Harry Contopanagos and George F. Sterman. “Principal value resummation”. In: *Nucl. Phys. B* 419 (1994), pp. 77–104. DOI: 10.1016/0550-3213(94)90358-1. arXiv: hep-ph/9310313.
- [441] Stefano Catani et al. “The Resummation of soft gluons in hadronic collisions”. In: *Nucl. Phys. B* 478 (1996), pp. 273–310. DOI: 10.1016/0550-3213(96)00399-9. arXiv: hep-ph/9604351.
- [442] Jonathan L. Feng, Shufang Su, and Fumihiro Takayama. “Lower limit on dark matter production at the large hadron collider”. In: *Phys. Rev. Lett.* 96 (2006), p. 151802. DOI: 10.1103/PhysRevLett.96.151802. arXiv: hep-ph/0503117.
- [443] Yang Bai, Patrick J. Fox, and Roni Harnik. “The Tevatron at the Frontier of Dark Matter Direct Detection”. In: *JHEP* 12 (2010), p. 048. DOI: 10.1007/JHEP12(2010)048. arXiv: 1005.3797 [hep-ph].
- [444] Albert M Sirunyan et al. “Search for supersymmetry in multijet events with missing transverse momentum in proton-proton collisions at 13 TeV”. In: *Phys. Rev. D* 96.3 (2017), p. 032003. DOI: 10.1103/PhysRevD.96.032003. arXiv: 1704.07781 [hep-ex].

- [445] The Cms Collaboration et al. “Search for supersymmetry in proton-proton collisions at 13 TeV in final states with jets and missing transverse momentum”. In: *JHEP* 10 (2019), p. 244. DOI: 10.1007/JHEP10(2019)244. arXiv: 1908.04722 [hep-ex].
- [446] Armen Tumasyan et al. “Search for electroweak production of charginos and neutralinos in proton-proton collisions at $\sqrt{s} = 13$ TeV”. In: (June 2021). arXiv: 2106.14246 [hep-ex].
- [447] Georges Aad et al. “Search for squarks and gluinos in final states with jets and missing transverse momentum using 139 fb^{-1} of $\sqrt{s} = 13$ TeV pp collision data with the ATLAS detector”. In: *JHEP* 02 (2021), p. 143. DOI: 10.1007/JHEP02(2021)143. arXiv: 2010.14293 [hep-ex].
- [448] Georges Aad et al. “Search for squarks and gluinos in final states with one isolated lepton, jets, and missing transverse momentum at $\sqrt{s} = 13$ with the ATLAS detector”. In: *Eur. Phys. J. C* 81.7 (2021). [Erratum: *Eur.Phys.J.C* 81, 956 (2021)], p. 600. DOI: 10.1140/epjc/s10052-021-09748-8. arXiv: 2101.01629 [hep-ex].
- [449] J. F. Gunion and Howard E. Haber. “Higgs Bosons in Supersymmetric Models. 1.” In: *Nucl. Phys. B* 272 (1986). [Erratum: *Nucl.Phys.B* 402, 567–569 (1993)], p. 1. DOI: 10.1016/0550-3213(86)90340-8.
- [450] Giuseppe Bozzi, Benjamin Fuks, and Michael Klasen. “Non-diagonal and mixed squark production at hadron colliders”. In: *Phys. Rev. D* 72 (2005), p. 035016. DOI: 10.1103/PhysRevD.72.035016. arXiv: hep-ph/0507073.
- [451] Benjamin Fuks, Bjorn Herrmann, and Michael Klasen. “Flavour Violation in Gauge-Mediated Supersymmetry Breaking Models: Experimental Constraints and Phenomenology at the LHC”. In: *Nucl. Phys. B* 810 (2009), pp. 266–299. DOI: 10.1016/j.nuclphysb.2008.11.020. arXiv: 0808.1104 [hep-ph].
- [452] Benjamin Fuks, Bjorn Herrmann, and Michael Klasen. “Phenomenology of anomaly-mediated supersymmetry breaking scenarios with non-minimal flavour violation”. In: *Phys. Rev. D* 86 (2012), p. 015002. DOI: 10.1103/PhysRevD.86.015002. arXiv: 1112.4838 [hep-ph].
- [453] Karen De Causmaecker et al. “General squark flavour mixing: constraints, phenomenology and benchmarks”. In: *JHEP* 11 (2015), p. 125. DOI: 10.1007/JHEP11(2015)125. arXiv: 1509.05414 [hep-ph].
- [454] Amit Chakraborty et al. “Flavour-violating decays of mixed top-charm squarks at the LHC”. In: *Eur. Phys. J. C* 78.10 (2018), p. 844. DOI: 10.1140/epjc/s10052-018-6331-x. arXiv: 1808.07488 [hep-ph].
- [455] John C. Collins, Frank Wilczek, and A. Zee. “Low-Energy Manifestations of Heavy Particles: Application to the Neutral Current”. In: *Phys. Rev. D* 18 (1978), p. 242. DOI: 10.1103/PhysRevD.18.242.
- [456] William A. Bardeen et al. “Deep Inelastic Scattering Beyond the Leading Order in Asymptotically Free Gauge Theories”. In: *Phys. Rev. D* 18 (1978), p. 3998. DOI: 10.1103/PhysRevD.18.3998.
- [457] William J. Marciano. “Flavor Thresholds and Lambda in the Modified Minimal Subtraction Prescription”. In: *Phys. Rev. D* 29 (1984), p. 580. DOI: 10.1103/PhysRevD.29.580.
- [458] Stephen P. Martin and Michael T. Vaughn. “Regularization dependence of running couplings in softly broken supersymmetry”. In: *Phys. Lett. B* 318 (1993), pp. 331–337. DOI: 10.1016/0370-2693(93)90136-6. arXiv: hep-ph/9308222.
- [459] Vincent Michel Theeuwes. “Soft Gluon Resummation for Heavy Particle Production at the Large Hadron Collider”. dissertation. Westfälischen Wilhelms-Universität Münster, 2015.

- [460] Nikolaos Kidonakis. “Single top production at the Tevatron: Threshold resummation and finite-order soft gluon corrections”. In: *Phys. Rev. D* 74 (2006), p. 114012. DOI: 10.1103/PhysRevD.74.114012. arXiv: hep-ph/0609287.
- [461] Eric Laenen, Gianluca Oderda, and George F. Sterman. “Resummation of threshold corrections for single particle inclusive cross-sections”. In: *Phys. Lett. B* 438 (1998), pp. 173–183. DOI: 10.1016/S0370-2693(98)00960-5. arXiv: hep-ph/9806467.
- [462] W. Porod and F. Staub. “SPHeno 3.1: Extensions including flavour, CP-phases and models beyond the MSSM”. In: *Comput. Phys. Commun.* 183 (2012), pp. 2458–2469. DOI: 10.1016/j.cpc.2012.05.021. arXiv: 1104.1573 [hep-ph].
- [463] E. Bagnaschi et al. “Likelihood Analysis of the pMSSM11 in Light of LHC 13-TeV Data”. In: *Eur. Phys. J. C* 78.3 (2018), p. 256. DOI: 10.1140/epjc/s10052-018-5697-0. arXiv: 1710.11091 [hep-ph].
- [464] B. Abi et al. “Measurement of the Positive Muon Anomalous Magnetic Moment to 0.46 ppm”. In: *Phys. Rev. Lett.* 126.14 (2021), p. 141801. DOI: 10.1103/PhysRevLett.126.141801. arXiv: 2104.03281 [hep-ex].
- [465] Juan Rojo. “Progress in the NNPDF global analyses of proton structure”. In: *55th Rencontres de Moriond on QCD and High Energy Interactions*. Apr. 2021. arXiv: 2104.09174 [hep-ph].
- [466] Richard D. Ball et al. “The PDF4LHC21 combination of global PDF fits for the LHC Run III”. In: *J. Phys. G* 49.8 (2022), p. 080501. DOI: 10.1088/1361-6471/ac7216. arXiv: 2203.05506 [hep-ph].
- [467] Peter Z. Skands et al. “SUSY Les Houches accord: Interfacing SUSY spectrum calculators, decay packages, and event generators”. In: *JHEP* 07 (2004), p. 036. DOI: 10.1088/1126-6708/2004/07/036. arXiv: hep-ph/0311123.
- [468] Benjamin Fuks et al. “Realistic simplified gaugino-higgsino models in the MSSM”. In: *Eur. Phys. J. C* 78.3 (2018), p. 209. DOI: 10.1140/epjc/s10052-018-5695-2. arXiv: 1710.09941 [hep-ph].
- [469] Richard D. Ball et al. “Parton distributions from high-precision collider data”. In: *Eur. Phys. J. C* 77.10 (2017), p. 663. DOI: 10.1140/epjc/s10052-017-5199-5. arXiv: 1706.00428 [hep-ph].
- [470] Richard D. Ball et al. “Parton distributions and new physics searches: the Drell–Yan forward–backward asymmetry as a case study”. In: *Eur. Phys. J. C* 82.12 (2022), p. 1160. DOI: 10.1140/epjc/s10052-022-11133-y. arXiv: 2209.08115 [hep-ph].
- [471] J. Fiaschi et al. “Z′-boson dilepton searches and the high-x quark density”. In: *Phys. Lett. B* 841 (2023), p. 137915. DOI: 10.1016/j.physletb.2023.137915. arXiv: 2211.06188 [hep-ph].
- [472] S. Alekhin et al. “Parton distribution functions, α_s , and heavy-quark masses for LHC Run II”. In: *Phys. Rev. D* 96.1 (2017), p. 014011. DOI: 10.1103/PhysRevD.96.014011. arXiv: 1701.05838 [hep-ph].
- [473] Albert M Sirunyan et al. “Search for new physics in events with two soft oppositely charged leptons and missing transverse momentum in proton-proton collisions at $\sqrt{s} = 13$ TeV”. In: *Phys. Lett. B* 782 (2018), pp. 440–467. DOI: 10.1016/j.physletb.2018.05.062. arXiv: 1801.01846 [hep-ex].
- [474] Georges Aad et al. “Searches for electroweak production of supersymmetric particles with compressed mass spectra in $\sqrt{s} = 13$ TeV pp collisions with the ATLAS detector”. In: *Phys. Rev. D* 101.5 (2020), p. 052005. DOI: 10.1103/PhysRevD.101.052005. arXiv: 1911.12606 [hep-ex].

- [475] Georges Aad et al. “Search for chargino–neutralino pair production in final states with three leptons and missing transverse momentum in $\sqrt{s} = 13$ TeV pp collisions with the ATLAS detector”. In: *Eur. Phys. J. C* 81.12 (2021), p. 1118. DOI: 10.1140/epjc/s10052-021-09749-7. arXiv: 2106.01676 [hep-ex].
- [476] Iñaki Lara et al. “Monojet signatures from gluino and squark decays”. In: *JHEP* 10 (2022), p. 150. DOI: 10.1007/JHEP10(2022)150. arXiv: 2208.01651 [hep-ph].
- [477] ATLAS Collaboration. *Reproducing searches for new physics with the ATLAS experiment through publication of full statistical likelihoods*. Tech. rep. ATL-PHYS-PUB-2019-029. 2019. URL: <http://cds.cern.ch/record/2684863>.
- [478] CMS Collaboration. *Simplified likelihood for the re-interpretation of public CMS results*. Tech. rep. CMS-NOTE-2017-001. Geneva: CERN, Jan. 2017.
- [479] Jack Y. Araz et al. “Strength in numbers: Optimal and scalable combination of LHC new-physics searches”. In: *SciPost Phys.* 14.4 (2023), p. 077. DOI: 10.21468/SciPostPhys.14.4.077. arXiv: 2209.00025 [hep-ph].
- [480] Alexander Feike. “Combination and Reinterpretation of LHC SUSY Searches”. Master’s Thesis. Universität Münster, 2024. URL: https://www.uni-muenster.de/imperia/md/content/physik_tp/theses/klasen/feike_msc.pdf.
- [481] Mohammad Mahdi Altakach et al. “Global LHC constraints on electroweak-inos with SModelS v2.3”. In: (Dec. 2023). arXiv: 2312.16635 [hep-ph].
- [482] Gaël Alguero et al. “Signal region combination with full and simplified likelihoods in MadAnalysis 5”. In: *SciPost Phys.* 14.1 (2023), p. 009. DOI: 10.21468/SciPostPhys.14.1.009. arXiv: 2206.14870 [hep-ph].
- [483] Celine Degrande et al. “UFO - The Universal FeynRules Output”. In: *Comput. Phys. Commun.* 183 (2012), pp. 1201–1214. DOI: 10.1016/j.cpc.2012.01.022. arXiv: 1108.2040 [hep-ph].
- [484] Claude Duhr and Benjamin Fuks. “A superspace module for the FeynRules package”. In: *Comput. Phys. Commun.* 182 (2011), pp. 2404–2426. DOI: 10.1016/j.cpc.2011.06.009. arXiv: 1102.4191 [hep-ph].
- [485] Neil D. Christensen and Claude Duhr. “FeynRules - Feynman rules made easy”. In: *Comput. Phys. Commun.* 180 (2009), pp. 1614–1641. DOI: 10.1016/j.cpc.2009.02.018. arXiv: 0806.4194 [hep-ph].
- [486] Adam Alloul et al. “FeynRules 2.0 - A complete toolbox for tree-level phenomenology”. In: *Comput. Phys. Commun.* 185 (2014), pp. 2250–2300. DOI: 10.1016/j.cpc.2014.04.012. arXiv: 1310.1921 [hep-ph].
- [487] Wim Beenakker et al. “NNLL-fast: predictions for coloured supersymmetric particle production at the LHC with threshold and Coulomb resummation”. In: *JHEP* 12 (2016), p. 133. DOI: 10.1007/JHEP12(2016)133. arXiv: 1607.07741 [hep-ph].
- [488] W. Beenakker et al. “Squark and gluino production at hadron colliders”. In: *Nucl. Phys. B* 492 (1997), pp. 51–103. DOI: 10.1016/S0550-3213(97)80027-2. arXiv: hep-ph/9610490.
- [489] Ulrich Langenfeld and Sven-Olaf Moch. “Higher-order soft corrections to squark hadro-production”. In: *Phys. Lett. B* 675 (2009), pp. 210–221. DOI: 10.1016/j.physletb.2009.04.002. arXiv: 0901.0802 [hep-ph].
- [490] A. Kulesza and L. Motyka. “Threshold resummation for squark-antisquark and gluino-pair production at the LHC”. In: *Phys. Rev. Lett.* 102 (2009), p. 111802. DOI: 10.1103/PhysRevLett.102.111802. arXiv: 0807.2405 [hep-ph].

- [491] A. Kulesza and L. Motyka. “Soft gluon resummation for the production of gluino-gluino and squark-antisquark pairs at the LHC”. In: *Phys. Rev. D* 80 (2009), p. 095004. DOI: 10.1103/PhysRevD.80.095004. arXiv: 0905.4749 [hep-ph].
- [492] Wim Beenakker et al. “Soft-gluon resummation for squark and gluino hadroproduction”. In: *JHEP* 12 (2009), p. 041. DOI: 10.1088/1126-6708/2009/12/041. arXiv: 0909.4418 [hep-ph].
- [493] Wim Beenakker et al. “NNLL resummation for squark and gluino production at the LHC”. In: *JHEP* 12 (2014), p. 023. DOI: 10.1007/JHEP12(2014)023. arXiv: 1404.3134 [hep-ph].
- [494] Wim Beenakker et al. “NLO+NLL squark and gluino production cross-sections with threshold-improved parton distributions”. In: *Eur. Phys. J. C* 76.2 (2016), p. 53. DOI: 10.1140/epjc/s10052-016-3892-4. arXiv: 1510.00375 [hep-ph].
- [495] W. Beenakker, R. Hopker, and M. Spira. “PROSPINO: A Program for the production of supersymmetric particles in next-to-leading order QCD”. In: (Nov. 1996). arXiv: hep-ph/9611232.
- [496] Guang-ping Gao et al. “Loop effects and nondecoupling property of SUSY QCD in $g b \rightarrow t H$ ”. In: *Phys. Rev. D* 66 (2002), p. 015007. DOI: 10.1103/PhysRevD.66.015007. arXiv: hep-ph/0202016.
- [497] Eric Conte, Benjamin Fuks, and Guillaume Serret. “MadAnalysis 5, A User-Friendly Framework for Collider Phenomenology”. In: *Comput. Phys. Commun.* 184 (2013), pp. 222–256. DOI: 10.1016/j.cpc.2012.09.009. arXiv: 1206.1599 [hep-ph].
- [498] Eric Conte et al. “Designing and recasting LHC analyses with MadAnalysis 5”. In: *Eur. Phys. J. C* 74.10 (2014), p. 3103. DOI: 10.1140/epjc/s10052-014-3103-0. arXiv: 1405.3982 [hep-ph].
- [499] Eric Conte and Benjamin Fuks. “Confronting new physics theories to LHC data with MADANALYSIS 5”. In: *Int. J. Mod. Phys. A* 33.28 (2018), p. 1830027. DOI: 10.1142/S0217751X18300272. arXiv: 1808.00480 [hep-ph].
- [500] J. de Favereau et al. “DELPHES 3, A modular framework for fast simulation of a generic collider experiment”. In: *JHEP* 02 (2014), p. 057. DOI: 10.1007/JHEP02(2014)057. arXiv: 1307.6346 [hep-ex].
- [501] Michele Selvaggi. “DELPHES 3: A modular framework for fast-simulation of generic collider experiments”. In: *J. Phys. Conf. Ser.* 523 (2014). Ed. by Jianxiong Wang, p. 012033. DOI: 10.1088/1742-6596/523/1/012033.
- [502] Jack Y. Araz, Benjamin Fuks, and Georgios Polykratis. “Simplified fast detector simulation in MADANALYSIS 5”. In: *Eur. Phys. J. C* 81.4 (2021), p. 329. DOI: 10.1140/epjc/s10052-021-09052-5. arXiv: 2006.09387 [hep-ph].
- [503] Georges Aad et al. “Search for new phenomena in events with an energetic jet and missing transverse momentum in pp collisions at $\sqrt{s}=13$ TeV with the ATLAS detector”. In: *Phys. Rev. D* 103.11 (2021), p. 112006. DOI: 10.1103/PhysRevD.103.112006. arXiv: 2102.10874 [hep-ex].
- [504] Armen Tumasyan et al. “Search for new particles in events with energetic jets and large missing transverse momentum in proton-proton collisions at $\sqrt{s}=13$ TeV”. In: *JHEP* 11 (2021), p. 153. DOI: 10.1007/JHEP11(2021)153. arXiv: 2107.13021 [hep-ex].
- [505] Federico Ambrogio. “Implementation of a search for squarks and gluinos in the multi-jet + missing energy channel (139 fb⁻¹; 13 TeV; ATLAS-CONF-2019-040)”. Version V1. In: (2021). DOI: 10.14428/DVN/NW3NPG. URL: <https://doi.org/10.14428/DVN/NW3NPG>.

- [506] Diyar Agin. “Implementation of a search for new physics with jets and missing transverse energy (139/fb; 13 TeV; ATLAS-EXOT-2018-06)”. Version V1. In: (2023). DOI: 10.14428/DVN/REPAMM. URL: <https://doi.org/10.14428/DVN/REPAMM>.
- [507] Mrowietz Malte, Sam Bein, and Jory Sonneveld. “Re-implementation of a search for supersymmetry in the HT/missing HT channel (137 fb-1; CMS-SUSY-19-006)”. Version V6. In: (2020). DOI: 10.14428/DVN/4DEJQM. URL: <https://doi.org/10.14428/DVN/4DEJQM>.
- [508] Andreas Albert. “Implementation of a search for new phenomena in events featuring energetic jets and missing transverse energy (137 fb-1; 13 TeV; CMS-EXO-20-004)”. Version V2. In: (2021). DOI: 10.14428/DVN/IRF7ZL. URL: <https://doi.org/10.14428/DVN/IRF7ZL>.
- [509] B. Dumont et al. “Toward a public analysis database for LHC new physics searches using MADANALYSIS 5”. In: *Eur. Phys. J. C* 75.2 (2015), p. 56. DOI: 10.1140/epjc/s10052-014-3242-3. arXiv: 1407.3278 [hep-ph].
- [510] Jack Y. Araz, Mariana Frank, and Benjamin Fuks. “Reinterpreting the results of the LHC with MadAnalysis 5: uncertainties and higher-luminosity estimates”. In: *Eur. Phys. J. C* 80.6 (2020), p. 531. DOI: 10.1140/epjc/s10052-020-8076-6. arXiv: 1910.11418 [hep-ph].
- [511] Jinheung Kim et al. “Implementation of the ATLAS-SUSY-2018-06 analysis in the MadAnalysis 5 framework (electroweakinos with Jigsaw variables; 139 fb¹)”. In: *Mod. Phys. Lett. A* 36.01 (2021), p. 2141004. DOI: 10.1142/S0217732321410042.
- [512] Malte Mrowietz, Sam Bein, and Jory Sonneveld. “Implementation of the CMS-SUSY-19-006 analysis in the MadAnalysis 5 framework (supersymmetry with large hadronic activity and missing transverse energy; 137 fb¹)”. In: *Mod. Phys. Lett. A* 36.01 (2021), p. 2141007. DOI: 10.1142/S0217732321410078.
- [513] Benjamin Fuks et al. “Proceedings of the second MadAnalysis 5 workshop on LHC recasting in Korea”. In: *Mod. Phys. Lett. A* 36.01 (2021), p. 2102001. DOI: 10.1142/S0217732321020016. arXiv: 2101.02245 [hep-ph].
- [514] Jack Y. Araz. “Spey: smooth inference for reinterpretation studies”. In: *SciPost Phys.* 16 (2024), p. 032. DOI: 10.21468/SciPostPhys.16.1.032. arXiv: 2307.06996 [hep-ph].
- [515] Gavin P. Salam and Gregory Soyez. “A Practical Seedless Infrared-Safe Cone jet algorithm”. In: *JHEP* 05 (2007), p. 086. DOI: 10.1088/1126-6708/2007/05/086. arXiv: 0704.0292 [hep-ph].
- [516] Michelangelo L. Mangano et al. “Matching matrix elements and shower evolution for top-quark production in hadronic collisions”. In: *JHEP* 01 (2007), p. 013. DOI: 10.1088/1126-6708/2007/01/013. arXiv: hep-ph/0611129.
- [517] Johan Alwall et al. “Comparative study of various algorithms for the merging of parton showers and matrix elements in hadronic collisions”. In: *Eur. Phys. J. C* 53 (2008), pp. 473–500. DOI: 10.1140/epjc/s10052-007-0490-5. arXiv: 0706.2569 [hep-ph].
- [518] Rikkert Frederix and Stefano Frixione. “Merging meets matching in MC@NLO”. In: *JHEP* 12 (2012), p. 061. DOI: 10.1007/JHEP12(2012)061. arXiv: 1209.6215 [hep-ph].
- [519] Thomas Gehrmann et al. “NLO QCD matrix elements + parton showers in $e^+e^- \rightarrow$ hadrons”. In: *JHEP* 01 (2013), p. 144. DOI: 10.1007/JHEP01(2013)144. arXiv: 1207.5031 [hep-ph].

Acknowledgements

I would like to express my gratitude to several individuals who have significantly contributed to the completion of this thesis. First and foremost, I would like to thank my supervisor, Michael Klasen, for his support and guidance throughout the course of my research. I am particularly grateful for the opportunity to participate in numerous conferences and workshops and therefore to travel a lot. I would also like to extend my sincere thanks to my second examiner, Christian Klein-Bösing, for making it possible for me to visit CERN. Furthermore, I thank Benjamin Fuks, whom I only met recently in person, despite working together for some years. We had many online discussions, and his experience helped us greatly in turning initial ideas into a final publication.

I thank Karol Kovařík for his help in starting my career in high-energy physics during my Bachelor's thesis and his continuous efforts to improving the undergraduate program. I would also like to thank Juri Fiaschi for getting me started with the work on Resummino in my Master's thesis and for his help in establishing the NLO+NLL resummation for the squark-electroweakino process. A special mention goes to Tomáš Ježo for the valuable experience and support during the publication of our papers. Your constructive feedback and discussions were instrumental in refining some of my ideas and taught me a lot about the intricacies of academia.

Many thanks to Luca Wiggering, my contact person for questions and valuable expertise. I am also grateful to Alexander Feike and Mathias Kuschick for the lively and productive exchanges we shared in the office. I want to acknowledge the efforts of my proofreaders for their work in improving this thesis.

Additionally, I owe thanks to Julian Jeggle and Jan Wissmann for their effort and timely responses in managing the administration of the workstations and servers at the Institute for Theoretical Physics. Next, I want to thank everyone in the department for creating a productive and enjoyable environment, despite at times keeping us admins busy.

I would also like to express my appreciation to the University of Münster, especially the PALMA cluster and its team, for providing the platform and resources to undertake and complete this work. I would like to thank the BMBF and GRK 2149 for their financial support throughout my studies, lectures and conferences.

Finally, thank you to my family and friends for their support and encouragement throughout my studies.

Alexander Puck Neuwirth

Lebenslauf

Zur Person

Geburtsdatum 03.07.1998
Geburtsort Waiblingen
Staatsangehörigkeit Deutsch
Eltern Hans und Eva Neuwirth
Familienstand Ledig
Geschlecht Männlich
Anschrift Weichselstr. 5a
48167 Münster
Email alexander.neuwirth@uni-muenster.de
alexander@neuwirth-informatik.de
Telefon +49 02506 4453012
Mobil +49 176 45903166



Hochschulstudium

Promotionsstudium in Physik

2021-2024 Promotion in Physik an der Universität Münster
Titel "Präzisionsrechnungen zu Photonen, Jets und BSM-Teilchen am LHC"
Schwerpunkt Theoretische Teilchenphysik
Betreuer Prof. Dr. Klasen
19.03.2022 56. Rencontres de Moriond QCD mit Förderung
- 26.03.2022
06.07.2022 CTEQ Schule zu QCD und Electroschwacher Phenomenologie in Pittsburgh
- 16.07.2022
07.07.2022 ICHEP22 Bologna remote
27.09.2022 Theory talk at the ALICE FSP meeting 2022 on "Prompt photon production with
- 30.09.2022 two jets"
04.11.2022 Resummino presentation at CERN SUSY group Meeting remote
25.03.2023 Poster presentation on direct photon + 2 jets at Hard Probes 2023
- 31.03.2023
06.06.2023 Talk at the "Parton Shower and Resummation" workshop 2023
- 08.06.2023
09.10.2023 Talk at the "Python in HEP" workshop 2023
- 12.10.2023
23.10.2023 Poster and Flashtalk at the "Forward Physics and QCD at the LHC and EIC"
- 27.10.2023 workshop 2023
13.11.2023 Attend the "Event generators' and N(n)LO codes' acceleration" workshop 2023
- 14.11.2023

- 19.01.2024 EIC theory visit at BNL and Pittsburgh
- 09.02.2024
- 05.03.2024 deRSE 2024 conference talk on EESSI
- 07.03.2024

Masterstudium in Physik

- 2019-2021 Masterstudium in Physik an der Universität Münster mit Nebenfach Mathematik
- 15.10.2021 Masterarbeit mit Gesamtnote 1,0 (sehr gut)
 - Titel "Resummationsvorhersagen für die assoziierte Produktion von Squarks und Electroweakinos am LHC"
- Schwerpunkt Theoretische Teilchenphysik
 - Betreuer Prof. Dr. Klasen
- 25.07.2021 52. Herbstschule Maria Laach für Hochenergiephysik
- 03.08.2021

Bachelorstudium in Physik

- 2016-2019 Bachelorstudium in Physik an der Universität Münster mit Nebenfach Informatik
- 12.09.2019 Bachelorarbeit mit Gesamtnote 1,0 (mit Auszeichnung)
 - Titel "Monte-Carlo-Generierung von 3-Jet Events bei Elektron-Positron-Annihilation"
- Schwerpunkt Theoretische Teilchenphysik
 - Betreuer Prof. Dr. Klasen

Tätigkeiten

- Seit 03.2021 Mitglied in der Physik Fachschaft Universität Münster
 - 09.2020 Übungsgruppenleiter für theoretische Physik (Quantenmechanik und Quantentheorie)
 - 10.2022 an der Universität Münster
- Since 10.2020 Administration der Server and Workstations des Institus für Theoretische Physik an der Universität Münster
 - 07.2020 Netzwerk Teilchenwelt Fellow
 - 02.2022
- Seit 03.2022 Netzwerk Teilchenwelt Mediator
 - 11.2021 Assoziiertes Mitglied im Graduiertenkolleg 2149 "Starke und Schwache Wechselwirkung - von Hadronen zur Dunklen Materie" an der Universität Münster
 - 04.2022
- Seit 05.2022 Vollmitglied im Graduiertenkolleg 2149 "Starke und Schwache Wechselwirkung - von Hadronen zur Dunklen Materie" an der Universität Münster

Schulbildung

- 2016 Abschluss Abitur mit Durchschnittsnote 1,2 und MINT-EC-Zertifikat
- 2013-2016 Gymnasium Wolbeck
- 2008-2013 Remstal-Gymnasium
- 2004-2008 Grundschule Strümpfelbach